MEASURING AND MODELLING THE ABSOLUTE OPTICAL CROSS-SECTIONS OF INDIVIDUAL NANO-OBJECTS

ATTILIO ZILLI

Thesis submitted to Cardiff University
for the degree of Doctor of Philosophy

FEBRUARY 2018

SUPERVISORS

Prof. Paola Borri, School of Biosciences

Prof. Wolfgang Langbein, School of Physics and Astronomy

This document was typeset using the typographical look-and-feel `classicthesis` developed by André Miede. The style was inspired by Robert Bringhurst's seminal book on typography "*The Elements of Typographic Style*". `classicthesis` is available for both LaTeX and LyX at the following URL:

`https://bitbucket.org/amiede/classicthesis/`

Attilio Zilli, *Measuring and modelling the absolute optical cross-sections of individual nano-objects*.

Dedicated to the memory of my friend and colleague
Jūris Kiškis

When I am laid in earth
May my wrongs create
No trouble in thy breast;
Remember me, remember me,
But ah! forget my fate.

—Henry Purcell, *Dido and Aeneas*

ABSTRACT

Nanoparticles are ubiquitous in nature, and the number of technological applications exploiting nano-objects, either synthesized chemically or fabricated lithographically, is in steady rise. In particular, metal nano-objects exhibit resonant modes corresponding to an enhanced coupling to electromagnetic radiation. The interaction of light with a nano-object is wholly described by its cross-sections for absorption and elastic scattering. In this thesis we present a method to measure the absolute amplitude of the cross-sections. Differently from currently available techniques, we account for the finite angular collection of the objective via an analytical model of the scattering process, thereby rendering our method accurate also for objects dominated by scattering and high numerical aperture detection. The model of scattering assumes that the nano-object is placed at a planar dielectric interface, representing the substrate, and a homogeneous optical environment is obtained as a limiting case. The accuracy of the quantitative method was tested on several model systems using two widespread experimental techniques: Microspectroscopy and widefield imaging, which are both implemented with a simple experimental set-up, constituted by a commercial microscope equipped with an imaging spectrometer or a camera. In order to quantitatively simulate microscopy experiments, a realistic description of the excitation must be included in numerical models. In this thesis we describe novel modelling practices which reproduce typical coherent or incoherent microscope illumination. Comparison of quantitative experimental and numerical results is used to estimate parameters describing the geometry of a nano-object, such as the diameter or

the aspect ratio. In conjunction with the high-throughput capabilities of widefield image analysis, quantitative cross-section measurements and optical characterization of the geometry can provide a thorough statistical appraisal of the dispersity of the structural and optical properties of a sample. Therefore, this thesis represents a significant step towards an 'all-optical' characterization of nano-objects, complementing costly and time-consuming electron microscopy techniques.

ACKNOWLEDGEMENTS

When embarking onto a PhD degree, formal supervision is always granted and therefore should not need to be acknowledged. However, many other cases I have witnessed have shown me that supervision of good quality is on the contrary far from common: With their wise guidance — and occasionally a gentle push — Paola Borri and Wolfgang Langbein have led me to achievements I never knew I was capable of.

I am also indebted to many members of our Quantum Optoelectronics & Biophotonics group, particularly to all those in the School of Biosciences where I have been based over the four years of my PhD. I would like to mention first Lukas Payne, who patiently assisted me with his image analysis software and was willing to tweak it overnight in order to fulfil every odd request of mine. George Zoriniants introduced me to the marvels of the Ettore set-up, and was always available to open his Landau with me whenever I turned to him with my poor understanding of electromagnetic theory. Whenever you cannot make sense of the set-up behaviour, or you are looking for that particular filter which has always been in that box (and now is not), Iestyn Pope is actually who you should be looking for: He came to my aid in countless occasions. Thanks to Yisu Wang for his practical help in sample preparation, and for elegantly pretending not to know I have been using his chemicals all along. And last but not least, thanks to Naya Giannakopoulou for the many conversations — sometimes we also talked about science.

I am grateful to the two examiners sitting in my *viva*, Otto Muskens (external) and Egor Muljarov (internal), for the time they spent reading through this thesis; their valuable recom-

mendations helped me to improve the clarity of many figures and the readability of a few sections.

My position has been part of a network called FINON, gathering twelve PhD projects in several institutions throughout Europe. I would like to give credit to the whole finonship for being such an amazing team against many odds, and always being there for each other when in need: Jūris Kiškis, Carolina Rendón Barraza, Alberto Lombardini, Marie Didier, Alexandra Paul, Michael Stührenberg, Diana Ribeiro, Amala Elizabeth, Xiao Ling, Vitalijs Zubkovs, Siyuan Wang, Steffi Jung, and our indefatigable representative Naya Giannakopoulou.

Within the framework of the FINON, my secondment at the Institut Fresnel in Marseille was a great experience, rich in scientific and human content. I am grateful to Sophie Brasselet for hosting me in the MOSAIC group, to Carolina Rendón Barraza for taking good care of me during my stay (inside and outside the lab), and to Naveen K. Balla, my last resort to operate the set-up when I eventually put myself to do some measurements.

This work was supported by the European Commission, Research Executive Agency — Marie Curie Actions 607842 FINON ITN-2013

OUTLINE

Scattering and absorption of light by small particles underpin several everyday-life natural phenomena, such as the colours of the sky and the clouds, the hues of rainbows and irides, and the opalescence of some precious stones. Much attention has been drawn in particular to the optical properties of metal nano-objects (NOs), which are ruled by the presence of plasmon resonances and display a rich phenomenology. The fundamental concepts and the main results of the electromagnetic theory describing the interaction of light with NOs are presented in CH. 1. Further discussion is devoted to the case of a NO near a planar dielectric interface, which corresponds to a common experimental configuration in microscopy, where NOs are placed on a transparent substrate for imaging. CH. 1

The strong coupling of metal NOs with electromagnetic radiation at the plasmon resonance offers ample potential to mould the flow of light at the nanoscale. SEC. 2.1 reviews the operating principles of a few relevant technological applications selected amongst the numerous proposed. Now, the sensitive dependence of the optical properties on the size, shape, and material composition of the NO provides the opportunity to tailor these properties to the needs of a specific application. Over the last few decades the capability to fabricate NOs — via either chemical synthesis or lithographic techniques — has in fact reached a high degree of control; on the other hand, the experimental means to characterize accurately their optical properties are still defective to some extent. Specifically, the optical properties are fully described by the optical cross-sections (OCS) spectra for the active optical processes (here scattering and ab- CH. 2

sorption), but to date only a handful of techniques have been proposed which can measure the OCS amplitude in absolute units at the single NO level. As highlighted in SEC. 2.2, all these techniques require costly equipment, as well as significant expertise to operate it and to extract the OCS amplitude from the data. As a result, while much effort has been devoted to investigating the effect of the size and shape of the NO on the spectral features of the OCS (that is, the position and width of the plasmon resonances), only a few experimental measurements of absolute OCS amplitude have been reported so far.

CH. 5 The core content of this thesis, presented in CH. 5, is a novel data analysis procedure to retrieve the absolute OCS from micro-spectroscopy or widefield imaging measurements. These two techniques are somewhat complementary: Micro-spectroscopy yields detailed spectral information, whereas widefield imaging provides a high-sensitivity and high-throughput characterization, e. g. of a colloidal sample. The quantitative analysis relies on the knowledge of the angular distribution of the radiation scattered by the NO. Essentially, this is required because only a fraction of the total scattering falls within the acceptance of the objective and is thereby detected. Such angular distribution can be computed through either numerical or analytical models. In order to minimize the amount of work demanded to the end user of our quantitative method, we developed an analytical model of scattering by a NO placed on a dielectric substrate under incoherent microscope illumination. The two main assumptions of the model — which are reasonably well met in many cases of interest — require that the NO is much smaller than the wavelength of the exciting light, and that the mismatch between the refractive indices of the substrate and the medium where the NO is immersed is not too large. The full derivation is provided for various forms of the polarizability tensor representing the most commonly encountered geomet-

ries of plasmonic modes. Although the analytical calculations involved are rather cumbersome, these have been automated into a stand-alone executable which only requires a few experimental parameters as user input.

In contrast with other quantitative techniques, the data required for quantitative measurements can be acquired via a simple experimental set-up — namely, a commercial microscope equipped with a camera or a spectrometer — with a few small modifications and one-off calibrations. We tested our quantitative method on three model systems: Gold spheres in a homogeneous optical environment; polystyrene spheres in air deposited onto a glass substrate; and elongated gold nanocrystals (so-called nanorods). In the latter case, to assess how accurately our analytical model accounts for the presence of an interface, we correlated two measurements of the same nanorods in different immersion media: Air and oil matching the refractive index of the glass substrate. These samples and configurations are all relevant for applications and widely studied in literature, and together encompass a large variety of material and geometrical features. The experimental set-up and measurement procedure adopted, and the results thereby obtained, are discussed in CH. 6. While the optical properties of individual NOs constitute *per se* valuable physical information, they can also be used to infer structural information: By comparing or fitting numerical or theoretical OCS to the experimental data some parameters describing the geometry of the object (e. g. the diameter of a sphere, length and width of a rod, etc.) can be estimated; such an optical sizing is performed for the three model systems above.

CH. 6

We computed numerically the OCS of individual NOs close to an interface using a commercially-available software implementing the finite element method. The numerical tools we relied on for electromagnetic simulations are introduced in

CH. 4

SEC. 4.1. The model we used is discussed in SEC. 4.2 along with the main results obtained for the most complex system we studied: A gold nanorod placed on a dielectric substrate.

CH. 3 While the resonant modes of a system are determined by its geometry and material composition solely, their amplitudes in scattering and absorption spectra depend on the exciting polarization. Now, in order to achieve a high spatial resolution, illumination in modern microscopes is often focused by high numerical aperture lenses. This means exciting the NO with a large range of incidence directions, and hence of polarizations. When modelling the OCS it is therefore essential to reproduce the microscope illumination too, for a meaningful comparison with experimental results; on the other hand, computed OCS reported in literature are obtained using a coherent plane wave, just because it is the simplest excitation to input. On the contrary, in SEC. 3.1 we present two approaches beyond current modelling practise to reproduce incoherent microscope illumination in numerical simulations.

CH. 3 An additional topic included in this thesis is the numerical
CH. 4 simulation of coherent nonlinear scattering processes. Specifically, we modelled an experiment where coherent-anti-Stokes Raman scattering is enhanced by the intense local fields in the vicinity of an individual metal nanoparticle. SEC. 4.3 discusses the main features of the experiment and its implementation in the model, both of which contain significant elements of novelty. We also explain how to compute the experimental observables in the model, and show preliminary comparison with experimental data. Importantly, the tightly-focused, coherent illumination used for measurements must be reproduced in the model using an exact vectorial description of the objective point-spread function given in SEC. 3.2.

CONTENTS

LIST OF FIGURES

ACRONYMS

4WM	four-wave mixing
AR	aspect ratio
BF	brightfield
BFP	back focal plane
CARS	coherent anti-Stokes Raman scattering
CCD	charge-coupled device
CMOS	complementary metal-oxide-semiconductor
CPU	central processing unit
CTAB	cetyl-trimethyl-ammonium-bromide
DDA	discrete dipole approximation
DF	darkfield
DIC	differential interference contrast
DLS	dynamic light scattering
EWFD	electromagnetic waves frequency domain
FDTD	finite-difference time-domain
FEM	finite element method
FF	far field
FWHM	full width at half maximum
GNR	gold nanorod
GNS	gold nanosphere
IR	infrared
LED	light-emitting diode
LSPR	localized surface plasmon resonance

NA	numerical aperture
NF	near field
NO	nano-object
NP	nanoparticle
OCS	optical cross-sections
OPO	optical parametric oscillator
PEC	perfect electric conductor
PI	photothermal imaging
PMC	perfect magnetic conductor
PML	perfectly matched layer
PSF	point spread function
PT	photothermal therapy
QWLSI	quadriwave lateral shearing interferometry
RAM	random access memory
RHS	right-hand side
RMS	root mean square
ROI	region of interest
SMS	spatial modulation spectroscopy
SNR	signal-to-noise ratio
SVEA	slowly-varying envelope approximation
TEM	transmission electron microscopy
THG	third harmonic generation
TIR	total internal reflection
URL	uniform resource locator
UV	ultraviolet
VIS	visible

Part I

BACKGROUND AND MOTIVATION

1

OPTICAL PROPERTIES OF NANO-OBJECTS

In 1959 R. P. Feynman delivered a now celebrated talk[1] titled *There's plenty of room at the bottom*, where he speculated on the opportunities and the challenges presented by the "problem of manipulating and controlling things on a small scale", namely what we call today *nanotechnology*. Although the laws of classical physics governing the nanoscale are long known, and no new fundamental principles are to be found, the "strange phenomena that occur in complex situations" have proven stunningly fecund of conceptual implications and technological applications. In fact, over the last few decades, several of Feynman's dream scenarios — such as miniaturized computers and electron microscopes with atomic resolution — have become available, when not affordable, commercial products. Particularly, the advances of chemical synthesis and lithographic fabrication techniques allow us nowadays to manipulate matter with high accuracy almost down to the atomic scale; and we are commencing to appreciate the reach of Feynman's prediction: "When we have some control of the arrangement of things on a small scale, we will get an enormously greater range of possible properties that substances can have, and of different things that we can do."

When optical properties are concerned, a nano-object (NO) can be loosely defined as an object[i] having size smaller than the wavelength of light λ. As this work focuses on the optical

i This umbrella term is deliberately used to encompass different sorts of *objects*: Individual particles, aggregates, composite structures and tiny features of macroscopic objects, such as sharp tips.

frequencies ranging from the near infrared (IR) to the near ultraviolet (UV), this definition covers objects with at least one dimension $\sim 100\,\text{nm}$ or less. This size is comparable to several fundamental quantities ruling the electromagnetics of the system, such as λ and, for metals, the mean free path of carrier diffusion and the skin depth. As a results, and in contrast to macroscopic objects, the optical properties of NOs depend on their size and shape often in complex fashions, hence originating a rich phenomenology and a large potential to harness the material properties for applications.

On the other end of the scale, we will not call NOs those with at least one dimension less than a few nm, corresponding to a few atoms, whose properties are described through quantum theory.[ii] NOs can be further categorized according to their *macroscopic dimensionality*, defined as the number of dimensions $\gtrsim 100\,\text{nm}$. Relevant examples for science and technology are magnetic nanoparticles (0D), semiconducting nanowires (1D) and metallic thin films (2D). Although many considerations can be generalized to NOs having a larger dimensionality, in this work we refer specifically to 0D objects. Among these, we reserve the term nanoparticle (NP) to individual objects having simple shapes — thus excluding complex lithographic structures, oligomers, and aggregates.

1.1 SCATTERING, ABSORPTION, AND EXTINCTION

A spatial heterogeneity of the optical properties in a physical system gives always rise to *scattering* of electromagnetic radiation. Scattered light is radiated by the accelerated electric

ii Semiconducting NOs are an exceptional case, inasmuch as they display quantum behaviour (such as the energy quantization due to carrier confinement in quantum dots) for NOs up to tens of nm in size.

charges (free or bound to atoms) in the obstacle, which are set in motion by the impinging electric field $\mathbf{E}_i$. Part of the incident electromagnetic energy can be transferred to the atomic lattice (through collisions, in a naive classical picture) and is thereby converted into heat via *absorption*. Several natural phenomena originate from scattering and absorption of light by NOs, such as the colours of the sky and the clouds, the reduction of visibility due to haze and smoke, the hues of rainbows and irides; to give another example, much scattering theory has been developed in order to investigate the composition of interstellar dust. There has been therefore a longstanding effort to investigate both theoretically and experimentally the interaction of small objects with radiation,[2,3] starting with the pioneering work by J. Tyndall, Lord Rayleigh and L. Lorenz in the second half of the XIX century.

Let us consider an electromagnetic mode in a homogeneous, infinite space: This could be a plane wave with an infinite wavefront, or a a spatially-localized beam. The insertion of a NO removes some power from the mode, which is for example transferred to other spatial modes via scattering. The optical cross-sections (OCS) describe the coupling strength of light with the NO for each optical processes: Scattering, absorption, fluorescence, and so on. They are indicated by σ and defined as the power P removed from the mode by the process considered and normalized to the incident intensity I_i

$$\sigma \equiv P/I_i \,. \tag{1.1}$$

Hence σ have the unit of an area and can be thought of as the equivalent surface parallel to the wavefront where the interaction would occur in a simplistic ray optics picture. We emphasize that the OCS are not an intrinsic property of the target alone, but depend as well on the properties of the mode considered, e. g. on the polarization for a plane wave. The OCS are typically

positive quantities — $\sigma < 0$ would indicate the NO is a medium with optical gain.

For the total power P_{ext} removed by the target from the incident mode EQ. (1.1) defines the *extinction* cross-section σ_{ext}. In those cases — such as for all NOs discussed in this thesis — where the yield of inelastic (e. g. Raman) scattering, fluorescence, and nonlinear interactions is negligible with respect to absorption and elastic scattering, one has

$$\sigma_{ext} = \sigma_{abs} + \sigma_{sca} \,. \tag{1.2}$$

In ray optics, σ_{ext} is tantamount to the intuitive concept of *shadow*. In particular, for opaque objects under plane wave illumination, it coincides with the geometrical cross-section σ_{geo} transverse to the propagation direction of the wave. The interaction of light with NOs is governed by diffraction, and therefore a wave optics description is inescapable.[iii] Extinction can thus be regarded as the wave optics generalization of shadow, where in general $\sigma_{ext} \neq \sigma_{geo}$. In the rest of this section, we will review a few analytical expressions of the OCS under various assumptions.

Let us treat first the simple case of a NO with size $D \ll \lambda$.[2,4] In such scenario, the exciting field is constant over the volume V of the NO, and therefore this regime is referred to as the *electrostatic approximation*. Lord Rayleigh provided the first analytical treatment of scattering by subwavelength spheres in order to explain the blue colour of the sky.[5] Instead of a complete mathematical derivation, we will present here the elegant dimen-

iii In fact, a ray optics treatment of scattering is often inadequate even for macroscopic objects. For instance, wave optics calculations show that a large ($D \gg \lambda$) opaque sphere has $\sigma_{ext} = 2\sigma_{geo}$. This surprising result, known as *extinction paradox*, is due to diffraction of light passing outside the sphere, corresponding to scattering at extremely small angles, see Bohren and Huffman[2] (§4.4.3).

sional argument put forward by Rayleigh himself.[iv] He argued that, at any given distance r from the scatterer, the amplitude of the scattered wave must be proportional to the amplitude of the exciting one, and their ratio can depend solely on a handful of relevant quantities

$$\frac{A_{sca}}{A_i} \propto f(r, \lambda, c, V, \varepsilon_0\varepsilon_{NO}, \varepsilon_0\varepsilon_m) \tag{1.3}$$

being ε_{NO} and ε_m the relative permittivities of the NO and the surrounding medium, respectively. Now, the ratio (1.3) is adimensional, and the speed of light c is the only argument of f having a time dimension; consequently, f cannot depend on c. Similarly, since $\varepsilon_0\varepsilon_{NO}$ and $\varepsilon_0\varepsilon_m$ are the sole arguments with a mass dimension, they can only appear within an adimensional function g of their ratio. Moreover, A_{sca} is directly proportional to V by virtue of the superposition property of the linear process considered: Two identical NOs would scatter exactly twice as much as an individual one. Finally, A_{sca} is inversely proportional to r because of energy flux conservation: The scattered wave is an expanding spherical wave with an angular modulation superimposed. Putting together these observations, and disregarding angular dependencies and other constant factors

$$\frac{A_{sca}}{A_i} \propto \frac{V}{r\lambda^2}\, g\left(\frac{\varepsilon_{NO}}{\varepsilon_m}\right) \tag{1.4}$$

so that the unknown spectral dependence has been determined. Assuming ε_{NO} and ε_m have a weak dispersion,[v] EQ. (1.4) implies that short wavelength components are scattered more effectively. This explains why the sky appears blue,[vi] whereas

iv A further virtue of this reasoning versus the analytical calculations resides in its generality: No assumptions are made concerning the NO shape.

v The scope of this consideration is thus limited in practice to dielectric NOs.

vi It is not violet because the Sun emission is centred in the green. Conversely, the Sun itself appears yellow when observed directly, because the shorter

pictures taken outside the Earth's atmosphere show that, in absence of scattering, the sky is actually jet black.

In agreement with the dimensional argument presented above, exact calculations for a small sphere ($D \ll \lambda$) illuminated by an unpolarized plane wave yield[2]

$$I_{sca} = \frac{1+\cos^2\theta}{2r^2}\left(\frac{2\pi}{\lambda}\right)^4\left(\frac{D}{2}\right)^6\left|\frac{\varepsilon_{NO}-\varepsilon_m}{\varepsilon_{NO}+2\varepsilon_m}\right|^2 I_i \qquad (1.5)$$

where θ is the scattering angle with respect to the propagation direction. Now, EQ. (1.5) corresponds to the intensity radiated by an oscillating electric dipole[vii] of amplitude $p = \varepsilon_0\varepsilon_m\alpha E_i$ using the polarizability[viii]

$$\alpha = \frac{\pi}{2}D^3\frac{\varepsilon_{NO}-\varepsilon_m}{\varepsilon_{NO}+2\varepsilon_m}. \qquad (1.6)$$

Thus the scattering of a small NO can be described as the radiation of an appropriate set of electric dipoles; this holds regardless of the NO shape, although exact analytical expressions of α are known only for a few simple shapes, such as just seen for the sphere. This description, known as *dipole approximation*, is of great conceptual value, and we will rely on it for several derivations in the following.

---

wavelength components of its emission are removed by scattering — even more so at sunset, when the sun rays follow a longer path in the atmosphere, so that the Sun appears orange or red.

vii Precisely, being the excitation unpolarized, it is the average of the intensities radiated by any two dipoles orthogonal to each other and to the propagation direction of the impinging wave.

viii Different definitions of α are given in literature; in this work it is defined as having units of m^3 via $p = \varepsilon_0\varepsilon_r\alpha E$. In particular, the expression (1.6) is analogous to the Clausius–Mossotti (or Lorentz–Lorenz) relation, which is derived using a model equivalent to the problem presented here: A spherical inclusion in a homogeneous medium excited by a static field. Maier[6] (§5.1) reports a simple derivation of this results.

We conclude the overview of the electrostatic approximation by providing the expressions of the OCS for a sphere under plane wave excitation. The scattered power P_{sca} is the flux of I_{sca} given by EQ. (1.5) across a spherical surface of arbitrary radius r; by substituting P_{sca} into EQ. (1.1) one obtains[ix]

$$\sigma_{sca} = \frac{2\pi^5}{3}\frac{D^6}{\lambda^4}\left|\frac{\varepsilon_{NO}-\varepsilon_m}{\varepsilon_{NO}+2\varepsilon_m}\right|^2 = \frac{k^4}{6\pi}|\alpha|^2 \tag{1.7}$$

where EQ. (1.6) was used in the last equality. As for absorption, one has[2]

$$\sigma_{abs} = \pi^2\frac{D^3}{\lambda}\,\mathrm{Im}\left[\frac{\varepsilon_{NO}-\varepsilon_m}{\varepsilon_{NO}+2\varepsilon_m}\right] = k\,\mathrm{Im}\,\alpha\,. \tag{1.8}$$

Note that $\sigma_{sca} \propto D^6$ whereas $\sigma_{abs} \propto D^3$: Large NOs are generally dominated by scattering, and small ones by absorption unless transparent. For metal NOs (which are good absorbers) the cross-over between the two regimes occurs typically between $D = 50\,\mathrm{nm}$ and $100\,\mathrm{nm}$. An exact solution in the electrostatic approximation has been derived for a tri-axial ellipsoid, also in the case of multiple concentric shells of different materials.[2]

Looking for a theoretical justification of the variety of colours displayed by colloidal suspensions[x] of metal NPs (more on these in SEC. 1.2) in 1908 G. Mie derived the exact solution of Maxwell's equations for a sphere in a homogeneous medium.[7] Unlike previous works on this subject, Mie did not make any

ix Throughout this thesis λ, k, and c indicate respectively the wavelength, wavevector, and speed of light in the medium; the corresponding quantities in vacuum are λ_0, k_0, and c_0.

x In chemistry, a *suspension* is a mixture of microscopic "particles" (which can as well be in liquid or gas phase) within a host medium; contrary to a solution, the two phases are separated. A *colloid* is a suspension of particles so small that they do not settle on a typical experiment timescale.

assumptions on the size of the sphere, nor on the material composition of the sphere and the embedding medium. The calculations are based on the decomposition of the total electric field into the *exciting field*, which would be there in absence of the object, and the *scattered field* due to the object perturbation: $\mathbf{E}_{tot} = \mathbf{E}_{exc} + \mathbf{E}_{sca}$. As a result, the time-averaged Poynting vector, representing the electromagnetic energy flux, is decomposed as $\mathbf{S}_{tot} = \mathbf{S}_{exc} + \mathbf{S}_{ext} + \mathbf{S}_{sca}$; the cross term $\mathbf{S}_{ext}$ accounts for extinction, which stems from the interference between the incident and the scattered waves.[xi] As will be shown in SEC. 4.1, this formalism is pivotal in order to solve the wave equation in the frequency domain.

The generality of Mie's approach laid the foundations of modern scattering theory, and the large number of experimental results he was able to explain ensured the long-lasting notoriety of his work, which is regarded as one of the earliest triumphs of Maxwell's electromagnetics. The solution for a sphere has later been generalized to more complex geometries, such as spheroids, cylinders, layered spheres and aggregates of spheres. Mie's theory, albeit conceptually straightforward, involves rather cumbersome calculations, which are generally solved numerically; we refer the reader to the book by Quinten[8] for a modern presentation of the theory and the ensuing extensions.

A fundamental result of wave scattering theory, independent of the size and shape of the scatterer, is the *optical theorem*[9]

$$\sigma_{ext} = \frac{4\pi}{k E_i^2} \operatorname{Im}\left[\mathbf{E}_{exc}^* \cdot \mathbf{E}_\infty(\hat{\mathbf{k}}_{exc})\right]. \tag{1.9}$$

For the theorem to hold in this form, $\mathbf{E}_{exc}$ must be a plane wave travelling along $\hat{\mathbf{k}}_{exc}$; $\mathbf{E}_\infty(\hat{\mathbf{r}}) = \lim_{r\to\infty} r\,\mathbf{E}_{sca}(\mathbf{r})$ is the pro-

xi See Bohren and Huffman[22] (§3.3) for the explicit expression of the various $\mathbf{S}$ terms and a more thorough discussion of their physical meaning.

jection of $\mathbf{E}_{sca}$ to the far field (FF).[xii] EQ. (1.9) thus relates the extinction to the forward scattering at an infinite distance from the object. Looking at EQ. (1.9) one might wonder why the absorptive contribution to extinction does not show up explicitly, and how can the forward scattering account for the total extinction, when the scattered wave carries in all direction. As to the first point, one needs to consider that scattering and absorption are not independent phenomena: The scattering amplitude depends also on the electric field within the object, which is in turn affected by the absorptive response of the object material. The forward direction dependence in the optical theorem stems instead from the coherence between the incident and the scattered wave. The extinction is the net energy flow of the interference term between these two fields. Even in the limit $r \to \infty$, the angular distribution of this flow depends on r for all directions except forwards: Being the extinction obviously independent of r, it cannot but be related to the interference in this very direction.[9]

1.2 METAL NANO-OBJECTS

M. Faraday is often credited for being the first scientist conducting systematic research into the field of nanoscience. In the 1850s he was investigating the transmission of light through gold films of subwavelength thickness, when he noticed that the residuals of the chemical etching of gold leaves had a rather peculiar appearance. In particular he observed that, by adding phosphorus to a gold chloride solution, "gold is reduced to exceedingly fine particles, which becoming diffuse, produce a beautiful ruby fluid"[10] such as the one in FIG. 1.1. He started

xii On P. 92 a more precise definition of $\mathbf{E}_{\infty}$ will be provided, and it will be shown how to operatively compute $\mathbf{E}_{\infty}$.

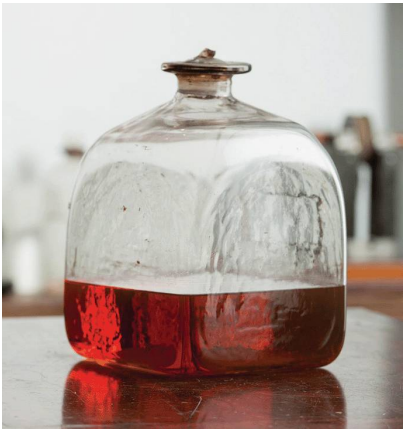

FIGURE 1.1: The "ruby fluid" prepared by M. Faraday on display at the Faraday Museum in London. It is a colloidal suspension of gold NPs, whose spectrally selective absorption endows the mixture with its characteristic colour. Credit: Royal Institution/Paul Wilkinson.

experimenting extensively with the chemistry of gold colloids, and observed a range of different blue and violet hues "for the production of which I can see no reason to imagine any other variation than the existence of particles of intermediate sizes or proportions." These early studies mark the beginning of *nanoplasmonics*, which studies the interaction of metal NOs with radiation and is currently a very active research field, with thousands of papers published every year.[11,12]

The response of metals to electromagnetic excitation is underpinned by the conduction electrons, which are free to move inside the metal volume, bounded solely by the NO surface. This free electron gas is called *plasma*, and is cast into periodic oscillation by $\mathbf{E}_{\text{exc}}$. In first approximation, such system can be described as a harmonic oscillator driven by $\mathbf{E}_{\text{exc}}$, while the accumulation of opposite charges at either end of the NO produces a restoring force, and the collisions of the electrons between themselves or with the ionic lattice create a damping mechanism. The resonant frequency of the oscillator, where the coupling to the driving force is maximum — that is, the energy transfer from $\mathbf{E}_{\text{exc}}$ to the plasma is most efficient — is determined by the geometry and material properties of the system. The

corresponding coherent, resonant plasma excitation is called *localized surface plasmon resonance* (LSPR), with emphasis on the spatial confinement of the excitation at the NO,[xiii] in opposition to *surface plasmon polaritons*, which travel along the interface between a medium and a dielectric.[6] By virtue of the intricate dependence of the LSPR frequency, amplitude, and lifetime on the parameters of the systems, metal NOs are the subject of ongoing fundamental research more than 150 years after their discovery.[13,14]

LSPRs manifest themselves in OCS spectra as peaks occurring close to the minimum of the denominator of α given by EQ. (1.6), corresponding to the condition

$$\operatorname{Re}\varepsilon_{\mathrm{NO}}(\lambda_0) = -2\varepsilon_{\mathrm{m}} \tag{1.10}$$

where a non-absorbing embedding medium was assumed ($\operatorname{Im}\varepsilon_{\mathrm{m}} = 0$). In literature EQ. (1.10) is often referred to as the *Fröhlich condition*, and for an immersion medium with $\varepsilon_{\mathrm{m}} > 0$ it can only be fulfilled if $\operatorname{Re}\varepsilon_{\mathrm{NO}} < 0$, that is, by NOs of metallic character.[xiv] In FIG. 1.2 we display $\varepsilon(\lambda_0)$ for silver and gold, which are the two most investigated plasmonic materials. Let us postpone the comparison between different datasets to SEC. 6.2, and concentrate here on the general features of ε.

The electronic structure of copper, silver, and gold is characterized by a completely full *d* band;[19] the UV features of ε correspond to transitions from the *d*-band to just above the Fermi level in the conduction band.[xv] In particular, for gold the *d* band extends from the UV well into the visible (VIS) range, up to

xiii For NOs having size comparable to or smaller than the skin depth ($\Delta \simeq 40\,\mathrm{nm}$ is a typical value for metals at optical frequencies) the LSPR extends over the whole volume rather than the surface only.

xiv An equivalent argument holds for $\varepsilon_{\mathrm{NO}} \in \mathbb{R}$ and $\varepsilon_{\mathrm{m}} \in \mathbb{C}$, namely for dielectric inclusions within a metal volume.

xv Precisely $4d \rightarrow 5sp$ in silver and $5d \rightarrow 6sp$ in gold.

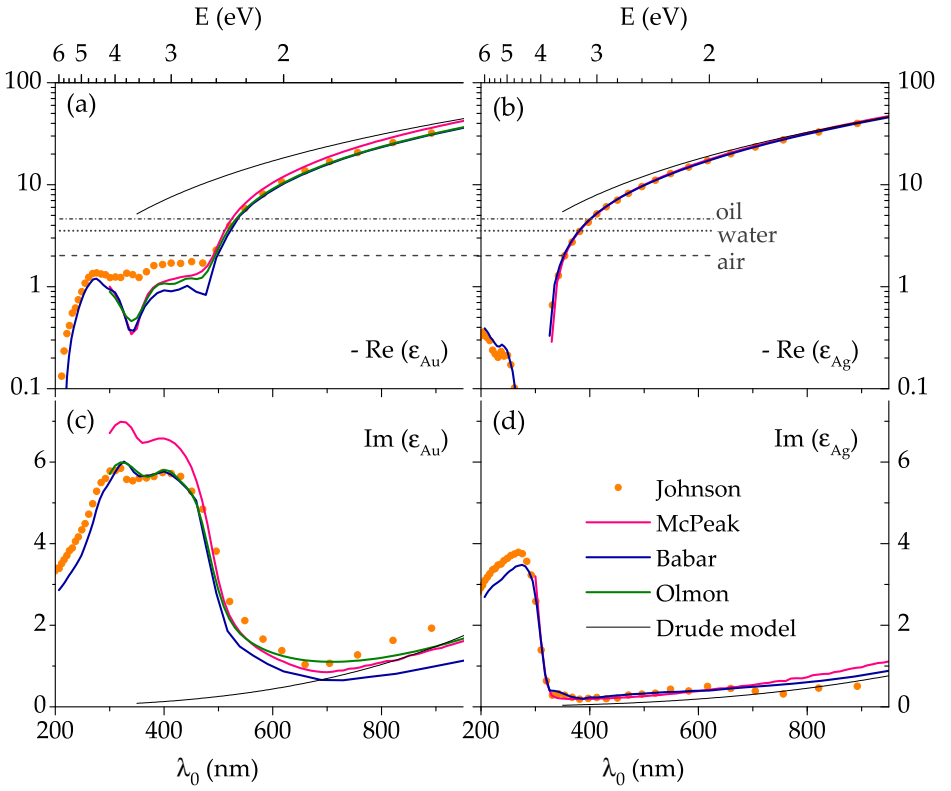

FIGURE 1.2: Relative permittivity ε of Au (a,c) and Ag (b,d) as a function of wavelength λ_0. Coloured lines are experimental datasets, whose source is indicated by the legend.[15–18] The thin black line is the Drude model (1.11) with parameters $\varpi_{Au} = 8.8\,\text{eV}$, $\varpi_{Ag} = 9.0\,\text{eV}$, $\gamma_{Au} = 50\,\text{meV}$, and $\gamma_{Ag} = 21\,\text{meV}$ (see http://www.wave-scattering.com/drudefit.html, visited on 13/10/2017). The horizontal lines are $2\varepsilon_m$ (approximately constant in this wavelength range) for typical immersion media used in experiments: (- - -) air, $n = 1.00$; (⋯) water, $n = 1.33$; (-·-) immersion oil matching microscope glass, $n = 1.52$.

550 nm (green): The selective absorption of short wavelengths, whereas long ones are reflected, lends to the bulk metal its distinctive yellow colour. At longer wavelengths, and to a better degree for silver, ε is described well by the Drude–Lorentz free-electron model[19]

$$\varepsilon(\omega) = 1 - \frac{\varpi^2}{\omega^2 + i\gamma\omega} \tag{1.11}$$

where the *plasma frequency* ϖ and the *relaxation rate* γ are material parameters. Graphically, EQ. (1.10) corresponds to the intersection of $-\operatorname{Re}\varepsilon$ and $2\varepsilon_m$, assumed constant in the spectral range where the LSPR occurs; the predicted effect of an optically denser embedding medium is thus a redshift of the LSPR.

LSPRs decay quickly (~10 fs); such a short lifetime reflects into broad plasmon peaks (10 to 100 nm FWHM) in σ_{abs} and σ_{sca} spectra. Generally speaking, plasmonic excitations decay via both non-radiative and radiative processes. *Non-radiative damping* is due in first place to electron–electron collisions leading to a hot carrier energy distribution on a 100 fs timescale. Thereafter the hot plasma thermalizes with the lattice via electron–phonon scattering (1 to 10 ps) eventually transforming the incident electromagnetic energy into heat (absorption). The non-radiative damping in a bulk material is represented by $\operatorname{Im}\varepsilon$.[xvi] For instance, one can rewrite EQ. (1.8) so to highlight it is a Lorentzian function of $\operatorname{Re}\varepsilon_{NO}$ (not of λ)

$$\sigma_{abs}(\lambda) = 3\pi^2\varepsilon_m\frac{D^3}{\lambda}\frac{\operatorname{Im}\varepsilon_{NO}}{(\operatorname{Re}\varepsilon_{NO} + 2\varepsilon_m)^2 + (\operatorname{Im}\varepsilon_{NO})^2} \tag{1.12}$$

[xvi] *Surface damping* is an additional non-radiative relaxation mechanism not accounted for by the bulk ε. It corresponds to collisions of the electrons against the material boundaries, and is therefore important for NOs having a size comparable to or smaller than the electron mean free path (approximately 40 nm in gold). Molecules chemically adsorbed to the NO surface can also contribute to line broadening with *chemical interface damping*.

with peak value $\sigma_{abs}(\lambda_{LSPR}) \propto \left[\operatorname{Im} \varepsilon_{NO}(\lambda_{LSPR})\right]^{-1}$ and full width at half maximum FWHM $= 2 \operatorname{Im} \varepsilon_{NO}(\lambda_{LSPR})$. *Radiative damping* corresponds instead to elastic scattering of the incident light, and dominates for large NOs; conversely, it is not included in a dipole limit treatment, and indeed does not appear in EQ. (1.12). In summary, $\operatorname{Re} \varepsilon_{NO}$ determines the spectral position of the LSPR, while $\operatorname{Im} \varepsilon_{NO}$ rules its peak amplitude and width.

Some examples of LSPRs in metal NPs are presented in FIG. 1.3. The gold nanosphere (GNS) in FIG. 1.3c has $\lambda_{LSPR} = 530\,\text{nm}$, in good agreement with a prediction based on the Fröhlich condition, see FIG. 1.2a. The non-resonant extinction on the short wavelength side of the LSPR is due to the interband absorption discussed above. The absorption of blue and green light by small GNSs results in a preferential transmission of longer wavelengths by colloidal solutions, thereby giving rise to the ruby tint observed by Faraday. GNSs are known to display often irregular shapes as in FIG. 6.5c; here a slight ellipticity brings about a sizeable optical anisotropy.

In comparison to the GNS in FIG. 1.3c, the silver nanospheres in FIG. 1.3a have a much sharper LSPR: $\sigma_{ext}/\sigma_{geo} = 14$ for the $D = 30\,\text{nm}$ one, whereas for the GNS this value is only 3.6. This stems from the exceptionally low non-radiative damping of silver ($\operatorname{Im} \varepsilon_{Ag}(\lambda_{LSPR}) \simeq 0.2$ against $\operatorname{Im} \varepsilon_{Au}(\lambda_{LSPR}) \simeq 2$, see FIG. 1.2d and c) which endows it with the most pronounced plasmonic features amongst metals in the near IR–VIS range. However, silver is easily oxidized; and indeed in FIG. 1.3a the 30 nm redshift of λ_{LSPR} with respect to the solution peak suggests the individual NP has somehow degraded after deposition. In contrast, the extraordinary chemical stability of gold against oxidation and corrosion means gold NOs are inert and non-toxic for biological tissues. For this reason, albeit alternative plasmonic materials are increasingly investigated, gold is still by far the

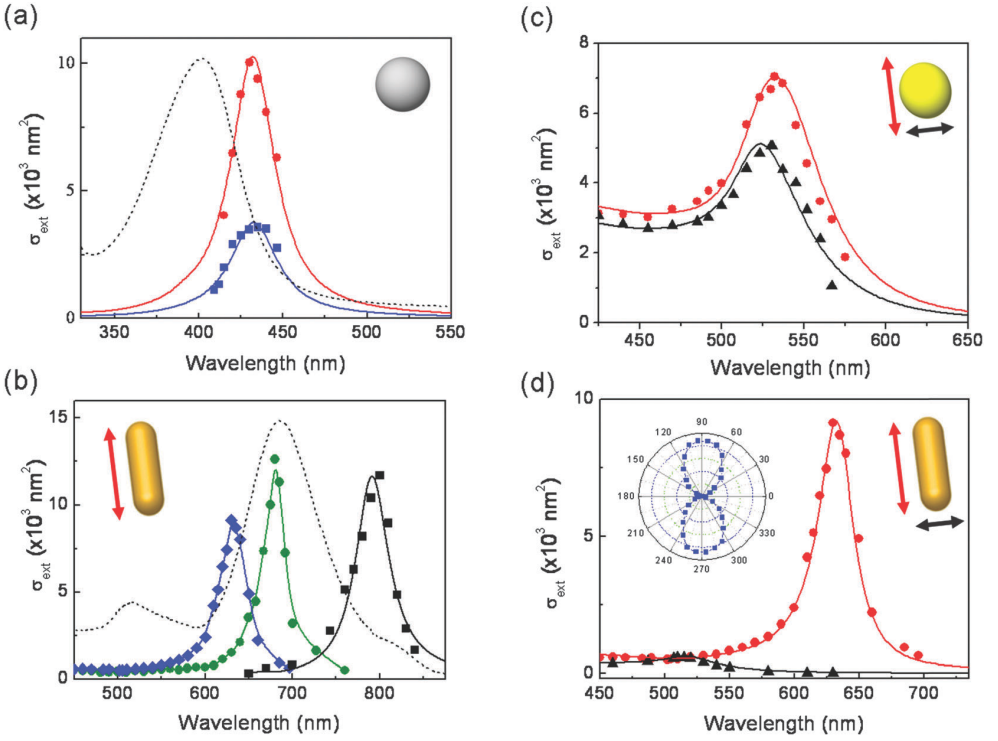

FIGURE 1.3: Absolute extinction spectra $\sigma_{ext}(\lambda_0)$ of individual metal NPs in an unspecified dielectric environment. (a) Silver spheres of diameter D = 30 nm (circles) and D = 21 nm (squares). (b) Gold rods of aspect ratio (AR) 2.5, 3.0, and 4.0 with increasing LSPR wavelength. (c) A slightly elliptical gold NP with long and short axis 50 nm (circles) and 46 nm (triangles). (d) A gold rod of length 20.5 nm and AR = 2; (inset) excitation polarization dependence at 630 nm. The spectra were acquired under linearly polarized illumination with orientation: (a) irrelevant; (b) along the rod; (c,d) along the long (circles) and short (triangles) NP axis. Solid lines are fits with: (a,b) A Lorentzian function like EQ. (1.12), (c) an analytical model for an ellipsoid in the dipole limit, or (d) numerical simulations. The dotted line in (a) and (b) is the normalized extinction spectrum of the colloidal solution. Reproduced with permission from Crut et al.[20] © 2014 The Royal Society of Chemistry.

most popular; and the synthesis and applications of gold NPs nowadays almost stand as a field on their own.[21]

In addition to material properties, the LSPR depends largely on the shape and size of the NO. Moreover, non-spherical NOs support multiple LSPRs, or *plasmonic modes*, and as the symmetry is reduced, their frequency degeneracy is lifted, so that less regular shapes correspond to more complex scattering and absorption spectra. We emphasize that EQ. (1.10) refers specifically to a sphere of $D \ll \lambda$ and, although the considerations made so far are qualitatively valid in general, a different form of the Fröhlich condition holds for other NOs. Nonetheless, as discussed in SEC. 1.1, analytical theories are limited to simple shapes, and to compute the plasmonic modes of a given geometry one often has to resort to numerical simulations.

Elongated NPs provide an example of shape dependence which is very relevant for applications too. A prolate rotation ellipsoid of length L and diameter D in the electrostatic limit ($L \ll \lambda$) can be treated analytically by means of a generalized form of Rayleigh's calculations,[2] and is found to support a transverse ($\perp$) and a longitudinal ($\parallel$) mode, which can be selectively excited by $\mathbf{E}_{exc}$ polarized respectively across or along the long axis of the ellipsoid. These two modes are visible in FIG. 1.3d for a gold nanorod (GNR). In the electrostatic limit $\lambda_\perp$ is fixed and coincides with the LSPR of a sphere, which is the limiting case where the two modes are degenerate. $\lambda_\parallel$ on the other hand depends linearly on the aspect ratio $AR = L/D$ of the NP; using an experimental dataset[15] for $\varepsilon_{Au}(\lambda_0)$ Link et al.[22] provided the fitting formula

$$\lambda_\parallel[\text{nm}] = (53.7\,AR - 42.3)\,\varepsilon_m + 495. \tag{1.13}$$

Such a redshift of $\lambda_\parallel$ as the AR increases is observed experimentally in FIG. 1.3c. As the LSPR redshifts, it becomes sharper

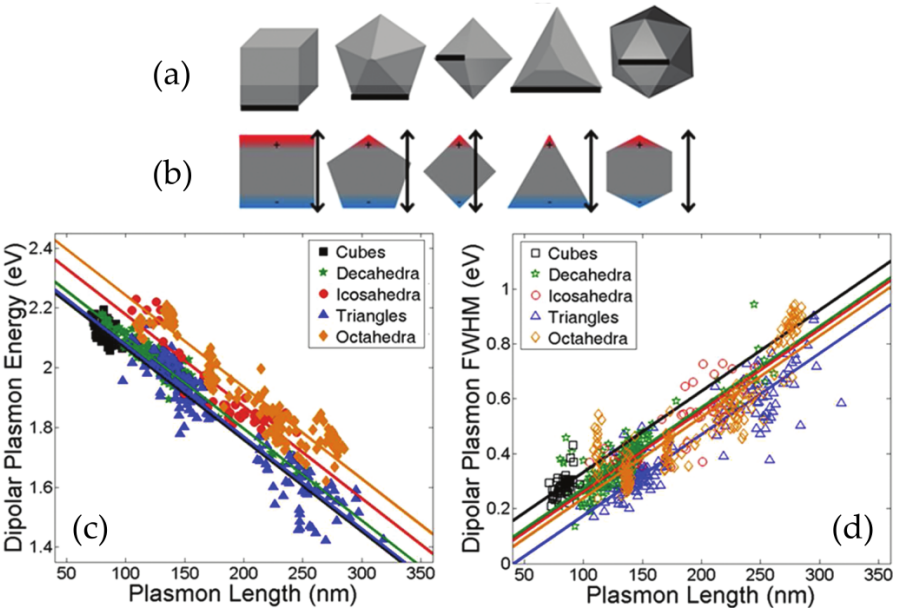

FIGURE 1.4: (a) Side length and (b) plasmon length L_p of the dipolar plasmonic mode for various NP shapes. (c) Peak energy and (d) FWHM of the LSPR as a function of L_p for the shapes in (b). Reproduced with permission from Ringe et al.[23] © 2012 American Chemical Society.

inasmuch as it experiences a lower damping: As can be seen in FIG. 1.2c, Im ε_{Au} has a minimum at about 700 nm.

In the electrostatic approximation, the natural unit of length of the problem, namely λ, is obliterated, and therefore the plasmonic modes depend only on the shape of the NO, but not on its absolute size. Nevertheless, for NOs having size $D \gtrsim \lambda/10$ the electrostatic approximation becomes increasingly crude, and substantial size effects are observed. The most physically sound quantity to parametrize the size dependence and meaningfully compare different NP shapes is the *plasmon length* L_p, defined[23] as the distance between regions of opposite charge created by $\mathbf{E}_{exc}$, see FIG. 1.4b. Now, due to the finiteness of the speed

of light, charges at one end of the NO react to changes at the opposite end with a phase difference of approximately kL_p, and thus the oscillation period increases as a result of such delayed response.[24,xvii] This simple argument predicts a linear redshift of λ_{LSPR} as L_p increases, which is compatible with the experimental data in FIG. 1.4c. The increase of radiative damping, which dominates over non-radiative losses for large NOs, brings about a broadening of the LSPR that is also roughly proportional to L_p in this size range, see FIG. 1.4d. In fact, Faraday observed blue and violet hues in some of its colloids, and interpreted them correctly as due to a different degrees of chemically-induced aggregation between the NPs.[10] The origin of those colours is now clear: The LSPR of a large NO such as an aggregate is shifted towards the IR, so that the red part of the VIS spectrum is absorbed and the remaining blue components are preferentially transmitted.

NOs can support high order resonant modes, corresponding to a more complex distribution of the polarization charges, such as quadrupole ($l = 2$), hexapole ($l = 3$),... Multipolar resonances occur at higher energy with respect to the dipolar mode ($l = 1$), and are generally narrower due to a reduced radiative broadening. However, since they require more nodes in the charge distribution, they can only be excited when E_{exc} varies significantly over the NO volume. Therefore, the dipolar mode rules the response of small NOs — in the dipole limit, indeed — whereas spectra of larger NOs feature increasing contributions from multipolar modes. FIG. 1.5 exemplifies this behaviour for a spherical NP in water: The quadrupolar mode takes over the dipolar mode for $D > 180\,nm$ and the LSPR peak correspondingly flattens into a much broader plasmonic band,

xvii Hence the size dependence is also referred to as a *retardation effect*.

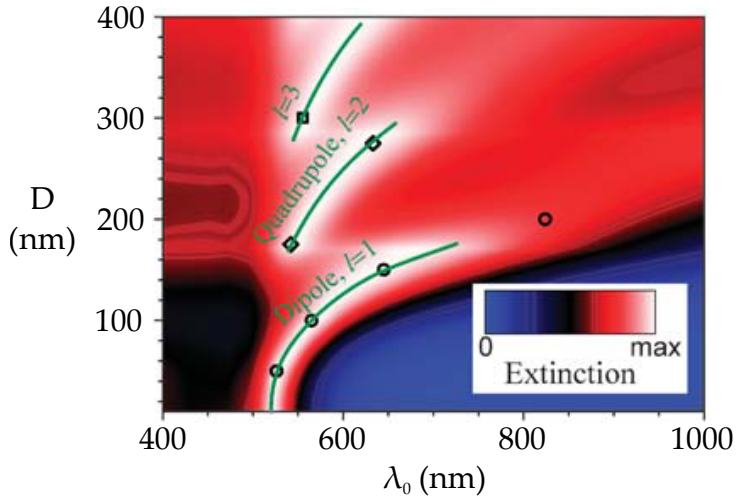

FIGURE 1.5: Normalized extinction spectra $\sigma_{ext}(\lambda_0)$ of a GNS in water computed for a varying diameter D. The three plasmonic modes with $l = 1, 2, 3$ are highlighted. Reproduced with permission from Myroshnychenko et al.[24] © 2008 The Royal Society of Chemistry.

thereby bridging the nanoscopic resonant behaviour to the macroscopic non-resonant response.

1.3 NANO-OBJECTS CLOSE TO A PLANAR INTERFACE

In the previous section we discussed how ε_m affects the LSPR, but limited ourselves to the simple case of a homogeneous optical environment. To produce it experimentally one can to cover the NO with a fluid matching the refractive index of the substrate, embed it in a solid matrix, or suspend it within an optical trap. Nevertheless, a planar interface in the vicinity of the NO is commonly encountered in microscopy experiments as well as in plasmonic devices. For instance, lithographic NOs are fabricated directly on a substrate, and metal colloids are typically dropcast onto a glass slide for imaging purposes.

The electromagnetic response of a NO close to a planar interface can be computed through the *multipole expansion method* (also known as generalized Mie theory), which consists in expanding the electromagnetic fields on the basis of vector spherical harmonics, whose expansion coefficients are obtained by imposing the appropriate boundary conditions at the material interfaces.[25,26] Lermé et al.[27] reported an extensive presentation of the method along with a systematic collection of the OCS spectra of a sphere on a substrate as a function of the parameters of the system. Even though the codes implementing the multipole expansion method are orders of magnitude faster than a brute-force numerical solution of Maxwell's equation, they are not nearly as flexible when it comes to modify the geometry of the system; and for this very reason they are less popular among experimentalists.

A simpler analytical description can be drawn within the electrostatic approximation and, albeit potentially less accurate, it comes handy in many circumstances. In this limit, and regardless of the NO shape, a plasmonic mode is described as an electric dipole oscillating at the frequency of $\mathbf{E}_{\mathrm{exc}}$ and oriented along the plasmon length as in FIG. 1.4b. The radiation of a dipole close to a planar interface has been studied first by Sommerfeld[28] in 1909, in relation to the transmission of radio waves along the Earth surface. The problem requires that the contours of constant phase match at the interface, while the phase velocities normal to the interface differ in the two media. Only the excitation of evanescent modes in both media along with the propagating ones make it possible to satisfy the boundary conditions. A rigorous analytical solution for a dipole having arbitrary distance and orientation with respect to the interface has been published by Lukosz and Kunz,[29–32] including in particular the angular distribution of the power

radiated in the FF. A complete derivation of these results is reported by Novotny and Hecht[33] (§10).

In electrostatics, $\mathbf{E}$ inside a given region of interest V is determined uniquely by the charges contained therein and the value of the electric potential ϕ at its boundary ∂V.[xviii] By altering the charges and materials specifications outside V one can thus formulate an *equivalent problem*, whose solution inside V (but not outside) will correspond to the original problem so long as $\phi\big|_{\partial V}$ is left unchanged. An easier equivalent problem is often obtained by adding fictitious point charges outside V in order to simplify the materials specification, e. g. so to have $\varepsilon = \varepsilon_V$ everywhere. These are called *image charges* because the prototypical problem of a charge in front of a planar interface (dielectric or conducting) is reduced to a homogeneous medium by adding an opposite charge in the symmetric position with respect to the interface.

The image charge method can be thus applied straightforwardly to the case of a NO close to a planar interface[24] and provide an intuitive picture of how the LSPRs are affected.[34] Specifically, in the dipole limit, the substrate (medium 1) may be replaced by an *image dipole* so that (only in medium 2, where the NO is placed) the NO–substrate system resembles a dimer as depicted in FIG. 1.6. The amplitudes of the image dipole and the physical dipole are proportional via[33]

$$\mathbf{p}^{\parallel}_{\text{im}} = -\frac{\varepsilon_1 - \varepsilon_2}{\varepsilon_1 + \varepsilon_2}\,\mathbf{p}^{\parallel}_{\text{ph}} \quad \text{and} \quad \mathbf{p}^{\perp}_{\text{im}} = +\frac{\varepsilon_1 - \varepsilon_2}{\varepsilon_1 + \varepsilon_2}\,\mathbf{p}^{\perp}_{\text{ph}} \tag{1.14}$$

where the dipoles have been decomposed into their components $\parallel$ and $\perp$ to the interface. Often the symmetry of the problem dictates the existence of modes oriented either $\parallel$ or $\perp$ to

xviii Formally, this statement is the Uniqueness theorem for Poisson's equation with Dirichlet boundary conditions.

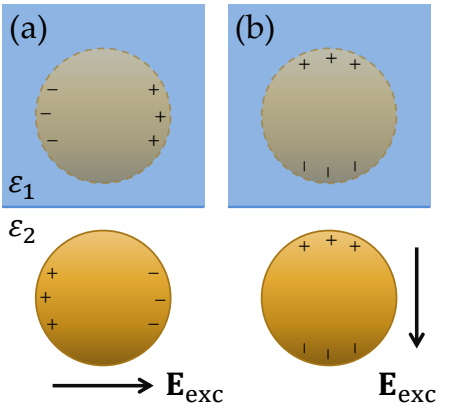

FIGURE 1.6: Image charge method applied to a NO close to a planar interface. The physical dipole (medium 2) and the image dipole (medium 1) have symmetric positions with respect to the interface; their relative orientation represents the case $\varepsilon_1 > \varepsilon_2$. The exciting field $\mathbf{E}_{exc}$ is (a) parallel, or (b) perpendicular to the interface.

the interface. For instance, in the case of a sphere the symmetry breaking due to the presence of the interface lifts the degeneracy of the isotropic mode, which is split into a doubly-degenerate planar mode and a linear mode, respectively $\parallel$ and $\perp$ to the interface. Although in the following we explicitly refer to $\parallel$ and $\perp$ modes, analogous considerations apply for a mode of arbitrary orientation.

Let us assume $\varepsilon_1 > \varepsilon_2$, corresponding to the orientation of the image dipoles in FIG. 1.6. The effect of the substrate is equivalent to the electrostatic interaction between the physical and the image dipole. In particular, for both orientations of $\mathbf{E}_{exc}$ in FIG. 1.6 regions of opposite charge are brought closer: The ensuing attractive interaction brings about an energetically advantageous configuration, and a redshift of the NO–substrate resonances with respect to the LSPR in a homogeneous ε_2 medium.[xix] Note that for the $\perp$ mode the regions of opposite charge are closer, so that the coupling with the image (i. e. the substrate) is stronger, and the redshift larger with respect to the $\parallel$ mode, to an extent depending on the specific geometry con-

[xix] According to EQ. (1.14), for $\varepsilon_1 < \varepsilon_2$ the image dipole orientation is reversed, and the modes are blueshifted instead.

sidered. According to EQ. (1.14), the higher the dielectric mismatch, the stronger the NO image and, consequently, the larger the splitting between the otherwise degenerate sphere modes. For interfaces with relatively low mismatch, such as air/glass, the mode splitting is often smaller than their linewidth, resulting in a broadened peak rather than a doublet.

The image charge method can be used to compute an *effective background permittivity* ε_{eff} of a homogeneous medium replacing the interface as the NO environment.[35] Note that ε_{eff} depends on the orientation of the mode considered, thereby being able to predict the substrate-induced mode splitting. Albeit approximate, the effective medium approach is quite popular, because it predicts in an elementary way the redshift of the LSPRs stemming from NO–substrate interactions. However, other important properties of the NO–substrate system — such as the absolute amplitude of the OCS, or the angular distribution of the scattered power — cannot be addressed within the frame of this description.

1.4 TRANSMISSION AND REFLECTION AT A PLANAR DIELECTRIC INTERFACE

In order to measure and model the OCS of NOs, a description of the microscope illumination as an incoherent superposition of plane waves is developed in this thesis — particularly in SEC. 3.1.1. The transmission and reflection of a plane wave at an planar interface must be included in the description for dealing with the case of a NO on a substrate discussed in the previous section. This topic is extensively covered in most textbooks of optics, for instance by Hecht[36] (§4.6). Therefore, in this section we will limit ourselves to recapitulate the main fea-

tures of the system's behaviour and introduce some concepts and formulas we will refer to in the following.

The geometry of the problem is drawn in FIG. 1.7. A planar interface $z = 0$ separates two media of refractive index n_1 and n_2. In this thesis, we assume these are non-absorbing ($n_1, n_2 \in \mathbb{R}$) and non-magnetic ($\mu_1 = \mu_2 = \mu_0$). The incident (subscript i) wavefront is split at the interface into a transmitted (t) and a reflected (r) wave. The propagation direction $\hat{\mathbf{k}}$ of these waves is identified via a polar angle θ and and azimuthal angle φ. The polar angles are related through the law of specular reflection $\theta_r = \pi - \theta_i$ and Snell's law $n_1 \sin\theta_i = n_2 \sin\theta_t$. As for the azimuthal angles, the planar nature of the problem implies $\varphi_i = \varphi_r = \varphi_t$. The longitudinal plane $\varphi = \varphi_i$ represented in FIG. 1.7 is named *plane of incidence*. The directions parallel (p) and perpendicular (s) to the plane of incidence $\varphi = \varphi_i$ form the most convenient basis to decompose $\mathbf{E}$, because the p and s components preserve their polarization upon transmission and reflection.

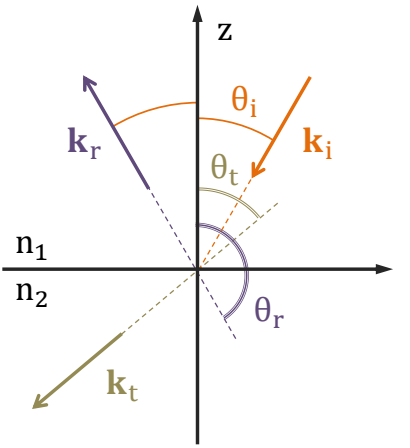

FIGURE 1.7: Transmission and reflection of a plane wave at a planar dielectric interface $z = 0$. n_1 and n_2 are the real refractive indices of the two media. $\mathbf{k}$ and θ are the direction and polar angle of propagation of the incident (subscript i), transmitted (t), and reflected (r) wave.

The dynamic properties of transmission and reflection are expressed by the *Fresnel coefficients* for p and s polarization, defined as field amplitude ratios

$$t_p \equiv \frac{E_{t,p}}{E_{i,p}} = \frac{2n_1 \cos\theta_i}{n_2 \cos\theta_i + n_1 \cos\theta_t}, \quad r_p \equiv \frac{E_{r,p}}{E_{i,p}} = \frac{n_2}{n_1} t_p - 1, \tag{1.15p}$$

$$t_s \equiv \frac{E_{t,s}}{E_{i,s}} = \frac{2n_1 \cos\theta_i}{n_1 \cos\theta_i + n_2 \cos\theta_t}, \quad r_s \equiv \frac{E_{r,s}}{E_{i,s}} = t_s - 1. \tag{1.15s}$$

The derivation of EQ. (1.15) relies on the continuity at the interface of $\mathbf{E}_{\parallel}$ and $\mathbf{B}_{\perp}$ see for instance Hecht[36] (§4.6.2). The *transmittance* T and *reflectance* R are defined respectively as the fraction of the incident power transmitted and reflected by the interface to the FF. Their expression in terms of the amplitude coefficients is readily found using the expression for the intensity of a plane wave $I = \frac{1}{2} n c_0 \varepsilon_0 |\mathbf{E}|^2$

$$T \equiv \frac{P_t}{P_i} = \frac{n_2 \cos\theta_t}{n_1 \cos\theta_i} |t|^2, \qquad R \equiv \frac{P_r}{P_i} = |r|^2 \tag{1.16}$$

where the cosine ratio accounts for the variation of the transmitted beam section. Energy conservation translates to $T + R = 1$: Since we are considering non absorbing media, the incident light can be either transmitted or reflected. The coefficients (1.15) and (1.16) are shown in FIG. 1.8 as functions of θ_i for an air/glass (left panels) and a glass/air (right panels) interface.

Let us comment first on the FF coefficients in FIG. 1.8e,f. For large angles of incidence T drops to 0, and any interface becomes highly reflective: In practice, one can verify that a window or a puddle looked at a grazing incidence acts like a mirror. Two notable values of θ_i, namely θ_B and θ_c, are indicated by vertical grey lines. The *Brewster's angle* $\theta_B = \arctan(n_2/n_1)$ is indicated by a downward arrow and has the property $T_p(\theta_B) = 1$,

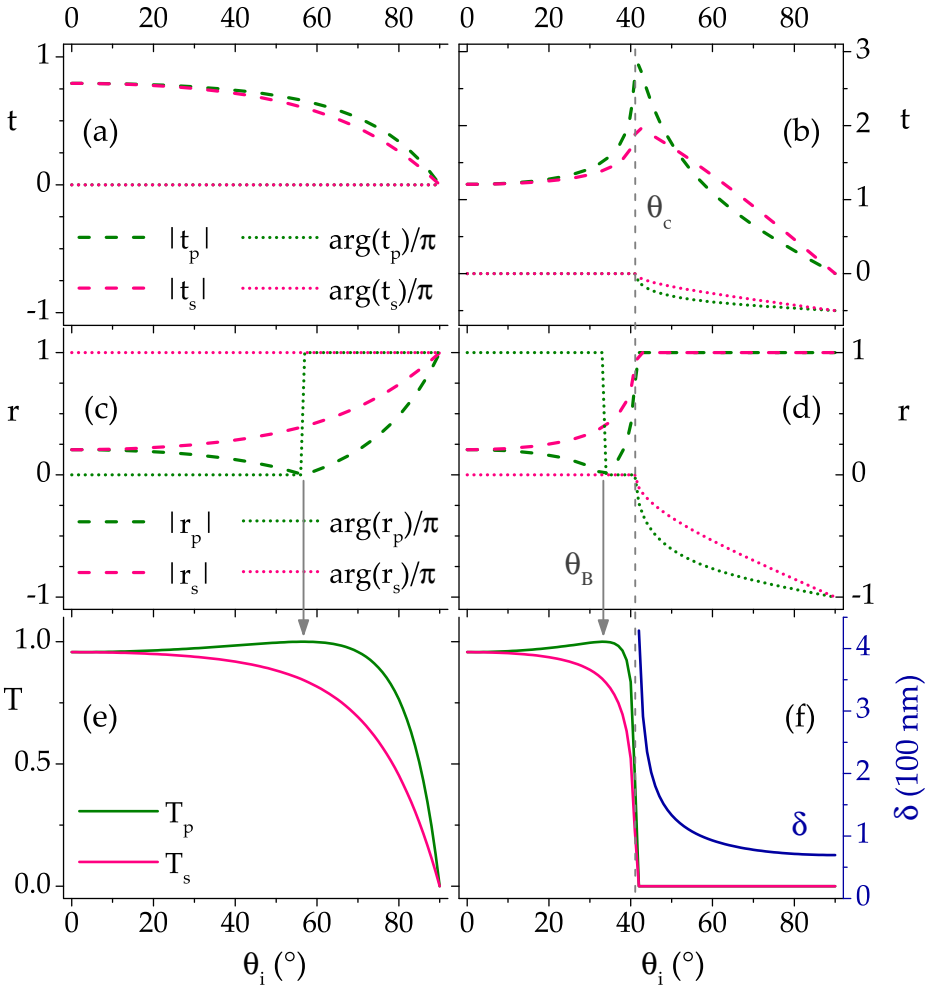

FIGURE 1.8: Fresnel coefficients t and r, and transmittance T as a function of the angle of incidence θ_i for the p (green) and s (pink) polarization components. In (f) the characteristic decay length δ of the evanescent wave is computed via EQ. (1.17) at $\lambda_0 = 500\,\text{nm}$. The Brewster's angle θ_B and the critical angle θ_c are indicated by a vertical arrow and a dashed line respectively.
(a,c,e) Air/glass interface $n_1 = 1.00$, $n_2 = 1.52$, $\theta_B = 56.7°$.
(b,d,f) Glass/air interface $n_1 = 1.52$, $n_2 = 1.00$, $\theta_B = 33.3°$, $\theta_c = 41.1°$.

implying that the light reflected at $\theta_i = \theta_B$ is completely s-polarized. Mathematically, θ_B is the solution[xx] of $r_p(\theta_i) = 0$. Geometrically, it corresponds to the condition $\theta_i + \theta_t = \pi/2$, or equivalently $\mathbf{k}_r \parallel \mathbf{E}_{t,p}$: The microscopic dipoles induced in medium 2, which are the source of the reflected wave, do not radiate along $\mathbf{k}_r$.

The *critical angle* $\theta_c = \arcsin(n_2/n_1)$ is indicated by a vertical dashed line in FIG. 1.8f and only exists for $n_1 > n_2$, i. e. when $\theta_t > \theta_i$. It corresponds to grazing transmission ($\theta_t = \pi/2$) and for $\theta_i \geqslant \theta_c$ one has $T = 0$: All light is reflected back into the optically denser medium and therefore this regime is named total internal reflection (TIR). In the TIR regime, Snell's law implies $\sin\theta_t = \frac{n_1}{n_2}\sin\theta_i > 1$, which cannot be fulfilled by a real value of θ_t. Indeed, $\cos\theta_t = i\sqrt{\sin^2\theta_t - 1}$ is imaginary, and so is $k_{t,z} = -n_2 k_0 \cos\theta_t$.[xxi] This means that the propagation term $e^{ik_t\cdot r}$ of the transmitted field[xxii] contains now a real exponential $E_t(z) \propto e^{z/\delta}$: Such an electric field decaying exponentially for $z < 0$ is usually called *evanescent wave*. The characteristic decay length δ of the evanescent field

$$\delta(\theta_i) = -\frac{i}{k_{t,z}} = \frac{\lambda_0}{2\pi}\left(n_1^2\sin^2\theta_i - n_2^2\right)^{-1/2} \tag{1.17}$$

is plotted in FIG. 1.8f for $\lambda_0 = 500\,\text{nm}$.

Let us finally comment on the Fresnel coefficients plotted in FIG. 1.8, panels a to d. Unlike T and R, t and r are complex numbers, and their argument is the phase shift at $z = 0$ of E_t and

xx Other solutions outside the physical domain $\theta_i \in [0, \pi/2]$ are discarded.

xxi When taking the square root of $\cos^2\theta_t = 1 - \sin^2\theta_t$ we discarded the negative solution. In fact, an opposite sign of $k_{t,z}$ corresponds to E_t exponentially increasing away from the interface — namely $\delta < 0$, see EQ. (1.17) below. This is incompatible with the boundary conditions imposed, prescribing no incoming field from the side of medium 2.

xxii We will derive the explicit field expressions later on, see EQ. (3.2).

E_r with respect to E_i.[xxiii] As shown in FIG. 1.8a,b, E_t is always in phase with E_i except in the TIR region, where it drifts progressively out of phase. On the other hand, E_r is in antiphase with E_i in a wide range of θ_i values, and $\arg(r_p)$ displays a π jump at $\theta_i = \theta_B$, see FIG. 1.8c,d. Interestingly, $|t| > 1$ close to θ_c in FIG. 1.8b: Albeit in the TIR regime no transmitted wave propagates to the FF ($T = 0$), and the net energy flux across the interface is null, just below the interface the amplitude E_t of the evanescent wave is almost three times larger than E_i.[xxiv]

xxiii By definition, two p-polarized fields are in (anti)phase when their components *perpendicular* to the interface are (anti)parallel.

xxiv TIR fluorescence microscopy (TIRFM) relies on this very observation.

2

TECHNOLOGICAL APPLICATIONS AND EXPERIMENTAL TECHNIQUES

The bright colours of metal colloids were highly prized already by ancient civilizations,[i] who employed them for their artistic endeavours, as testified by the vivid blue paint of Maya frescoes[37] as well as by numerous examples of Chinese porcelains, Roman mosaics, and Japanese glassware.[38] The most illustrious among these artefacts is probably the Roman chalice in FIG. 2.1 known as Lycurgus Cup from the mythological subject carved on its exterior. The Cup displays a marked dichroism, appearing red when lit from behind and green under frontal illumination. This effect is produced by NPs of a silver–gold alloy about 50 nm in size dispersed throughout the glass matrix.[39] These NPs absorb and scatter light to a similar extent, and their LSPR falls in the green region of the spectrum, so that transmitted (i. e., non-absorbed) light is red and reflected (i. e. scattered) light is green.

Although practical recipes to create brightly-coloured paints and stained glass have been known for a long time, modern scientists obviously yearn for a much finer degree of control, resulting in countless applications of NOs being proposed, demonstrated, and refined since the outburst of nanotechnology a few decades ago, with several having already made their way into the market. Moreover, a detailed understanding of the physical mechanisms underpinning the optical properties of NOs, joint to the steady advancements in the related synthesis and

i Louis and Pluchery[21] (§1) provide an extensive overview of the use of gold NPs throughout history.

FIGURE 2.1: The Lycurgus cup is an example of use of the chromatic properties of metal colloids for artistic purposes. It is currently on display at the British Museum in London. Image downloaded from the Museum website, free for non-commercial use.

fabrication techniques, means nowadays we strive to produce NOs having properties tailored in view of a specific application. Leaving aside the myriad applications exploiting the mechanical and chemical properties of NOs, or their catalytic activity, in the following section we will focus on how the optical properties of metal NOs can be put to best use.

2.1 SELECTED APPLICATIONS

Plasmonic NOs offer large potentiality for moulding the flow of light at the nanoscale. Similarly to the antennas widely used in communications to send and receive radio signals, NOs allow to effectively couple near field (NF) to far field (FF), that is, in-

tercept propagating radiation and confine it, or conversely pick up a local signal and emit it. However, since the resonant frequency increases for smaller sizes, these *nano-antennas* operate in the VIS range rather than at radio frequencies.[40,41] For instance, simple dipole nano-antennas are capable of amplifying the signal generated by an emitter placed in the NF,[42] as well as controlling the directionality of the emission to the FF.[43]

A well-known effect in the electrostatics of metals, sometimes called *lighting rod effect*, is the accumulation of free surface charges at sharp spatial features, bringing about an increase of E in the vicinity of the surface. With their nanometric radius of curvature, metal NOs originate a large local enhancement of E, which is further boosted by plasmonic resonances.[44] For instance, the fluorescence of a single molecule placed inside the gap of a "bowtie" dimer displays a 1000-fold enhancement under resonant excitation of the dipolar plasmonic mode.[45] Owing to their ability to confine light to a small volume, metal NOs are often described as a nanoscale equivalent to dielectric lenses[46] — which essentially is a slightly different take on the aforementioned nano-antenna concept. FIG. 2.2 shows how the LSPR of a metal sphere concentrates the flow of light, providing the simplest example of a *nano-lens*. Now, traditional lenses are

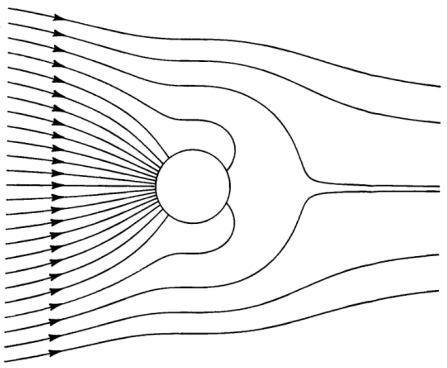

FIGURE 2.2: An Al sphere in the dipole limit is illuminated by a plane wave resonant to its LSPR at $\lambda_{\text{LSPR}} = 148\,\text{nm}$ in vacuum. The oriented lines represent the energy flux $\mathbf{S}_{\text{exc}} + \mathbf{S}_{\text{ext}}$, i. e. excluding the scattered component, see P. 10. From Bohren and Huffman[2] © 1998 Wiley-VCH Verlag.

placed in the FF with respect to the focus, resulting in a focal spot limited in size by diffraction to $\gtrsim \lambda/2$. Plasmonic NOs, conversely, concentrate light in the NF and thus are bound by no fundamental principles barring the ultimate atomic structure of matter. On the other hand, metal resonators are characterized by much higher losses than their dielectric counterparts, meaning lower quality factors $Q \equiv \lambda_{res}/\text{FWHM}$ are obtained: In practice $Q_{met} \lesssim 10^2$ against $Q_{diel} \lesssim 10^6$.

It is worth emphasizing that NOs retain as well most of the features of bulk metals, including a large electrical and thermal conductivity, a good mechanical and thermal stability, and a high catalytic activity enhanced by their large surface-to-volume ratio. On top of that, metal NOs offer an extensively tuneable optical response (see SEC. 1.2) and can be miniaturized down to a few nm using available growth and fabrication techniques, so that the possibilities for device design are virtually countless. Having briefly highlighted the key advantages offered by metal NOs for light manipulation at the nanoscale, we will henceforth narrow down our review to a few, highly relevant application of metal NPs; further reading on the applications of metal NOs in photonics is contained in previously cited books and reviews.[4,6,11–14,21,41,44,47]

PHOTOTHERMAL THERAPY Owing to their low cytotoxicity and ease of chemical functionalization, gold NPs gained much attention within the steadily-rising field of *nano-medicine* both as intrinsic drug agents and as drug delivery vehicles.[48] In particular, the potentialities for an efficient light-to-heat conversion with a high degree of spatial and temporal control renders gold NPs ideal photosensitizer elements for photothermal therapy (PT) — i. e. the destruction of tumoral tissues using hyperthermia.[49]

In PT, the NPs are first chemically functionalized so to facilitate specific binding and uptake by cancer cells. The colloid is then injected into the sample/patient and within a few hours NPs accumulate inside the tumoral cells. Afterwards, the tumour region is irradiated (typically by a continuous-wave laser source having intensity ~W/cm², low enough not to damage healthy tissues) resonantly with the LSPR of the NPs which, thanks to their large σ_{abs}, are effectively heated. The large surface-to-volume ratio characterizing NOs guarantees they cool efficiently rather than reshape or melt altogether; thereby heat is released locally in a controlled way, selectively killing the malignant cells.[ii]

The NPs used in PT must satisfy two essential requirements: (i) they must have a large *absorption quantum yield* $Y_{abs} = \sigma_{abs}/\sigma_{exc}$; and (ii) their LSPR must fall within the (partial) transparency window (700 nm to 1000 nm) of biological tissue to allow excitation from an external source.[iii] By putting together EQ. (1.2), EQ. (1.7), and EQ. (1.8) one finds $Y_{abs} \propto D^{-3}$ so that the condition (i) is fulfilled by small NPs, which are also more easily internalized by cells via endocytosis. As for (ii), elongated NPs are perhaps the most common choice:[50] EQ. (1.13) indicates that the LSPR of an ellipsoid can be tuned from the green (AR = 1) to the near IR by increasing its AR. PT has proven successful on mice as early as 2004,[51] and clinical trials on humans have been performed too.[52]

ENERGY HARVESTING Several applications of metal NPs have been explored for devices harvesting solar energy, such as photovoltaic cells, thermal collectors, and photocatalytic systems. For instance, *plasmonic energy conversion* relies on

ii Incidentally, the whole process reminds a bit the idea of "swallowing the surgeon" put forward by Feynman in his talk mentioned in the opening.[1]

iii Alternatively, an optical fibre can be used to perform PT on deep tumours.

the sizeable emission of hot electrons (photoelectric effect) following the decay of a LSPR excitation, which can be collected to generate a photocurrent.[53] On the other hand, metal NPs have also demonstrated the capability to improve the performance of conventional photovoltaic devices, namely, those based on electron–hole separation upon absorption of light by semiconducting materials.[54]

The thickness of the semiconducting absorbing layer is a critical parameter in solar cell design. One would like to reduce it as much as possible, to cut down costs and improve the efficiency. In fact, an optimum performance is achieved when the material thickness is much smaller than the average diffusion length of the minority carriers, so that radiative electron–hole recombination is minimized. However, silicon — by far the cheapest and most used semiconductor for commercial photovoltaics — displays poor absorbance of the 600 nm to 1100 nm spectral range. Consequently, in order to collect most of the solar emission, an optically-thick absorption layer must be used, typically about 200 µm in conventional wafer-based crystalline silicon solar cells.

Metal NPs can improve the absorption efficiency of the semiconductor layer, thus permitting to reduce its thickness. A possible design, proposed first by Stuart and Hall,[55] is illustrated in FIG. 2.3a. The NPs placed on the front surface of the cell strongly scatter the plane wavefront of sunlight, and thus redistribute it over a larger angular range, effectively increasing the optical path length in the absorbing layer. As will be shown below (see FIG. 5.1) a dipole close to a dielectric interface radiates preferentially towards the denser medium, so that power losses by back-scattering here are negligible. A metallic rear reflector and multiple scattering events further increase light trapping within the semiconductor layer. An alternative concept presented in FIG. 2.3b exploits instead the local field enhancement by

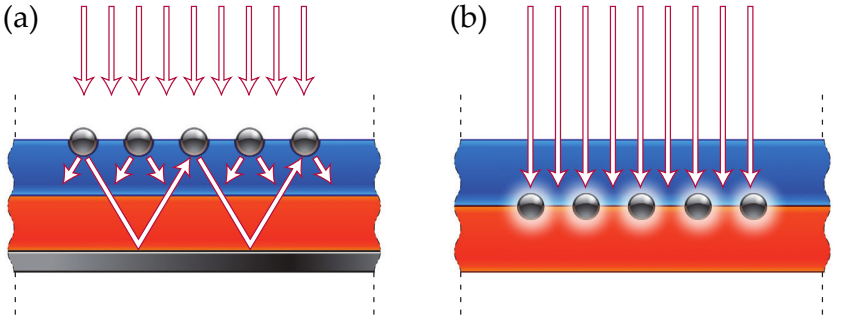

FIGURE 2.3: Design concepts for improving the absorption efficiency of solar cells using metal NPs. The blue and orange layers represent the p- and n-doped semiconductors. (a) The NPs at the front of the cell redistribute the impinging light (arrows) over a larger angle by scattering. Multiple scattering events and a metallic rear reflector result in additional light trapping. (b) The field enhancement close to the surface of NPs placed at the junction boost the photocarrier generation. Reproduced with permission from Atwater and Polman[54] © 2010 Macmillan Publishers Ltd.

the NPs to boost the photocarrier generation in proximity of the junction where collection occurs.

In both designs, an efficient energy conversion to electricity is achieved when the power is absorbed by the semiconductor, rather than dissipated in the metal through Ohmic losses. Therefore in the first scheme, where the impinging light is redistributed via scattering, the NPs should have a large *scattering quantum yield* $Y_{sca} = \sigma_{sca}/\sigma_{exc}$. Conversely in the second scheme, where NPs act as antennas, i. e. capturing the propagating electromagnetic energy, a large Y_{abs} is required. Thus, in order to minimize parasitic losses in the metal, absorption in the semiconductor must occur on a timescale shorter than the plasmon decay time,[iv] typically 10 fs to 50 fs.

iv For $Y_{abs} \gg Y_{sca}$ the plasmon lifetime is limited by non-radiative processes.

PLASMONIC SENSING Metal NPs are largely employed for chemical and biological sensing,[56] notably in the biomedical field for *in vitro* diagnostics.[48] Amongst the numerous sensing methods available, we will describe the principle of a few schemes based on LSPRs. Typically, the NP surface is functionalized (e. g. with an antibody) to bind to a target analyte, such as a hormone or an enzyme. In a simple, qualitative assay a certain region of the sensitive element — say, a stripe of paper — is also functionalized to bind to the same analyte, and thus in its presence the NPs accumulate in the functionalized region as they are flushed along the stripe. The appearance of the colour due to the LSPR indicates therefore a positive result of the assay. For instance, the red tint observed in commercial pregnancy tests is the very same as Faraday's ruby fluid (FIG. 1.1), being due to the LSPR of small gold NPs.

A more elaborate sensing scheme exploits the dependence of the LSPR on its immediate dielectric environment,[57] see EQ. (1.10). This concept provides a rapid response and is *label-free*, in the sense that under ideal conditions the signal is only due to the presence of the target analyte. In contrast, the vast majority of biological sensing techniques, such as immunoassays, use two or more antibodies carrying a *label* (e. g. a fluorescent molecule or a radioisotope) which produce the observed signal upon binding to the target. Nonetheless, the presence of labels can affect the interactions to be studied, so whenever possible label-free techniques should be preferred.

As the sensed species usually are optically denser than the buffer medium (e. g. aqueous solution), and for metals $\mathrm{Re}\,\varepsilon$ increases with λ_0 in the LSPR region (see FIG. 1.2), the presence of an analyte adsorbed to the NP surface is revealed by a red shift of the LSPR.[v] By constructing a calibration curve of the LSPR

v The LSPR can be affected via other mechanisms in addition to the permittivity, thus expanding the scope of plasmonic sensing to a wider range of

shift as a function of the analyte concentration, this scheme can yield quantitative results. A different functionalization of various regions of the sensitive element permits to test multiple species at the same time. The sensitivity of a plasmonic sensor can be quantified by a *figure of merit* defined as

$$\text{FOM} \equiv \frac{d\lambda_{\text{LSPR}}}{dn_m} \text{FWHM}_{\text{LSPR}}^{-1} \tag{2.1}$$

Systematic research, performed in particular by the group lead by M. El-Sayed, has demonstrated that, in terms of sensitivity, rods are better than spheres, silver NPs are better than gold ones, and large NPs are better than small ones. More recently, Fano resonances have been proposed for ultra-sensitive plasmonic sensing by virtue of their steep dispersion profiles.[59]

Being the field enhancement limited to the immediate vicinity ($\lesssim 10\,\text{nm}$) of the metal surface, sensing based on individual NPs provides access with FF optical techniques to information on the local environment with a spatial resolution much below the $\sim \lambda/2$ diffraction limit. Moreover, single NOs make more accurate sensors than ensembles, since $\text{FWHM}_{\text{LSPR}}$ in EQ. (2.1) does not suffer from inhomogeneous broadening due to size dispersity.[vi] Single-NO plasmonic sensing has been demonstrated capable of detecting biomolecules with high sensitivity and selectivity, investigating the kinetics of chemical and electrochemical reactions, and monitoring *in situ* and in real time biological processes in living cells.[60] However, as will be discussed in SEC. 2.2, single-NO techniques require more complex set-ups

phenomena. For instance, when the LSPR of the NO (donor) overlaps with the absorption spectra of an adsorbed molecule (acceptor), the resonant energy transfer is observed as a quenching dip in the LSPR spectrum, because the donor provides a channel competing with the radiative decay.[58]

vi The dotted lines in FIG. 1.3a,b provide two examples of inhomogeneously broadened ensemble spectra.

in comparison to the UV/VIS spectroscopy used for ensemble measurements, and thus the aforementioned applications have been so far confined to research environments.

Similarly to the case of the image dipole discussed in SEC. 1.3,[vii] the dipolar plasmonic mode of a dimer is polarized along the NP separation as in FIG. 1.6b and redshifted with respect to the LSPR of each individual NP.[61] The increasing LSPR shift as the dimer gap is reduced can be used to monitor with nanometric accuracy changes of the conformation of a single molecule acting as a spacer element between the two NPs.[48,62] Our group has proposed the phase of a four-wave mixing (4WM) signal as an alternative observable to monitor the interparticle distance[63] in such *plasmon ruler* scheme.

LABELS FOR IMAGING In optical microscopy, staining is a routinely used procedure to enhance the contrast of images and highlight specific structures. However, conventional labels suffer from several limitations: They bleach (fluorophores), blink (quantum dots), are cytotoxic (radioisotopes, quantum dots), and in general can perturb the biological processes one wants to investigate. Metal NPs — and particularly gold ones — on the other hand are highly biocompatible, photostable,[viii] and are believed not to interfere with biological processes, thus standing as ideal candidates for cell labelling and *in vivo* imaging.[47,48] The NPs can be visualized via various optical

vii Although the mechanism of mode hybridization is the same described in the case of the image dipole, additional modes are present in a dimer, but not all modes are radiatively active. In particular, modes with a null net dipole moment, such as the quadrupolar mode in FIG. 1.6a, do not couple to radiation in the dipole limit and are therefore named *dark modes*. The dipolar mode polarized across the NP separation is active instead, and is blueshifted with respect to the LSPR of each individual NP.

viii The gold colloids prepared by M. Faraday are still optically active more than 150 years after their synthesis, see FIG. 1.1.

processes; let use briefly review the most common imaging modalities.

The simplest option is possibly to address elastic scattering using the *darkfield* microscopy technique described in SEC. 2.2.2. The previously cited work from Huang et al.[50] demonstrates that GNRs can be functionalized to have high affinity for malignant cancer cells and scatter in the near IR spectral window where the attenuation from biological tissues is low. This approach relies on the large σ_{sca} of metal NPs at the LSPR to make them visible over the diffuse scattering originated by the numerous cellular structures and corpuscles. Since $\sigma_{sca} \propto D^6$ according to EQ. (1.7), relatively large NPs are required, say at least 30 nm in size. Other detection methods in use, such as the *photothermal* and *photoacoustic* imaging, rely instead on σ_{abs}.[48] Nonetheless, the laser-induced heating of the target (mediated by the NPs) may alter the biochemistry of the cell and is therefore a major drawback of these techniques.

Amongst elements and simple compounds, metals have very large values of $\chi^{(3)}$, see Boyd[64] (§4.2).[ix] This suggests metal NPs can be imaged with high contrast when a 4WM (i.e. third-order) process is observed.[65] Moreover, nonlinear imaging has intrinsic 3D resolution and is free from any linear fluorescence and scattering background whenever the signal has higher frequency than all other fields involved. Various processes permit detection at the single NP level and have been proposed as imaging modalities, including *two photon fluorescence*[66] and *third harmonic generation*.[67] In particular, our group developed a degenerate, collinear 4WM scheme[x] *triply-resonant* with the LSPR of small gold NPs.[68] Rejection of elastically-scattered laser light

ix The crystal structure of plasmonic metals (fcc) has inversion symmetry[19] and thus second-order processes are forbidden in the bulk.[64]

x This specific 4WM process is in fact a pump–probe scheme and is also known in literature as *transient absorption spectroscopy*.

along with all incoherent background components is achieved with a phase-sensitive interferometric detection scheme similar to the one described on p. 107, which picks up exclusively the coherent 4WM signal. FIG. 2.4 displays a high spatial correlation between fluorescence and 4WM signal, while the latter provides a better contrast being free from scattering and autofluorescence background. Recently, a more sophisticated version of the same technique was proven capable of background-free 3D localization of individual gold NPs with nanometric accuracy (better than 20 nm in plane and 1 nm axially) on a 1 ms time scale using single-point acquisition (i. e. without raster scanning), thereby demonstrating its potential for monitoring in real time single-particle trafficking inside complex cellular environments.[69]

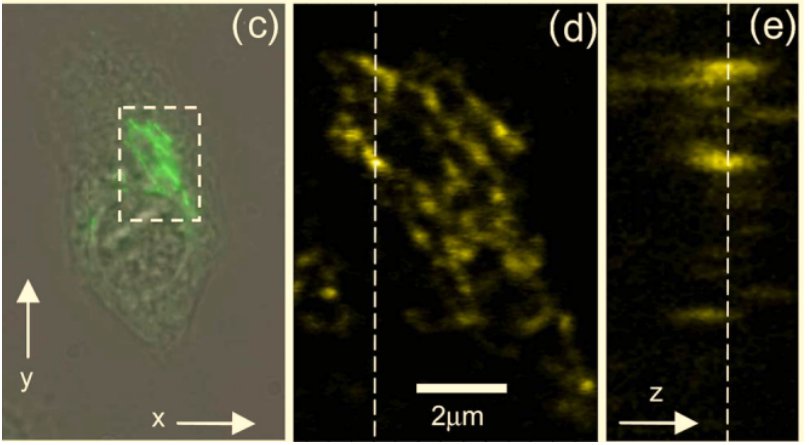

FIGURE 2.4: A HepG2 cell where the Golgi apparatus is stained with Alexa488 fluorophore and 5 nm gold NPs. (c) Overlay of phase contrast and epifluorescence images. (d,e) 4WM intensity images of the Golgi region identified by the dashed frame in (a). The xy (d) and yz (e) planes intersect at the dashed line. (d) and (e) share the same spatial scale and normalized linear colour scale. Reproduced with permission from Masia et al.[68] © 2009 Optical Society of America.

2.2 SINGLE-NANO-OBJECT EXPERIMENTAL TECHNIQUES

In the previous section we have described several applications of metal NOs, and highlighted how their performance can be optimized relying on a precise knowledge of σ_{sca} and σ_{abs} — in terms of both their spectral dispersion and absolute amplitude. Now, the sensitive dependence of the OCS on the geometry of the NO and its local environment provides on one hand large potential for tailoring the optical properties in view of a specific application, but implies as well that ensemble measurements are hampered by the unavoidable dispersity of the sample. Much effort has been therefore devoted over the last two decades in order to develop and refine experimental techniques capable of measuring the OCS of a single NO.[20,70] The rest of this chapter is devoted to the description of the operating principle of the main experimental tools currently available. We limit ourselves to FF optical techniques, whose spatial resolution is limited by diffraction; NF characterization of single NOs is reviewed by Ringe et al.[13] (§2.2).

2.2.1 *Raster-scanning modulation-based techniques*

Let us make first some general considerations on the detection of small NOs. By putting together EQ. (1.7) and EQ. (1.8) one finds $\sigma_{sca}/\sigma_{abs} \propto D^3$, meaning that small NOs are dominated by absorption. Therefore, according to EQ. (1.2), one has $\sigma_{ext} \simeq \sigma_{abs}$ in this regime. In order to get a feeling for the quantities involved, consider that a $D = 5\,nm$ GNS has[xi] $\sigma_{ext} = 11\,nm^2$ at $\lambda_{LSPR} = 533\,nm$, whereas the diffraction-limited point spread function (PSF) of a laser beam has a characteristic lateral

xi The σ_{ext} spectrum in the electrostatic limit was calculated using EQ. (1.8) and the Johnson and Christy[15] $\varepsilon(\lambda_0)$ dataset for gold.

size $D_{PSF} \simeq \lambda_{LSPR}/n_m/2$. The reduction of the transmittance T defined by EQ. (1.16) due to the presence of the GNS is then

$$\Delta T = T - T^{NO} = \frac{P_t - P_t^{NO}}{P_i} = \frac{P_{ext}}{P_i} = \frac{\sigma_{ext}}{A_{PSF}} \sim \frac{\sigma_{ext}}{D_{PSF}^2} \sim 10^{-4} \quad (2.2)$$

where $A_{PSF} = \pi D_{PSF}^2 = P_i/I_i$ is the equivalent illuminated area.

Such a small variation can be detected only by effectively abating the noise level. For instance, laser intensity fluctuations are effectively suppressed by a *balanced detection* scheme, where the laser output is split into a *signal* (passing through the sample) and a *reference* beam (not passing through); in a typical arrangement, signal and reference are made to interfere, and the difference between the two exit arms of the interferometer is detected, so to pick up the interference term and reject common-mode noise. *Shot noise* is instead intrinsic to the photon statistics of the light source, see SEC. B.3, and in a shot noise-limited regime the signal-to-noise ratio (SNR) can be improved only by increasing the number of photons detected.[xii] Another major source of noise in experiments are the thermal, electrical and mechanical fluctuations of all set-up parameters, which together result in a $\propto \nu^{-1}$ spectral power distribution. This ubiquitous *pink noise* can be virtually eliminated by modulating in time the signal amplitude, which is tantamount to up-shifting it, typically to a radio frequency (100 Hz to 100 MHz). This concept is usually implemented along with *lock-in amplification*, which is also very effective in reducing *white noise* via a narrow spectral filter centred at the modulation frequency.

xii In practice, this is achieved increasing the excitation power and the integration time. The excitation power is limited either by the maximum source power available or by the sample ability to withstand photodamage. The integration time is limited either by the duration of the investigated phenomenon or (unless the signal is modulated) by the typical timescale of set-up fluctuations, namely the pink noise described just below.

SPATIAL MODULATION SPECTROSCOPY A straightforward way to modulate the extinction signal is to move periodically the NO under the laser beam using a piezoelectric sample holder. Known as spatial modulation spectroscopy (SMS), this technique has been pioneered by the group of F. Vallée; in their first work[71] the sample holder was harmonically oscillated at $\nu = 1.5\,\text{kHz}$ and the signal was demodulated at ν and 2ν using a lock-in amplifier. This detection scheme resulted in a $\sigma_{ext} \simeq 2\,\text{nm}^2$ sensitivity. While first implemented in a transmission geometry, a reflection version of the SMS has proven capable of measuring the extinction of NOs deposited onto an opaque substrate.[72]

When the amount of scattering collected is negligible,[xiii] and relying on an accurate knowledge of the spatial profile of the illumination intensity, SMS provides an absolute measurement of σ_{ext}.[73] SMS has been successfully applied to investigate a variety of NOs, including metal NPs, carbon nanotubes and semiconducting nanowires.[20] Examples of quantitative SMS spectra of metal NPs are presented in FIG. 1.3 (symbols). While tight focusing leads to the the maximum sensitivity, large foci have well-defined transverse polarization and ease the analysis, resulting in a better accuracy. It is also possible to replace the laser source with an incoherent broadband lamp, the PSF being the image of a pinhole in the illumination path.[73] A broadband source permits to acquire simultaneously many spectral points, with a trade-off between sensitivity and spectral resolution.

A more sophisticated implementation of the technique is able to measure the absolute value of both σ_{abs} and σ_{sca} at the same time, thus providing a complete optical characterization of a NO with no size restrictions.[74] The experimental set-up is shown

xiii This contribution diminishes the measured extinction. Generally speaking, it is negligible for NO dominated by absorption and for small NA collection.

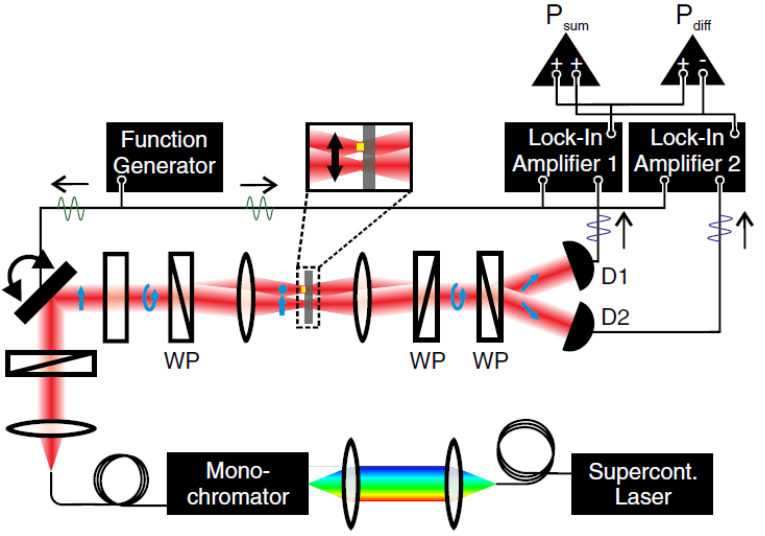

FIGURE 2.5: Interferometric scheme allowing a simultaneous and quantitative measurement of σ_{abs} and σ_{sca} of individual NOs. WP are Wollaston prisms inducing a 40 µm displacement between the two cross-polarized beams; D1, D2 are identical InGaAs photodetectors; the two objectives are aspheric lenses of NA = 1.3. Reproduced with permission from Husnik et al.[74] © 2012 American Physical Society

in FIG. 2.5: Two cross-polarized, loosely focused beams are scanned in parallel on the sample, one (*signal*) impinging on the NO and the other one (*reference*) serving as the second input arm of a common path interferometer.[xiv] A balanced, dual lock-in detection scheme provides the phase information required to separate the absorption and scattering contribution to extinction. Modulation was performed by keeping the NO fixed and moving the beam instead using a mirror galvanometer, whereby a higher modulation frequency can be achieved. Nevertheless, sensitivity is limited by the intrinsic signal oscil-

xiv This arrangement is not dissimilar from the differential interference contrast introduced below.

lations due to the periodic alteration of the optical path ("aperturing" effect), and in fact rather large nano-antennas ($D \simeq 200\,nm$) were measured in this work.

PHOTOTHERMAL IMAGING The strong absorption and fast local heat release characterizing small metal NOs gives rise to steep temperature gradients in the surrounding environment. The temperature[xv] dependence of the refractive index of the surrounding medium $n_m(T)$ creates a *thermal lens*, which can be probed by a laser beam non-resonant with the LSPR (*probe*). By modulating the heating beam resonant with the LSPR (*pump*), and demodulating the transmitted probe at the same frequency using a lock-in amplifier, one can sensitively detect the small index variations induced by the presence of a NO, resulting in a signal proportional to σ_{abs}.

Such a photothermal imaging (PI) modality has been pioneered by the group of M. Orrit.[75] A later refinement of the technique adopted a *heterodyne interferometric detection* scheme, measuring the beat note between the probe signal and the scattered signal, modulated at the pump frequency.[76] This simpler approach increased the sensitivity down to $\sigma_{abs} \simeq 0.2\,nm^2$ — an order of magnitude better than SMS — and enabled the authors to detect a cluster of 67 gold atoms. It must be noted, however, that such an extreme sensitivity was obtained by raising the pump laser power up to 3.5 mW. In general, being based on a sizeable heating of the NO surroundings, PI methods are affected by background absorption and limited in scope for biological imaging.

The PT signal originates from the modification of n_m, hence provides a rather indirect estimate of absorption of the NO,

[xv] In this thesis, the symbol T is used for both transmittance and temperature; the meaning should hopefully be clear from the context.

which functions only as the light coupling element. Nonetheless, a recently-reported technique based on the PT effect proved capable of measuring absolute values of σ_{abs}.[77] It was named quadriwave lateral shearing interferometry (QWLSI), and consists in detecting the thermally-induced distortion of a planar optical wavefront reflected at the NO position. σ_{abs} can be retrieved from the measured optical path difference profile using a simple mathematical model, which assumes in particular that no absorption occurs in the environment, and that the NO can be represented as a point-like heat source; a precise knowledge of the material properties ($n_m(T)$, thermal conductivity) of the environment is required too. Note that this novel technique is much less sensitive than the "standard" PI, being limited to $\sigma_{abs} \sim 10^3\,nm^2$.[77]

POLARIZATION MODULATION MICROSCOPY Another possibility for modulating the signal amplitude is switching the polarization of the exciting light between any two orthogonal states, denoted $\parallel$ and $\perp$,[xvi] using for instance a photoelastic modulator. The transmitted laser beam is monitored via a lock-in amplifier referenced to twice the modulation frequency, resulting in a reading proportional to $\sigma_{\parallel} - \sigma_{\perp}$. We emphasize that the anisotropy of the extinction is measured rather than its absolute value. This technique is thus meant to address NOs displaying an anisotropic or chiral optical response (either intrinsic to the material or due to their shape) and has in fact been first applied to GNRs.[78]

xvi Typically, these are either linearly polarized along perpendicular directions, or circularly polarized with opposite handedness.

2.2.2 *Widefield imaging techniques*

In the techniques discussed in SEC. 2.2.1 a point-like source is imaged by the objective on the sample plane, where it appears as a spot of diffraction-limited size. To obtain a 2D or 3D image the spot is scanned over the ROI in a raster fashion, and the signal is acquired with a single channel detector. This means imaging can be quite slow, in so far as acquisition time increases along with the size of the imaged area, the spatial resolution (more pixels acquired), and the SNR (longer pixel dwell time, or multiple frames averaged).

Alternatively, when a large portion of the sample plane is illuminated, an image can be acquired simultaneously using a rectangular array such as a complementary metal-oxide-semiconductor (CMOS) sensor or a charge-coupled device (CCD) camera. An even widefield illumination is commonly achieved by focusing the source image in the back focal plane (BFP) of a *condenser lens*, and placing the sample in the front focal plane thereof, so that the source image is completely defocused at the sample plane; this arrangement is known as *Köhler illumination*. A different illumination modality consists in raster scanning a light spot fast enough to average multiple complete runs within the acquisition time of the detector. This approach requires a more complicated instrumentation, but offers a specific advantage: Since each position of the sample is illuminated periodically, the low-frequency noise can be rejected by narrowing the detection bandwidth, in a lock-in-like fashion. Two broad categories of widefield microscopy can be distinguished:

BRIGHTFIELD (BF) when the direction ranges of illumination and detection have some overlap. In this modality absorbing and scattering objects appear dark on a bright background as they remove some exciting light from the detection range.

DARKFIELD (DF) when the direction ranges of illumination and detection have no overlap. In this modality scattering objects appear bright on a dark background as they scatter some exciting light into the detection range.

DARKFIELD SCATTERING MICROSCOPY The *ultramicroscope* invented by R. A. Zsygmondy and H. Siedentopf[xvii] at the turn of the XX century is the first example of DF imaging.[79] In the original design, illumination passed through the sample at a right angle with respect to the direction of observation, so that only the scattered light was collected by the objective. Since its inception, this instrument has been particularly suited for investigating the optical properties of highly-scattering metal colloids, and one of its inventors (Zsygmondy, in 1925) indeed won the Nobel prize in Chemistry[xviii] for such studies, concerning in particular the microscopic origin of the colour of cranberry glass, like for example the Lycurgus Cup in FIG. 2.1.

Following the success of the ultramicroscope, various DF geometries have been devised; for instance, the scheme shown in FIG. 2.6a has been adopted for all the measurements presented in this thesis. A circular stop placed in the BFP of the condenser lens blocks the illumination of numerical aperture $\mathrm{NA_i} < \underline{\mathrm{NA}}_{\mathrm{DF}}$, so that a hollow cone of light illuminates the sample. When the NOs to be investigated are placed on an optical interface as in FIG. 2.6a (that is, in medium 2 where illumination come from medium 1, and collection occurs from medium 2), under the condition $\underline{\mathrm{NA}}_{\mathrm{DF}} > n_2$ the illumination is totally internally reflected into medium n_1, so that no transmitted light is col-

xvii At the time, the researchers were working for the manufacturer of optical instruments Carl Zeiss AG.

xviii Motivation of the prize: "For his demonstration of the heterogeneous nature of colloid solutions and for the methods he used, which have since become fundamental in modern colloid chemistry."

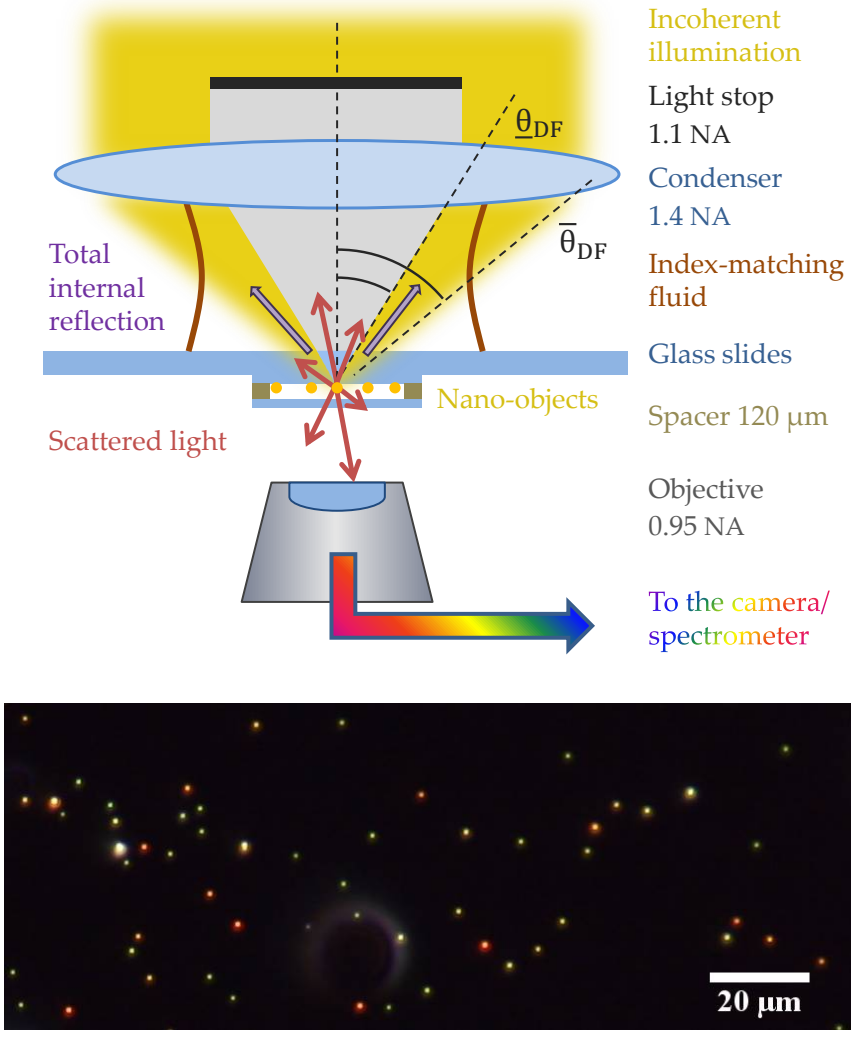

FIGURE 2.6: (a) Illumination and detection geometry we used for DF microscopy experiments. (b) DF micrograph of (nominally) D = 60 nm GNSs in a homogeneous $n = 1.52$ optical environment taken with a 0.95 NA dry objective and a commercial colour camera.

lected by the objective; nonetheless, the NOs in the NF of the interface are excited by the evanescent field and a fraction of the resulting scattering is detected.[xix] More in general, the condition $\underline{\text{NA}}_{\text{DF}} > \text{NA}_{\text{obj}}$ ensures no transmitted light falls within the acceptance of the objective even if transmitted to medium 2. FIG. 2.6b is a typical DF image acquired with our set-up: NOs appear as bright, unresolved spots on a dark background. The spectrally selective response of metal NOs yields a wide range of distinct colours, whereas dielectric debris and glass imperfections scatter indistinctly the whole lamp spectrum.

The DF signal is thus proportional to σ_{sca}, but the determination of its absolute amplitude is inherently difficult, inasmuch as only a fraction of the total scattering is collected, which depends on the angular ranges of detection and collection, as well as on the geometry and local environment of the NO. In fact, the quantitative determination of the OCS using widefield microscopy is a novel result presented in this thesis, and the methodology we devised will be discussed in detail in CH. 5 and CH. 6. To our knowledge, the work by Anderson et al.[80] is the only claim to date of a quantitative measurement of σ_{sca} using DF microscopy. In fact, the authors calibrate the proportionality with the DF signal $\sigma_{\text{sca}} = K\, S_{\text{NO}}^{\text{DF}}$ using spherical GNSs, whose σ_{sca} is predicted by Mie's formulas. However, K depends on the excitation and collection geometry, so that the calibration must be repeated whenever these are changed. Furthermore, the scattering pattern, and hence K, depends on the geometry the NO and its optical environment so that, in the end, the calibration holds solely for small spheres in a homogeneous environment: The very case used for calibration!

In BF imaging, where σ_{ext} is addressed, the SNR is limited by the shot noise of the transmitted light (i. e., the fluctuations of

xix This mechanism is analogous to TIR fluorescence microscopy (TIRFM).

the bright background). Conversely, DF schemes have in principle infinite sensitivity, because there is no background, so that an arbitrarily small signal could be detected given a long enough exposure time. However, a diffuse background due to scatterers other than the NOs, such as microscopic debris and the intrinsic roughness of the glass substrate, pose an actual limit. In practice, with a good microscope one can see through the eyepiece scatterers on clean glass having $\sigma_{sca} \sim 10^3\,nm^2$, corresponding to a $D \simeq 30\,nm$ gold sphere or a $D \simeq 20\,nm$ silver sphere in a $n = 1.52$ optical environment. On the other hand, detection in a highly scattering environment, such as for instance within a cell, is comparatively more challenging.

INTERFEROMETRIC SCHEMES We just discussed how background illumination is rejected in DF, while it limits the sensitivity of transmission BF measurements. In interferometric scattering measurements (iSCAT) it is used to increase the sensitivity instead. Although common path interferometers of various kinds had been used much before to detect scattering of NOs,[81] this concept has been revived and applied to metal NPs only in relatively recent times.[82] In iSCAT the reflected light is collected rather than the transmitted one, and the reflected field E_{ref} functions as a reference, amplifying the scattering signal in a homodyne[xx] fashion. Moreover, the interference term $|E_{ref}E^*_{sca}|$ detected has a less unfavourable scaling ($\propto D^3$) in comparison to direct scattering measurements ($\propto D^6$), rendering this technique more adequate to investigate small NOs.[81]

Laser excitation is preferred for interferometric measurements, because the visibility of the interference fringes is increased by the high degree of coherence of the source. In the

xx In *homodyne* detection the signal and the reference have exactly the same frequency; in comparison, for optical heterodyning, the frequency of either beam is shifted, and the beat note between them is detected.

most recent implementations of iSCAT, widefield illumination is achieved via fast scanning of the laser spot (up to 100 kHz by means of acousto-optic deflectors) so that the ROI is completely scanned hundreds of times within the integration time of the imaging sensor (few ms), and the SNR is boosted using a narrow detection band. The signal observed is proportional to σ_{sca}, but the complicate geometry of the interferential process involved impedes a quantitative assessment. iSCAT has recently proven capable of both fast imaging down to the ms time scale, and high sensitivity by detecting a single dye molecule.[81]

Differential interference contrast (DIC) microscopy was developed in 1952 by G. Nomarski, and features as well a common-path interferometric scheme, quite similar to the one shown in FIG. 2.5. The illumination beam is split by a Wollaston prism into two orthogonally-polarized components, which are laterally displaced by ~100 nm. When recombined after the objective by a twin Wollaston prism, they interfere according to their optical path difference. This technique is particularly suited to investigate phase objects (i. e. non-absorbing) and can provide quantitative informations. For instance, an analysis method developed by our group is able to retrieve from the phase image the thickness of a lipid bilayer (transparent, about 4 nm thick) with a sub-nanometre accuracy.[83] DIC has been successfully applied to NPs as well, e. g. in order to monitor the rotational motion of GNRs in complex environments[84] and to measure the size of nanodiamonds.[85]

Part II

NUMERICAL SIMULATIONS

3

ANALYTICAL DESCRIPTIONS OF MICROSCOPE ILLUMINATION

Modern optical microscopes often employ high numerical aperture (NA) objectives to improve the spatial resolution: As more directional information is collected, a more faithful representation of the imaged object can be reconstructed. More precisely, the lateral FWHM of the PSF — i.e. the image produced by a point-like source — is limited by diffraction to $\text{FWHM}_{\text{PSF}} \simeq \lambda/\text{NA}_{\text{obj}}$ even for an aberration-free lens. In practice, when imaging NOs a tighter PSF leads to an enhanced sensitivity and ability to discriminate adjacent NOs.[i] In order to exploit the full NA of the objective lens in transmission contrast, a condenser lens of matching NA must be used for illuminating the sample. Furthermore, for DF imaging one needs $\text{NA}_{\text{i}} > \text{NA}_{\text{obj}}$ as discussed in SEC. 2.2.2. The reader is referred to SEC. 6.1 for details on our optical microscopy set-up.

Focusing the illumination onto the sample plane means that each point of the condenser BFP is mapped onto a direction of incidence (θ_i, φ_i) converging towards the axis of the optical system, say z. In other terms, the input propagation direction, typically along z, is bent by the condenser, and the input polarization state thereby modified with the introduction of a z component. The amplitude of such a longitudinal component increases with θ_i and therefore cannot be neglected when high NA illumination is used. As already discussed in CH. 1, the geometry and material composition of the NO and its environment

i The PSFs of NOs closer than FWHM_{PSF} merge into a single spot, and cannot be distinguished from an individual object (except for an increased intensity).

determine the resonant modes of the system; to what extent a given mode is excited depends instead on the properties of the illumination, including its polarization. Therefore, accurate quantitative results can be obtained from experiments and simulations only if the data analysis and modelling practices adopted take into account the actual polarization content of microscope illumination. On the other hand, most investigations in nanoplasmonics have so far concentrated on the spectral signatures of metal NOs, i. e. on the position and width of the LSPRs, rather than on the absolute OCS magnitude. Consequently, little attention has been paid to the role of the exciting polarization, and numerical models routinely use plane waves (mostly with normal incidence to the substrate) to address the resonances exhibited by a given system and compare these to experiments.

Broadly speaking, two kinds of excitation can be employed:

INCOHERENT ILLUMINATION can be obtained by focusing the collimated emission from a tungsten-halogen lamp or a light-emitting diode (LED). Waves with different directions of incidence bear no fixed phase relation and thus they do not interfere at the focus.

COHERENT ILLUMINATION can be obtained by focusing a laser beam. Waves with different directions of incidence interfere when brought together into the focus, thereby originating a PSF.

In this chapter, several mathematical descriptions of coherent and incoherent microscope illumination are developed. In particular, various analytical expressions of $\mathbf{E}$ in the focal region are derived, which will be used to represent the exciting field in the numerical and analytical models of scattering experiments presented in the ensuing chapters.

3.1 INCOHERENT ILLUMINATION

3.1.1 *Electric field above and below a planar dielectric interface*

We already treated at a basic level the classical problem of the transmission and reflection of a plane wave at a planar dielectric interface in SEC. 1.4. In this section we will build on those materials and derive the analytical expression $\mathbf{E}(x, y, z)$ of the electric field above and below the optical interface. It will be then discussed how incoherent microscope illumination can be described as an incoherent superposition of such fields. This mathematical description of the excitation will be used in our models — both numerical, see SEC. 4.2, and analytical, see SEC. 5.3 — of light scattering by a NO in microscopy experiments.

The geometry of the problem is depicted in FIG. 3.1a, which is essentially FIG. 1.7 with the p and s field polarizations added. It is convenient to introduce the notation $\widehat{\mathbf{p}} \equiv \widehat{\mathbf{E}}_p$ and $\widehat{\mathbf{s}} \equiv \widehat{\mathbf{E}}_s$. By comparing the wavectors and fields of each wave in FIG. 3.1a to the versors of the standard spherical coordinates in FIG. 3.1b, one finds the two triads share the same directions in every point of space: $(\widehat{\mathbf{k}}, \widehat{\mathbf{p}}, \widehat{\mathbf{s}}) = (-\widehat{\mathbf{r}}, \widehat{\boldsymbol{\theta}}, \widehat{\boldsymbol{\varphi}})$.[ii] This observation suggests that spherical coordinates make the most natural choice to tackle this problem.[iii]

ii Incidentally, the alternative formulation of the law of specular reflection $\theta_r = \theta_i$ and $\varphi_r = \varphi_i + \pi$ — albeit common in literature — would not allow such a convenient identification for the reflected wave too.

iii Intuitively, this stems from its translational symmetry: Time-averaged physical quantities cannot depend on the x and y coordinates defining the plane of the interface; they are expected to depend instead on the propagation direction (θ_i, φ_i) of the impinging wave.

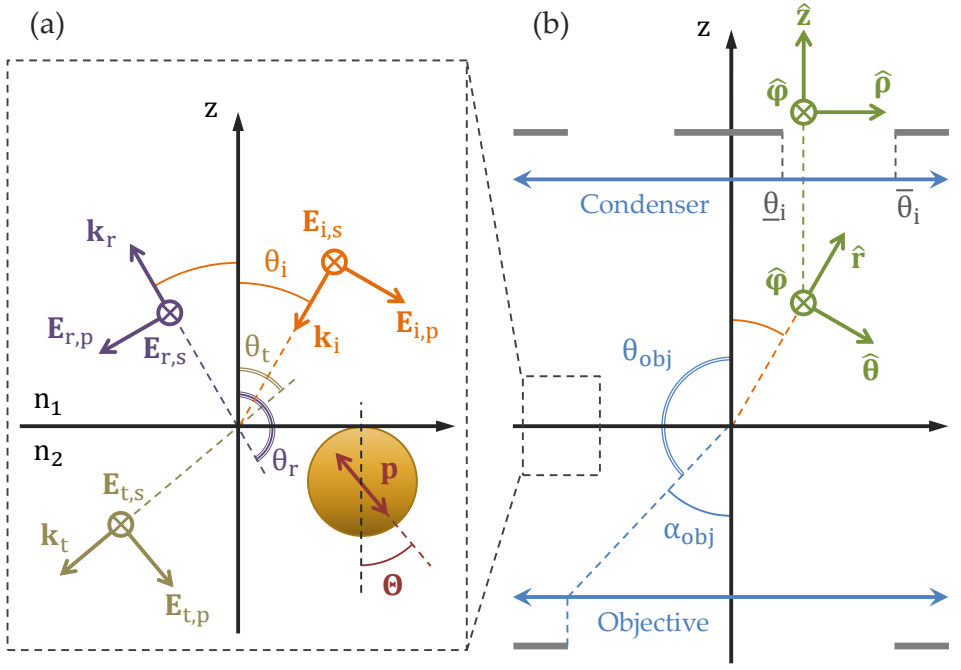

FIGURE 3.1: (a) Two dielectric media with refractive indices n_1 and n_2 are separated by the plane $z = 0$. A plane wave $\mathbf{E}_i$ incident on the interface originates a reflected $\mathbf{E}_r$ and a transmitted $\mathbf{E}_t$ wave. The plane of incidence $\varphi = \varphi_i$ is represented, so that the p and s component of the fields are respectively parallel and perpendicular to the plane of the page. The field orientation depicted corresponds to $n_1 > n_2$ and $\theta_B < \theta_i < \theta_c$. The exciting field induces an electric dipole moment $\mathbf{p}$ in a NO placed near the interface, which forms and angle Θ with respect to the normal to the interface. (b) The angular ranges of illumination $\theta \in [\underline{\theta}_i, \overline{\theta}_i]$ and collection $\theta \in [\theta_{obj}, \pi]$ are determined by circular light stops placed in the BFP of the condenser and objective lens. Cylindrical (ρ, z, φ) and spherical (r, θ, φ) coordinates (green versors) are employed respectively in the back and front spaces of the lenses. (a) is a close-up on the interface in (b), as suggested by the dashed frames.

In Cartesian components, the spherical versors read

$$\hat{\mathbf{r}} = \begin{bmatrix} \sin\theta\cos\varphi \\ \sin\theta\sin\varphi \\ \cos\theta \end{bmatrix}; \quad \hat{\boldsymbol{\theta}} = \begin{bmatrix} \cos\theta\cos\varphi \\ \cos\theta\sin\varphi \\ -\sin\theta \end{bmatrix}; \quad \hat{\boldsymbol{\varphi}} = \begin{bmatrix} -\sin\varphi \\ \cos\varphi \\ 0 \end{bmatrix}. \tag{3.1}$$

The wavevector of the incident (subscript i) wave is $\mathbf{k}_i = -k_i\,\hat{\mathbf{r}}(\theta_i, \varphi_i)$, and equivalent expressions hold for the reflected ($i \to r$) and transmitted ($i \to t$) wave; the respective wavenumbers are $k_i = k_r = n_1 k_0$ and $k_t = n_2 k_0$. As for the field orientations, one has $\hat{\mathbf{p}}_i = \hat{\boldsymbol{\theta}}(\theta_i, \varphi_i)$ and $\hat{\mathbf{s}}_i = \hat{\boldsymbol{\varphi}}(\varphi_i)$ for the incident wave, and equivalent expressions for the reflected and transmitted ones.

We are now able to express conveniently all the field components involved in terms of the Fresnel coefficients (1.15)

$$\mathbf{E}_{i,p} = E_i\,\hat{\mathbf{p}}_i\,e^{ik_i\cdot\mathbf{r}}, \quad \mathbf{E}_{r,p} = r_p E_i\,\hat{\mathbf{p}}_r\,e^{ik_r\cdot\mathbf{r}}, \quad \mathbf{E}_{t,p} = t_p E_i\,\hat{\mathbf{p}}_t\,e^{ik_t\cdot\mathbf{r}}, \tag{3.2p}$$

$$\mathbf{E}_{i,s} = E_i\,\hat{\mathbf{s}}_i\,e^{ik_i\cdot\mathbf{r}}, \quad \mathbf{E}_{r,s} = r_s E_i\,\hat{\mathbf{s}}_r\,e^{ik_r\cdot\mathbf{r}}, \quad \mathbf{E}_{t,s} = t_s E_i\,\hat{\mathbf{s}}_t\,e^{ik_t\cdot\mathbf{r}}, \tag{3.2s}$$

where the time dependence given by a common oscillating factor $e^{-i\omega t}$ has been omitted.[iv] Eventually, EQ. (3.2) can be used to write down the analytical expression $\mathbf{E}(x, y, z)$ we were

[iv] By taking the phase of $\mathbf{E}_i$ as reference, one has $E_{i,p} = E_{i,s} = E_i \in \mathbb{R}$.

after. $\mathbf{E}$ in medium 1 is the coherent superposition of the incident and reflected fields[v]

$$\begin{aligned}\mathbf{E}_{1,p}(\theta_i, \varphi_i) &= \mathbf{E}_{i,p} + \mathbf{E}_{r,p} \\ &= E_i \begin{bmatrix} \cos\theta_i \cos\varphi_i \left(e^{ik_{i,z}z} - r_p\, e^{-ik_{i,z}z}\right) \\ \cos\theta_i \sin\varphi_i \left(e^{ik_{i,z}z} - r_p\, e^{-ik_{i,z}z}\right) \\ -\sin\theta_i \left(e^{ik_{i,z}z} + r_p\, e^{-ik_{i,z}z}\right) \end{bmatrix} e^{i(k_{i,x}x + k_{i,y}y)},\end{aligned} \tag{3.3p}$$

$$\begin{aligned}\mathbf{E}_{1,s}(\theta_i, \varphi_i) &= \mathbf{E}_{i,s} + \mathbf{E}_{r,s} \\ &= E_i \begin{bmatrix} -\sin\varphi_i \\ \cos\varphi_i \\ 0 \end{bmatrix} \left(e^{ik_{i,z}z} + r_s\, e^{-ik_{i,z}z}\right) e^{i(k_{i,x}x + k_{i,y}y)},\end{aligned} \tag{3.3s}$$

whereas $\mathbf{E}$ in medium 2 coincides with the transmitted field

$$\mathbf{E}_{2,p}(\theta_i, \varphi_i) = \mathbf{E}_{t,p} = t_p E_i \begin{bmatrix} \cos\theta_t \cos\varphi_i \\ \cos\theta_t \sin\varphi_i \\ -\sin\theta_t \end{bmatrix} e^{ik_t \cdot \mathbf{r}}, \tag{3.4p}$$

$$\mathbf{E}_{2,s}(\theta_i, \varphi_i) = \mathbf{E}_{t,s} = t_s E_i \begin{bmatrix} -\sin\varphi_i \\ \cos\varphi_i \\ 0 \end{bmatrix} e^{ik_t \cdot \mathbf{r}}. \tag{3.4s}$$

Note that the fields (3.3) and (3.4) depend only on the direction of incidence, as all other variables can be expressed as functions of (θ_i, φ_i), see SEC. 1.4.

v COMSOL adopts the electrical engineering sign convention $E \propto e^{-ik\cdot r} e^{i\omega t}$ for a wave propagating along $\mathbf{r}$, which is the complex conjugate of the optics sign convention used in this thesis. The conjugate of EQ. (3.3) and EQ. (3.4) should therefore be input as exciting field in COMSOL.

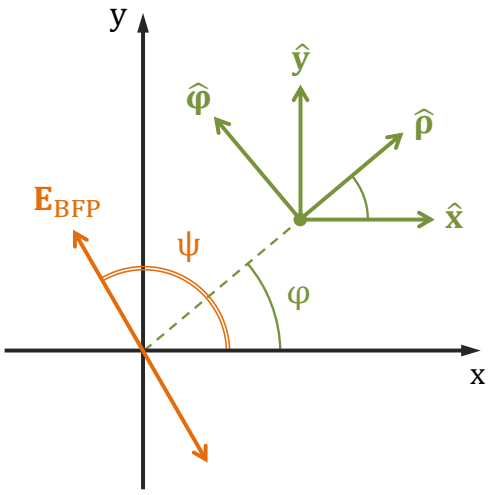

FIGURE 3.2: The BFP of the condenser is represented. $(\hat{x}, \hat{y})$ and $(\hat{\rho}, \hat{\varphi})$ are the basis versors of Cartesian and cylindrical coordinates respectively. The linearly polarized electric field $\mathbf{E}_{\mathrm{BFP}}$ forms an angle $\psi \in [0, \pi)$ with $\hat{x}$.

LINEARLY POLARIZED ILLUMINATION Consider a linearly polarized illumination in the BFP of the condenser. The azimuth ψ identifies the polarization direction as in FIG. 3.2, so that

$$\mathbf{E}_{\mathrm{BFP}} = \left[\cos\psi\, \hat{\mathbf{x}} + \sin\psi\, \hat{\mathbf{y}} \right] E_i\, e^{-2\pi i z/\lambda_0} \tag{3.5}$$

where the harmonic time dependence $e^{-i\omega t}$ has been omitted as usual. The illumination is assumed to be homogeneous[vi] over the BFP, so that $|\mathbf{E}_{\mathrm{BFP}}| = E_i$ is independent of the position (ρ, φ) in the plane. As shown in FIG. 3.2, the basis versors of Cartesian and cylindrical coordinates are related by a rotation around $\hat{z}$ represented by the rotation matrix $\mathbf{R}_{\hat{z}}$

$$\begin{bmatrix} \hat{\mathbf{x}} \\ \hat{\mathbf{y}} \end{bmatrix} = \mathbf{R}_{\hat{z}}(-\varphi) \begin{bmatrix} \hat{\boldsymbol{\rho}} \\ \hat{\boldsymbol{\varphi}} \end{bmatrix} = \begin{bmatrix} \cos\varphi\, \hat{\boldsymbol{\rho}} - \sin\varphi\, \hat{\boldsymbol{\varphi}} \\ \sin\varphi\, \hat{\boldsymbol{\rho}} + \cos\varphi\, \hat{\boldsymbol{\varphi}} \end{bmatrix}. \tag{3.6}$$

$\mathbf{E}_{\mathrm{BFP}}$ can be thereby expressed in terms of the cylindrical versors

$$\mathbf{E}_{\mathrm{BFP}}(\varphi) = \left[\cos(\psi - \varphi)\hat{\boldsymbol{\rho}} + \sin(\psi - \varphi)\hat{\boldsymbol{\varphi}} \right] E_i\, e^{-2\pi i z/\lambda_0} \tag{3.7}$$

vi In our set-up a homogeneous illumination is obtained via a suitable diffuser inserted in the illumination path, see FIG. B.2 and related discussion.

Let us now calculate $\mathbf{E}$ corresponding to the direction of incidence (θ_i, φ_i) in the front space of the condenser, where the spherical coordinate (r, θ, φ) are used. As illustrated by FIG. 3.1b, the condenser focuses the collimated illumination onto the sample plane by converting the propagation direction $-\hat{\mathbf{z}}$ into $-\hat{\mathbf{r}}$, so that the resulting wavevector is $\mathbf{k}_i = -k_i\,\hat{\mathbf{r}}(\theta_i, \varphi_i)$. Concurrently, the radial component $\hat{\boldsymbol{\rho}}(\varphi_i)$ of the field is rotated into a polar one $\hat{\boldsymbol{\theta}}(\theta_i, \varphi_i) = \hat{\mathbf{p}}_i$, while the tangential component $\hat{\boldsymbol{\varphi}}(\varphi_i) = \hat{\mathbf{s}}_i$ is left unchanged. Thus the incident electric field reads

$$\begin{aligned}\mathbf{E}_i(\theta_i, \varphi_i) &= \left[\cos(\psi - \varphi_i)\,\hat{\mathbf{p}}_i + \sin(\psi - \varphi_i)\,\hat{\mathbf{s}}_i\right] E_i\, e^{ik_i \cdot r} \\ &= \cos(\psi - \varphi_i)\mathbf{E}_{i,p} + \sin(\psi - \varphi_i)\mathbf{E}_{i,s}\end{aligned} \tag{3.8}$$

namely, a coherent superposition of the p and s fields defined by EQ. (3.2). Moreover, since the p and s components are not mixed upon reflection or transmission, an analogous expression holds for the reflected (i→r) and transmitted (i→t) waves.

We can eventually write via EQ. (3.8) the electric field above and below the interface, namely $\mathbf{E}_1 = \mathbf{E}_i + \mathbf{E}_r$ and $\mathbf{E}_2 = \mathbf{E}_t$

$$\mathbf{E}_1(\theta_i, \varphi_i) = \cos(\psi - \varphi_i)\,\mathbf{E}_{1,p} + \sin(\psi - \varphi_i)\,\mathbf{E}_{1,s} \tag{3.9-1}$$

$$\mathbf{E}_2(\theta_i, \varphi_i) = \cos(\psi - \varphi_i)\,\mathbf{E}_{2,p} + \sin(\psi - \varphi_i)\,\mathbf{E}_{2,s} \tag{3.9-2}$$

with $\mathbf{E}_{1,p}$, $\mathbf{E}_{1,s}$ and $\mathbf{E}_{2,p}$, $\mathbf{E}_{2,s}$ given by EQ. (3.3) and EQ. (3.4).

INCOHERENT SUPERPOSITION Due to the incoherent illumination assumption, waves having different directions of incidence bear no definite phase relation; hence they do not interfere when brought together in the focal region, and a PSF is not created. Incoherent microscope illumination is therefore described as an *incoherent superposition* — that is, whereby field intensities rather than amplitudes are summed over the angular range of illumination — of the waves EQ. (3.9-1) and EQ. (3.9-2)

in medium 1 and 2. For unpolarized illumination, however, the p and s components are mutually incoherent too, and thus they must not be summed; EQ. (3.9) should instead be replaced by EQ. (3.3) and EQ. (3.4).

3.1.2 *Directional cross-section averaging*

Optical microscopy experiments address the OCS under microscope (superscript m) illumination $\sigma^{m} \equiv P^{m}/I_{i}^{m}$; on the other hand, the analytical approaches outlined in SEC. 1.1 and the numerical methods presented in SEC. 4.2 compute the OCS under plane wave (pw) excitation $\sigma^{pw} \equiv P^{pw}/I_{i}^{pw}$. We remind the reader that in the OCS definition P is the power removed from the exciting mode by a NO through a given optical process (e. g. P_{abs} for absorption) and I_i is the incident intensity, see EQ. (1.1);. In this section a mathematical relation between σ^{m} and σ^{pw} is derived, allowing us to compare experimental results with theory and numerical simulations. To do so, we need first to develop a description of the microscope illumination.

An *aplanatic* optical system is defined as free of both off-axis coma and spherical aberration. It converts an impinging plane wave into a spherical one converging in its front focus, as sketched in FIG. 3.3a. Mapping a planar surface into a spherical one involves a local stretching by a factor $1/\cos\theta_i$, see FIG. 3.3b. This can be obtained formally by transforming to polar coordinates the infinitesimal area element of the planar wavefront

$$dA = \rho_i \, d\rho_i \, d\varphi_i = f^2 n^2 \cos\theta_i \sin\theta_i \, d\theta_i \, d\varphi_i = \cos\theta_i \, d\Sigma_{fn} \tag{3.10}$$

where f is the focal length in vacuum. In the second equality of EQ. (3.10) we used the identity $\rho_i = f\,NA_i = fn\sin\theta_i$, which is known as *Abbe's sine condition*: It characterizes aplanatic systems and is necessary and sufficient to avoid off-axis

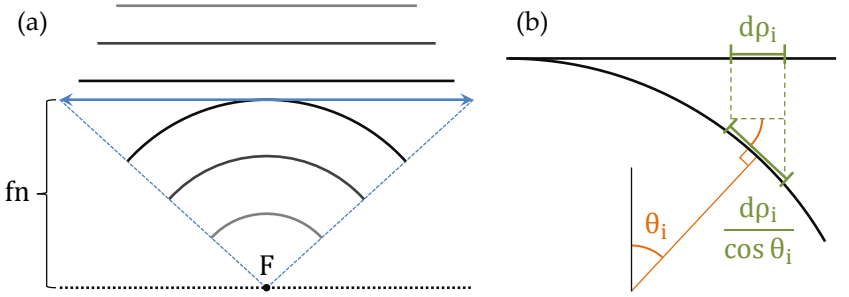

FIGURE 3.3: An aplanatic optical system (double arrow) converts a portion of a plane wavefront into a portion of a spherical wavefront converging at the focus F. f denotes the focal length in vacuum and n the refractive index of the front medium, i. e. the lower half-space. (a) Contours of constant phase. (b) Magnified portion of the plane and spherical wavefronts.

coma. In the last expression we highlighted the infinitesimal surface element $d\Sigma_{fn}$ of the spherical wavefront with radius fn. Since the transmitted power is spread over a larger surface element $d\Sigma_{fn} = dA/\cos\theta_i$, the intensity (which is power per unit area) of the microscope illumination decreases for larger values of θ_i proportionally to the *aplanatic cosine factor* $\cos\theta_i$.

The condenser lens used in our microscope is aplanatic to a good approximation, so the above considerations hold. In analogy to a typical experimental configuration, we assume an axially-symmetric illumination defined by the angular ranges $\varphi_i \in [0, 2\pi)$ and $\theta_i \in [\underline{\theta}_i, \overline{\theta}_i]$, with $\underline{\theta}_i$ and $\overline{\theta}_i$ determined by suitable stops in the BFP of the condenser as in FIG. 3.1b. Now, when an incoherent source such as an incandescent filament is used, the BFP is not filled by a single planar wavefront, but rather covered by small (coherence length is $\sim\lambda$) illumination patches incoherent to each other. As a result, instead of a converging spherical wave, the microscope illumination is

better described as an incoherent superposition of plane waves impinging from all directions θ_i, φ_i, see P. 64.

Thus the power removed from the microscope illumination by the NO is the sum of all individual plane wave contributions[vii]

$$P^m = \int_{A_{BFP}} P^{pw}\, dA \propto \int_{\underline{\theta}_i}^{\bar{\theta}_i} \int_0^{2\pi} P_{pw} \cos\theta_i \sin\theta_i \, d\theta_i \, d\varphi_i \qquad (3.11)$$

where the first integration runs over the illuminated area in the BFP of the condenser. The aplanatic cosine factor has been introduced in the last equality via EQ. (3.10). An expression analogous to EQ. (3.11) can be written for the incident intensity

$$I^m = \int_{A_{BFP}} I^{pw}\, dA \propto I^{pw} \int_{\underline{\theta}_i}^{\bar{\theta}_i} \int_0^{2\pi} \cos\theta_i \sin\theta_i \, d\theta_i \, d\varphi_i \,. \qquad (3.12)$$

Note that since a constant I^{pw} is used in simulations, it can be taken out of the integral (3.12). Putting together EQ. (3.11) and EQ. (3.12) one obtains

$$\sigma^m \equiv \frac{P^m}{I_i^m} = \frac{\int_{\underline{\theta}_i}^{\bar{\theta}_i} \int_0^{2\pi} \sigma^{pw} \cos\theta_i \sin\theta_i \, d\theta_i \, d\varphi_i}{\int_{\underline{\theta}_i}^{\bar{\theta}_i} \int_0^{2\pi} \cos\theta_i \sin\theta_i \, d\theta_i \, d\varphi_i} = \langle \sigma^{pw} \rangle_{A_{BFP}}. \qquad (3.13)$$

The last equality in EQ. (3.13) highlights the intuitive meaning of the formula: σ^m is the average of σ^{pw} over A_{BFP}. The $\cos\theta_i$ and $\sin\theta_i$ weighing factors appear because the integration is performed over Ω_i rather than over A_{BFP}; specifically, they mimic the results of a homogeneous sampling of ρ_i and φ_i in the BFP.

Let us assume first the excitation is linearly polarized (pol subscript) along ψ in the BFP. With the exception of a sphere

vii We sum the (infinitesimal) contributions of an infinite number of exciting waves; in other words, the integrand is an areal or angular power density.

immersed in a homogeneous medium, σ^{pw} then depends on θ_i, φ_i, and ψ. In practice, one can only perform a finite number of simulations, and therefore EQ. (3.13) must be approximated to a discrete sum

$$\sigma^{m}_{pol}(\psi) \simeq \frac{\sum_{m,n} \cos\theta_{i,m} \sin\theta_{i,m}\, \sigma^{pw}(\theta_{i,m}, \varphi_{i,n}, \psi)}{n \sum_{m} \cos\theta_{i,m} \sin\theta_{i,m}} \tag{3.14}$$

where the indices m and n are positive integers. Thus computing EQ. (3.14) involves $m \times n$ simulations: The finer the sampling of the illumination range, the better the OCS are approximated, at the expense of a larger number of simulations.

For unpolarized excitation (unp), to each direction of incidence corresponds a plane wave with incoherent p and s components. In this case $P^{pw} = \frac{1}{2}(P^p + P^s)$ has to be replaced in EQ. (3.11), while $I^p = I^s = I^{pw}$ is used in simulations. Thus EQ. (3.13) yields

$$\sigma^{m}_{unp} \simeq \frac{\sum_{m,n} \cos\theta_{i,m} \sin\theta_{i,m} \left[\sigma^{p}(\theta_{i,m}, \varphi_{i,n}) + \sigma^{s}(\theta_{i,m}, \varphi_{i,n})\right]}{2n \sum_{m} \cos\theta_{i,m} \sin\theta_{i,m}} \tag{3.15}$$

which requires $2(m \times n)$ simulations. We emphasize that EQ. (3.14) and EQ. (3.15) refer to equidistant angular sampling.[viii]

When the NO has specific symmetries, the φ_i domain for averaging can be reduced by exploiting the symmetry of the problem (excitation + NO) in order to speed up the computation; in particular, if the NO (with the appropriate axis orientation):

viii Mathematically, $\Delta\theta_i = \theta_{i,m+1} - \theta_{i,m}$ and $\Delta\varphi_i = \varphi_{i,n+1} - \varphi_{i,n}$ are constants. The optimum sampling (i. e. the one requiring the least samples to achieve a given accuracy) — albeit less straightforward to implement in practical simulations — would rather be $(\Delta\theta_i)' = \Delta\theta_i \cos\theta_i$ and $(\Delta\varphi_i)' = \Delta\varphi_i \sin\theta_i$. As the optimum sampling corresponds to a homogeneous sampling of A_{BFP}, if adopted the $\cos\theta_i$ and $\sin\theta_i$ weighing factors would have to be removed from EQ. (3.14) and EQ. (3.15).

- has $x = 0$ as a mirror plane (such as for a heterodimer or a tetrahedron), the domain can be reduced to $\varphi_i \in [0, \pi)$ for excitation polarized along $\hat{\mathbf{x}}$ or $\hat{\mathbf{y}}$, or else unpolarized.
- has both $x = 0$ and $y = 0$ as mirror planes (such as for a rod, a homodimer or a cube), the domain can be reduced to $\varphi_i \in [0, \pi)$ under a generic linearly polarized illumination, and to $\varphi_i \in [0, \pi/2)$ for excitation polarized along $\hat{\mathbf{x}}$ or $\hat{\mathbf{y}}$, or else unpolarized.
- has $\hat{\mathbf{z}}$ as a continuous rotation axis (such as for a sphere or a disc), $\sigma^m_{pol} = \sigma^m_{unp}$ so that any single value of φ_i can be used.

Summarizing, EQ. (3.14) and EQ. (3.15) express the OCS under microscope illumination as an average of the OCS under plane wave excitation, thus permitting a direct comparison of experimental measurements with numerical simulations.

3.1.3 *The equivalent p-polarized wave method*

While averaging the results of several simulations as discussed in the previous section leads to accurate results — inasmuch as the illumination range is sampled densely enough — it is also computationally expensive. This motivated us to develop an alternative, approximate approach to compute the OCS under microscope illumination with a single simulation. Our idea is to use as excitation a plane wave whose intensity I^p_j matches the intensity of the microscope illumination I^m_j along each Cartesian axis $j = x, y, z$. Note that a p-polarized wave must be used, because an s-polarized wave has null z component and cannot reproduce the longitudinal component of the microscope illumination. The OCS obtained with such an *equivalent p-polarized wave* equal the OCS under microscope illumination when the following assumptions are met:

1. The NO is small enough ($D \ll \lambda$) that the exciting field $\mathbf{E}_{exc}$ can be considered constant constant over the NO volume (*electrostatic approximation*).
2. The polarizability tensor $\boldsymbol{\alpha}$ describing the investigated mode is diagonal in the Cartesian coordinate system. In SEC. 5.3 we will enumerate a number of NOs whose modes satisfy this requirement.
3. Any phase relation between the Cartesian components of the field is disregarded. While this does not affect modes with uniaxial $\boldsymbol{\alpha}$, it might introduce errors when simulating modes with planar or isotropic $\boldsymbol{\alpha}$.

We begin by writing down the expression of I_j^m for incoherent, linearly-polarized microscope illumination: It is in fact analogous to EQ. (3.12) giving the total incident intensity

$$I_{pol,j}^m(\psi) \propto 2 \int_{\underline{\theta}_i}^{\bar{\theta}_i} d\theta_i \cos\theta_i \sin\theta_i \int_0^{\pi} d\varphi_i \left|\mathbf{E}_{exc,j}(\theta_i, \varphi_i, \psi)\right|^2. \quad (3.16)$$

Note that the twofold symmetry of the polarized illumination has been exploited to halve the azimuthal integration range, so to speed up the numerical computation.[ix] In EQ. (3.16) $\mathbf{E}_{exc}$ is the plane wave $\mathbf{E}_1$ or $\mathbf{E}_2$ given by EQ. (3.9-1) or EQ. (3.9-2) respectively above and below the $z = 0$ interface. $I_{pol,j}^m$ is thereby defined as a piecewise function of z — unless the NO is immersed in a homogeneous medium; in the TIR regime ($\bar{\theta}_i > \theta_c$) the evanescent decay for $z < 0$ adds a further z dependence to $I_{pol,j}^m$. Under unpolarized excitation the intensities of the p and s components must be summed rather than the fields; that

ix In fact, the integration over φ_i in EQ. (3.16) can be performed explicitly for each j; see for instance the calculation for $|E_{2,x}|^2$ in EQ. (5.25). However, the computation of EQ. (3.16) is fast enough (~ 0.1 s) for practical purposes, so we will not report here the integrated expressions.

is, the integrand in EQ. (3.16) must be replaced by $\left|E_{p,j}\right|^2+\left|E_{s,j}\right|^2$. Using the explicit expressions (3.3) or (3.4) of the fields one finds $I^m_{unp,j} = I^m_{pol,j}(\pi/4)$, and the discussion can therefore be limited to the polarized case.

Now we want to find the parameters describing the equivalent p-polarized wave, namely its azimuthal $\varphi_{i,p}$ and polar $\theta_{i,p}$ angles of incidence, and its amplitude $E_{i,p}$. These can be determined by imposing $I^p_j = I^m_{pol,j}$ for $j = x, y, z$ at a given position $z = z_{NO}$. In order to provide a concrete example of the calculations involved, let us consider the case $\mathbf{E}_{exc} = \mathbf{E}_2$, corresponding to our typical experimental configuration where the NO is placed in medium 2 as in FIG. 3.1. One then has[x] $I^p_j \propto \left|E_{p,j}\right|^2$ where $E_{p,j}$ is given by EQ. (3.4p), and the requirement $I^p_j(z_{NO}) = I^m_{pol,j}(z_{NO})$ translates into the system

$$\begin{cases} \cos^2\varphi_{i,p}\left|\cos\theta_{t,p}\, e^{ik_{t,z}z_{NO}}\, t_p\right|^2 E^2_{i,p} = I^m_{pol,x}(z_{NO}) & [\mathcal{X}] \\ \sin^2\varphi_{i,p}\left|\cos\theta_{t,p}\, e^{ik_{t,z}z_{NO}}\, t_p\right|^2 E^2_{i,p} = I^m_{pol,y}(z_{NO}) & [\mathcal{Y}] \\ \left|\sin\theta_{t,p}\, e^{ik_{t,z}z_{NO}}\, t_p\right|^2 E^2_{i,p} = I^m_{pol,z}(z_{NO}) & [\mathcal{Z}] \end{cases} \tag{3.17}$$

where $\varphi_{i,p}$, $\theta_{i,p}$, and $E_{i,p}$ are the unknowns.[xi] Although general conditions for the existence and unicity of the solutions (such as the Rouché-Capelli theorem for linear systems) do not hold here, some solutions of the system (3.17) in terms of the parameters[xii] $I^m_{pol,j}$ are not hard to find.

x Note that the same proportionality factor $\frac{1}{2}nc_0\varepsilon_0$ has been omitted from the definitions of I^p_j here and of I^m_j in EQ. (3.16).

xi The dependence on $\theta_{i,p}$ is implicit in $\theta_{t,p}$ (Snell's law) and t_p, see EQ. (1.15p).

xii To unburden the notation, z_{NO} in $I^m_{pol,j}(z_{NO})$ will henceforth be omitted.

Having labelled with $\mathcal{X}$, $\mathcal{Y}$, and $\mathcal{Z}$ the three equations according to the value assumed by j on the RHS one has

$$\frac{\mathcal{Y}}{\mathcal{X}} \Longrightarrow \tan^2 \varphi_{i,p} = I^m_{pol,y} / I^m_{pol,x} \tag{3.18φ}$$

$$\frac{\mathcal{Z}}{\mathcal{X}+\mathcal{Y}} \Longrightarrow \frac{\sin^2 \theta_{t,p}}{\left|\cos^2 \theta_{t,p}\right|} = I^m_z / I^m_{\parallel} \tag{3.18θ}$$

$$\mathcal{X}+\mathcal{Y}+\mathcal{Z} \Longrightarrow \left(\left|\cos^2 \theta_{t,p}\right| + \sin^2 \theta_{t,p}\right) \left| e^{ik_{t,z} z_{NO}} t_p \right|^2 E^2_{i,p} = I^m \tag{3.18E}$$

where we have introduced $I^m_{\parallel} \equiv I^m_{pol,x} + I^m_{pol,y}$ and $I^m \equiv I^m_{\parallel} + I^m_{pol,z}$. Note that the pol subscript has been dropped for axially-symmetric quantities such as I^m_z and $I^m_{\parallel}$ which do not depend on ψ — as can be verified explicitly via their definition (3.16) — and hence are the same regardless of the polarization of the illumination. As discussed on P. 29, $\cos\theta_{t,p}$ is imaginary in the TIR regime (whereas $\sin\theta_{t,p}$ is always real), so that the absolute values in EQ. (3.18θ) and (3.18E) lead to two cases

$$\left|\cos^2 \theta_{t,p}\right| = \begin{cases} 1 - \sin^2 \theta_{t,p} & \text{for } \theta_{i,p} \leqslant \theta_c \\ \sin^2 \theta_{t,p} - 1 & \text{for } \theta_{i,p} > \theta_c \end{cases} \tag{3.19}$$

corresponding to the transmission and TIR regime respectively. When we restrict ourselves to the physical ranges of the unknowns — namely $\varphi_{i,p} \in [0, \pi)$, $\theta_{i,p} \in [0, \pi/2)$, and $E_{i,p} \geqslant 0$ — the *transmission solution* of the system (3.17) is

$$\begin{cases} \varphi_{i,p} = \arctan \sqrt{I^m_{pol,y} / I^m_{pol,x}} & \text{(3.20φ)} \\ \theta_{i,p} = \arcsin \left(\dfrac{n_2}{n_1} \sqrt{I^m_z / I^m} \right) & \text{(3.20θ)} \\ E_{i,p} = \sqrt{I^m} \Big/ \left| t_p(\theta_{i,p}) \right| & \text{(3.20E)} \end{cases}$$

while the TIR *solution* is

$$\begin{cases} \varphi_{i,p} = \arctan \sqrt{I^m_{pol,y}/I^m_{pol,x}} & (3.21\varphi) \\ \theta_{i,p} = \arcsin \dfrac{n_2/n_1}{\sqrt{1 - I^m_{\parallel}/I^m_z}} & (3.21\theta) \\ E_{i,p} = \dfrac{e^{-ik_{t,z}(\theta_{i,p})z_{NO}}}{\left|t_p(\theta_{i,p})\right|} \sqrt{\dfrac{I^m}{2\left(\frac{n_1}{n_2}\sin\theta_{i,p}\right)^2 - 1}} & (3.21E) \end{cases}$$

Note that $e^{ik_{t,z}z_{NO}}$ is an oscillatory factor with modulus 1 for $\theta_{i,p} \leqslant \theta_c$, whereas in the TIR regime it is real and can be taken out of the modulus in EQ. (3.21E). As suggested by the presence of the pol subscript, in the solutions (3.20) and (3.21) only $\varphi_{i,p}$ depends on the exciting polarization ψ. Thus, the solutions for unpolarized (or circularly polarized) illumination are the same (3.20) and (3.21) with $\varphi_{i,p}\big|_{\psi=\pi/4} = \pi/4$.

The solutions (3.20) and (3.21) exist only when the argument of the arcsin in EQ. (3.20θ) and (3.21θ) is $\leqslant 1$, which occurs if[xiii]

$$\frac{I^m_{\parallel}}{I^m_z} \begin{cases} \geqslant \left(\frac{n_2}{n_1}\right)^2 - 1 & \text{for } \theta_{i,p} \leqslant \theta_c \\ \leqslant 1 - \left(\frac{n_2}{n_1}\right)^2 & \text{for } \theta_{i,p} > \theta_c \end{cases} \tag{3.22}$$

Although expressing EQ. (3.22) as an explicit function of n_1, n_2, $\underline{\theta}_i$, and $\overline{\theta}_i$ is difficult, some general observations can be made.

THE TRANSMISSION SOLUTION always exists for $n_1 \geqslant n_2$, while for $n_1 < n_2$ it does not when I^m_z is large, which however only occurs for high NA illumination and strongly mismatched interfaces.

xiii It is easy to check the condition EQ. (3.22) ensures as well the radicands in EQ. (3.21θ) and EQ. (3.21E) are positive.

THE TIR SOLUTION does not exist for $n_1 \leqslant n_2$ (when TIR cannot occur), while for $n_1 > n_2$ a large I_z^m is still required. For instance, when a glass/air interface is considered, the solution exists only in a few degree θ_i range around θ_c.

We have implemented the formulas above into the code A.1 executable in MATLAB® (a computing environment including both numerical and symbolic functionalities) in order to calculate $I_{pol,j}^m$ and the resulting parameters of the equivalent p-polarized wave. As an exemplary result, the transmission solution (3.20) for a glass/air interface is shown in FIG. 3.4. In the small NA limit $\langle\theta_i\rangle \ll 1$, where the microscope illumination exhibits no longitudinal polarization component, one has $\varphi_{i,p} = \psi$ and $\theta_{i,p} = \langle\theta_i\rangle$; the cross-polarized component introduced by the condenser at larger NAs causes $\varphi_{i,p}$ to drift towards $\pi/4$, which is the solution for unpolarized illumination. $E_{i,p} \to 0$ in both the small and large NA limit, respectively because of the factors $\sin\theta_i$ and $\cos\theta_i$ factor in EQ. (3.16); physically, $I_{pol,y}^m \to 0$ because either the illuminated area A_{BFP} (for $\langle\theta_i\rangle \to 0$) or the transmission efficiency (for $\langle\theta_i\rangle \to \pi/2$) of the condenser becomes null. All variables present a discontinuity of the first derivative at $\langle\theta_i\rangle = \theta_c$; in particular, $E_{i,p}$ mirrors the trend of $|t_p|$ and $|t_s|$ in FIG. 1.8b, exhibiting an enhanced NF transmission close to θ_c.

We are currently planning a systematic comparison of the OCS obtained with the directional averaging formulas presented in SEC. 3.1.2. Within the limits where a good approximation is provided, the equivalent p-polarized wave method greatly simplifies[xiv] the numerical computation of the OCS under microscope illumination, which can be quantitatively compared with experimental results.

xiv In comparison, the directional averaging method typically requires 10 to 100 simulations instead of 1.

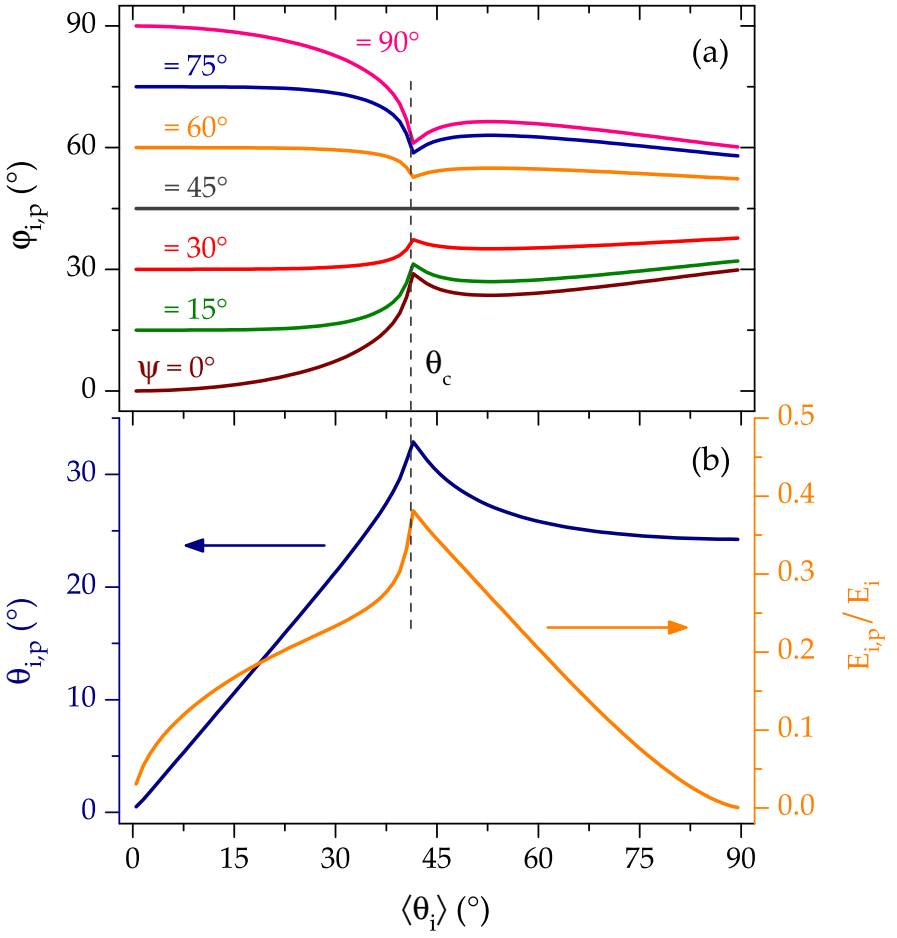

FIGURE 3.4: Parameters of the equivalent p-polarized wave as functions of the average angle of incidence $\langle\theta_i\rangle$. The transmission solution (3.20) was computed for $n_1 = 1.52$, $n_2 = 1.00$, $\lambda_0 = 550\,\text{nm}$ and $z_{NO} = -20\,\text{nm}$. A narrow conical illumination of width $\overline{\theta}_i - \underline{\theta}_i = 1°$ has been used, so that $\langle\theta_i\rangle \simeq (\overline{\theta}_i + \underline{\theta}_i)/2$. The dashed line indicates the critical angle $\theta_c = 41.1°$; the discontinuity in the parameters is slightly offset with respect to θ_c due to the finite illumination range.

3.2 COHERENT ILLUMINATION

3.2.1 *An approximate scalar description*

Consider an infinite, homogeneous medium which is non-absorbing ($\varepsilon \in \mathbb{R}$) and non-magnetic ($\mu = \mu_0$). Since μ (as well as ε) is independent of $\mathbf{r}$, the formulation of electromagnetics in the frequency domain (expressed by EQ. (4.2), which will be derived later on) reads

$$\nabla \times \left(\nabla \times \mathbf{E}\right) - \omega^2 \varepsilon \mu \mathbf{E} = i\omega\mu \mathbf{J}. \tag{3.23}$$

Assuming that the dielectric considered is electrically neutral ($\rho = 0$) and a perfect insulator ($\mathbf{J} = 0$), EQ. (3.23) reduces to the *Helmholtz equation*[xv]

$$\left(\nabla^2 + k^2\right)\mathbf{E} = 0\,. \tag{3.24}$$

where the angular wavenumber $k = \omega/c = \omega\sqrt{\varepsilon\mu}$ has been introduced.

We want now to find a solution of EQ. (3.24) having the form

$$\mathbf{E}(\mathbf{r}) = \mathbf{E}_0\, A(\mathbf{r}) e^{ikz} \tag{3.25}$$

namely, a *carrier* plane wave propagating along $\hat{z}$ modulated by a complex *envelope* $A(\mathbf{r})$. EQ. (3.25) is a *scalar description* because the polarization $\mathbf{E}_0 \perp z$ of the beam is taken as a constant. By substituting EQ. (3.25) into EQ. (3.24) one obtains

$$\nabla_\perp^2 A + 2ik\,\partial_z A + \partial_z^2 A = 0 \tag{3.26}$$

[xv] The first term of EQ. (3.23) is manipulated via the BAC–CAB identity

$$\nabla \times (\nabla \times \mathbf{E}) = \nabla(\nabla \cdot \mathbf{E}) - (\nabla \cdot \nabla)\mathbf{E} = -\nabla^2 \mathbf{E}$$

where in the last equality we used EQ. (4.1)-(I) and $\rho = 0$.

where $\nabla_\perp^2 \equiv \partial_x^2 + \partial_y^2$ is the *transverse Laplacian* operator. Let us also assume that $A(\mathbf{r})$ varies slowly along the propagation direction: This is called slowly-varying envelope approximation (SVEA). Under the SVEA EQ. (3.25) describes a *paraxial wave*, namely a wave whose wavefront normals form small angles with the propagation direction. For a paraxial wave the scalar Helmholtz equation (3.26) simplifies to[xvi]

$$\nabla_\perp^2 A + 2ik\,\partial_z A = 0 \tag{3.27}$$

which is referred to as the *paraxial Helmholtz equation*.

An important solution of EQ. (3.27) is the *Gaussian beam*[xvii]

$$\mathbf{E} = \mathbf{E}_0 \frac{w_0}{w(z)} \exp\left(-\frac{\rho^2}{w^2(z)}\right) \exp i\left(kz + k\frac{\rho^2}{2R(z)} - \phi_G(z)\right) \tag{3.28}$$

$\rho = x^2 + y^2$	Radial coordinate
$w_0 = \lambda/(\pi \mathrm{NA})$	Beam waist
$z_R = \pi w_0^2/\lambda$	Rayleigh range
$w(z) = w_0\sqrt{1 + (z/z_R)^2}$	Beam width
$R(z) = z\left[1 + (z_R/z)^2\right]$	Radius of curvature
$\phi_G(z) = \arctan(z/z_R)$	Gouy phase shift

which describes a beam propagating along[xviii] $\hat{z}$ and focused at the plane $z = 0$. The name stems from the Gaussian profile of the transverse electric field. Amongst many notable properties, the angular divergence of Gaussian beams is the minimum permitted by the wave equation for a given beam width and, for

xvi The SVEA implies $\partial_z^2 A \ll k\partial_z A$, see Saleh and Teich[86] (§2.2c).

xvii Saleh and Teich[86] (§3.1) present the detailed derivation and a thorough discussion of the properties of Gaussian beams.

xviii The complex conjugate of EQ. (3.28) is implemented in COMSOL due to the sign convention it adopts, see footnote v on P. 62.

this reason, most lasers are designed to emit a Gaussian beam. In the paraxial approximation, a Gaussian beam is transformed into another Gaussian beam upon reflection or transmission by a spherical lens or a spherical mirror:[xix] This unique property stems from the fact that the Fourier transform of a Gaussian function is another Gaussian function.

The numerical simulations presented in this thesis were performed with the commercial software COMSOL Multiphysics®; electromagnetic modelling in COMSOL will be discussed in SEC. 4.1. As Gaussian beam is the most widespread kind of experimental coherent source, COMSOL provides EQ. (3.28) as a predefined excitation field. Now, EQ. (3.28) is a solution of the paraxial Helmholtz equation (3.27), but only an approximate solution of the vectorial Helmholtz (3.24) equation under the SVEA. However, when the beam is focused to a small spot $w_0 \sim \lambda$ the SVEA is inadequate and EQ. (3.28) deviates significantly from a solution of the vectorial Helmholtz equation. This behaviour was observed in COMSOL for $w_0 \simeq \lambda/5$, see FIG. 3.5a. Firstly, $E(\mathbf{r})$ is not axially-symmetric — the symmetry being broken by the polarization $\mathbf{E}_0$; and secondly, $\max_{\mathbf{r}} E$ is well below the focal plane and is less than half of the nominal value E_0. We will further discuss in SEC. 4.1 (see in particular FIG. 4.1 with reference to the example of a paraxial Gaussian beam) why issues with approximate field descriptions arise in numerical simulations, and how the error resulting from the approximation can be quantified.

In summary, a tightly-focused wave requires $A(\mathbf{r})$ to vary significantly over distances $\sim \lambda$, and thus cannot be treated in the scalar approximation as a paraxial wave. A *vectorial description* is required instead, i. e. involving a polarization varying along

xix See Saleh and Teich[86] (§3.2).

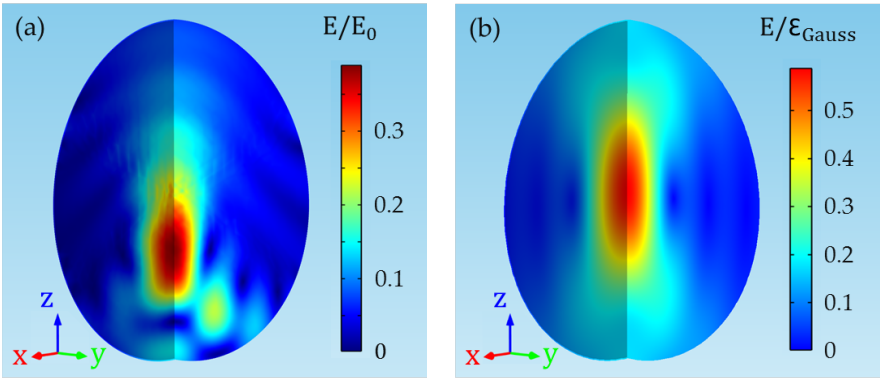

FIGURE 3.5: Normalized amplitude of the total electric field computed in COMSOL for $n = 1.52$, $\lambda_0 = 820\,\text{nm}$, NA $= 1.45$. The simulated volume is centred at the focus $\mathbf{r} = 0$ and has a radius $R_{sim} = 1\,\mu\text{m}$. The exciting field is (a) a paraxial Gaussian beam: E/E_0 is given by EQ. (3.28) for $\mathbf{E}_0 \parallel \hat{\mathbf{x}}$; and (b) a focused plane wavefront with polarization along $\hat{\mathbf{x}}$ and a Gaussian field profile in the BFP of the focusing lens: $E/\mathcal{E}_{Gauss}$ is given by EQ. (3.29), EQ. (3.30) and EQ. (3.36).

the propagation direction and having a nonzero longitudinal component in the focal region.

3.2.2 *An exact vectorial description*

As soon as sources of coherent radiation became available, at first in the form of masers (an early type of laser emitting in the microwave range), the need for an exact analytical description of the emitted electrical field arose. In particular, Richards and Wolf[87] considered a monochromatic plane wave converted by an aplanatic lens system into a converging spherical wavefront as in FIG. 3.3a, and calculated the electric field $\mathbf{E}$ in the focal region without relying on the paraxial approximation. Recast into the notation used throughout this work, the formulas for

a plane wave linearly polarized along $\hat{x}$ and propagating along $\hat{z}$ read[xx]

$$\mathbf{E} = \mathcal{E} \begin{bmatrix} -i\,\mathcal{J}_2 \cos 2\varphi + \mathcal{J}_0 \\ -i\,\mathcal{J}_2 \sin 2\varphi \\ +2\,\mathcal{J}_1 \cos\varphi \end{bmatrix} \tag{3.29}$$

$$\mathcal{J}_0(u,v) = \int_0^\alpha J_0\left(\frac{v\sin\theta}{\sin\alpha}\right) \exp\left(i\frac{u\cos\theta}{\sin^2\alpha}\right) \times (1+\cos\theta)\sin\theta\sqrt{\cos\theta}\,d\theta \tag{3.30-0}$$

$$\mathcal{J}_1(u,v) = \int_0^\alpha J_1\left(\frac{v\sin\theta}{\sin\alpha}\right) \exp\left(i\frac{u\cos\theta}{\sin^2\alpha}\right) \times \sin^2\theta\sqrt{\cos\theta}\,d\theta \tag{3.30-1}$$

$$\mathcal{J}_2(u,v) = \int_0^\alpha J_2\left(\frac{v\sin\theta}{\sin\alpha}\right) \exp\left(i\frac{u\cos\theta}{\sin^2\alpha}\right) \times (1-\cos\theta)\sin\theta\sqrt{\cos\theta}\,d\theta \tag{3.30-2}$$

(r,θ,φ)	Standard spherical coordinates
$u = kr\cos\theta\sin^2\alpha$	Longitudinal coordinate
$v = kr\sin\theta\sin\alpha$	Transversal coordinate
$k = 2\pi n/\lambda_0$	Wavevector in medium
$\alpha = \arcsin(\mathrm{NA}/n)$	Angular aperture of the lens
$J_m \quad (m = 0,1,2,\dots)$	Bessel functions of the first kind

Let us now calculate the field amplitude $\mathcal{E}$ for two types of electric field profile over the BFP of the focusing lens: A plane wave (subscript pw) and a Gaussian beam (Gauss).

xx The complex conjugate of $\mathbf{E}$ given by EQ. (3.29) should be used as exciting field in COMSOL due to the sign convention it adopts, see footnote v on P. 62.

PLANE WAVE According to Richards and Wolf, the electric field amplitude in the image space $\mathcal{E}_{pw}$ and in the object space E_{pw} in vacuum (subscript 0) are related via $\mathcal{E}_{pw,0} = \pi f \lambda_0^{-1} E_{pw,0}$ where f is the focal length of the focusing lens. In order to take into account the presence of an immersion fluid, one can imagine to immerse the whole set-up (i. e., both sides of the lens) into a medium of refractive index n. The expression just given is still valid provided all quantities are replaced by their corresponding value in the medium

$$\mathcal{E}_{pw} = \pi (nf) \lambda^{-1} E_{pw} = \pi n^2 f \frac{\nu}{c_0} E_{pw} \tag{3.31}$$

We want now to express E_{pw} in terms of the input power, so to relate $\mathcal{E}_{pw}$ to the experimental parameters. Be P_{avg} the average power, measured before the microscope port and delivered to the objective lens.[xxi] When pulsed excitation is used, a characteristic pulse power can be defined by dividing P_{avg} by the duty cycle of the source: $P_{pulse} = P_{avg}/(T_{pulse} R_{pulse})$, being T_{pulse} and R_{pulse} the pulse duration and repetition rate, respectively. Now, P_{pulse} and E_{pw} are simply related as follows

$$\begin{aligned} P_{pulse} = \pi \rho_{BFP}^2 \times I_{pw} = \pi f^2 NA^2 \times \frac{1}{2} n c_0 \varepsilon_0 \left| E_{pw} \right|^2 \\ \longrightarrow E_{pw} = \frac{1}{fNA} \sqrt{\frac{2 P_{pulse}}{\pi n c_0 \varepsilon_0}} \, . \end{aligned} \tag{3.32}$$

In the second equality we used Abbe's sine condition for aplanatic[xxii] lenses $\rho_{BFP} = f\,NA$, where ρ_{BFP} is the radius of the illuminated region in the BFP of the focusing lens. Finally, (3.32) is

xxi As we are only interested here in estimating an order of magnitude, we can neglect the small losses due to intermediate elements in the optical path.

xxii Which is assumed as well by Richards and Wolf, and is indeed a good approximation for real microscope objectives.

substituted into EQ. (3.31) in order to express $\mathcal{E}_{pw}$ as a function of the experimental parameters

$$\mathcal{E}_{pw} = \frac{\nu}{NA}\sqrt{\frac{2\pi n^3}{\varepsilon_0 c_0^3}\frac{P_{avg}}{T_{pulse}R_{pulse}}}\,. \tag{3.33}$$

GAUSSIAN BEAM EQ. (3.31) and EQ. (3.33) refer to a plane wave yielding a homogeneous illumination over the BFP of the focusing lens. On the other hand, when laser beams are used, the field amplitude typically has a Gaussian radial profile as in EQ. (3.28)

$$E_{Gauss} = E_{BFP}\exp\left[-\left(\frac{\rho}{w_{BFP}}\right)^2\right] = E_{BFP}\exp\left[-\left(\frac{1}{F}\frac{\sin\theta}{\sin\alpha}\right)^2\right] \tag{3.34}$$

where E_{BFP} and w_{BFP} are the amplitude and width of the Gaussian beam at the BFP of the focusing lens. In the last equality we introduced the *filling factor* $F \equiv w_{BFP}/\rho_{BFP}$. We have inserted E_{Gauss}/E_{BFP} inside the integrals (3.30) in order to simulate a Gaussian excitation.

Such a Gaussian weighing reduces the input power by the factor

$$C_{Gauss} = \frac{1}{\pi\rho_{BFP}^2 E_{BFP}^2}\int_0^{\rho_{BFP}} E_{Gauss}^2\, 2\pi\rho\, d\rho = \frac{F^2}{2}\left(1 - e^{-2/F^2}\right) \tag{3.35}$$

with respect to a plane wave of amplitude $E_{pw} = E_{Gauss}\big|_{\rho=0}$. In the limit of large overfilling ($w_{BFP} \gg \rho_{BFP}$) one has $F \gg 1$, and EQ. (3.35) yields $C_{Gauss} \simeq 1$,[xxiii] reducing to the plane wave case as expected. In our experiments we used $F \simeq 1$ for both the pump and the Stokes beam, within a $\pm 10\,\%$ uncertainty corresponding to the measurement accuracy and repeatability

[xxiii] In order to prove this limit, substitute $x = -2/F^2$ in EQ. (3.35) and apply L'Hôpital's rule to the resulting $\frac{0}{0}$ indeterminate form.

—in fact, the set-up has been optimized to stay as close as possible to this optimum value. This means the input power is more than halved ($C_{Gauss}|_{F=1} = 0.43$) with respect to plane wave excitation. In order to keep unaltered the power transmitted to the focal region, $\mathcal{E}_{pw}$ must be correspondingly increased by rescaling the input power P_{avg} in EQ. (3.33)

$$\mathcal{E}_{Gauss} = \frac{\nu}{NA}\sqrt{\frac{2\pi n^3}{\varepsilon_0 c^3}\frac{P_{avg}/C_{Gauss}}{T_{pulse}R_{pulse}}} = \frac{\mathcal{E}_{pw}}{\sqrt{C_{Gauss}}}. \tag{3.36}$$

The focused Gaussian beam described by EQ. (3.29) —including the Gaussian weighing in the integrals (3.30)— was simulated in COMSOL for a tight focusing (NA = 1.45), see FIG. 3.5b. When compared to a paraxial Gaussian beam having the same NA in FIG. 3.5a, the PSF exhibits a more regular shape and is centred at the nominal focus $\mathbf{r} = 0$. Note that it is not axially symmetric, but slightly elongated along the direction of the exciting polarization $\hat{\mathbf{x}}$; two lateral fringes are visible as well, analogous to the characteristic rings of the Airy pattern.[xxiv] We checked the accuracy of the normalization to $\mathcal{E}_{Gauss}$ given by EQ. (3.36) by measuring the power transmitted through the focal plane, which indeed tends to P_{pulse} as R_{sim} is made large with respect to the lateral size of the PSF, so that the beam is not significantly cropped by the simulation boundaries. In SEC. 4.2 we will show how the analytical description introduced in this section can be used to model actual microscopy experiments.

[xxiv] The PSF is described by an Airy function in the Fraunhofer diffraction regime, which involves a paraxial approximation.

4

LIGHT SCATTERING MODELS

As the nanotechnology and nanoplasmonic fields progress, new nanostructures and assemblies with an increasing degree of structural complexity are fabricated and studied. Their optical properties depend on size, shape, and local environment, often in a sensitive and complicated way. However — although they provide valuable estimates and physical insight — the available theoretical approaches which we have reviewed in CH. 1 are limited to a few simple geometries. These considerations, along with the steady improvements of hardware and software for computing, explains why, over the last two decades, numerical modelling has become an essential tool for theoretical studies of the optical properties of NOs.

4.1 ELECTROMAGNETIC SIMULATIONS IN COMSOL

Several numerical approaches are available for electromagnetic simulations,[88,89] the most popular being the discrete dipole approximation (DDA), the finite-difference time-domain (FDTD) method, and the finite element method (FEM). Our choice fell on the last by reason of its peculiar advantages:

GENERALITY of the approach, which allows to couple different classes of physical phenomena (electromagnetic waves, heat conduction, continuum mechanics, etc.) within the same model. In fact, the FEM is essentially a mathematical algorithm to discretize and solve partial differential equations, and as such it can be applied to the most disparate

fields of science. Conversely, the FDTD is most suited to deal with time-domain simulations in electrodynamics, and DDA is specifically restricted to scattering problems.

FLEXIBILITY in handling irregular geometries and fine features within large domains. In contrast with cubic grid-based methods such as DDA and FDTD, the non-regular tetrahedral adaptive mesh used to discretize space in the FEM, can approximate more accurately curved surfaces and be selectively refined in specific areas of interest.

While a comprehensive description of the theoretical principles and practical implementation of the FEM for electromagnetic modelling[90,91,i] is beyond the scope of this work, we shall describe here the salient features of its implementation towards our modelling purposes.

For our simulations we have relied on the commercial software COMSOL Multiphysics®, which implements the FEM within a convenient user interface. All models discussed in this work have been solved via the *Electromagnetic waves, frequency domain* (EWFD) interface[ii] included in the *Wave optics module* as well as in the RF *module*.[iii] The EWFD interface looks for a monochromatic solution of the Maxwell's equations, that is, it assumes that all fields and sources have a harmonic time dependence $e^{-i\omega t}$ with a given frequency ω. Under this assumption, the

i https://www.comsol.com/multiphysics/finite-element-method (visited on 15/06/2017) provides a concise introduction to the FEM in COMSOL.

ii In the COMSOL terminology, an *interface* corresponds to a specific partial differential equation being solved. Several interfaces related to a certain class of physical phenomena are grouped and sold together as a *module*.

iii The COMSOL blog entries "Computational electromagnetics modeling, which module to use?" and "Guide to frequency domain wave electromagnetics modeling" (both visited on 15/06/2017) together provide an overview of the computational tools offered by COMSOL for electromagnetics modelling, discussing their range of applicability and the typical problems they are suitable to solve.

Maxwell's equations in the frequency domain (where $\partial_t \to -i\omega$) read

$$\begin{aligned} &\text{(I)} \quad \nabla \cdot \mathbf{D} = \rho \qquad &&\text{(III)} \quad \nabla \times \mathbf{E} = +i\omega\mathbf{B} \\ &\text{(II)} \quad \nabla \cdot \mathbf{B} = 0 \qquad &&\text{(IV)} \quad \nabla \times \mathbf{H} = -i\omega\mathbf{D} + \mathbf{J} \end{aligned} \tag{4.1}$$

and are complemented by the constitutive relations $\mathbf{B} = \mu\mathbf{H}$ and $\mathbf{D} = \varepsilon\mathbf{E}$.[iv] The material properties are thereby introduced in EQ. (4.1) by the complex-valued tensors ε and μ, which depend in general on $\mathbf{r}$ and ω.

By taking the curl of EQ. (4.1)-(III) and substituting with (IV)

$$\nabla \times \mu^{-1}(\nabla \times \mathbf{E}) - \omega^2\varepsilon\mathbf{E} = i\omega\mathbf{J}. \tag{4.2}$$

We have now reformulated electromagnetics in terms of $\mathbf{E}$ alone,[v] since the external current $\mathbf{J}$ does not originate from the fields. Indeed, EQ. (4.2) is the equation implemented in the EWFD interface, which is thus suitable to solve models having the following characteristics:

LINEAR RESPONSE ε and μ, which represent the material properties, are independent of $\mathbf{E}$.

MONOCHROMATIC PROCESSES Since the model is solved for a single value of ω at a time, inelastic scattering processes cannot be treated.

STATIONARY SOLUTIONS The time-independent formulation of electromagnetics cannot describe transient phenomena.

iv The source term $-i\omega\mathbf{D}$ on the RHS of EQ. (4.1)-(IV) can be broken down into a *displacement* current density $\mathbf{J}_d = -i\omega\,\mathrm{Re}(\varepsilon)\mathbf{E}$ and a *conduction* current density $\mathbf{J}_c = \omega\,\mathrm{Im}(\varepsilon)\mathbf{E}$. In particular, for $\omega \neq 0$ the latter can be written in terms of the AC *electrical conductivity* $\sigma = \omega\,\mathrm{Im}(\varepsilon)$ as $\mathbf{J}_c = \sigma\mathbf{E}$, which is the local form of Ohm's law.

v This formulation is not fully equivalent to EQ. (4.1), as it was obtained by taking a curl. Indeed, if $\mathbf{E}_{sol}$ is a solution of EQ. (4.1) then $\mathbf{E}_{sol} + \mathbf{E}'$ is a solution of EQ. (4.2) whenever $\nabla \times \mathbf{E}' = 0$. In practice, these spurious solutions must be discarded by checking them against EQ. (4.1).

SIZE LIMITATIONS The size of the modelled structure should be comparable to the wavelength λ; as a rule of thumb, ranging from $\lambda/100$ to 10λ.[vi]

Directly solving (4.2) is known as the *full field formulation* of the electromagnetics. An external excitation can be introduced within the simulation volume by specifying an analytical expression of $\mathbf{J}(\mathbf{r})$; an example of this will be presented in SEC. 4.3. On the other hand, in many cases of practical interest, the excitation comes from a distant source in form of radiation. Radiative excitation can be input into the simulation volume through a *Port boundary condition*. This can be thought of as a transparent gateway for a specific spatial mode, which can pass through in both directions without suffering reflection losses. However, in practice Ports can handle plane waves solely, and are more suited to transmission models — e. g. waveguides. A different approach named *scattered field formulation* is more adequate to treat the scattering phenomena we are interested to.

SCATTERED FIELD FORMULATION In this description, the total electric field $\mathbf{E}_{\text{tot}}$ is decomposed into the *scattered field* and the *exciting field*:[vii] $\mathbf{E}_{\text{tot}} = \mathbf{E}_{\text{sca}} + \mathbf{E}_{\text{exc}}$, see P. 10. Let us define the linear differential operator $\mathcal{D} \equiv \nabla \times \mu^{-1} \nabla \times -\omega^2 \varepsilon$ so that the partial differential equation (4.2) reads $\mathcal{D}\mathbf{E} = i\omega\mathbf{J}$. The scattered field formulation then is expressed by

$$\mathcal{D}\mathbf{E}_{\text{sca}} = i\omega\mathbf{J} - \mathcal{D}\mathbf{E}_{\text{exc}} \tag{4.3}$$

vi Rather than a physical assumption, this is a practical limit imposed by memory requirements; other modules and interfaces are available in COMSOL to model objects having a size below (AC/DC *module* for the quasi-static regime) or above (*ray optics module*) the specified range.

vii In the less perspicuous terminology of COMSOL these are referred to as *relative* and *background* fields respectively.

where $\mathbf{E}_{sca}$ is the variable solved for by COMSOL, while $\mathbf{E}_{exc}$ is known, and represents the electric field in absence of the studied object. $\mathbf{E}_{exc}$ can be specified either via an analytical description provided by the user,[viii] or pointwise as a numerical vector field, usually obtained from a previous solving step; in this chapter, examples of both approaches will be presented.

In EQ. (4.3) $\mathbf{J}$ represents a source introduced within the simulation volume, and $\mathbf{E}_{exc}$ the radiative excitation coming from a distant source. Let us consider the case of a purely radiative excitation ($\mathbf{J} = 0$) — which is the archetypical scattering problem. Now, if $\mathbf{E}_{exc}$ is a well-defined exciting field (namely, a solution of Maxwell's equations in absence of the object) then it satisfies the homogeneous EQ. (4.2), i. e. $\mathcal{D}\mathbf{E}_{exc} = 0$, and the source term of EQ. (4.3) is null, so that it yields $\mathbf{E}_{sca} = 0$ as expected since no object is present. Conversely, if $\mathcal{D}\mathbf{E}_{exc} \neq 0$, some "self-scattering" is observed even in absence of the object; more precisely, if $\mathbf{E}_{exc}$ differs by an error $\mathbf{E}'$ from a solution of the homogeneous EQ. (4.2), then $\mathcal{D}\mathbf{E}'$ acts as a source term in EQ. (4.3). This observation provides a handy way to verify if $\mathbf{E}_{exc}$ is indeed a well-defined exciting field: When solving the model without the object the calculated $\mathbf{E}_{sca}$ should be null up to numerical terms.

Let us now present an example of this procedure applied to a paraxial Gaussian beam. As discussed in SEC. 3.2.1, this is a solution of Helmholtz equation only in the paraxial approximation, which holds so long as $w_0 \gg \lambda$. As a consequence, significant self-scattering occurs for tightly focused beams as exemplified in FIG. 4.1. Trying to achieve a PSF as narrow as $w_0 = \lambda/5$ results in a self-scattering E_{sca} (FIG. 4.1b) comparable to the excitation E_{exc} (FIG. 4.1a). As a consequence, $E_{tot} =$

viii In fact, COMSOL includes plane waves and Gaussian beams as built-in expressions of $\mathbf{E}_{exc}$, and other explicit descriptions for $\mathbf{E}_{sca}$ are seldom seen in current modelling practice.

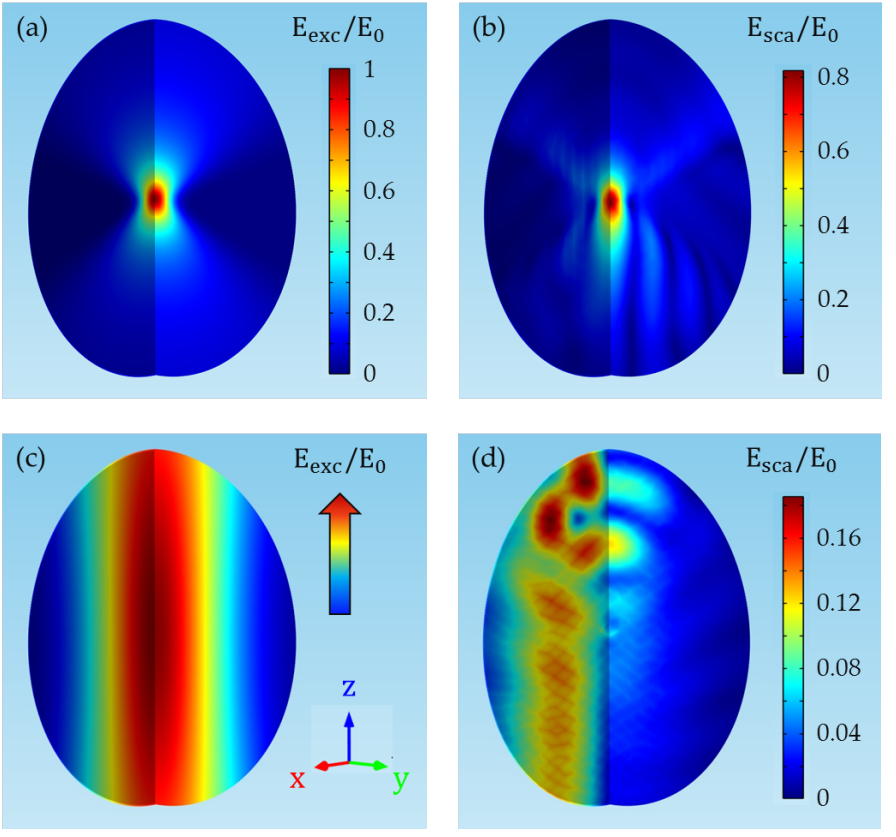

FIGURE 4.1: Self-scattering in a homogeneous $n = 1.52$ medium of the paraxial Gaussian beam (3.28) with $\mathbf{E}_0 \parallel \hat{\mathbf{x}}$ computed in COMSOL for $\lambda_0 = 820\,\text{nm}$. The normalized amplitude of the (a,c) exciting field E_{exc}/E_0, and (b,d) scattered field E_{sca}/E_0 is represented. The simulated volume is centred at the focus $\mathbf{r} = 0$ and has a radius $r_{sim} = 1\,\mu\text{m}$. (a,b) NA $= 1.45$ resulting in $w_0 \simeq \lambda/5$; (c,d) NA $= 0.32$ resulting in $w_0 \simeq \lambda$. The colour scale in (c) is the same as in (a).

$E_{sca} + E_{exc}$ (FIG. 3.5a) deviates heavily from an ideal PSF shape as discussed in SEC. 3.2.1. Less dramatic effects are observed in FIG. 4.1d for $w_0 \simeq \lambda$, with $E_{sca} \simeq 0.2E_{exc}$, so that E_{tot} closely resembles E_{exc} (FIG. 4.1c).

An indicator quantifying the amount of self-scattering is the *relative* L^2 *error*[ix]

$$\text{RLE} = \sqrt{\int_{V_{sim}} |\mathbf{E}_{sca}|^2 \, dV \Big/ \int_{V_{sim}} |\mathbf{E}_{exc}|^2 \, dV} \tag{4.4}$$

and a given expression of $\mathbf{E}_{exc}$ should be used only if it gives RLE $\ll 1$. For instance, $w_0 \simeq \lambda/5$ and $w_0 \simeq \lambda$ (i.e. the values used in FIG. 4.1) result in RLE $= 0.98$ and RLE $= 0.17$ respectively. In comparison, the PSF represented in FIG. 3.5b, which is obtained via an exact vectorial description, corresponds to RLE $= 6.1 \times 10^{-5}$. A value RLE $\lesssim 10^{-3}$ is found for Gaussian beams having $w_0 \geqslant 2\lambda$, demonstrating that the paraxial approximation is appropriate in this regime.[x]

MODELLING AN INFINITE SPACE Often, when solving wave electromagnetics problems, one would like to model a system placed in unbounded free space. Nonetheless, when using the FEM the simulated volume must be finite-sized to be solved in a finite memory, and indeed as small as possible (in practice down to $\sim\lambda$ for the EWFD) to minimize the computation time required. Several numerical tools in COMSOL are devised to circumvent this practical limitation.

Open boundaries for radiation are usually mimicked by a perfectly matched layer (PML), which can be thought of as a perfectly absorbing boundary. In fact, the impedance mismatch

ix L^2 indicates that the standard Euclidean norm is used.

x The COMSOL blog entry "Understanding the paraxial Gaussian beam formula" (visited on 15/06/2017) further characterizes the validity scope of the paraxial approximation.

caused by a simple truncation of the simulation domain would cause the radiation to be reflected back into the simulation domain. Mathematically, a PML implements a profile of ε and μ describing a complex-valued coordinate stretch in the outward direction,[90] which converts propagating waves into decaying ones, whose amplitude drops off exponentially. An effective PML typically is a $\sim \lambda/2$-thick domain enclosing completely the simulated region, with a sufficiently fine meshing (4 to 6 elements across). In practice, good PMLs achieve a reflection $R \lesssim 10^{-4}$ in a wide range of angles of incidence $\theta_{inc} \lesssim 70°$, and a worsening performance when grazing incidence is approached. *Scattering boundary conditions* provide a less computationally expensive, but also less effective alternative to PMLs.[xi]

For every radiating solution of Maxwell's equations having real frequency it can be demonstrated that[91,xii]

$$\mathbf{E}_{sca}(\mathbf{r}) = \frac{e^{ikr}}{r}\left[\mathbf{E}_\infty(\hat{\mathbf{r}}) + O\left(\frac{1}{r}\right)\right] \quad \text{for } r \to \infty \tag{4.5}$$

which expresses the intuitive fact that, far away from the scatterer, the scattered field is an expanding spherical wave with a superimposed amplitude modulation dependent on the direction $\hat{\mathbf{r}}$. The region where $\mathbf{E}_{sca}$ is dominated by r^{-1} terms is named FF region; typically, in scattering problems this condition is met at least 10λ away from the scatterer. The NF region is instead dominated by higher-order terms falling off as r^{-2}, r^{-3}, exc. In optical microscopy, the detectors — in our case, the objective and condenser lenses — are usually placed in the FF of the studied object. These lenses collect the signal over a finite

xi The COMSOL blog entry "Using perfectly matched layers and scattering boundary conditions for wave electromagnetics problems" (visited on 15/06/2017) compares the performances of PMLs and scattering boundary conditions.

xii Like in COMSOL, we are adopting here the engineers' sign convention e^{-ikr}.

solid angle, called *acceptance*. Now, according to EQ. (4.5), the density of the scattered energy flux (represented by the time-averaged Poynting vector) in the FF is

$$\mathbf{S}_\infty(\mathbf{r}) = \frac{1}{2r^2} n c_0 \varepsilon_0 \left|\mathbf{E}_\infty(\hat{\mathbf{r}})\right|^2 \hat{\mathbf{r}}. \tag{4.6}$$

and the angular distribution of scattered power[xiii] $\mathcal{P}(\hat{\mathbf{r}}) = r^2 S_\infty \propto E_\infty^2$ does not depend on r. Close to the scatterer $\mathbf{S}_{sca}$ has instead a more complex expression, and the scattering pattern is ill-defined, as the energy flux in a given direction depends on r. Practically, this means we cannot compute the measured power by integrating $r^2 S_{NF}$ over the detector acceptance; on the other hand, simulating a volume so large that the boundaries are effectively placed in the FF, would require huge computational resources.

In order to deal with this issue, COMSOL provides the opportunity in post-processing to invoke *far-field variables* in specified domains. In particular, $\mathbf{E}_\infty(\hat{\mathbf{r}})$ is computed via the *Stratton-Chu transform*[92]

$$\mathbf{E}_\infty = -\frac{ik}{4\pi}\hat{\mathbf{r}} \times \int_{\Sigma_{FF}} \left[\hat{\mathbf{n}} \times \mathbf{E} - \sqrt{\frac{\mu}{\varepsilon}}\,\hat{\mathbf{r}} \times (\hat{\mathbf{n}} \times \mathbf{H})\right] e^{ik\mathbf{r}\cdot\hat{\mathbf{r}}}\, d\Sigma \tag{4.7}$$

where the surface integration is performed over the outer boundary Σ_{FF} of the FF domain and $\hat{\mathbf{n}}$ identifies the normal to Σ_{FF} in every point. Note that calculating the $\mathbf{E}_\infty(\theta, \varphi)$ over a 4π solid angle can be rather expensive computationally since the integral in EQ. (4.7) must be evaluated for each direction (θ, φ). According to EQ. (4.5) or EQ. (4.7) $[E_\infty] = [V]$: Although customarily denoted with an E symbol, E_∞ is not an electric

[xiii] $\mathcal{P}$ is defined so that $\mathbf{S}\, d\mathbf{A} = \mathcal{P}\, d\Omega$; the calligraphic font is used for consistency with the notation adopted in CH. 5. Often $\mathcal{P}(\hat{\mathbf{r}})$ and $E_\infty^2(\hat{\mathbf{r}})$ are both referred to simply as *scattering pattern*.

field.[xiv] $\mathbf{E}_{sca}$ at a given distance r is computed via EQ. (4.5); neglecting $O(r^{-1})$ terms implies this is accurate only in the FF.

4.2 A MODEL OF ELASTIC SCATTERING

The COMSOL model discussed in this section simulates the scattering and absorption of a plane wave by a NO placed close to a dielectric interface. The case of a homogeneous immersion medium is obtained as the limiting case $n_1 = n_2$. Experimental observables such as the absolute OCS and the scattering pattern can be computed by the model.

4.2.1 *Geometry and solvers*

FIG. 4.2a provides an overview of the typical geometry and meshing of the model. A complete 3D geometry must be simulated, in order to address the dependence on the excitation direction and compute the OCS under microscope illumination. V_{sim} is taken as a sphere centred at the origin, and the optical interface is the $z = 0$ plane. A radius $r_{sim} = \lambda_0/(2n_{min})$ where $n_{min} \equiv \min(n_1, n_2)$ is used — enough to put the simulation boundaries outside the reactive NF region[xv] of the NO. V_{sim} is meshed with a free tetrahedral mesh having a maximum element size of $\lambda_0/(5n)$ in the n_1 and n_2 media, which ensures a sufficient sampling of the electric field. Following the guidelines of P. 92, V_{sim} is encircled by a PML of homogeneous thickness $t_{PML} = \lambda_0/(2n_{avg})$ where $n_{avg} = (n_1 + n_2)/2$, meshed

xiv Nonetheless, in COMSOL (v. 4.4) $\mathbf{E}_\infty$ (i. e. variables `normEfar`, `Efarx`, etc.) is attributed a V/m unit. Consequently, $r/[m]$ instead of r must be used for implementing EQ. (4.5) and EQ. (4.6), see the COMSOL blog entry "2 methods for simulating radiated fields in COMSOL Multiphysics®".

xv The *reactive near-field* is defined in antenna theory as the nearest region of the NF, where the coupling of the field with the emitter is significant.

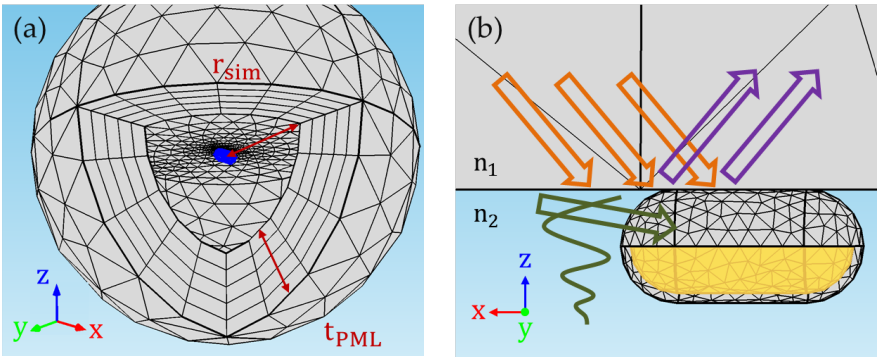

FIGURE 4.2: Typical geometry and meshing of a COMSOL model of elastic scattering by a NO on a substrate. (a) Overview of the simulated volume V_{sim}, a sphere of radius r_{sim} encircled by a PML of homogeneous thickness t_{PML}. A NO (blue) is placed in the middle of V_{sim}, below the $z = 0$ optical interface. (b) Close-up of the NO, a GNR coated by a dielectric shell; a quarter of the shell is hidden to reveal the gold core (yellow). The exciting plane waves are represented by arrows along the propagation direction, while the wavy line represents the evanescent wave; orange, purple, and green indicate incident, transmitted, and reflected light as in FIG. 3.1a.

with a swept mesh of five elements of constant thickness along the radial direction.[xvi]

FIG. 4.2b is a close-up of the NO, placed in medium 2 and in contact with the interface. A GNR coated by a thin dielectric shell has been used as exemplary NO for model development and testing. All figures and results in this section refer to a 67 nm × 28 nm gold[18] cylinder with spherical end caps, surrounded by a $n_{CTAB} = 1.43$ shell having homogeneous thickness $t_{CTAB} = 3.2$ nm; the GNR is placed on a glass/air ($n_1 = 1.52$,

[xvi] This compromise between PML thickness and sampling is acceptable when n_1 and n_2 do not differ much. For highly mismatched interfaces, piling up enough elements of radial thickness $\lambda_0/(10n_{max})$ to obtain $t_{pml} = \lambda_0/(2n_{min})$ ensures accurate results.

$n_2 = 1.00$) interface and excited resonantly with its longitudinal LSPR at $\lambda_{\parallel} = 620\,\text{nm}$. A free tetrahedral meshing is adopted for the NO, with the mesh element size manually capped to 12 nm in the metal volume, and automatically constrained by the geometry within the dielectric shell. The model has been optimized — i. e. V_{sim} has been expanded and the mesh has been refined — until the OCS showed no dependence on the parameters within a tolerance of approximately 1 %. For NO having finer features than here, the object meshing should be refined, while for NO bigger than 100 nm a larger r_{sim} is likely needed.

Radiative excitation is introduced in the model as a plane wave propagating from medium 1 in a direction specified by the user. As depicted in FIG. 4.2b, the NO in medium 2 is excited by the transmitted field — either propagating or evanescent when $\theta_i < \theta_c$ or $\theta_i > \theta_c$. In COMSOL, plane wave excitation is implemented via the scattered field formulation EQ. (4.3) of the EWFD interface. The model includes three such interfaces; any combination thereof can be solved for in a model run, by activating them in the selected frequency domain study step. One interface corresponds to a user-specified linear polarization in the condenser BFP, $\mathbf{E}_{exc}$ being given by EQ. (3.9); this should be solved in order to simulate polarized microscope illumination via EQ. (3.14). The other two interfaces correspond to a p- and an s-polarized wave, $\mathbf{E}_{exc}$ being given respectively by EQ. (3.3) for $z > 0$, and EQ. (3.4) for $z > 0$; these should be both solved in order to simulate unpolarized illumination via EQ. (3.15).

4.2.2 *Post-processing and results*

A solution of this model consists in the value of the electromagnetic field components at every node of the spatial mesh.

The field itself and other derived quantities can be visualized in space as false colour maps like those shown in FIG. 4.3. Although they cannot directly be compared to experimental results, these maps provide valuable physical insight and are helpful for highlighting inconsistencies and finding mistakes during the development of the model.

The density of power dissipated through *Joule* (or *resistive*) *heating* $Q_{Joule} = \frac{1}{2}\,\mathrm{Re}\,(\mathbf{J}_c \cdot \mathbf{E}^*_{tot})$ is plotted in FIG. 4.3a. Simply put, Joule heating results from the free electrons in the metal which are accelerated by $\mathbf{E}_{exc}$ and collide with the ion lattice, so that their kinetic energy K_e is transformed into lattice vibration, i. e. thermal energy. Now, $K_e = \frac{1}{2} m_e v_e^2$, and thus Q_{Joule} is maximum where v_e is, namely, in the middle point $x = 0$ of the oscillation of the electron cloud. Furthermore, inside the metal at a distance d from the surface Q_{Joule} is decreased by the

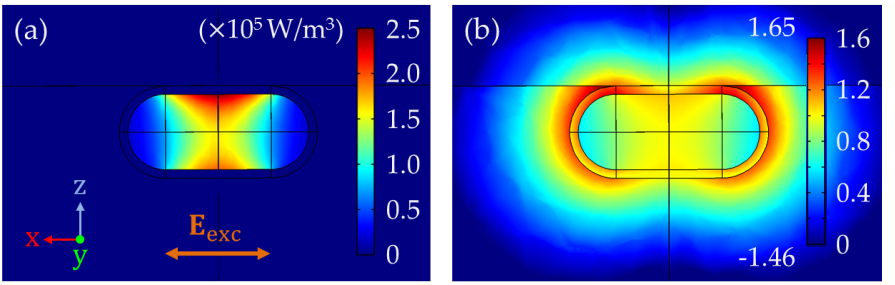

FIGURE 4.3: Solution of the elastic scattering model for a GNR. The exciting field $\mathbf{E}_{exc}$ (orange arrow) propagates along $-\hat{z}$ ($\theta_i = 0$) and is polarized along the rod axis ($\psi = 0$); all geometry parameters as specified in the text. (a) Density of power dissipated through resistive heating Q_{Joule}. (b) Normalized amplitude of the scattered electric field $\log_{10} E_{sca}/E_i$. The colour scale has been cropped to enhance the contrast; the maximum and minimum values over the simulated volume are reported at the top and bottom on the left of the scale.

factor $e^{-d/\Delta}$, where $\Delta \simeq 30\,\mathrm{nm}$ is the skin depth for gold at the excitation wavelength $\lambda_{\parallel} = 620\,\mathrm{nm}$.

E_{sca}/E_i is plotted in FIG. 4.3b and displays the field distribution peculiar to the emission of a dipole oriented along $\hat{x}$. The field lines exit the rod ends, where the line density is highest, and E_{tot} is locally enhanced up to a factor 45. The field amplitude across interfaces obeys the conditions $\varepsilon_1 E_1^{\perp} = \varepsilon_2 E_2^{\perp}$ and $E_1^{\parallel} = E_2^{\parallel}$. Indeed, the largest discontinuity of E_{sca} is observed at the rod ends, while E_{sca} is approximately continuous along the z axis, where the field lines are parallel to the rod surface. Moreover, at the air/glass interface $n_1 > n_2$ implies $E_1 \leqslant E_2$, the equal sign corresponding to the case $E^{\perp} = 0$.

The experimental observables can be computed from the microscopic quantities plotted in FIG. 4.3. The OCS are defined by EQ. (1.1), where $I_i = \frac{1}{2} n_1 c_0 \varepsilon_0 E_i^2$ results directly from the model input parameters. The absorbed power is computed by integrating Q_{Joule} over the NO volume

$$P_{abs} = \int_{V_{NO}} Q_{Joule}\, dV. \tag{4.8}$$

The scattered power is the flux of the time-averaged scattered Poynting vector $\mathbf{S}_{sca} = \frac{1}{2}\,\mathrm{Re}\,(\mathbf{E}_{sca} \times \mathbf{H}_{sca}^{*})$ across the NO surface

$$P_{sca} = \int_{\Sigma_{NO}} \mathbf{S}_{sca} \cdot \hat{\mathbf{n}}\, d\Sigma \tag{4.9}$$

where $\hat{\mathbf{n}}$ is the versor normal to Σ_{NO} in each point. Eventually, σ_{ext} can be calculated using EQ. (4.8), EQ. (4.9), and $P_{ext} = P_{abs} + P_{sca}$. An alternative route to compute σ_{ext}, which does not require an explicit integration, but relies on FF variables instead, is provided by the optical theorem. The form (1.9) refers to a homogeneous immersion medium, but generalizations of the theorem can be found in literature for a scatterer close to an optical interface[93] or embedded across it[94].

In order to compute the power scattered within a given solid angle Ω (being P_{sca} the extreme case for $\Omega = 4\pi$), information on the angular distribution of the scattering is required; namely, the scattering pattern (4.7) must be used. In particular, the scattered power measured in microscopy experiments is the energy flux across a spherical cap[xvii] corresponding to the objective acceptance Ω_{obj}

$$P_{obj} = \int_{\Sigma_{obj}} S_\infty \, d\Sigma \tag{4.10}$$

where S_∞ is given by EQ. (4.6). Σ_{obj} is often a virtual surface rather than a physical one: In our model it lies on the boundary of the physical domains (i.e. the inner boundary of the PML). Note that EQ. (4.7) assumes a homogeneous optical environment, and in fact COMSOL recommends to perform the near-to-far field transform over the boundary of a homogeneous domain completely surrounding the scatterer. While COMSOL has pledged to address this issue in future releases, with current versions (up to v5.2) P_{obj} might be inaccurate when an optical interface is included within the FF domain. Alternative numerical approaches to circumvent this shortcoming have been proposed in literature.[95]

The dependence of the OCS on the propagation direction of the exciting plane wave is shown in FIG. 4.4 for a GNR. Note that for $\varphi_i = \psi$ and $\varphi_i = \psi + \pi/2$ the wave is p- and s-polarized respectively, with intermediate values of φ_i corresponding to a mixed character with a gradually varying p and s proportion. To explain the trend of σ (at a given wavelength σ_{sca} or σ_{ext} differ from σ_{abs} only by a constant factor independent from the excitation), we observe that, to a good approximation, the GNR is a local probe of $|\mathbf{E}_{2,x}|^2$ given by EQ. (3.9-2). Therefore, σ depends both on the polarization of $\mathbf{E}_{2,x}$ and on its amplitude,

xvii Over a sphere one has $\mathbf{S}_\infty \parallel \hat{\mathbf{n}} \equiv \hat{\mathbf{r}}$ and a constant value of $r = r_\Sigma$.

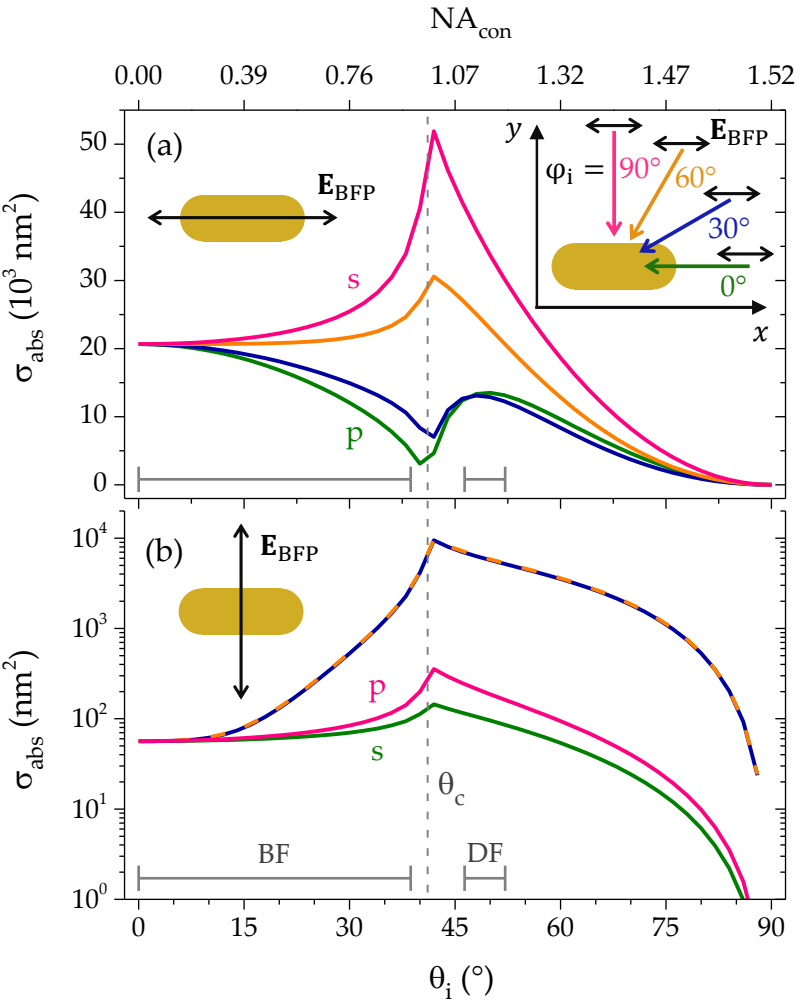

FIGURE 4.4: Absorption cross-section σ_{abs} of a GNR as a function of the polar θ_i and azimuthal φ_i angles of incidence of the exciting plane wave. The parameters of the model are given in the text. The exciting polarization in the condenser BFP lies (a) along ($\psi = 0$) or (b) across ($\psi = \pi/2$) the rod axis. The dashed line is the critical angle $\theta_c = 41.1°$. The marked ranges of θ_i correspond to typical BF (NA_i from 0 to 0.95) and DF (NA_i from 1.1 to 1.2) illumination we use in experiments.

which is proportional to $|t|$. Indeed, the transmitted s wave is always parallel to the interface, so that $\sigma^s(\theta_i) \propto |t_s(\theta_i)|^2$, and a maximum is observed at θ_c, in agreement with FIG. 1.8b. Note that the absolute value of $\sigma^s(\psi = 90°)$ (in FIG. 4.4b) is smaller by a factor ~ 500 than $\sigma^s(\psi = 0)$ (in FIG. 4.4a) as a result of the lower polarizability of the GNR along its short axis and of the non-resonant excitation with respect to the transverse mode. On the other hand, the transmitted p wave has a component perpendicular to the interface which increases approaching θ_c, where $\mathbf{E}_{2,x}$ is totally cross-polarized to the rod regardless of ψ. $\sigma^p(\theta_i)$ is thus a minimum for $\psi = 0$ and a maximum for $\psi = 90°$ — in the latter case, $\sigma^p > \sigma^s$ because $|t_p| > |t_s|$. For $\psi = 0$, σ_{abs} varies gradually between the extrema just described for waves with a mixed p and s character. Conversely, for $\psi = 90°$, a field component along the rod is introduced by focusing, which is maximum for $\varphi_i = 45°$. Indeed, via EQ. (3.9-2) one obtains $\sigma \propto |E_{2,x}(\psi = 90°)|^2 \propto \sin^2 2\varphi_i$, which also explains why the same value for σ is obtained for $\varphi_i = 30°$ and $\varphi_i = 60°$.

In a typical microscopy experiment the illumination contains a wide range of excitation directions, as indicated in FIG. 4.4. The large variations of σ observed over such angular ranges highlight the importance of accounting for the excitation used in experiments, and motivated us to develop the approaches described in SEC. 3.2 to reproduce the microscope illumination in numerical models. The model described in this section will be used in CH. 6 to investigate the spectral properties of various NO and to benchmark the results of quantitative OCS measurements.

COMPARISON TO LITERATURE Let us conclude by comparing the salient features of our model to the state of the art,[xviii]

xviii In this review we shall limit ourselves to FEM models.

and emphasize the elements of novelty introduced therein. Modelling the optical properties of NOs in a homogeneous environment is nowadays a common practice, and several related model templates can be found online and are provided by COMSOL as tutorials. In particular, the way we compute the OCS and the scattering pattern is well known.[34,96,97]

However, only few models including an optical interface in the vicinity of the NO are reported in literature. The main challenge posed by such a geometry is that $\mathbf{E}_{\text{exc}}$ is not a simple plane wave any more. A widespread workaround relies on a two-step scheme:[34] First, the NO is removed and $\mathbf{E}$ above and below the interface is computed using the full field formulation; this serves as $\mathbf{E}_{\text{exc}}$ for a second EWFD solver (now including the NO) computing the scattering. Besides being cumbersome, this procedure comes with a further fundamental limitation. The absorbing boundary conditions (e. g. a PML) after the interface not only absorb any plane wave propagating outwards, but also any incident evanescent field when TIR occurs. To avoid this, one cannot but put the boundary much farther from the interface than the evanescent decay length δ; in practice, this means a large model is required to obtain accurate results for close-to-critical excitation since $\delta \xrightarrow{\theta_i \to \theta_c} \infty$, see EQ. (1.17).

We have instead calculated the explicit expression of the field above and below the interface and used it as $\mathbf{E}_{\text{exc}}$; Zhang et al.[96] adopted the same method (seemingly only for normal incidence), although they do not provide details. This approach is obviously neater and faster than computing numerically $\mathbf{E}_{\text{exc}}$, as a single solving step is required. In practice, with the parameters listed above, our model is solved by a common workstation (Intel® Core™ i7 CPU, 64 GiB RAM) in approximately 15 s. In comparison, the equivalent two-step implementation requires 5 to 10 times longer; such a performance boost is ex-

tremely advantageous when a complete spectrum (order of 100 simulations) has to be computed.

Our main innovation with respect to current modelling practice are the methods described in SEC. 3.1, which we have devised to reproduce the microscope illumination using plane wave simulations — either averaging several or calculating an "equivalent" one. In fact, there are no reports in literature of analogous concerns. For instance, the experimental set-up used by Knight et al.[34] features a DF configuration with a light needle of negligible directional spread, that can be mimicked by a plane wave.[xix] Davletshin et al.,[97] on the other hand, apparently attempted fitting SMS data using a plane wave impinging orthogonally onto the substrate instead of some model for a laser PSF.[xx] Lastly, the work by Zhang et al.[96] is exclusively computational, and implements in the model an excitation structured to address selectively the bright and dark mode of a nanocube.

4.3 A MODEL OF NONLINEAR SCATTERING

4.3.1 *Motivation and theoretical background*

Inelastic Raman scattering addresses the low frequency vibrational and rotational modes of the sample (~ 100 meV) using light in the VIS and near IR range (~ 1 eV). Raman techniques are important tools for analytical chemistry, allowing to determine the chemical composition with minimal sample condi-

xix A cause of concern with their model is the use of FF calculations analogously to EQ. (4.10); as we noted on P. 99, this might lead to invalid results when the FF domain is optically inhomogeneous.

xx They also use strange boundary conditions: There are perfect electric conductor (PEC) and perfect magnetic conductor (PMC) seemingly implementing unphysical geometries, and the PML is limited to one side of the geometry, instead of enclosing it completely.

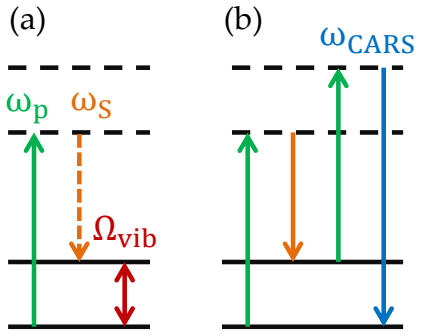

FIGURE 4.5: Energy diagram of (a) spontaneous Raman and (b) CARS resonant with a vibrational transition. The dashed lines represent virtual energy states. The dashed and solid downward arrows indicate spontaneous and stimulated emission.

tioning, and providing information on molecular conformation and symmetry. In general, optical processes can be classified according to their *order*, corresponding to the power dependence of the output intensity on the input intensity. Linear (i. e. first-order) Raman scattering consists in a radiative excitation of the target to a virtual energy state followed by a spontaneous radiative decay to a different vibrational state than the initial one, see FIG. 4.5a. Spontaneous emission results in an incoherent signal, meaning the fields radiated by different oscillators in the sample have no definite phase relation.

Nonlinear Raman processes,[98] on the other hand, typically involve stimulated emission, being the microscopic oscillators driven at the phase difference of the input fields, so that a coherent signal is produced. It can be shown that for incoherent emission, due to random interference, the intensity is proportional to the number N of oscillators, whereas for coherent emission it is proportional to N^2; as a result, stimulated Raman processes can yield intensities order of magnitudes larger than spontaneous ones, thus permitting video-rate vibrational imaging under moderate ($\sim$100 mW) excitation power.

For instance, coherent anti-Stokes Raman scattering (CARS) is a 4WM optical process, whereby a *pump* field p and a lower

frequency *Stokes* (S) field interact through the third-order polarizability $\chi^{(3)}$ of the sample to create an *anti-Stokes*[xxi] field having frequency $\omega_{CARS} = 2\omega_p - \omega_S$ and intensity $I_{CARS} \propto |\chi^{(3)}|^2 E_p^4 E_S^2$. A vibrational transition can be resonantly driven by the beat frequency $\omega_p - \omega_S = \Omega_{vib}$ as in FIG. 4.5b. Detecting an anti-Stokes signal is advantageous, forasmuch as all (single- and multi-photon) Stokes contributions can be rejected by spectral filtering, resulting in measurements free from fluorescence background. Owing to its chemical selectivity and high sensitivity, joint to the enhanced 3D resolution intrinsic to nonlinear processes, CARS microscopy has become a popular technique for imaging biological samples.[99,xxii]

Metal NOs produce a strong 4WM signal at the LSPR owing to the plasmon-enhanced local fields just inside the metal surface, see Wang et al.[65] (§6). One then expects the third-order response of an analyte placed just outside the metal surface to be analogously enhanced. Indeed, such phenomenon has been widely observed when probing a large volume of the analyte, e. g. by mixing the sample to a silver colloid[100] or dispersing it over a nanostructured gold surface.[101] Even though sensitivity permitting single-molecule detection has been demonstrated using such substrates,[102] achieving the same result using individual NOs — albeit more challenging — is still of great interest, because the locality of the field enhancement could yield spatial information below the diffraction limit affecting FF imaging, such as conventional CARS microscopy.

In 2003, CARS enhancement by individual spherical gold NPs was reported;[103] however, these results have not been hitherto

xxi The terms Stokes and anti-Stokes designate any emission at a frequency respectively lower or higher than the pump field.

xxii In particular, it is the technique of choice for imaging lipids, whose high density of C-H bonds corresponds to a large CARS susceptibility.

reproduced.[xxiii] Apart from this isolated claim, there have been to date only few reports of CARS enhancement by individual NOs, exploiting the large plasmonic enhancement at a sharp metal tip[104] or inside narrow gaps, such as between two spherical gold NPs[105] of a gold disc quadrumer.[106] While complex nanostructures of this kind can be engineered to provide the highest enhancement, they are not ideal for applications to biological microscopy (particularly in reference to thick, live specimens) as they are unable to penetrate tissues and cells, and to probe 3D structures. Conversely, as discussed in SEC. 2.1, metal NPs are suitable labels for live imaging, but provide lower enhancement; therefore, to measure NP-enhanced CARS, one must refine the detection scheme and maximize its sensitivity.

In general the CARS signal is made up of two contributions, the resonant (vibrational) signal and the non-resonant (electronic) background — due to 4WM processes occurring in the gold volume or in the probed medium itself. Hence, one must selectively suppress the non-resonant term as a prerequisite towards a shot-noise-limited signal. There are several ways to achieve this; for instance, the work by Yampolsky et al.[105] cited above utilizes a time-resolved detection scheme. We opted instead for a phase-resolved detection scheme exploiting the coherent nature of the resonant signal, wherein the CARS signal is interfered with an external *reference* beam (often referred to as *local oscillator*) matched as for spatial mode and wavelength, and the mixing term is measured. This technique is named *heterodyne* detection, and has been applied to CARS both for bulk measurements[107] and for microscopic imaging.[108]

xxiii In fact, the 4WM background due to the intrinsic gold nonlinearity was likely measured instead, and a control experiment without the CARS substrate was not provided. Moreover, no clear evidence was given that the signal was measured from single NPs rather than aggregates, and thermal reshaping is expected at the high excitation power used.

P. Borri and W. Langbein have recently designed and performed experiments to investigate the CARS enhancement by a single metal NP; the outcome was successful, and a manuscript reporting the results is in preparation at the time of writing. Besides being the first experimental observation of such phenomenon, several elements of novelty have been introduced in the detection scheme:

- The CARS signal is modulated at a frequency (77 MHz) close to the laser repetition rate (80 MHz). The beat in the radio-frequency (3 MHz) resulting from the interference with the reference is measured in amplitude and phase using a dual-channel lock-in amplifier; this permits a simultaneous measurement of the real and the imaginary part of $\mathbf{E}_{\mathrm{CARS}}$.
- While CARS generated in the bulk propagates forwards (i. e. along the exciting beams), the signal produced by the dipolar field in the vicinity of the NP radiates in all directions. In contrast to previous works, we have therefore collected the signal in an *epi* configuration, that is, through the objective used for excitation, allowing us to investigate selectively the NP-enhanced CARS.[xxiv]
- Whereas previous works scanned the reference beam onto the sample alongside with the pump and the Stokes, we use an external reference. This allows us to use a high reference power (~ 1 mW), and to reject the common-mode classical noise of the reference via a balanced detection scheme.

For further details on the experiment, not relevant to the numerical model discussed here, the reader is referred to previ-

xxiv It is essential to illuminate the NP from side of the non-resonant substrate, otherwise one would also collect CARS generated in bulk before it, and back-scattered into the objective by the NP or the interface.

ous publications describing our typical CARS set-up[109] and our implementation of heterodyne detection.[110]

A numerical model of NO-enhanced CARS was developed in COMSOL, in order to provide a touchstone for our experimental results and additional physical insight into the system's behaviour. Several experimental observables can be computed, such as the angular distribution of the CARS emission in the FF, and the CARS signal resulting from forward or backward collection, either with or without heterodyning. More generally, the model can serve as a template to quantitatively simulate nonlinear microscopy experiments. Several elements of novelty are introduced with respect to the state of the art, particularly a two-step solving scheme to mimic nonlinear processes, and analytical formulas for simulating tightly-focused, coherent illumination and heterodyne detection.

4.3.2 *Geometry and solvers*

The geometry is similar to the linear scattering model depicted in FIG. 4.2a: V_{sim} is a sphere[xxv] halved by the optical interface $z = 0$. However, with respect to the same figure, the z axis here is reversed: The NO is placed on the interface in medium 1 ($z > 0$) and the illumination propagates along $\hat{z}$. We have performed simulations for different NOs: A GNS of diameter $D = 50\,nm$ and a $67\,nm \times 28\,nm$ bare GNR identical to the one described in SEC. 4.2 apart from the absence of the dielectric shell. Moreover, simulations of an empty interface and of a homogeneous medium have been performed as controls.

The pump and Stokes beams are both polarized along $\hat{x}$ in the BFP of the objective. Once the exciting polarization is fixed — differently from the linear scattering model discussed

xxv The optimum value of r_{sim} to be used will be discussed in the following.

in SEC. 4.2 — one can exploit the symmetries of the problem ($\mathbf{E}_{exc}$+NO) in order to speed up the solution of the model as well as the FF calculations. In fact, for an object having $x = 0$ and $y = 0$ as mirror planes, only a quarter of the physical geometry needs to be solved for. In this case the symmetry is implemented by a PEC and a PMC boundary condition assigned respectively to the $x = 0$ and $y = 0$ plane. A PEC boundary corresponds to the condition $\hat{\mathbf{n}} \times \mathbf{E} = 0$, implying the sign of $\mathbf{E}_{\parallel}$ is reversed and the sign of $\mathbf{E}_{\perp}$ is conserved across the interface. Complementarily, a PMC boundary corresponds to the condition $\hat{\mathbf{n}} \times \mathbf{H} = 0$, implying the sign of $\mathbf{E}_{\parallel}$ is conserved and the sign of $\mathbf{E}_{\perp}$ is reversed across the interface.

The geometry we have just described is solved for at the three wavelengths λ_p, λ_S, and λ_{CARS} using a slightly different mesh. A free tetrahedral mesh is used for the physical domains, with a maximum element size capped to $\lambda_0/n/5$. The triangular mesh at the NO boundary (along with the expansion rate in the adjacent domains) can be controlled to selectively refine the meshing near the metal surface, where the fields have steeper gradients; for the NO considered here, a maximum surface element size 8 nm ensures a sufficiently fine spatial sampling. V_{sim} is encircled by a PML of homogeneous thickness $t_{pml} \geqslant \lambda_p/n/5$ and meshed by sweeping four (for λ_p, λ_S) or five (for λ_{CARS}) elements of constant radial thickness, in line with the recommendations reported on P. 92.

Let us now describe the linear and nonlinear material properties attributed to the various physical domains. The substrate (fused silica, $n = 1.52$) is index-matched by the immersion medium (silicone oil), so that there is no interface in the linear optical properties. Strictly speaking, this is a limitation of the model, inasmuch as the formulas describing the coherent excitation hold in a homogeneous space solely. Nonetheless, a lowly mismatched interface (e. g. glass/water) corresponds

to $R < 10\,\%$, and therefore the results are likely to be still accurate if the linear interface is not included in the model. The frequency-dependent permittivity of gold[18] is used in the model in tabular form; in SEC. 6.2 we will compare various datasets from literature.

The magnitude of the 4WM polarization is proportional to the third-order susceptibility $\chi^{(3)}$ of the material. For glass, we adopted the value $\chi^{(3)}_{\text{glass}} = 2 \times 10^{-22}\,\text{m}^2/\text{V}^2$ measured with third harmonic generation (THG).[111] The complex $\chi^{(3)}_{\text{oil}}$ was quantitatively measured relative to the glass substrate using techniques previously developed within our group;[112,xxvi] the resulting spectra are shown in FIG. 4.6a and present a vibrational resonance at $3050\,\text{cm}^{-1}$, corresponding to stretching mode of the H-C=C bond in the styrene ring. The values of $\chi^{(3)}$ reported in literature for gold span over several order of magnitudes from $10^{-14}\,\text{m}^2/\text{V}^2$ to $10^{-19}\,\text{m}^2/\text{V}^2$, as various techniques are utilized, which employ laser pulses of different duration and probe different contributions to the nonlinear response over various time scales.[113] We adopted the value $\chi^{(3)}_{\text{gold}} = 2 \times 10^{-19}\,\text{m}^2/\text{V}^2$ reported by Renger et al.,[114] who studied the same 4WM process we have modelled, and used pulses of duration and wavelength close to our experiment.

Previous simulations of 4WM processes used COMSOL to solve simultaneously the coupled wave equations in the frequency domain for the input and the generated fields.[115,116] This approach employs the full-field formulation of the EWFD interface (where excitation is input through Ports) and is thus limited to plane wave excitation; in fact, the cited works investigated the enhancement of 4WM processes by large plasmonic metas-

xxvi The software for hyperspectral image analysis has been developed by F. Masia and W. Langbein; the measurement of $\chi^{(3)}_{\text{gold}}$ was performed by I. Pope.

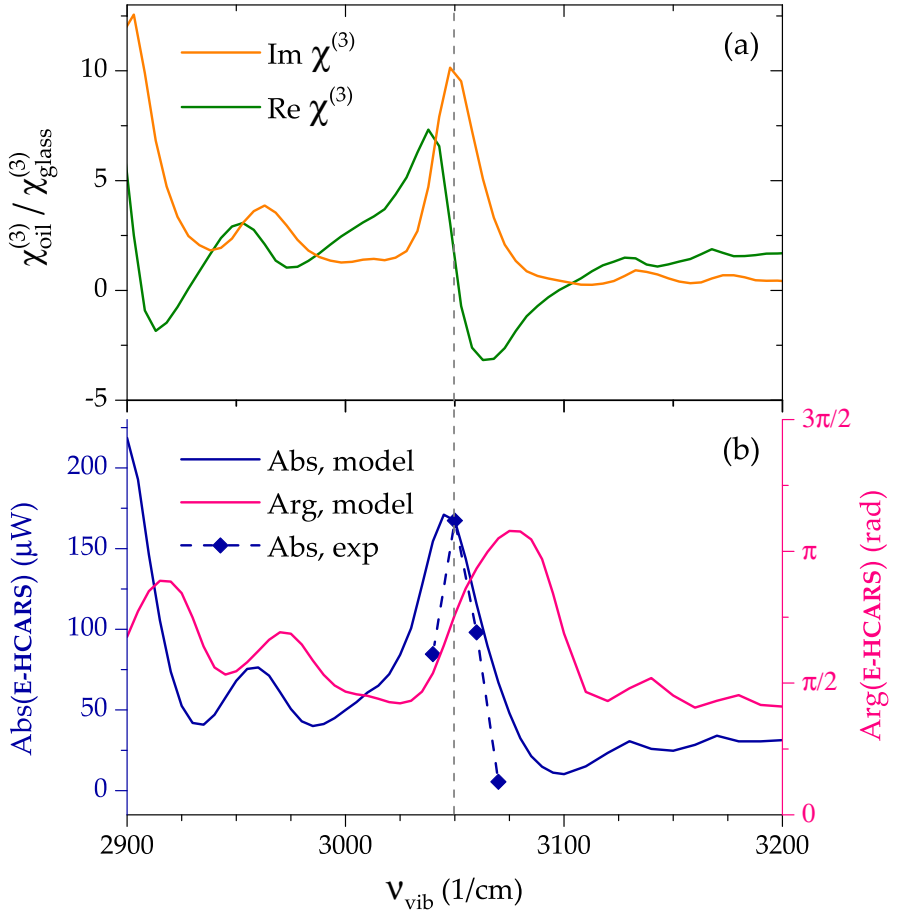

FIGURE 4.6: (a) Third-order susceptibility $\chi^{(3)}$ of silicone oil relative to glass (microscope slide) and (b) E-HCARS signal (4.14) as functions of the vibrational wavenumber ν_{vib}. The experimental dataset (diamonds) has been rescaled to arbitrary units. The vertical dashed line at $\nu_{\text{vib}} = 3050\,\text{cm}^{-1}$ is a guide to the eye.

urfaces. In order to simulate nonlinear microscopy experiments —where the exciting beams are tightly focused and cannot be approximated by plane waves— we devised instead a solving scheme consisting in two sequential steps: (i) The scattering of the input pump and Stokes beam is computed; (ii) the resulting solutions $\mathbf{E}_p$ and $\mathbf{E}_S$ (total fields) drive the nonlinear emission. This decoupled scheme assumes the nonlinear process is weak enough not to affect significantly $\mathbf{E}_p$ and $\mathbf{E}_S$. This assumption, often referred to as *undepleted pump approximation*, is amply met in our experiment where $P_p, P_S \sim$ mW and $P_{CARS} \sim$ nW. Let us now take a closer look at the implementation of this workflow.

The first EWFD interface runs twice: Once at the pump and once at the Stokes frequency. In our set-up, the pump at $\lambda_p = 820\,\text{nm}$ is the direct output of a Ti:Sa pulsed laser, while the Stokes and the reference are produced by an optical parametric oscillator (OPO). The spectral focusing used in the experiment is mimicked in the model by tuning ν_S to address a given $\Omega_{vib} = \omega_p - \omega_S$; For instance $\nu_{C\text{-}H} = 3050\,\text{cm}^{-1}$ (corresponding to $\lambda_{CARS} = 656\,\text{nm}$) is driven using $\lambda_S = 1094\,\text{nm}$. The scattered field formulation (4.3) is used, where $\mathbf{E}_{exc}$ is given by the analytical description we introduced in SEC. 3.2.2 for a coherent, linearly polarized beam tightly focused by a high NA lens (we use $NA_{obj} = 1.45$). A Gaussian field profile as in EQ. (3.34) is assumed in the BFP of the objective. The field amplitude is thus given by EQ. (3.36) with the characteristic experimental values $P_{avg} = 1\,\text{mW}$, $T_{pulse} = 1\,\text{ps}$, and $R_{pulse} = 80\,\text{MHz}$, so that $P_{pulse} = 12.5\,\text{W}$. In our microscope, the input beams have a filling factor close to $F_p = F_S = 1$.[xxvii] As discussed on P. 91, $\mathbf{E}_{sca}$ is null in a homogeneous medium, so that $\mathbf{E}_{tot} = \mathbf{E}_{exc}$, see FIG. 3.5b. In presence of a NO, E_{sca} displays a dipolar pat-

xxvii When underfilling the lens ($F < 1$), the NA of the objective is not fully exploited, and the resolution is spoiled; when overfilling ($F > 1$), a significant fraction of input power is squandered.

tern similar to FIG. 4.3b. However, being the excitation off-resonance with the LSPR, a smaller field enhancement is observed here; for instance, in the case of the GNR at λ_p one has $\max_r (E_{tot}/E_{exc}) = 5.6$, to be compared with the factor 45 found at $\lambda_{||}$, see P. 98.

The second EWFD interface implements the full field formulation (4.2) in absence of radiative excitation, the source being the external current $\mathbf{J}$ on the RHS. $\mathbf{J}$ is related to the external polarization density $\mathbf{P}$ via

$$\mathbf{J} = \partial_t \mathbf{P} = -i\omega \mathbf{P} \tag{4.11}$$

where the harmonic assumption of the EWFD interface has been used in the last equality. Specifically, in the CARS process, $\mathbf{P}_{CARS}$ is driven at the frequency ω_{CARS} by the beat between $\mathbf{E}_p$ and $\mathbf{E}_S$ and can thus be expressed as a function of the solutions of the first interface[117,xxviii]

$$\mathbf{P}_{CARS} = 6\varepsilon_0 \chi^{(3)}_{1122} \left(\mathbf{E}_p \cdot \mathbf{E}_S^*\right) \mathbf{E}_p + 3\varepsilon_0 \chi^{(3)}_{1221} \left(\mathbf{E}_p \cdot \mathbf{E}_p\right) \mathbf{E}_S^*. \tag{4.12}$$

A classical derivation of EQ. (4.12) within the scalar approximation is reported by Boyd[64] (§10.3), providing insight into the microscopic origin of the two terms of the third-order polarization density. In particular, $\chi^{(3)}_{1221} = 2\chi^{(3)}_{1122}$ is found.[xxix]

The typical results of the second interface are summarized in FIG. 4.7. Panel (a) refers to simulation in bulk oil: The spatial distribution of the CARS sources J_{CARS} mirrors E_{exc} shown in FIG. 3.5b. The resulting emission E_{CARS} builds up forwards due to the conservation of photon momentum $k_{CARS} = 2k_p - k_S$,

xxviii The work cited[117] is the first experimental report of CARS; the authors at the time were doing their researches at the Ford motor company but, ironically, the acronym CARS was adopted only some years later.

xxix Close to resonance $\chi^{(3)}$ depends on ω and the permutation of the field indices (known in literature as *Kleinman's symmetry*) is not allowed.

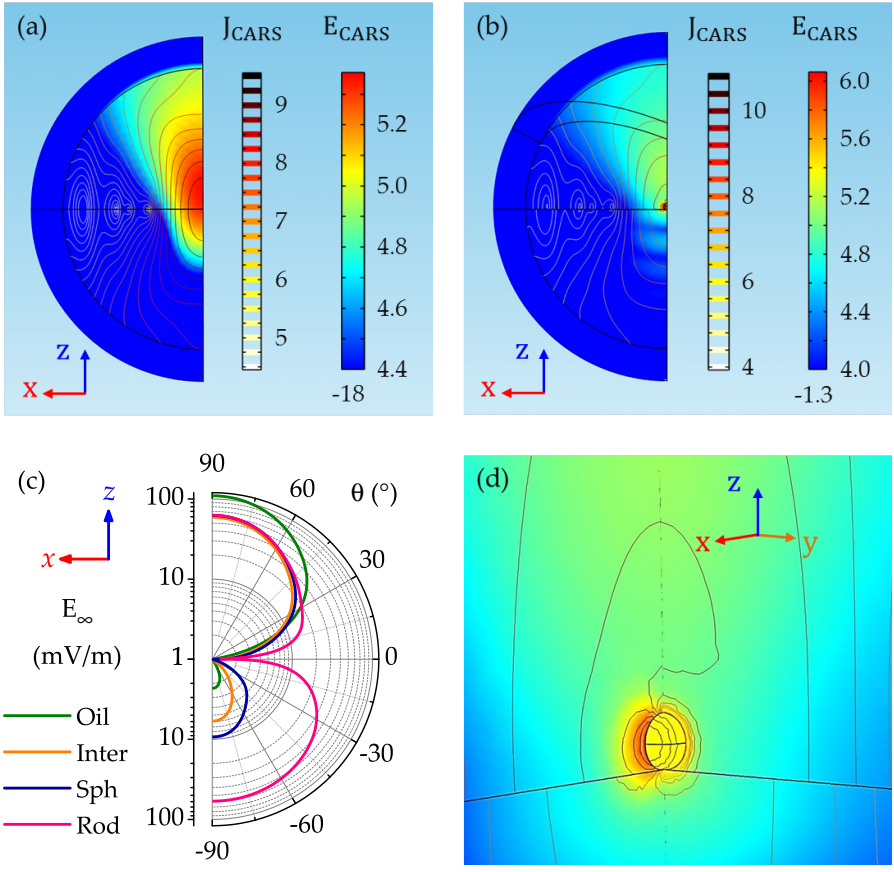

FIGURE 4.7: Nonlinear current $\log_{10}\left[J_{CARS}/(A/m^2)\right]$ (contour plot) and emitted field $\log_{10}\left[E_{CARS}/(V/m)\right]$ (false colours) for CARS (a) in a homogeneous medium, and (b) enhanced by a GNS placed onto a non-resonant substrate; (d) close-up on the GNS whose surface is coloured in yellow. The colour scales have been cropped to enhance contrast: The lowest value assumed over the represented volume is reported at the bottom of the scales. (c) FF pattern E_∞ of CARS emission for different targets: Bulk oil, an empty interface, a GNS, and a GNR. The simulated volume is a sphere of radius $r_{sim} = 1200\,nm$ and refractive index $n = 1.52$; all other parameters as specified in the text.

and is absorbed by the PML encircling V_{sim}. In FIG. 4.7b and FIG. 4.7d, the field is enhanced by a GNS placed on a non-resonant glass substrate. The mismatch in $\chi^{(3)}$ introduced by the interface creates a discontinuity in J_{CARS}, which is larger in the resonant medium. The backward CARS emission resulting from the discontinuity of J_{CARS} and the presence of the NO interferes with the (weak) forward CARS emission generated in the bulk substrate, giving thereby rise to fringes of E_{CARS}.

The FF pattern of E_{CARS} computed using EQ. (4.7) is plotted in FIG. 4.7c for different targets. For bulk oil, *trans* (i. e. along the propagation direction of the exciting beams) emission dominates; in fact, we will show later that the tiny *epi* (i. e. opposite the propagation direction of the exciting beams) emission observed is a numerical artefact. Introducing an interface reduces the trans emission because the amount of resonant material is halved. On the other hand, some epi emission is created by the discontinuity in the source distribution, and enhanced when a NO is added. Indeed, the large field enhancement generated by a GNR results in an almost symmetric pattern, with a similar amount of power emitted forwards and backwards.

4.3.3 *Post-processing and results*

In our experiments the CARS emission both in the trans and the epi direction can be measured simultaneously via the condenser and the objective respectively. In particular, the intensity T-CARS of the trans-detected CARS signal is recorded by a photomultiplier placed after suitable spectral filters. In the model, T-CARS is computed by integrating the FF Poynting

vector EQ. (4.6) over a spherical cap (defined on the boundary of V_{sim}) corresponding to the acceptance of the condenser lens

$$\text{T-CARS} = \int_{\Sigma_{con}} S_\infty \, d\Sigma \,. \tag{4.13}$$

Note that in our model the integration is limited to a quarter of Σ_{con} thanks to the fourfold symmetry of the problem, so the result of EQ. (4.13) must be multiplied by 4.

In our experiments the epi emission is measured in amplitude and phase using the heterodyne detection scheme described on P. 106. The epi-detected heterodyne CARS signal E-HCARS is computed in the model by integrating the mixing term of the CARS field projected to the FF via EQ. (4.7) with the reference field $\mathbf{E}_{ref}$ over a spherical cap (defined on the boundary of V_{sim}) corresponding to the acceptance of the objective lens

$$\text{E-HCARS} = \frac{1}{r_{sim}} \times \frac{1}{2} n c_0 \varepsilon_0 \int_{\Sigma_{obj}} \mathbf{E}_\infty \cdot \mathbf{E}^*_{ref} \, d\Sigma \,. \tag{4.14}$$

As above, the integration is limited to a quarter of Σ_{obj} so the result of EQ. (4.14) must be multiplied by 4. We emphasize that E-HCARS is a complex signal, namely an interference measured in amplitude and phase, whereas T-CARS is a power and as such is real. EQ. (4.13) and EQ. (4.14) are the pulse peak powers; the average power measured in experiments is obtained by multiplying them with the duty cycle of the source $R_{pulse} T_{pulse}$.

In our set-up the reference beam is not transmitted through the sample, and mixing with the CARS signal occurs in the detection path after the objective. Nonetheless, in order to reproduce in the model the spatial mode matching — that is, projecting $\mathbf{E}_{CARS}$ onto $\mathbf{E}_{ref}$ as in EQ. (4.14) — we fictitiously transmit the reference beam through the objective into the simulation

space. Assuming a Gaussian field profile in the objective BFP as in EQ. (3.34) with a filling factor $F_{ref} = 1$ one has

$$\mathbf{E}_{ref}(r_{sim}) = \frac{E_0}{r_{sim}} \widehat{\mathbf{E}}_{ref} \exp\left[-\left(\frac{\sin^2\theta}{\sin^2\alpha_{obj}}\right)\right] \sqrt{-\cos\theta} \qquad (4.15)$$

where the aplanatic cosine factor has been introduced. Note that the phase term $e^{-ikr_{sim}}$ has been omitted from $\mathbf{E}_{ref}$ because it cancels out with the phase of the CARS field in EQ. (4.14). The peak amplitude E_0 is computed from the average reference power and duty cycle; we used here the typical experimental value $P_{ref} = 1\,\text{mW}$ corresponding to $E_0 = 8.8 \times 10^4\,\text{V/m}$. With calculations analogous to those leading to EQ. (3.8), a polarization along $\widehat{\mathbf{x}}$ (i. e. co-polarized with the excitation) in the BFP of the objective results in

$$\widehat{\mathbf{E}}_{ref} = -\widehat{\boldsymbol{\theta}}\cos\varphi - \widehat{\boldsymbol{\varphi}}\sin\varphi = \begin{bmatrix} -(\cos\theta+1)\cos^2\varphi + 1 \\ -(\cos\theta+1)\cos\varphi\sin\varphi \\ \sin\theta\cos\varphi \end{bmatrix}. \qquad (4.16)$$

The trans and epi signals measured for different targets are shown in FIG. 4.8 as a function of r_{sim}. The trans signal in bulk oil displayed in panel (a) increases with r_{sim} as more CARS sources are included within V_{sim}. In fact, FIG. 4.7a shows that J_{CARS} at $r_{sim} = 1200\,\text{nm}$ is still a few percent of its maximum value $J_{CARS}(0)$. Furthermore, the decrease of J_{CARS} is partially compensated by the increase of the corresponding volume, resulting in a rather slow convergence, and even more so when a smaller illumination NA produces a larger PSF. This means either large values of r_{sim} should be used to obtain accurate results,[xxx] or the underestimate due to domain truncation should

[xxx] This would limit in practice the applicability of the model, inasmuch as the computation time increases rapidly with r_{sim}: For instance, the model with a GNS on a substrate is computed in 78, 672 and 11 272 s for $r_{sim} = 500$, 1000 and 2000 nm on a common workstation (Intel Core i7 CPU, 64 GiB RAM).

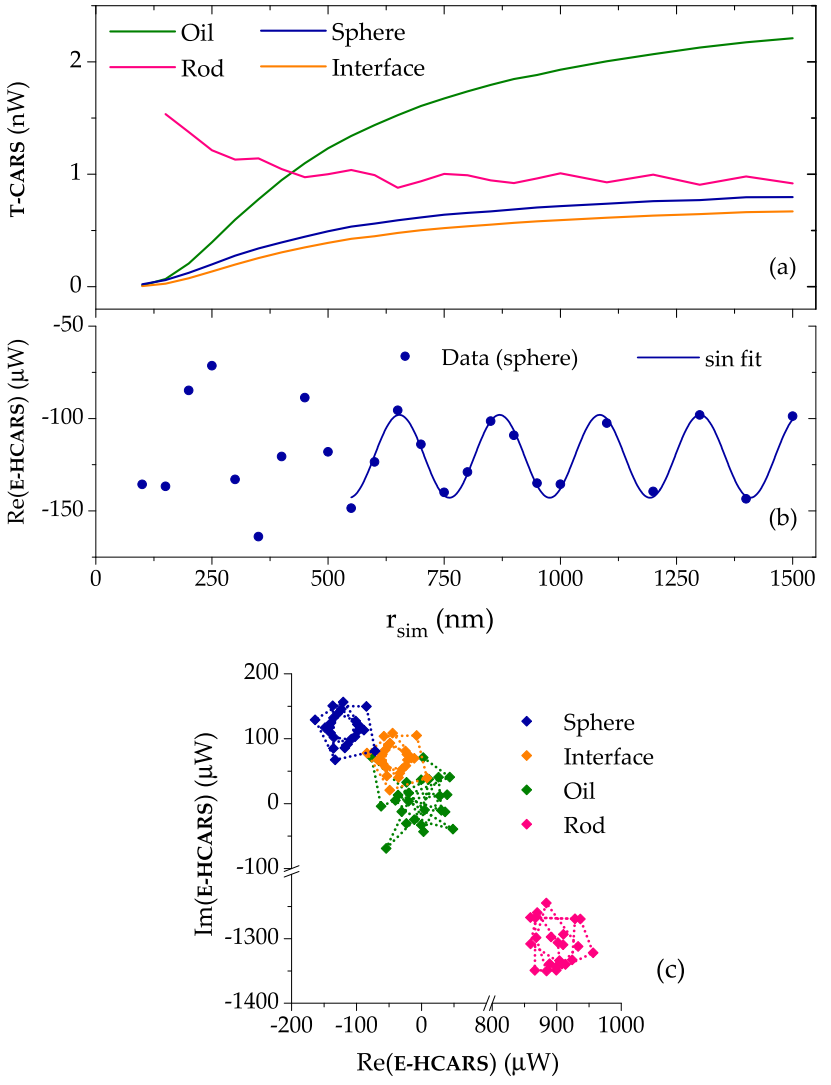

FIGURE 4.8: CARS signals as functions of the radius r_{sim} of the simulated volume for various targets: Bulk oil, and a substrate either empty, with a GNS, or with a GNR on it. (a) T-CARS signal (4.13) for a 1.4 NA collection. (b) Real part of the E-HCARS signal (4.14) signal for the GNS; The fitting function is $f(r_{sim}) = -120\,\mu W + 22.4\,\mu W \sin\left[2\pi\left(r_{sim} + 48\,nm\right)/216\,nm\right]$. (c) Trajectories of E-HCARS in the complex plane; the dotted lines join the data up to $r_{sim} = 1\,\mu m$.

be estimated and compensated for. T-CARS is diminished by more than 50 % when the amount of resonant material is halved by the introduction of a substrate. Adding a GNS increases T-CARS by 20 % with respect to an empty interface; interestingly, this is five to ten times more than our preliminary experimental observations. The decreasing trend with superimposed oscillations observed for a GNR suggests some amount of destructive interference occurs between $\mathbf{E}_{\mathrm{CARS}}$ generated at the rod tips and in the bulk material.

E-HCARS(r_{sim}) always exhibits oscillations as in FIG. 4.8b for the case of a GNS. The data are fitted well by a sinusoidal function with period $L = \lambda_{\mathrm{CARS}}/n/2 = 216\,\mathrm{nm}$. We tentatively ascribed this behaviour to a numerical artefact of the FF calculations due to the discretization introduced by the mesh at the boundary where the transform is computed.[xxxi] In our model, this is the edge of the simulated volume $r = r_{\mathrm{sim}}$, leading to a phase $2\pi r_{\mathrm{sim}}$, which appears as a circular trajectory in the complex plane in FIG. 4.8c. This artefact can be thus removed by averaging any two simulations corresponding to opposite points of the circle, i. e. whose r_{sim} differ by $L/2$. Also, radii larger than, say, 550 nm should be used in order to avoid the NF regime of small r_{sim}. For a GNR a less neat circle is drawn, suggesting other sources of numerical noise (proportional to the signal amplitude) are dominating in the regime where epi and trans emission have similar amplitudes. Averaging is not necessary here since the amplitude of the oscillations is rather

[xxxi] The periodicity observed hints at an interference occurring with a backward-propagating emission originating at $r = r_{\mathrm{sim}}$. To make sure this was not a spurious reflection of the trans emission, we refined and expanded the PML to no avail. Such backward-propagating emission could also be caused by the truncation of the simulation volume, which introduces an unphysical discontinuity of J_{CARS} at $r = r_{\mathrm{sim}}$. However, one would then expect the oscillations to be damped when r_{sim} is increased so to reduce the step height.

small (less than 10 %) compared to the magnitude of the signal. Lastly, a seemingly random data distribution centred at $(0,0)$ is observed for bulk oil, thus proving that the tiny E-HCARS observed in FIG. 4.7c is a numerical artefact indeed.

As discussed above, in the model λ_S can be tuned to address a different Ω_{vib}. The resulting E-HCARS spectrum (average of two simulations with r_{sim} differing by $L/2$) is reported in FIG. 4.6b. Roughly E-HCARS $\propto |\chi^{(3)}_{oil}|$ is found, with a distinct resonance at $\nu_{C\text{-}H} = 3050\,cm^{-1}$. This proves that the signal recorded is dominated by the CARS emission from the oil rather than by the non-resonant 4WM contribution from the gold. Preliminary experimental data exhibit an analogous resonant behaviour, but present a significantly narrower linewidth. Such an abrupt drop of the signal upon detuning could be a measurement artefact due to a loss of temporal superposition between the signal and the reference pulses; further experiments and analyses are being carried out.

An operative way to characterize experimentally the effect of a NO on the CARS signal is referencing to the empty interface.

$$\Xi = \left| \frac{\text{E-HCARS(NO)}}{\text{E-HCARS}(-)} \right| - 1 \tag{4.17}$$

defines the *epi enhancement parameter*. Generally speaking, Ξ is governed by two contrasting effects: (i) a volume of resonant material in the focus is replaced by the non-resonant NO; and (ii) the electric field in the vicinity of the NO is modified, consequently affecting the intensity and angular distribution of the CARS signal. (i) diminishes Ξ, while (ii) increases it, at least for field-enhancing NOs. Looking at FIG. 4.8c one finds $\Xi_{sph} = 1.1$ — to be compared with an experimental value $\Xi_{sph} = 0.75 \pm 0.05$ — and $\Xi_{rod} = 19$.

Part III

EXPERIMENTAL MEASUREMENTS

5

QUANTITATIVE DATA ANALYSIS

The definition (1.1) of the OCS indicates that they can be measured quantitatively by a concurrent detection of the NO signal and the excitation intensity. However, in microscopy experiments P_{sca} is difficult to quantify — both as a signal in scattering measurements and as a contribution in high NA extinction measurements — inasmuch as only a fraction of it is collected by the objective, depending on the geometry of the experiment in a non-trivial fashion. Moreover, P_{sca} is directly addressed in DF, whereas the excitation intensity is measured in BF, as discussed in SEC. 2.2.2; thus the different NA_i range of the two illumination modalities must be taken into account too.

We will introduce in SEC. 5.1 a theoretical framework which distils the considerations above into the expressions of the OCS as functions of experimentally *detected signals*. These include two *scattering parameters*, which are determined by the angular ranges of illumination and collection, as well as by the symmetry of the plasmonic mode and the refractive index of the NO environment. The rest of the chapter is devoted to the calculation of the scattering parameters for various symmetries of the plasmonic mode. Our analytical model assumes a NO in the dipole limit excited by incoherent microscope illumination. A dielectric interface placed close to the NO represent the substrate, and a homogeneous optical environment is obtained as a limit case. In CH. 6 we will show how to perform measurements in order to acquire the detected signals required for the quantitative analysis described in this chapter.

5.1 OPTICAL CROSS-SECTIONS IN ABSOLUTE UNITS

An image[i] $\mathcal{I}(x, y)$ of the sample can be captured using an imaging array such as a CCD or a CMOS camera. Its scale can be computed given the pixel pitch of the array and the optical magnification from the sample to the sensor. Let us consider a *detected region* A delimited within the scaled image. We define the corresponding *detected signal* as

$$S_A^l \equiv \frac{1}{t_{exp}} \int_A \mathcal{I}^l(x, y)\, dx\, dy\,. \tag{5.1}$$

where t_{exp} is the exposure time of $\mathcal{I}^l$. Throughout this chapter, the l superscript indicates the illumination condition whenever relevant. For instance $l = \text{BF}$ and $l = \text{DF}$ denote the illumination modalities defined on p. 50. The NO signal is measured when $A = A_{NO}$ encloses the whole[ii] PSF of an individual NO, and contains no other absorbers or scatterers.[iii] The local background is measured when $A = A_{bg}$ is a region close to the NO (few λ away) and "empty" — i. e. containing no absorbers or scatterers. If A_{NO} and A_{bg} have a different area the local background must be multiplied by A_{NO}/A_{bg} to apply our quantitative method. In this section, we will derive the expression of the OCS in terms of the following five detected signals:

- S_{NO}^{BF}, NO transmission signal under BF excitation;
- S_{NO}^{DF}, NO scattering signal under DF excitation;
- S_{bg}^{BF}, local background under BF excitation, which corresponds to the transmitted illumination;

i More precisely, we are describing as a scalar field a monochrome image or, equivalently, a single colour channel of a polychrome image.

ii A meaningful choice of size of A_{NO} for experiments is discussed on p. 163.

iii This is clearly an idealization: The presence of other NOs is unavoidable in practice (e. g. intrinsic glass roughness), but can be neglected so long as their absorption and scattering is much weaker than the NO.

- S_{bg}^{DF}, local background under DF excitation, which would be null in an ideal measurement;
- S^{dk},"dark" sensor readout, namely with no illumination (digitizer offset + dark current + ambient stray light).

A *detected power* P_A^l is the power radiated due to transmission and scattering from A into the acceptance of the objective lens. The five detected signals above are each proportional to a detected power via the overall optical efficiency ϵ of the detection path:[iv] $S_{NO}^{BF} = \epsilon P_{NO}^{BF}$, and so on. In fact, S_A^l defined by EQ. (5.1) has formally the units of a power, being $\mathcal{I}^l/t_{exp}$ an intensity; however, we will show in the following that only the relative magnitude of the detected signals is important, but not their absolute value, and thus for data analysis purposes they can be expressed in "instrumental units" like counts/s or pixel value/s. Furthermore, we emphasize that this formalism applies not only to imaging, but also to spectroscopic measurements where a *spectrum* $S_A^l(\lambda_0) = \epsilon(\lambda_0)P_A^l(\lambda_0)$ is recorded as a function of the emitted light wavelength λ_0.

Commonly, absorption is measured in BF and scattering in DF. The OCS definition (1.1) thus becomes

$$\sigma_{abs}^{BF} = P_{abs}^{BF}/I_i^{BF} \quad \text{and} \quad \sigma_{sca}^{DF} = P_{sca}^{DF}/I_i^{DF}. \tag{5.2}$$

We remind the meaning of the subscripts is: i = "incident in medium 1" and t = "transmitted to medium 2" as in FIG. 3.1a. We now want to manipulate EQ. (5.2) in order to express the OCS in terms of detected powers solely; let us begin with the denominators. The excitation power can be directly measured in BF as $P_i^{BF} \equiv P_t^{BF}/\tau^{BF} = (P_{bg}^{BF} - P^{dk})/\tau^{BF}$, where the parameter τ^{BF}

iv Experimentally, ϵ is the product of the transmittance or reflectance of each element in the optical path from the sample to the sensor, and the quantum efficiency of the sensor itself.

defined by the first equality accounts for transmission from medium 1 to 2. On the contrary, in DF the illumination is rejected and cannot be directly measured; still (given the source power is unaltered) P_i^{DF} is proportional to P_i^{BF} via a constant named ξ. Since in experiments A has a lateral size $\sim \lambda$ (see p. 163), I_i^l with $l \in \{BF, DF\}$ is approximately constant over A and $I_i^l = P_i^l/A$. The denominators of EQ. (5.2) are thus expressed in terms of detected powers as[v]

$$I_i^{BF} = \left(P_{bg}^{BF} - P^{dk}\right)/\left(A\tau^{BF}\right) \quad \text{and} \quad I_i^{DF} = \xi\, I_i^{BF} \tag{5.3}$$

and only the numerators are left to be calculated.

P_{sca}^l in the definition of σ_{sca}^l is the total scattering over the 4π solid angle, hence not directly associated to a detected signal defined as in EQ. (5.1). The detected scattered power is $P_{obj}^l = \eta^l P_{sca}^l$ where η^l is the fraction of scattered power collected by the objective. The total DF scattered power is thus

$$P_{sca}^{DF} = \left(P_{NO}^{DF} - P_{bg}^{DF}\right)/\eta^{DF}. \tag{5.4}$$

The extinction power directly measured in BF can be broken down as $P_{NO}^{BF} = P_{bg}^{BF} - P_{ext}^{BF} + P_{obj}^{BF}$, where P_{obj}^{BF} accounts for the forward scattering collected by the objective. So long as optical processes other than scattering and absorption are negligible, EQ. (1.2) translates into $P_{ext}^{BF} = P_{sca}^{BF} + P_{abs}^{BF}$, and

$$\begin{aligned} P_{abs}^{BF} &= P_{bg}^{BF} - P_{NO}^{BF} + P_{obj}^{BF} - P_{sca}^{BF} \\ &= P_{bg}^{BF} - P_{NO}^{BF} - (1-\eta^{BF})P_{sca}^{BF} \\ &\equiv P_{bg}^{BF} - P_{NO}^{BF} - \zeta(1-\eta^{BF})P_{sca}^{DF} \\ &= P_{bg}^{BF} - P_{NO}^{BF} - \zeta\frac{1-\eta^{BF}}{\eta^{DF}}(P_{NO}^{DF} - P_{bg}^{DF}) \end{aligned} \tag{5.5}$$

[v] A appearing in all subsequent formulas is in fact A_{NO}^{BF} (assuming S_{bg}^{BF} is rescaled if $A_{NO}^{BF} \neq A_{bg}^{BF}$). Since this is the only relevant A for the quantitative analysis the notation has been simplified.

where in the third equality we defined the new parameter ζ and in the fourth equality we used EQ. (5.4).

By substituting EQ. (5.3)–(5.5) into EQ. (5.2) the OCS are eventually expressed in terms of detected signals only

$$\sigma_{abs}^{BF} = A\tau^{BF}\frac{S_{bg}^{BF} - S_{NO}^{BF} - \zeta\frac{1-\eta^{BF}}{\eta^{DF}}(S_{NO}^{DF} - S_{bg}^{DF})}{S_{bg}^{BF} - S^{dk}} \tag{5.6a}$$

$$\sigma_{sca}^{DF} = A\tau^{BF}\frac{\xi}{\eta^{DF}}\frac{S_{NO}^{DF} - S_{bg}^{DF}}{S_{bg}^{BF} - S^{dk}} \tag{5.6s}$$

Note that ϵ, which is different for each set-up and hard to characterize, has cancelled out. Summarizing, the parameters appearing in EQ. (5.6) are defined as

$$\tau^{BF} \equiv \frac{P_t^{BF}}{P_i^{BF}}, \quad \xi \equiv \frac{P_i^{BF}}{P_i^{DF}}, \quad \zeta \equiv \frac{P_{sca}^{BF}}{P_{sca}^{DF}}, \quad \eta^l \equiv \frac{P_{obj}^l}{P_{sca}^l}, \tag{5.7}$$

and have the following physical meaning:

- The *transmission parameter* τ^{BF} is the fraction of incident power transmitted from medium 1 to 2 (in the FF);
- The *illumination parameter* ξ is the ratio of the power incident on the sample under BF and DF illumination;
- The *excitation parameter* ζ accounts for the different response of the NO to the BF and DF polarization content;
- The *detection parameter* η^l is the fraction of scattered power collected by the microscope objective.

τ^{BF} is computed by averaging the transmittance (1.16) over the θ_i range of the experimental illumination

$$\tau^{BF} = \langle T \rangle^{BF} = \frac{\int_{\underline{\theta}_i^{BF}}^{\overline{\theta}_i^{BF}} \left[T_p(\theta_i) + T_s(\theta_i)\right] \cos\theta_i \sin\theta_i \, d\theta_i}{2\int_{\underline{\theta}_i^{BF}}^{\overline{\theta}_i^{BF}} \cos\theta_i \sin\theta_i \, d\theta_i} \tag{5.8}$$

where the line below and above a symbol indicates the minimum and maximum value delimiting the illumination range. Hence τ^{BF} depends on the NO environment via n_1 and n_2, and its maximum value $\tau^{BF} = 1$ is obtained for a homogeneous medium ($n_1 = n_2$). As for ξ, the intensity at the sample plane is proportional to the illuminated area A^l_{BFP} defined by the light stops in the BFP of the condenser lens as in FIG. 3.1b; thus

$$\xi = \frac{A^{BF}_{BFP}}{A^{DF}_{BFP}} = \frac{\pi\left(\overline{\rho}_i^{BF}\right)^2}{\pi(\overline{\rho}_i^{DF})^2 - \pi\left(\underline{\rho}_i^{DF}\right)^2} = \frac{(\overline{NA}_i^{BF})^2}{(\overline{NA}_i^{DF})^2 - (\underline{NA}_i^{DF})^2}\,, \qquad (5.9)$$

where Abbe's sine condition $\rho_i = f_{con}\, NA_i$ has been used in the last equality. EQ. (5.9) assumes a homogeneous illumination over the BFP, which can be produced in experiments using a suitable diffuser, see FIG. 6.3, FIG. B.2, and related discussion. Note that ξ depends solely on the microscope configuration, and is independent of the measured NO and its environment. By contrast, the *scattering parameters* ζ and η^l depend also on the response of the NO. We shall now embark on the calculation of the scattering parameters for several types of NOs.

5.2 DIPOLE RADIATION NEAR A PLANAR INTERFACE

The main piece of information required to compute η^l is the angular distribution[vi] $\mathcal{P}_{NO}(\theta, \varphi)$ of the power scattered by the NO to the FF, often referred to as *scattering pattern*. Once $\mathcal{P}_{NO}$ is known, P^l_{sca} and P^l_{obj} appearing in EQ. (5.7) can be computed by integrating it over the appropriate solid angles, namely $\Omega = 4\pi$ and Ω_{obj}. Clearly, an analytical expression of $\mathcal{P}_{NO}$ can only be obtained for a simplified model of the investigated system. For a small enough NO (in practice, $D \lesssim \lambda/10$) the exciting electric field $\mathbf{E}_{exc}$ is approximately constant over the NO volume. Within such *electrostatic* or *dipole approximation*, the scattering of a plane wave can be described as radiation from a single dipole placed at the (point-like) NO position. The model of choice for the environment is a planar dielectric interface: As discussed in SEC. 1.3, this is a relevant scenario for optical studies of NOs, and a homogeneous medium can be described too for $n_1 = n_2$.

We report here for convenience the expression of $\mathcal{P}(\theta, \varphi)$ calculated by Lukosz and Kunz[29–32] for an oscillating electric dipole. It has been recast into the notation used throughout this thesis, and simplified by assuming a null distance z_{NO} of the dipole from the interface: This describes a NO deposited on the substrate and within the dipole limit $D \ll \lambda$ which implies $z_{NO} \simeq D/2 \ll \lambda$. Following Lukosz and Kunz, we define the emission angles θ_1 and θ_2 in media 1 and 2 relative to the z axis analogously to θ_i and θ_t in FIG. 3.1a, so that $\theta_{1,2} \in [0, \pi/2]$ and $n_1 \sin\theta_1 = n_2 \sin\theta_2$.[vii]

vi We reserve the calligraphic font $\mathcal{P}$ to angular power distributions (in sr^{-1}), while integrated powers are indicated with the standard mathematical font.

vii The corresponding angle $\theta \in [0, \pi]$ in standard polar coordinates is $\theta = \theta_1$ in medium 1 and $\theta \equiv \pi - \theta_2$ in medium 2.

In medium 1 the angular distribution of power radiated with p and s polarization is[32]

$$\mathcal{P}_{1,p}(\theta_1,\varphi) = \frac{3}{2\pi} n^3 \times \left\{ \frac{\cos\theta_1 \left[\cos\Theta \sin\theta_2 + \sin\Theta \cos\theta_2 \cos(\varphi - \Phi) \right]}{\cos\theta_1 + n\cos\theta_2} \right\}^2 \tag{5.10p}$$

$$\mathcal{P}_{1,s}(\theta_1,\varphi) = \frac{3}{2\pi} n^3 \left\{ \frac{\cos\theta_1 \sin\Theta \sin(\varphi - \Phi)}{n\cos\theta_1 + \cos\theta_2} \right\}^2 \tag{5.10s}$$

where the polar angles (Θ, Φ) define the dipole orientation as in FIG. 3.1a, and $n \equiv n_1/n_2$ is the refractive index ratio of the interface. EQ. (5.10) have to be replaced by

$$\mathcal{P}_{1,p}(\theta_1,\varphi) = \frac{3}{2\pi} \frac{n^3}{n^2-1} \cos^2\theta_1 \times \frac{n^2 \cos^2\Theta \sin^2\theta_1 + \sin^2\Theta \cos^2(\varphi - \Phi)(n^2 \sin^2\theta_1 - 1)}{(n^2+1)\sin^2\theta_1 - 1} \tag{5.11p}$$

$$\mathcal{P}_{1,s}(\theta_1,\varphi) = \frac{3}{2\pi} \frac{n^3}{n^2-1} \cos^2\theta_1 \sin^2\Theta \sin^2(\varphi - \Phi) \tag{5.11s}$$

in the regime where evanescent waves in the dipole's NF are transmitted as plane waves into medium 1 — namely, for $n > 1$ and $\theta_1 > \theta_{1,c} = \arcsin 1/n$.

In medium 2 the power distribution is

$$\mathcal{P}_{2,p}(\theta_2,\varphi) = \frac{3}{2\pi} \times \left\{ \frac{\cos\theta_2 \left[n\cos\Theta \sin\theta_2 - \sin\Theta \cos\theta_1 \cos(\varphi - \Phi) \right]}{\cos\theta_1 + n\cos\theta_2} \right\}^2 \tag{5.12p}$$

$$\mathcal{P}_{2,s}(\theta_2,\varphi) = \frac{3}{2\pi} \left\{ \frac{\cos\theta_2 \sin\Theta \sin(\varphi - \Phi)}{n\cos\theta_1 + \cos\theta_2} \right\}^2 \tag{5.12s}$$

which have to be replaced by

$$\mathcal{P}_{2,p}(\theta_2,\varphi) = \frac{3}{2\pi}\frac{1}{1-n^2}\cos^2\theta_2 \times \frac{n^4\cos^2\Theta\sin^2\theta_2 + \sin^2\Theta\cos^2(\varphi-\Phi)(\sin^2\theta_2 - n^2)}{(n^2+1)\sin^2\theta_2 - n^2} \tag{5.13p}$$

$$\mathcal{P}_{2,s}(\theta_2,\varphi) = \frac{3}{2\pi}\frac{1}{1-n^2}\cos^2\theta_2\sin^2\Theta\sin^2(\varphi-\Phi) \tag{5.13s}$$

in the regime where dipole radiation is totally internally reflected at the interface — namely, for $n < 1$ and $\theta_2 > \theta_{2,c} = \arcsin n$. Note the formulas above hold when the dipole is placed in medium 2 as in FIG. 3.1a. When the dipole is placed in medium 1 instead, the corresponding formulas are obtained by exchanging the subscripts 1 and 2 in EQ. (5.10)–(5.13) as well as in the definition of n. The overall power distribution $\mathcal{P}(\theta,\varphi) = \mathcal{P}_p + \mathcal{P}_s$ described by EQ. (5.10)–(5.13) is represented in FIG. 5.1 for an interface of glass with air, water, and index-matching immersion oil, and for dipoles having different orientations. Discontinuities of the distribution occur in the denser medium at the critical angle ($\theta_{1,c} = 41.1°$ in air and $\theta_{1,c} = 61.0°$ in water) as well as along the interface, where propagation is impeded.

NORMALIZATION OF THE ANGULAR POWER DISTRIBUTION

$\mathcal{P}(\theta,\varphi)$ is normalized to the total emitted power[viii] P_{tot} in units of $P_{iso} \equiv \lim_{z_{NO}\to\infty} P_{tot}(z_{NO})$, namely the total power radiated into an isotropic medium of refractive index n_2

$$\int_{4\pi} \mathcal{P}(\theta,\varphi)\,d\Omega = \frac{P_{tot}}{P_{iso}}. \tag{5.14}$$

viii P_{tot} is the power radiated by an individual dipole, not to be confused with P^{l}_{sca}, which is the power scattered by the NO, i. e. a collection of dipoles.

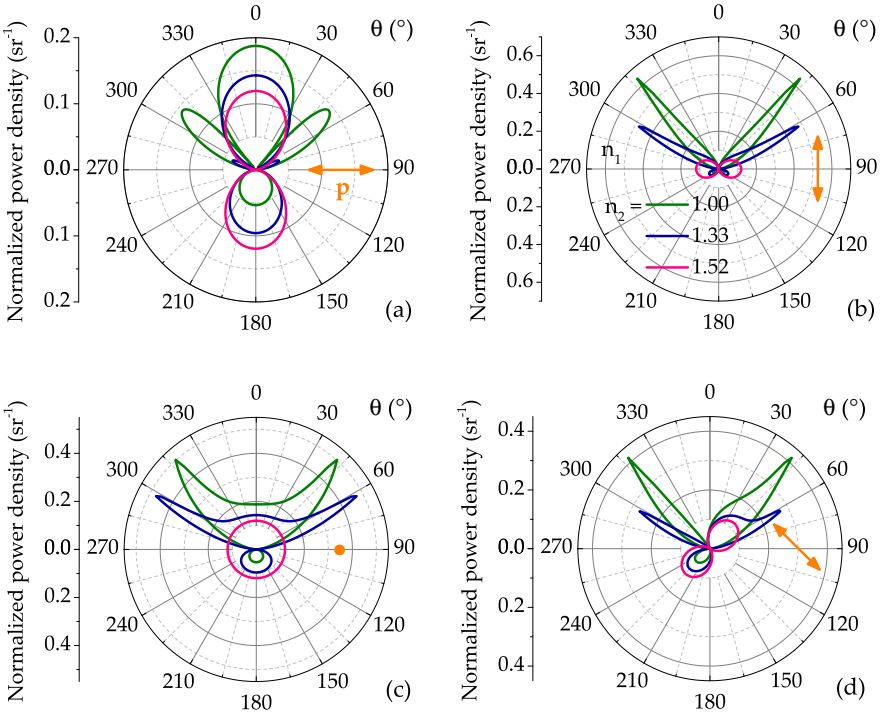

FIGURE 5.1: Normalized angular distribution $\mathcal{P}(\theta, 0) \times (P_{iso}/P_{tot})$ of the power radiated by an oscillating electric dipole placed at a planar dielectric interface $z = 0$. Medium 1 (above) and medium 2 (below) have refractive indices $n_1 = 1.52$ and n_2 as indicated in the legend of (b). The dipole is placed in medium 2 at a distance $z_{NO} = 0$ from the interface. The orange arrows/dot indicate the dipole orientation: (a) $\Theta = \pi/2$, $\Phi = 0$; (b) $\Theta = 0$; (c) $\Theta = \pi/2$, $\Phi = \pi/2$; (d) $\Theta = \pi/4$, $\Phi = 0$.

P_{iso} is related to the total power radiated in vacuum ($n_2 = 1$) via

$$P_{iso}(n_2) = n_2 P_{iso}(1) = n_2 \frac{p^2 \omega^4}{12\pi\varepsilon_0 c_0^3} \tag{5.15}$$

being p the amplitude of the dipole moment. The ω^4 frequency dependence is characteristic of dipole emission and featured for instance by EQ. (1.5). The power emitted by an arbitrarily oriented dipole can be decomposed into the contributions of two dipoles with orientation $\perp$ and $\parallel$ to the interface[30]

$$\frac{P_{tot}}{P_{iso}}(n, \Theta) = p_{e,\perp}(n)\cos^2\Theta + p_{e,\parallel}(n)\sin^2\Theta\,. \tag{5.16}$$

The coefficients in EQ. (5.16) can be expanded into a Taylor series in powers of $4\pi z_{NO}/\lambda_2$.[29] In the limit $z_{NO} = 0$ we adopted, only the zero-order terms of the expansions must be retained

$$p_{m,\perp} = \frac{2}{5}\frac{n^5 - 1}{n^2 - 1}, \tag{5.17a}$$

$$p_{m,\parallel} = \frac{1}{5}\frac{n^5 - 1}{n^2 - 1} - \frac{1}{2}\frac{n^2}{n+1}\left(1 - \frac{3n}{n^2+1}\right) - \frac{3}{2}\frac{n^4 \ln\left[(\sqrt{n^2+1} - n)(\sqrt{n^2+1} + 1)/n\right]}{(n^2+1)^{3/2}(n^2-1)}, \tag{5.17b}$$

$$p_{e,\perp} = \frac{2n^2}{n^2+1}p_{m,\parallel} - \frac{n^2-5}{n^2+1}p_{m,\perp} - 2, \tag{5.17c}$$

$$p_{e,\parallel} = \frac{3\,p_{m,\perp} - p_{m,\parallel}}{n^2+1}, \tag{5.17d}$$

where the m and e subscripts refer to a magnetic and an electric dipole respectively.

P_{tot}/P_{iso} given by EQ. (5.16) and EQ. (5.17) is a monotonic function of n as shown in FIG. 5.2. For $n = 1$ there is no interface and therefore $P_{tot} = P_{iso}$. For $n < 1$ one finds

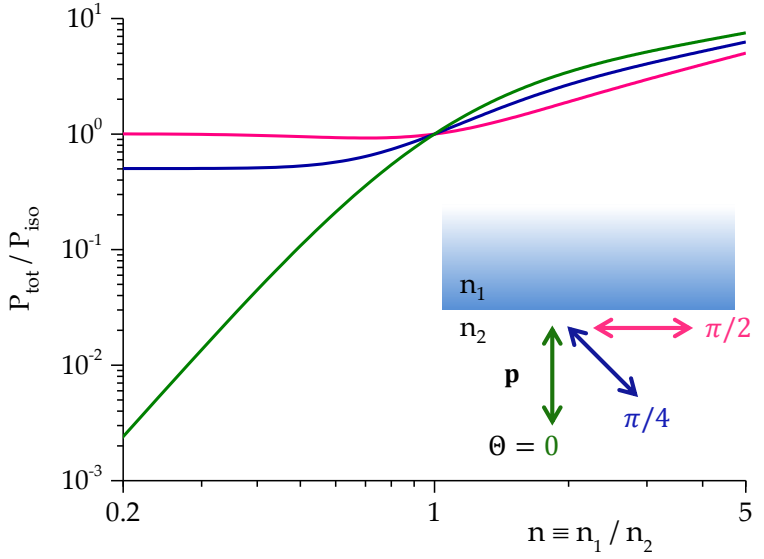

FIGURE 5.2: Total power P_{tot} radiated by an electric dipole $\mathbf{p}$ at a planar dielectric interface as a function of the refractive index ratio n. The power is expressed in units of the power P_{iso} emitted in medium 2 in absence of the interface. $\mathbf{p}$ is placed in medium 2 at a distance $z_{NO} = 0$ from the interface $z = 0$ and forms an angle Θ with the z axis.

$\lim_{n\to 0} (P_{tot}/P_{iso}) = \sin^2\Theta$, and in particular $P_{tot}/P_{iso} \propto n^3$ for a dipole perpendicular to the interface ($\Theta = 0$). In this case the dipolar field is screened by medium 1; such behaviour can be rationalized within the frame of the image charge method presented in SEC. 1.3. According to EQ. (1.14), for $n_1 < n_2$ the image dipole orientation is opposite to the physical dipole. The destructive interference between the emission of the two dipoles (or, equivalently, between the emission of the physical dipole and its reflection) causes the radiated power to decrease, and eventually vanish for $n \to 0$ when $p_{im} \to p_{ph}$.

5.3 CALCULATION OF THE SCATTERING PARAMETERS

Schematically, we model a scattering measurement as follows:

1. An electric dipole $\mathbf{p} = \varepsilon_0 \varepsilon_m \boldsymbol{\alpha} \mathbf{E}_{exc}$ is induced at the NO position; $\boldsymbol{\alpha}$ is the polarizability tensor of the NO and the explicit expression of the exciting field $\mathbf{E}_{exc}$ was derived in SEC. 3.1.1.
2. $\mathbf{p}$ radiates with the angular power distribution $\mathcal{P}(\theta, \varphi)$ reported in SEC. 5.2.
3. The scattered powers in the definition EQ. (5.7) of ζ and η^l are computed integrating $\mathcal{P}(\theta, \varphi)$ over the appropriate solid angles of excitation and detection as will be shown below.

Note that all interaction of the NO with the scattered field — in particular that reflected from the interface — is disregarded in this picture because 1. and 2. are independent, successive steps. This implies the following calculations hold solely for weak scatterers (consistent with our small particle assumption) or weakly reflecting interfaces.

In our experiments $\mathbf{p}$ is placed in medium 2, and thus $\mathbf{E}_{exc} = \mathbf{E}_2(\theta_i, \varphi_i)$. As discussed in SEC. 3.1.1, $\mathbf{E}_2$ with different (θ_i, φ_i) directions are incoherent, and therefore the detected scattering is calculated as an incoherent sum of the powers P_{tot} emitted by the excited dipoles

$$P^l_{det} = \int_{A^l_{BFP}} dA \int_{\Omega_{det}} d\Omega \; P_{iso} \, \mathcal{P}(\theta, \varphi) \tag{5.18}$$

where the integration is carried over the illuminated area A^l_{BFP} in the condenser BFP and the solid angle of detection Ω_{det}. Now, $\mathcal{P}$ depends on the excitation direction via $\Theta(\theta_i, \varphi_i)$ and

$\Phi(\theta_i, \varphi_i)$, while P_{iso} does via $p(\theta_i, \varphi_i)$, see EQ. (5.15). Thus the integral (5.18) can be rewritten in terms of the angular variables

$$P^l_{det}(\underline{\theta}^l_i, \overline{\theta}^l_i, \underline{\theta}_d, \overline{\theta}_d) \propto \int_{\underline{\theta}^l_i}^{\overline{\theta}^l_i} d\theta_i \, \cos\theta_i \sin\theta_i \int_0^{2\pi} d\varphi_i \times \int_{\underline{\theta}_d}^{\overline{\theta}_d} d\theta \, \sin\theta \int_0^{2\pi} d\varphi \, p^2(\theta_i, \varphi_i) \, \mathcal{P}(\theta_i, \varphi_i, \theta, \varphi) \, . \tag{5.19}$$

Since $\hat{z}$ is an axis of symmetry of the set-up, the azimuth variables span the full $[0, 2\pi)$ range, while we have denoted with lines under and over the symbol the lower and upper integration limit of the polar angles defining the illumination (subscript i) and detection (d) ranges. The aplanatic cosine factor has been introduced in EQ. (5.19) via EQ. (3.10); see FIG. 3.3 and related discussion for its meaning. All constant factors in EQ. (5.19) have been omitted since the scattering parameters (5.7) are defined as power ratios.[ix]

For the geometry depicted in FIG. 3.1b, the scattering parameters (5.7) in terms of the integral (5.19) read

$$\zeta = \frac{P^{BF}_{det}(\underline{\theta}^{BF}_i, \overline{\theta}^{BF}_i, 0, \pi)}{P^{DF}_{det}(\underline{\theta}^{DF}_i, \overline{\theta}^{DF}_i, 0, \pi)} \quad \text{and} \quad \eta^l = \frac{P^l_{det}(\underline{\theta}^l_i, \overline{\theta}^l_i, \theta_{obj}, \pi)}{P^l_{det}(\underline{\theta}^l_i, \overline{\theta}^l_i, 0, \pi)} . \tag{5.20}$$

The parameter values are calculated for given experimental conditions — namely, n_1, n_2 and the angular ranges — and for a given polarizability α. For NOs of optically isotropic materials, α is determined solely by the geometry of the object. In the following, explicit calculations are presented for several simple forms of α, describing the response of a large number

ix This choice is convenient because the parameters are thus made independent of the NO size (within the dipole approximation) and composition (assuming an isotropic material response), which affect the absolute value of P_{sca}, but not the resulting ratios.

of NO commonly investigated, including many plasmonic NO of simple geometry at their LSPR. Essentially, this involves deriving the explicit expression of the integral (5.19) when specific symmetries are assumed.

When $\boldsymbol{\alpha}$ has a well-defined direction with respect to the surface normal, the induced dipoles have a fixed (Θ, Φ) orientation regardless of the excitation polarization — the longitudinal LSPR of elongated NPs is a relevant example of such a system. Then $\mathcal{P}(\theta, \varphi)$ does not depend on (θ_i, φ_i), and EQ. (5.19) can be factorized into an *excitation integral* and a *detection integral*

$$L^l_{exc}(\underline{\theta}^l_i, \overline{\theta}^l_i) = \int_{\underline{\theta}^l_i}^{\overline{\theta}^l_i} d\theta_i \, \cos\theta_i \sin\theta_i \int_0^{2\pi} d\varphi_i \, p^2(\theta_i, \varphi_i) \,, \tag{5.21}$$

$$L_{det}(\underline{\theta}_d, \overline{\theta}_d) = \int_{\underline{\theta}_d}^{\overline{\theta}_d} d\theta \, \sin\theta \int_0^{2\pi} d\varphi \, \mathcal{P}(\theta, \varphi) \,. \tag{5.22}$$

L^l_{exc} describes the dipole power driven by $\mathbf{E}_{exc}$, and L_{det} is the power (in units of P_{iso}) emitted within a generic detection range Ω_d. These integrals are connected to the parameters of the same name: For $P^l_{det} = L^l_{exc} \, L_{det}$ EQ. (5.20) reduce to

$$\zeta = \frac{L_{exc}(\underline{\theta}^{BF}_i, \overline{\theta}^{BF}_i)}{L_{exc}(\underline{\theta}^{DF}_i, \overline{\theta}^{DF}_i)} \quad \text{and} \quad \eta^{BF} = \eta^{DF} = \frac{L_{det}(\theta_{obj}, \pi)}{L_{det}(0, \pi)} \tag{5.23}$$

with $L_{det}(0, \pi) = P_{tot}/P_{iso}$ given by EQ. (5.16) and EQ. (5.17).

5.3.1 *Uniaxial polarizability parallel to the interface*

Let us first consider the case of a uniaxial polarizability parallel to the interface — say along x without loss of generality: $\boldsymbol{\alpha} = \alpha \, \mathrm{diag}(1, 0, 0)$. Such $\boldsymbol{\alpha}$ describes well for instance the longitudinal LSPR of elongated NPs like *rods* lying on the substrate,

as well as the bonding mode of *dimers*, which is linearly polarized along the NP separation. As a result of the uniaxial $\boldsymbol{\alpha}$, only the x component of the field excites dipoles of amplitude

$$p(\theta_i, \varphi_i) = \varepsilon_0 \varepsilon_m |\boldsymbol{\alpha} \mathbf{E}_{exc}| = \varepsilon_0 \varepsilon_m \alpha \, |E_{2,x}|. \tag{5.24}$$

Using the expression of $E_{2,x}$ given by EQ. (3.4) and (3.9-2), the excitation integral (5.21) reads[x]

$$\begin{aligned} L^l_{exc}(\psi) \propto & \int_{\underline{\theta}^l_i}^{\bar{\theta}^l_i} d\theta_i \, \cos\theta_i \sin\theta_i \int_0^{2\pi} d\varphi_i \times \\ & \left| t_p \cos\theta_t \cos\varphi_i \cos(\psi - \varphi_i) - t_s \sin\varphi_i \sin(\psi - \varphi_i) \right|^2 \\ = & \frac{\pi}{2} \int_{\underline{\theta}^l_i}^{\bar{\theta}^l_i} d\theta_i \, \cos\theta_i \sin\theta_i \times \\ & \left\{ \left| t_p \cos\theta_t \right|^2 + \left| t_s \right|^2 + \frac{\cos 2\psi}{2} \left| t_p \cos\theta_t + t_s \right|^2 \right\} \end{aligned} \tag{5.25}$$

with an explicit dependence on the linear polarization ψ of the excitation in the condenser BFP. Note that t_p, t_s, and θ_t are all functions of θ_i, see SEC. 1.4. $\zeta(\psi)$ is computed by substituting EQ. (5.25) into EQ. (5.23).

The denominator of η^l in EQ. (5.23) is $P_{tot}/P_{iso}\big|_{\Theta=\pi/2} = p_{e,\perp}$. The detection integral (5.22) at the numerator is computed via EQ. (5.12) and (5.13) as collection occurs in medium 2

$$L_{det}(0, \alpha_{obj}) = 4 \int_0^{\alpha_{obj}} d\theta_2 \, \sin\theta_2 \int_0^{\pi/2} d\varphi \, \mathcal{P}_2(\theta_2, \varphi)\Big|_{\substack{\Theta=\pi/2 \\ \Phi=0}}. \tag{5.26}$$

The fourfold symmetry (with respect to the $x = 0$ and $y = 0$ planes) of $\mathcal{P}_2$ has been exploited to reduce the azimuth integration range to $\varphi \in [0, \pi/2]$; these symmetry considerations are

x Any constant factor (here $\varepsilon_0^2 \varepsilon_m^2 \alpha^2 E_i^2$) in front of the integral can be disregarded since ζ in EQ. (5.23) is defined as a ratio of L_{exc} with different extrema.

useful in order to reduce the time required for numerical integration. Note that the integration range of L_{det} has changed from $[\theta_{obj}, \pi]$ to $[0, \alpha_{obj}]$ because the integration now runs over θ_2 instead of θ — see FIG. 3.1b for the definition of these angles. $\eta^{BF} = \eta^{DF}$ is computed by substituting EQ. (5.26) to the numerator of EQ. (5.23).

UNPOLARIZED ILLUMINATION While η^l is independent of the excitation, $\zeta(\psi)$ has been derived assuming a linearly polarized illumination in the condenser BFP. For unpolarized illumination the p and s components of $\mathbf{E}_{exc}$ are incoherent instead, and the induced dipole moment is $p = \varepsilon_0 \varepsilon_m \alpha \left(|E_{2,p,x}| + |E_{2,p,y}|\right)$. Using the expressions (3.4) for the fields, one finds $L^l_{exc}(unp)$ is given by EQ. (5.25) without the terms containing ψ. Indeed, the reader can easily verify

$$L^l_{exc}(unp) = \frac{1}{2}\left[L^l_{exc}(\psi) + L^l_{exc}(\psi + \pi/2)\right] = L^l_{exc}(\pi/4)\,. \quad (5.27)$$

Using the definition (5.23) of ζ and EQ. (5.27) one has

$$\zeta(unp) \equiv \frac{L^{BF}_{exc}(unp)}{L^{DF}_{exc}(unp)} = \frac{L^{BF}_{exc}(\psi) + L^{BF}_{exc}(\psi + \pi/2)}{L^{DF}_{exc}(\psi) + L^{DF}_{exc}(\psi + \pi/2)}. \quad (5.28)$$

Note that in general $\zeta(unp) \neq [\zeta(\psi) + \zeta(\psi + \pi/2)]/2$. In the small NA limit $\bar{\theta}_i, \underline{\theta}_i \ll 1$ the modification of the BFP polarization introduced by the condenser is negligible, and light cross-polarized to the $\boldsymbol{\alpha}$ axis excites no dipoles: $L^l_{exc}(co) \gg L^l_{exc}(cross)$ and therefore $\zeta(unp) \to \zeta(co)$.

HOMOGENEOUS ENVIRONMENT In the special case $n = 1$ representing a homogeneous optical environment, a closed-form expression of the scattering parameters can be derived. This situation is of practical interest, as it corresponds to a NO covered by a fluid matching the refractive index of the

substrate, embedded in a solid matrix, or suspended within an optical trap. For $n = 1$ one has $t_p = t_s = 1$ and $\theta_t = \theta_i$, so that EQ. (5.25) simplifies to[xi]

$$L^l_{exc}(\psi) \propto \int_{\underline{\theta}^l_i}^{\bar{\theta}^l_i} d\theta_i \, \cos\theta_i \sin\theta_i \left\{ \cos^2\theta_i + 1 + \frac{\cos 2\psi}{2} \left(\cos\theta_i + 1 \right)^2 \right\}$$

$$= \left[\frac{\cos^4\theta_i}{4} + \frac{\cos^2\theta_i}{2} + \frac{\cos 2\psi}{2} \left(\frac{\cos^4\theta_i}{4} + 2\frac{\cos^3\theta_i}{3} + \frac{\cos^2\theta_i}{2} \right) \right]_{\bar{\theta}^l_i}^{\underline{\theta}^L_i}; \tag{5.29}$$

note that the extrema in the final expression are inverted with respect to the integral. The denominator of η^l is $P_{tot}/P_{iso}\big|_{n=1} = 1$, see FIG. 5.2. The numerator is the integral of $\mathcal{P}_2$ in a homogeneous environment, given by EQ. (5.12) for $n = 1$ and $\theta_1 = \theta_2$

$$\begin{aligned} \eta^l &= L_{det}(0, \alpha_{obj}) \\ &= \int_0^{\alpha_{obj}} d\theta_2 \, \sin\theta_2 \int_0^{2\pi} d\varphi \, \frac{3}{8\pi} \left\{ \cos^2\theta_2 \cos^2\varphi + \sin^2\varphi \right\} \\ &= \frac{1}{8} \left(4 - 3\cos\alpha_{obj} - \cos^3\alpha_{obj} \right). \end{aligned} \tag{5.30}$$

5.3.2 *Uniaxial polarizability perpendicular to the interface*

$\boldsymbol{\alpha} = \alpha \, \mathrm{diag}(0, 0, 1)$ describes well for instance the longitudinal mode of (short) *pillars* or *cones* standing on a substrate. Reasoning along the same lines as in SEC. 5.3.1, one has $p = \varepsilon_0 \varepsilon_m \alpha |E_{2,z}|$ and the excitation integral reads

$$L^l_{exc} \propto \pi \int_{\underline{\theta}^l_i}^{\bar{\theta}^l_i} \cos\theta_i \sin\theta_i \left| t_p \sin\theta_t \right|^2 d\theta_i \tag{5.31}$$

[xi] Analytical integration in this chapter is performed using $\int \cos^n x \sin x \, dx = -\frac{\cos^{n+1} x}{n+1}$ and $\int \cos x \sin^n x \, dx = \frac{\sin^{n+1} x}{n+1}$.

where we have exploited the axial symmetry with respect to $\hat{z}$ integrating over φ_i. Similarly, the detection integral is

$$L_{det}(0, \alpha_{obj}) = 2\pi \int_0^{\alpha_{obj}} \mathcal{P}_{2,p}(\theta_2, \varphi)\Big|_{\Theta=0} \sin\theta_2 \, d\theta_2 \tag{5.32}$$

as $\mathcal{P}_{2,s} \propto \sin^2\Theta$ vanishes for $\Theta = 0$ along with the φ dependence of $\mathcal{P}_{2,p}$, see EQ. (5.12) and (5.13). ζ and η^l are computed by substituting the integrals (5.31) and (5.32) into EQ. (5.23), while the denominator of η^l is $P_{tot}/P_{iso}\big|_{\Theta=0} = p_{e,\parallel}$.

For axially-symmetric modes like the ones considered in this and the next two sections, the powers in the definition (5.7) of the scattering parameters do not depend on ψ. Therefore, ζ and η^l are the same for every exciting polarization as well as for unpolarized illumination. Indeed, the latter case is computed by averaging any two orthogonal polarization directions as done in EQ. (5.27).

HOMOGENEOUS ENVIRONMENT With considerations analogous to SEC. 5.3.1, the integrals (5.31) and (5.32) simplify to

$$L_{exc}^l \propto \int_{\underline{\theta}_i^l}^{\bar{\theta}_i^l} \cos\theta_i \sin^3\theta_i \, d\theta_i = \frac{\sin^4\theta_i}{4}\Big|_{\underline{\theta}_i^l}^{\bar{\theta}_i^l}, \tag{5.33}$$

$$\begin{aligned} \eta^l =& L_{det}(0, \alpha_{obj}) = \int_0^{\alpha_{obj}} d\theta_2 \, \sin\theta_2 \int_0^{2\pi} d\varphi \, \frac{3}{8\pi} \sin^2\theta_2 \\ =& \frac{1}{4}\left(2 - 3\cos\alpha_{obj} + \cos^3\alpha_{obj}\right). \end{aligned} \tag{5.34}$$

5.3.3 *Isotropic planar polarizability parallel to the interface*

The plasmonic resonance of a thin *disc* lying on the substrate, or the transverse mode of a *rod* standing on it, is described well

by $\boldsymbol{\alpha} = \alpha\,\mathrm{diag}(1,1,0)$. One then has $p = \varepsilon_0\varepsilon_m\alpha\sqrt{|E_{2,x}|^2 + |E_{2,y}|^2}$ and ζ is computed using

$$L^l_{exc} \propto 2\pi \int_{\underline{\theta}^l_i}^{\bar{\theta}^l_i} d\theta_i \, \cos\theta_i \sin\theta_i \left\{ \left|t_p \cos\theta_t\right|^2 + \left|t_s\right|^2 \right\}. \qquad (5.35)$$

Not surprisingly, this result differs only by a proportionality factor from $L_{exc}(unp)$ calculated for $\boldsymbol{\alpha} = \alpha\,\mathrm{diag}(1,0,0)$, which is given by EQ. (5.25) without the polarization-dependent term. η^l on the other hand is the same found for $\boldsymbol{\alpha} = \alpha\,\mathrm{diag}(1,0,0)$: In fact, for $\Theta = \pi/2$ the azimuthal orientation of the dipole is irrelevant because of the axial symmetry of the collection.

HOMOGENEOUS ENVIRONMENT In accordance with the considerations just made for the general case, ζ is calculated using EQ. (5.29) without the polarization-dependent term and η^l is given by EQ. (5.30).

5.3.4 *Isotropic polarizability*

The isotropic optical response of a sphere is described by a scalar polarizability α. This case is inherently more complicated than the previous ones, inasmuch as the orientation of the dipoles is not fixed: $\mathbf{p} = \varepsilon_0\varepsilon_m\alpha\mathbf{E}_2(\theta_i, \varphi_i)$. As a consequence, $\mathcal{P}(\theta, \varphi)$ depends on (θ_i, φ_i) via (Θ, Φ), and the integral (5.19) cannot be separated into an excitation and a collection term. As discussed above, when $\hat{\boldsymbol{z}}$ is an axis of symmetry of the object, ζ and η^l do not depend on the exciting polarization: Calculations in this case are simplified by assuming unpolarized illumination. Once the symmetry breaking introduced by a linear polarization is removed, the excitation has axial symmetry too, and therefore we can limit ourselves to consider a single plane of incidence.

Choosing then $\varphi_i = 0$ without loss of generality, $\mathbf{E}_{exc} = \mathbf{E}_2$ given by EQ. (3.4) reduces to[xii]

$$\mathbf{E}_{2,p}(\theta_i, 0) = t_p \frac{E_i}{\sqrt{2}} \begin{bmatrix} \cos\theta_t \\ 0 \\ -\sin\theta_t \end{bmatrix} e^{ik_t \cdot r}, \tag{5.36p}$$

$$\mathbf{E}_{2,s}(\theta_i, 0) = t_s \frac{E_i}{\sqrt{2}} \begin{bmatrix} 0 \\ 1 \\ 0 \end{bmatrix} e^{ik_t \cdot r}. \tag{5.36s}$$

The p and s field components excite dipoles of amplitude

$$p_p = \varepsilon_0 \varepsilon_m \alpha E_{2,p} \propto |t_p| \quad \text{and} \quad p_s = \varepsilon_0 \varepsilon_m \alpha E_{2,s} \propto |t_s|. \tag{5.37}$$

For unpolarized illumination $\mathbf{E}_{2,p}$ and $\mathbf{E}_{2,s}$ are incoherent and the integrand in EQ. (5.19) (i.e. P_{tot}) is then the sum of the powers radiated by the p- and s-polarized dipoles

$$P^l_{det} \propto 2 \int_{\underline{\theta}^l_i}^{\bar{\theta}^l_i} d\theta_i \cos\theta_i \sin\theta_i \int_{\underline{\theta}_d}^{\bar{\theta}_d} d\theta \sin\theta \int_0^{\pi} d\varphi \times \left\{ |t_p|^2 \mathcal{P}(\theta, \varphi)\Big|_{\substack{\Theta=\pi/2-\mathrm{Re}(\theta_t) \\ \Phi=0}} + |t_s|^2 \mathcal{P}(\theta, \varphi)\Big|_{\substack{\Theta=\pi/2 \\ \Phi=\pi/2}} \right\}. \tag{5.38}$$

where $\mathcal{P}(\theta, \varphi)$ has only a twofold symmetry with respect to φ because $\mathbf{p}_p$ is not parallel to the interface. The real part appearing in the definition of Θ for the p dipole (hence Θ_p) fixes $\mathbf{p}_p \parallel \hat{z}$ for $\theta_i \geqslant \theta_{1,c}$, where only the imaginary part of θ_t varies; we will discuss soon the reasons and the effects of this approximation. Eventually, ζ and η^l are computed by substituting EQ. (5.38)

xii We emphasize that for unpolarized illumination $\mathbf{E}_{2,p}$ and $\mathbf{E}_{2,s}$ are incoherent, and therefore $\mathbf{E}_2$ is not their sum; EQ. (3.9) on the other hand specifically refers to linearly polarized illumination.

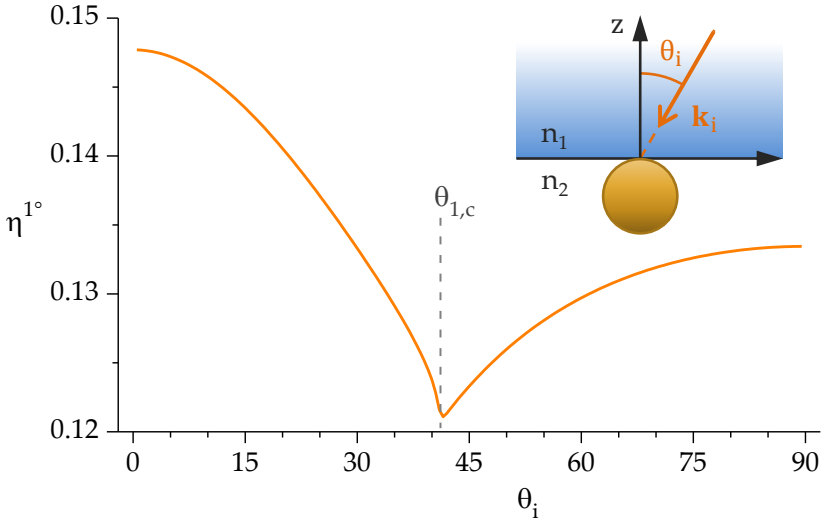

FIGURE 5.3: Fraction η^{1° of scattering collected by the objective (NA = 0.95) with a polar range of incidence $\theta_i \pm 0.5^\circ$. The scatterer is a small sphere in air ($n_2 = 1.00$) placed onto a glass substrate ($n_1 = 1.52$). The critical angle $\theta_{1,c} = 41.1^\circ$ is indicated.

into EQ. (5.20). Note that the explicit expressions (5.12)–(5.13) of $\mathcal{P}$ have to be evaluated only for the denominator of η^l; all other powers in EQ. (5.20) are integrals over $\Omega = 4\pi$ and can be simplified using EQ. (5.14).

So, to recap, the scattering pattern $\mathcal{P}_{NO}$ of a sphere (unlike all other previous cases) depends on the illumination. This is illustrated by FIG. 5.3, where the detection parameter is computed using a 1° wide illumination cone. A discontinuity[xiii] of $\eta^{1^\circ}(\theta_i)$ at $\theta_i = \theta_{1,c}$ separates two regimes:

- For $\theta_i < \theta_{1,c}$ one has $\Theta_p = \pi/2 - \theta_t$; as the p dipole progressively aligns to $-\hat{z}$ (where the objective is placed) less scattering is collected, see FIG. 5.1.

xiii Due to the finite (1°) width of the illumination cone, the plot displays in fact two discontinuities, occurring slightly above and below $\theta_{1,c}$ respectively.

- For $\theta_i \geqslant \theta_{1,c}$ one has $\Theta_p = 0$; having both p and s dipoles a fixed orientation, the trend is ruled by their relative amplitudes. Specifically, FIG. 1.8b shows that $|t_p|$ decreases more rapidly than $|t_s|$, and therefore the relative contribution to P_{obj} of the s dipole (which is favourably oriented with respect to the collection) increases with θ_i.

POLARIZATION IN THE TIR REGIME A peculiar property of the evanescent wave is the elliptical polarization of its p component: In the plane of incidence (say $\varphi = 0$) the last of EQ. (3.2p) becomes

$$\widehat{\mathbf{E}}_{t,p} = \widehat{\boldsymbol{\theta}}(\theta_t) = \begin{bmatrix} \cos\theta_t \\ 0 \\ -\sin\theta_t \end{bmatrix} = \begin{bmatrix} i\sqrt{\epsilon^{-2}-1} \\ 0 \\ -\epsilon^{-1} \end{bmatrix} \quad \text{with} \quad \frac{1}{\epsilon} = \frac{n_1}{n_2}\sin\theta_i. \tag{5.39}$$

According to EQ. (5.39), $\widehat{\mathbf{E}}_{t,p}$ describes an ellipse with its major axis along $\widehat{z}$ and eccentricity $\sqrt{1-(\widehat{\mathbf{p}}_t)_x^2/(\widehat{\mathbf{p}}_t)_z^2} = \epsilon$. In general $1 \geqslant \epsilon \geqslant n_2/n_1$ for $\theta_c \leqslant \theta_i \leqslant \pi/2$. At $\theta_i = \theta_c$ the ellipse degenerates into a line ($\epsilon = 1$) perpendicular to the interface, while ϵ decreases for larger values of θ_i up to grazing incidence, where the polarization is quasi-spherical ($\epsilon \ll 1$) for highly mismatched interfaces ($n_1 \gg n_2$).

In EQ. (5.38) we have set $\mathbf{p}_p \parallel \widehat{z}$ in the TIR regime, thereby neglecting the elliptic polarization of the exciting evanescent wave. This approximation cannot easily be avoided since the analytical expressions of $\mathcal{P}(\theta,\varphi)$ presented in SEC. 5.2 specifically refer to a dipole oscillating along a given direction. Nevertheless, the effect on the calculated scattering parameters is expected to be $\sim 1\,\%$ or smaller. Let us now make an estimate of the resulting error on η^l. The worst-case scenario where the largest error is committed occurs for a quasi-circular polarization at near-grazing incidence, which induces both x and z

polarization components at the NO position. The corresponding value of η^l falls therefore between $\eta^l|_{\theta_i=0}$ (where $\mathbf{p}_p \parallel \hat{\mathbf{x}}$) and $\eta^l|_{\theta_i=90°}$ (where $\mathbf{p}_p \parallel \hat{\mathbf{z}}$) in FIG. 5.3:[xiv] η^l for large θ_i is thereby underestimated by a few % as a result of our approximation. However, such large θ_i values have little weight in the angular average of EQ. (5.38) as they are hardly accessed in practice,[xv] and their contribution is anyway quenched by a lower $|t_p|$ as well as by the aplanatic $\cos\theta_i$ factor. Furthermore, the glass/water and glass/air interfaces used in most microscopy experiments are only moderately mismatched, resulting in rather large ϵ values.

HOMOGENEOUS ENVIRONMENT For $n = 1$ and $(\underline{\theta}_d, \overline{\theta}_d) = (0, \pi)$ both terms in EQ. (5.38) reduce to $P_{tot}/P_{iso} = 1$ and so

$$P^l_{sca} \propto 2\int_{\underline{\theta}^l_i}^{\overline{\theta}^l_i} \cos\theta_i \sin\theta_i \, d\theta_i = \sin^2\theta_i\Big|_{\underline{\theta}^l_i}^{\overline{\theta}^l_i}. \tag{5.40}$$

Comparing this result with EQ. (5.9) one finds $\zeta = \xi$. In fact, for an isotropic optical response — i. e. once the θ_i dependence introduced by the interface is removed — every $\mathbf{k}_i$ yields the same amount of scattering. In other words, $P_{sca} \propto P_{exc}$ with a proportionality constant independent from θ_i, so that the definitions (5.7) of ξ and ζ coincide.

xiv Note that both for $\theta_i = 0$ and $\theta_i = 90°$ one has $|t_p| = |t_s|$ (see FIG. 1.8a) implying $p_p = p_s$, and thus comparing the values of η^l at the two extremes of the θ_i range is legitimate. However, in this qualitative argument we are neglecting any effect of coherence between the x and z components of the polarization induced by the circular excitation.

xv Typical values in our experiments are $\overline{NA}_i^{BF} = 0.95$ and $\overline{NA}_i^{DF} = 1.2$, corresponding respectively to $\overline{\theta}_i^{BF} = 37°$ and $\overline{\theta}_i^{DF} = 52°$ for a glass/air interface.

For $n = 1$ and $(\underline{\theta}_d, \overline{\theta}_d) = (\theta_{obj}, \pi)$ EQ. (5.38) reduces to

$$P^l_{obj} \propto \int_{\underline{\theta}^l_i}^{\overline{\theta}^l_i} d\theta_i \, \cos\theta_i \sin\theta_i \int_0^{\alpha_{obj}} d\theta_2 \, \sin\theta_2 \times \frac{3}{8}\left\{3 + 3\cos^2\theta_i \cos^2\theta_2 - \cos^2\theta_i - \cos^2\theta_2\right\}. \tag{5.41}$$

EQ. (5.40) and EQ. (5.41) are respectively the denominator and the numerator of η^l; after some algebraic simplifications[xvi]

$$\eta^l \equiv \frac{P_{obj}}{P_{sca}} = \frac{1}{16}\left\{\left(8 - 9\cos\alpha_{obj} + \cos^3\alpha_{obj}\right) + \frac{3}{2}\left[\cos\overline{\theta}_i + \cos\underline{\theta}_i\right]\left(\cos\alpha_{obj} - \cos^3\alpha_{obj}\right)\right\}. \tag{5.42}$$

In the small NA limit $\overline{\theta}_i, \underline{\theta}_i \ll 1$, EQ. (5.42) simplifies to the expression (5.30) found for $\boldsymbol{\alpha} = \alpha\,\mathrm{diag}(1,0,0)$, as expected.

5.3.5 *Numerical computation of the scattering parameters*

RESULTS – MATLAB The expressions of the scattering parameters derived above have been implemented into the MATLAB code A.2 in order to perform numerical integration. The required user inputs are n_1, n_2, NA_{obj}, $\underline{NA}^{BF}_i$, $\overline{NA}^{BF}_i$, $\underline{NA}^{DF}_i$, and $\overline{NA}^{DF}_i$. FIG. 5.3 and FIG. 5.4 exemplify the results obtained with our typical experimental settings. In particular, the latter figure addresses the dependence of the scattering parameters on the environment n_2 surrounding a NO placed on a glass substrate. We observe that η^l increases with n_2, because the majority of the scattering goes towards the denser medium, see FIG. 5.1. While the trend is the same for all forms of $\boldsymbol{\alpha}$, the slope is steeper for $\mathbf{p} \parallel \hat{\boldsymbol{z}}$, whose radiation pattern is the most affected by the

[xvi] Payne[118] (§4.2.2) derived a similar expression of η^l for a sphere in a homogeneous medium, albeit not including the aplanatic cosine factor.

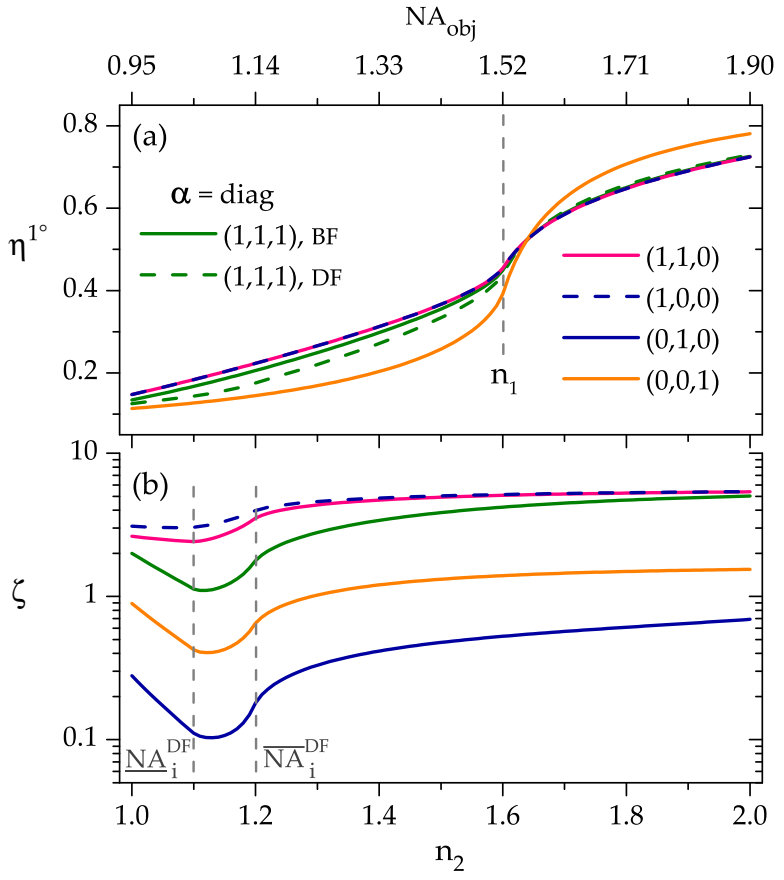

FIGURE 5.4: (a) detection parameter η^{l} and (b) excitation parameter ζ as functions of the refractive index n_2. The NO is placed at the interface in medium 2 and has polarizability α according to the legend in (a). Illumination comes from medium 1 ($n_1 = 1.52$) and is $\hat{x}$-polarized in the condenser BFP. Our typical experimental settings have been used for the illumination: $\underline{NA}_i^{BF} = 0$, $\overline{NA}_i^{BF} = 0.95$, $\underline{NA}_i^{DF} = 1.1$, $\underline{NA}_i^{DF} = 1.2$. To ease the interpretation, the angular range of collection $\alpha_{obj} \simeq 72°$ in medium 2 (corresponding to $NA_{obj} = 0.95$ in air) has been kept fixed, resulting in a collection NA proportional to n_2.

interface and presents the sharpest features, see FIG. 5.1b. A point of inflection occurs at $\mathrm{NA}_{obj} = n_1$ — corresponding to the condition $\alpha_{obj} = \theta_{2,c}$ — above which the peaked features of the scattering patterns enter Ω_{obj}. As discussed above for each specific case, η^l is independent of the illumination for all forms of $\boldsymbol{\alpha}$ considered except the isotropic one, for which η^{BF} and η^{DF} slightly differ.

The dependence of ζ on n_2 shown in FIG. 5.4b is ruled by the relative intensity of BF and DF illumination. Consequently, ζ is minimized for close-to-critical DF incidence, corresponding to the largest $|t_p|$ and $|t_s|$ values, see FIG. 1.8b. In fact, the highlighted interval $\underline{\mathrm{NA}}_i^{DF} < n_2 < \overline{\mathrm{NA}}_i^{DF}$ corresponds to $\underline{\theta}_i^{DF} < \theta_{1,c} < \overline{\theta}_i^{DF}$. Overall, in comparison with η^l, ζ depends more on $\boldsymbol{\alpha}$, the two extreme cases occurring for $\mathbf{p} \perp \boldsymbol{z}$ either co- or cross-polarized to $\mathbf{E}_{BFP}$. This happens because the uniaxial $\boldsymbol{\alpha}$ is the most sensitive to the different polarization content of BF and DF illumination. For instance, in FIG. 5.4 we used a DF range containing higher θ_i values with respect to BF, and hence a larger component cross-polarized to $\mathbf{E}_{BFP}$. A cross-polarized $\boldsymbol{\alpha}$ selectively picks it up, resulting in the lowest value of ζ achievable with the given illumination ranges.

OUTLOOK – COMSOL Let us summarize the main assumptions we made on the NO and its environment in order to compute the scattering parameters:[xvii]

1. The dipole approximation holds ($D \ll \lambda$).
2. The NO is a weak scatterer, or the interface is a weak reflector.

xvii The quantitative OCS formulas (5.6) are independent of these assumptions.

n_2	NA_{obj}	η^l analytical	$\eta^{(0)}$ numerical
1.52	1.45	0.384	0.386
1.00	0.95	0.148	0.184

TABLE 5.1: Fraction $\eta^{(0)}$ of the scattered power collected by a 0.95 NA microscope objective. The geometry is the one represented in FIG. 3.1 with $n_1 = 1.52$. The analytical results are obtained using EQ. (5.23) and EQ. (5.26) corresponding to a uniaxial polarizability. The numerical results are obtained using EQ. (4.9) and EQ. (4.10) for a rod lying on the substrate under normal ($\theta_i = 0$), co-polarized plane wave excitation; all the simulation parameters are given in SEC. 4.2.

3. The NO–interface separation is neglected ($z_{NO} = 0$); this approximation, however, is not inescapable since the expression of $\mathcal{P}$ with a generic z_{NO} is known.[32]
4. We considered only a few, simple forms of $\boldsymbol{\alpha}$; nonetheless, at least in principle, the scattering parameters can be computed via EQ. (5.19) for a generic $\boldsymbol{\alpha}$.

All limitations listed above can be overcome by simulating numerically the scattering process, e. g. using COMSOL and the techniques discussed in CH. 4. In practice, this permits to compute the scattering parameters for large objects ($D \sim \lambda$) having arbitrary shapes. Moreover, a complex NO environment can be simulated, including birefringent or chiral dielectrics, or multiple interfaces corresponding to NOs placed on thin films; a finite value of z_{NO} can be accounted for too.

For example, in the numerical model of scattering described in SEC. 4.2, P^l_{sca} and P^l_{obj} are computed respectively via EQ. (4.9) and EQ. (4.10). The θ_i range of BF and DF illumination can be reproduced with the equivalent p-polarized wave method described in SEC. 3.1.3 or — should it not prove accurate enough

—with the averaging formulas presented in SEC. 3.1.2. As a preliminary test, we used the numerical model to calculate $\eta^{(0)}$ for a rod lying on the substrate under normal co-polarized excitation. The results presented in TAB. 5.1 confirm the validity of our analytical calculations, inasmuch as an excellent agreement is found for a homogeneous environment. The discrepancy observed when an interface is introduced can be ascribed to the analytical calculations, as resulting from the omission of the nonzero "effective distance" separating the NO from the interface; or to the numerical model, as stemming from the failure of the near-to-far-field transform built in COMSOL in a non-homogeneous environment, see discussion on P. 99. We are planning further investigations into these matters.

Incidentally, another application of the numerical approach can be envisaged for coherent excitation, modelled e. g. as in SEC. 3.2.2. For instance, relying on a realistic implementation of the experimental excitation, one could compute P_{obj}/P_{sca} and P_{abs}/P_{sca} for a representative NO, and then be able to measure σ_{abs} and σ_{sca} in absolute units with quantitative extinction techniques such as the SMS introduced in SEC. 2.2.1.

6

EXPERIMENTAL SET-UP AND RESULTS

Looking back at the review we made in SEC. 2.2 of the main techniques capable of investigating the optical properties of individual NOs, one realizes that only a handful of them can provide accurate information on the amplitude of the OCS, in particular σ_{sca} being rather elusive. Specifically, conventional SMS provides absolute values of σ_{ext} so long as the amount of scattering collected is negligible.[73] Techniques based on the photothermal effect such as the QWLSI can estimate σ_{abs} via analytical models of the heating process.[77] Finally, none of the imaging modalities addressing σ_{sca} (such as DF microscopy or iSCAT) is easily made quantitative. In fact, to date solely the SMS version featuring a common path interferometer[74] provides a full quantitative characterization of the OCS.

However, the aforementioned raster-scanning, modulation-based techniques involve rather expensive optical and electronic equipment, including lasers, lock-in amplifiers, modulation elements, etc. Not only the experimental set-ups are difficult to operate; the analyses whereby the absolute OCS values are obtained demand a considerable degree of expertise too, inasmuch as calibrations specific to each experiment are required. For instance, in SMS one has to characterize the PSF of the exciting beam,[73] and for QWLSI the temperature profile around the absorber must be modelled.[77] For these reasons, the actual usage of these techniques has been limited so far to research groups with a well-established expertise on complex optical set-ups, whereas the majority of NO research still relies on more straightforward DF micro-spectroscopy studies.

In fact, the simplicity of a broadband widefield BF/DF set-up is unparalleled by other techniques: One only needs a commercial microscope equipped with a broadband lamp and a camera. As a widefield imaging technique, high-throughput characterization is possible via automated image analysis. By replacing the camera with a spectrometer, an extinction (in BF) or, more commonly, scattering (in DF) spectrum can be acquired at once[i] rather than pointwise by sweeping the wavelength of a monochromatic source. On the other hand, broadband widefield microscopy typically has two major shortcomings: (i) results are not quantitative; and (ii) it is limited to relatively large NOs. Nonetheless, in this chapter, it will be shown that: (*i*) the OCS can be measured in absolute units relying on the theoretical description developed in CH. 5; and (*ii*) with proper care, a sensitivity comparable to laser-based techniques can be achieved.

6.1 OUR OPTICAL MICROSCOPE

All measurements presented in this work have been performed with a commercial inverted[ii] microscope (Nikon, Eclipse Ti-U) with several home-built features added. In this section the instrument is described following the light path from the source. FIG. 6.1 is the optical diagram (not to scale) of our experimental set-up for spectroscopy and imaging.

Incoherent broadband illumination is provided by a 12 V, 100 W tungsten-halogen lamp (Philips, 77241) of adjustable power. Its emission spectrum is well described as blackbody radiation of temperature $T \simeq 2100\,K$ for $P = 30\,W$ and $T \simeq 2800\,K$ for $P = 100\,W$.[118] According to Wien's law, the emission peak

i Simultaneous spectral acquisition is also possible in a broadband SMS implementation described by Billaud et al.[73]

ii Meaning illumination comes from above the sample and collection occurs below it, as represented in FIG. 2.6a and FIG. 3.1.

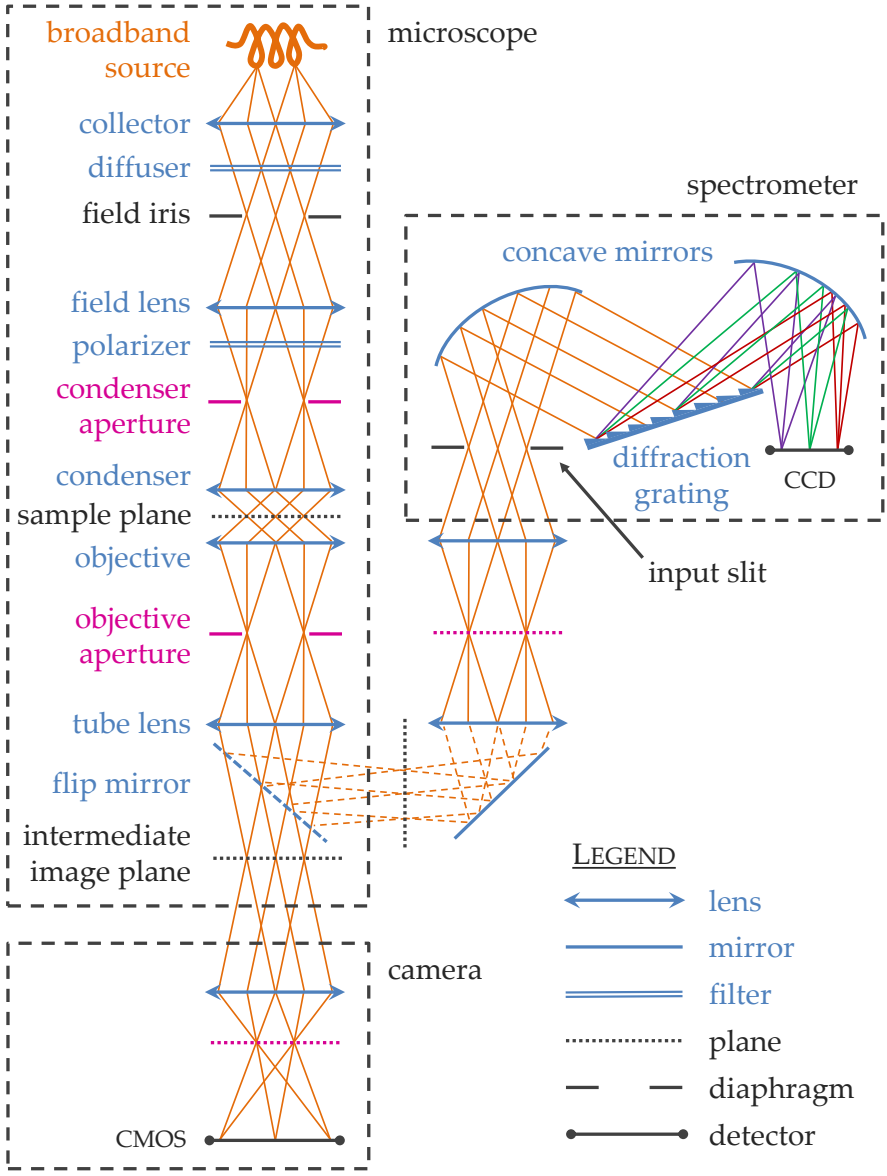

FIGURE 6.1: A simplified ray diagram of our micro-spectroscopy set-up. Black and magenta indicate the field and the aperture plane sets.

occurs at approximately 1.4 µm and 1.0 µm, respectively. This means most light is emitted in the near IR, with only a tail falling in the VIS range and no illumination below 400 nm for practical purposes. Still within the bulb housing, a collimated beam is created by a collector lens and undesired IR radiation is absorbed by a heat filter. Fluctuations of intensity ~ 1 % due to thermal drift occur on the time scale of 10 s.

Alternatively, a 4-wavelength source (Thorlabs, LED4D067) provides intense illumination combining the output of four LEDs. Our source includes the following LEDs (nominal average emission wavelength $\langle\lambda\rangle$/FWHM, both in nm): 405/13, 455/18, 530/33, 625/18; these can be independently switched on and their power increased up to 1 W. However, for some LEDs, a sizeable drift of $\langle\lambda\rangle$ with power was observed, with deviations up to 30 nm from the nominal value.

The illumination is focused on the sample by a 1.34 NA oil-immersion condenser (Nikon, T-C-HNAO) of front focal length $f_{con} = 10.5$ mm and working distance 1.95 mm. DF illumination is achieved as in FIG. 2.6a; to serve as light stops a set of discs was cut out of anodized (i. e. black) aluminium foil with sizes suiting different objectives, namely having $NA_{obj} < \underline{NA}_{DF}$. The selected DF disc is inserted in the condenser BFP (condenser aperture plane in FIG. 6.1) via a slider, which allows switching from BF to DF without the need to move the condenser nor the sample. Such a dual BF/DF functionality is essential for our quantitative protocol, but comes with some drawbacks too.

Particularly, BF and DF illumination, corresponding to small and large NAs respectively, are focused on different planes because of spherical aberration.[iii] Since Köhler illumination is adjusted in BF, spherical aberration brings about in first place a

iii Refocusing the condenser every time the illumination is switched from BF to DF is possible in principle but cumbersome in practice: For our quantitative method it should be done quickly and in a reproducible manner.

slight defocusing of DF illumination, meaning that in experiments ξ is larger than its theoretical value (5.9). Secondly, all analytical calculations presented in this work, assume the condenser is an aplanatic optical system — that is, free of spherical aberration. We have characterized the spherical aberration of the condenser, see FIG. B.1b and discussion in SEC. B.1. The aberration is larger at high NA, and thus for quantitative measurements we cropped the illumination down to $\overline{\mathrm{NA}}_{\mathrm{DF}} = 1.2$ in order to reduce the aforementioned issues.

The *field diaphragm* is an iris placed in a field plane[iv] before the condenser, so that it is visible on the sample plane and thereby defines the illuminated area. In fact, Köhler illumination is established by putting the field diaphragm in sharp focus, so that the image of the light source — which lies in an aperture plane — is completely defocused at the sample. As a general rule, the illuminated region should match or be smaller than the field of view in order to minimize stray light and diffuse scattering background. Nonetheless, because of the spherical aberration of the condenser the iris is slightly out of focus in DF, and therefore must be open enough to produce a homogeneous illumination over the imaged region free of shadowing effects.[v] Given a $\overline{\mathrm{NA}}_{\mathrm{DF}} = 1.2$ illumination, an opening yielding an illuminated region 0.5 mm across was found to be suitable in our set-up. We also emphasize that the field diaphragm opening must stay unchanged between BF and DF measurements (on

iv In modern microscopes, there are two notable sets of conjugate planes, which constitute a Fourier transform pair: The *field set*, conjugated to the sample plane and containing the corresponding spatial information (i. e. the sample image), and the *aperture set*, conjugated to the source and containing the directional information at the sample plane. In FIG. 6.1 the two sets are denoted in black an red, respectively.

v This is essential for our quantitative method: The measured BF illumination is used for referencing the OCS, and the DF intensity is inferred via ξ, which only accounts for variations of the NA_{i} range between BF and DF.

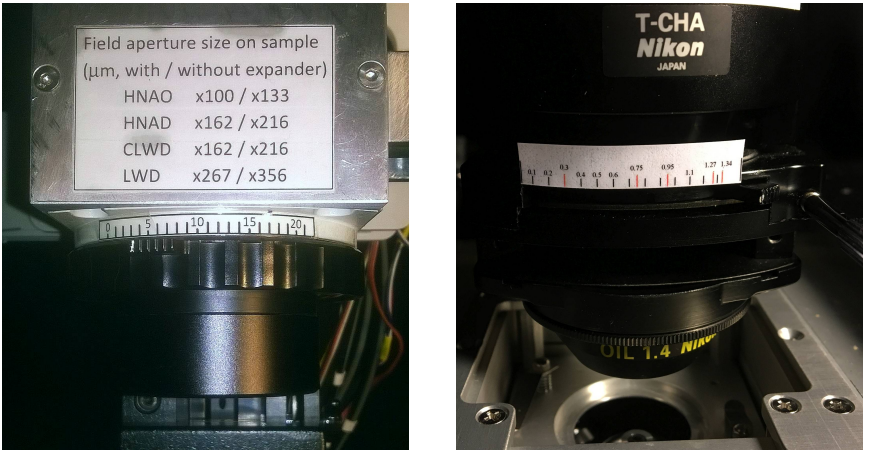

FIGURE 6.2: Home-built calibrated rulers: (Left) ruler for the field diaphragm, the reading is the lateral size of the illuminated region of the sample (different scaling factors to be use for different condensers).; (Right) ruler for the aperture diaphragm, the reading is $\overline{\text{NA}}_\text{i}$.

the same NO) not to alter the illumination intensity, which is proportional to the aperture area. In order to have reproducible illumination conditions, we fabricated a calibrated ruler for the field diaphragm, shown in the left panel of FIG. 6.2. To calibrate it, the iris size on the sample was measured straightforwardly from an image knowing the magnification of the optics and the physical pixel pitch of the imaging device.

$\overline{\text{NA}}_\text{i}$, the maximum illumination NA, is defined by the *aperture diaphragm*, an iris placed in an aperture plane before the condenser. For our quantitative method $\overline{\text{NA}}_\text{i}$ must be known and reproducible, and thus the aperture diaphragm must be calibrated too when a reading is not provided by the manufacturer. Now, when looking at the aperture set of planes[vi] the closing iris will enter the field of view when $\overline{\text{NA}}_\text{i} = \text{NA}_\text{obj}$. Using a set

vi For instance by removing one eyepiece; this is often referred to as *conoscopic* mode, in opposition to the usual *orthoscopic* imaging modality.

of objectives having a wide range of $\mathrm{NA}_{\mathrm{obj}}$, and interpolating the measured $\overline{\mathrm{NA}_{\mathrm{i}}}$ values, one can construct a calibration curve, and hence a ruler for the condenser aperture such as the one in the right panel of FIG. 6.2.[vii]

The analytical model of incoherent microscope illumination developed in SEC. 3.1 assumes a homogeneous electric field amplitude $|\mathbf{E}_{\mathrm{BFP}}|$ over the BFP of the condenser lens. This is achieved experimentally by inserting in the illumination path a *top hat* engineered diffuser (Thorlabs, ED1-C20), whose angular distribution of transmitted intensity has an approximately flat central region, see FIG. B.2 and related discussion in SEC. B.1. The lateral profile of the illumination power has been measured by scanning a photodiode (Thorlabs, power meter PM100 + Si sensor S120B) across the BFP, with a pierced dark mask over the sensitive area to increase the spatial resolution. The power profiles obtained with a standard ground glass diffuser (accessory of the Ti-U microscope) and the top-hat diffuser are shown in FIG. 6.3.

The standard diffuser is expected to yield a Gaussian angular distribution, and delivers indeed the highest intensity in the centre of the BFP, corresponding to low illumination NAs. Moreover, the orientation of the filament (which is visible once the diffuser is removed) is not completely obliterated. In summary, using the standard diffuser $|\mathbf{E}_{\mathrm{BFP}}|$ is a function of both ρ and φ. Conversely, the top-hat diffuser produces a rather constant $|\mathbf{E}_{\mathrm{BFP}}|$ over the BFP up to the edges of the aperture, albeit at the expense of squandering a greater share of power outside the optical path: A 4.3 transmitted power ratio (integrated over the whole aperture and averaged over the two orientations) between the two diffusers is measured in FIG. 6.3. Now, the barrel at the bottom of FIG. 6.2 (left) is a 4/3 beam expander

vii This calibration has been performed by L. Payne.

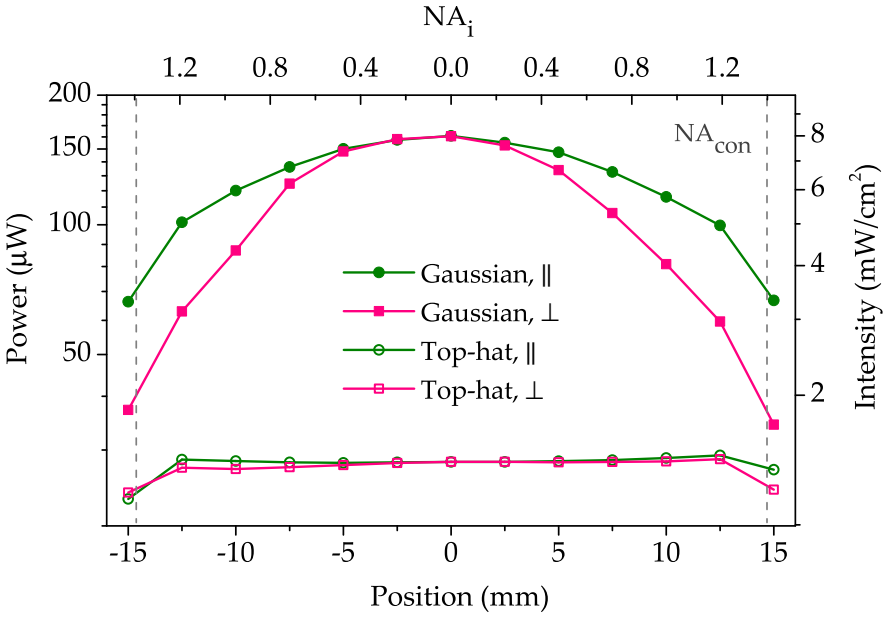

FIGURE 6.3: Spatial profiles of the illumination power in the BFP of the condenser when using a ground glass diffuser (solid symbols) or a top-hat diffuser (hollow symbols). The ⊥ and ∥ symbols in the legend refer to the orientation with respect to the image of the filament. Measurements were performed with 12 W illumination power, a 630 µm field of view on the sample, and no additional filters in the illumination path. Power and intensity are proportional via the area of the pinhole in the diode mask (see text) estimated as $\pi(0.8\,\mathrm{mm})^2$. NA_i (top axis) is the aplanatic NA derived from the bottom axis via Abbe's sine condition $\rho_i = f_{con} NA_i$; the real NA therefore differs slightly at high NAs because of spherical aberration. Vertical dashed lines at NA_i indicate the edges of the condenser back aperture.

— in fact, a Galilean telescope — used to magnify the filament image to fill the back aperture of the T-C-HNAO condenser. The wider angular spread of the top-hat diffuser renders the expander superfluous; upon its removal the transmitted power is increased by a factor $(4/3)^2$ with respect to FIG. 6.3 while still producing a flat enough intensity profile (approx. 10 % drop from centre to edges for $\perp$ profile).

A wire-grid reflective polarizer (MeCan, WGF™) can be inserted in the illumination path. The film (supported on plexiglass) is mounted on a rotatable servo polarizer to endow $\mathbf{E}_{\text{BFP}}$ with a linear polarization of choice. The polarizing performance of the polarizer film is reported in FIG. B.3 and related discussion.

The sample is mounted on a piezoelectric stage (Mad City Labs, nano-LP200), permitting 3D positioning with nanometric accuracy (0.4 nm nominal resolution).

Light is collected using a 40x, 0.95 NA dry objective (Nikon, CFI Plan Apochromat λ Series), corresponding to a $\alpha_{\text{obj}} = 72°$ acceptance in air. Unless differently specified, the illumination ranges we used in conjunction with this objective are $\text{NA}_{\text{BF}} \in [0, 0.95]$ and $\text{NA}_{\text{DF}} \in [1.1, 1.2]$; the corresponding angular ranges in oil are $\theta_{\text{BF}} \in [0, 38°]$ and $\theta_{\text{DF}} \in [46°, 52°]$. The microscope adopts an infinity-corrected design, where the intermediate image is created by a *tube lens*. A 1.5x tube lens has been used, resulting in an intermediate image magnified by a factor $M_{\text{int}} = M_{\text{obj}} \times M_{\text{tube}} = 60$.

6.2 ABSORPTION AND SCATTERING MICRO-SPECTROSCOPY

EQ. (5.6) express the OCS in terms of detected signals, with no prescription on a specific experimental technique to be used. In this section, we describe the acquisition of the detected signals using a micro-spectroscopy set-up, and test the accuracy of our

quantitative analysis on two model systems. As discussed in SEC. 2.2.2, DF micro-spectroscopy is a widespread technique for spectral characterization of NOs; current users need only small modifications — if any — and a few one-off calibrations to obtain quantitative results with a standard set-up.

INSTRUMENTATION AND PROCEDURE The microscope described in SEC. 6.1 is optically coupled[viii] to an imaging spectrometer (Horiba Jobin-Yvon, iHR550) with an asymmetric Czerny-Turner design of 550 mm focal length, see FIG. 6.1. The input slit is imaged 1:1 onto a 16-bit back-illuminated CCD sensor (Andor Newton, DU-971N) attached to the spectrometer body. The array contains $N_x \times N_y = 1600 \times 400$ square pixels of pitch $p = 16\,\mu m$ and a $1.5 \times 10^5\,e^-$ full-well capacity; it is cooled down to a $-60\,^\circ C$ operating temperature by a Peltier junction. The diffracting element is a square ruled grating having $L_g = 76\,mm$ side and $n_g = 100\,lines/mm$. Since plasmonic features are quite broad (the typical FWHM of dipolar modes is tens of nm) a low line density is suitable so to favour bandwidth over spectral resolution. Specifically, with this grating a $\Delta\lambda = 444\,nm$ bandwidth over the full sensor is obtained.

When the spectrometer is operated in *imaging mode* the reflective grating oriented at its $m = 0$ diffraction order acts as a mirror and the sample plane is imaged onto the CCD with no spectral dispersion. From the sample to the sensor a magnification $M_{tot} = 79$ has been measured shifting the sample by a known amount (via the nanometric stage) and comparing this to the observed displacement of the image of a point emitter.[ix] The imaging mode is useful to identify the NO to be meas-

viii The intermediate image plane of the objective is imaged onto the entrance slit of the spectrometer and the BFP onto the diffraction grating.

ix The magnification of the intermediate image plane at the entrance slit of the spectrometer is thus $M_{tot}/M_{int} = 1.33$. The discrepancy with respect to

ured and centre it with respect to the image of the entrance slit, which is initially wide open to have the largest field of view.

Afterwards, the slit is closed down to $W = 80\,\mu m$, and the grating turned so to disperse $\lambda_c = 600\,nm$ of the $m = 1$ diffraction order towards the centre of the CCD. In such *spectroscopic mode*, the image formed has one spectral axis (x) and one spatial axis (y). The spectral window $\lambda_c \pm \Delta\lambda/2$ extends thus from 378 nm to 822 nm, fitting well within the operating region of the set-up.[x] As discussed in SEC. B.2, with these settings the spectral resolution of the instrument is approximately proportional to W and equal to $\text{FWHM}_{\text{instr}} = 1.7\,nm$, see EQ. (B.3). $\delta\lambda = \Delta\lambda/N_x = 0.3\,nm/\text{pixel}$ is the bandwidth per pixel, so a $b_x = 2$ horizontal binning was used to double the signal while still being safely above the 2 samples/resolution prescribed by the Nyquist criterion.

The area A appearing in the definition EQ. (5.1) of a detected signal is the region of the sample whereupon the signal is acquired. In our micro-spectroscopy set-up A is delimited along the spectral axis by the slit edges, and along the spatial axis by the ROI of the sensor: We acquired the signal from a $b_y = 5$ pixel bin[xi] so to match the entrance slit width ($b_y p = W = 80\,\mu m$). Therefore, being defined on the sample, A is a square of side $W/M_{tot} \simeq 1\,\mu m$. This is large enough to accommodate the diffraction-limited image of the NO ($D_1 = 770\,nm$

---

the intended 1:1 imaging of the optical design can be explained by a few mm displacement of the lens focusing the image onto the entrance slit. M_{tot} must be accurately assessed because it enters EQ. (5.6) as a square (via A).

x Below 400 nm the transmittance of the 40x objective drops quickly and the incandescent lamp provides essentially no light; above 800 nm the quantum efficiency of the CCD and the relative efficiency of the grating are quite low. In particular, the grating has its blaze at 450 nm, but its response is rather flat and relative efficiency is above 40 % in the 400 nm to 800 nm range.

xi In BF the $b_x \times b_y = 2 \times 5$ binning is performed in the software (i. e. adding individual pixel counts) rather than on chip to avoid saturation.

at $\lambda = 600\,\mathrm{nm}$)[xii] and leave some room too for the drift of the apparatus (up to 100 nm per minute, due e. g. to thermal fluctuations) over the measurement time (~ minute). A larger A would result in a lower spectral resolution[xiii] and a worse SNR in BF, where more background would be picked up, with no significant increase in signal or stability.

In opposition to CMOS cameras, CCD devices contain only one — or, in some cases, a few — readout elements, which convert the pixel charge into an amplified analog signal. This implies pixels are not read simultaneously, but sequentially: Pixel lines are shifted towards the *serial register* at one edge of the sensor, which is transduced elementwise. Now, CCDs typically have no mechanical shutter, meaning additional counts can build up during the readout time, leading to various kinds of artefacts. These are particularly detrimental in BF, where the whole sensor is intensely illuminated. In particular, the spurious readout counts lead to an overestimate of S_{bg}^{BF}, which the OCS are referenced to in EQ. (5.6). To mitigate this effect, the fastest parallel shift and register readout settings available must be used in first place, given that readout noise is immaterial in this scenario. Secondly, as only a narrow stripe of the sensor needs to be read, we placed in a plane conjugate to the sensor a slit parallel to the spectral axis (i. e. perpendicular to the entrance slit), thereby restricting the illuminated region along the shift direction. The remaining spurious counts — originating both from direct illumination over the restricted region and stray light across the whole sensor — are a negligible fraction of the total so long as the exposure time t_{exp} is much

xii $D_1 = 1.22\lambda/\mathrm{NA}_{obj}$ is the diameter of the first dark ring of the Airy function; the bright spot enclosed contains 84 % of the total power. While the mathematical Airy function decays slowly, the short ($\sim \lambda/\overline{\mathrm{NA}_i}$) coherence length of lamp illumination suppresses the external fringes of experimental PSFs.

xiii $\mathrm{FWHM}_{instr} \propto W$, see EQ. (B.3)

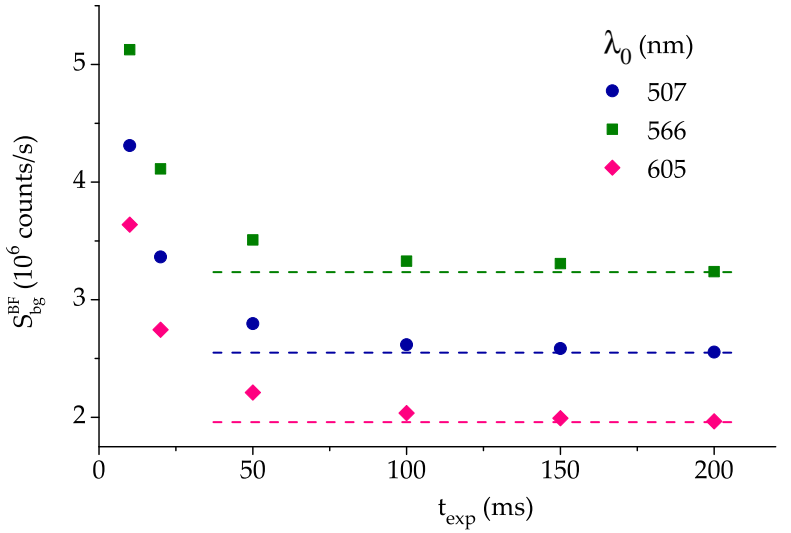

FIGURE 6.4: Detected BF illumination signal S_{bg}^{BF} against CCD exposure time t_{exp} at three different illumination wavelengths λ_0. The horizontal dashed lines are guides to the eye.

longer than the readout time (2 ms shifting plus 10 ms register readout in our measurements). Specifically, we observed deviations of S_{bg}^{BF} with respect to its long exposure value are ~1 % or less for $t_{exp} \geqslant 100$ ms,[xiv] see FIG. 6.4.

Different regions of the CCD sensor can be used to acquire simultaneously the background and the signal. In DF, we acquire five spectra with five adjacent stripes of equal binning $b_y = 5$ along the spatial direction. The central spectrum is S_{NO}^{DF}, the bins above and below are useful to adjust the y position (for intense scatterers they contain some leaked signal) and the top and bottom spectra are S_{bg}^{DF}, which is thereby measured over an empty square region of area A centred 2 µm away from the NO. Such a simultaneous referencing is feasible because DF offers

xiv Using a 2 mm slit; a tighter cropping would permit shorter exposure times.

an intrinsically high contrast, S_{NO}^{DF} and S_{bg}^{DF} typically differing by orders of magnitude.

Under BF illumination, S_{NO}^{BF} and S_{bg}^{BF} differ instead by $\Delta T \sim 10^{-2}$, and sometimes less, which is comparable to the pixel-to-pixel variations of quantum efficiency ($\sim 1\,\%$). It is therefore essential that S_{bg}^{BF} is acquired with the same pixels as S_{NO}^{BF}, which is done by displacing the NO a few µm sideways from the central bin. However, when S_{NO}^{BF} and S_{bg}^{BF} are measured successively using the central bin, the measurement is hampered by the fluctuations of the lamp intensity between the two acquisitions —again $\sim 1\,\%$, hence comparable to the measured extinction. The top and bottom bins[xv] must then be used to monitor the lamp intensity, and rescale S_{bg}^{BF} according to its variation as in EQ. (B.6a). With this expedient, a simultaneous acquisition is mimicked in the BF case too. Finally, we emphasize that all detected signals must be rescaled to take into account different acquisition parameters such as binning of the sensor, electronic gain, and so forth.

GOLD SPHERES As a first model system for testing our quantitative method, we used colloidal GNSs (BBI solutions, nominal size $\langle D \rangle = 60\,nm$) drop-cast on a microscope glass slide and immersed in index-matching silicone oil (Sigma-Aldrich, AP 150 Wacker) so that the NPs are immersed in a $n = 1.52$ homogeneous optical environment. A representative transmission electron microscopy (TEM) micrograph of the sample are shown in FIG. 6.5c. As widely reported in literature for GNSs, a polycrystalline structure and rather irregular shapes are observed, along with a size dispersity of about 10 %. FIG. 2.6b is

[xv] In BF we acquire three adjacent stripes of equal binning $b_y = 5$ rather than five, in order to have a faster readout and minimize the readout artefacts discussed above.

a DF micrograph of this sample, where isolated GNSs are seen as green-yellowish spots of similar luminosity. As discussed in SEC. 1.2 and SEC. 1.3, dimers and larger aggregates of NPs display a redshifted LSPR, and therefore they appear orange or red in DF, and are typically more intense. Dielectric debris and glass imperfections of all sizes appear pale yellow as the lamp spectrum, the small ones sometimes having white or pale blue hues according to the λ^{-4} dependence of Rayleigh scattering, see EQ. (1.7).

FIG. 6.5a and b display the absolute OCS spectra obtained with EQ. (5.6) and the following parameters:[xvi] $\tau^{BF} = 1$ from EQ. (5.8), $\xi = 2.11$ from EQ. (5.9), $\zeta = \xi$, see P. 146, $\eta^{BF} = 0.137$ and $\eta^{DF} = 0.113$ from EQ. (5.42). t_{exp} for DF spectra varied between 25 s and 40 s to achieve approximately 4×10^4 counts; 300 frames of $t_{exp} = 100$ ms were accumulated in BF in order to reduce the shot noise while keeping the total acquisition time below 1 minute (timescale of apparatus drift). Additional experimental parameters and the estimate of the shot noise can be found in SEC. B.3. The experimental spectra are compared to numerical simulations relative to GNSs of different D obtained with the model presented in SEC. 4.2 and Johnson and Christy[15] (J&C) $\varepsilon_{Au}(\lambda_0)$ dataset. For a NO of isotropic $\boldsymbol{\alpha}$ in a homogeneous environment the OCS under microscope illumination and under plane wave excitation coincide, and therefore no averaging of the model results is needed. Let us discuss the main spectral features first, and then the absolute amplitude.

The LSPR position in FIG. 6.5a and b is consistent between experiment and simulations, both showing a progressive redshift of the LSPR with increasing D, due to the retardation effects discussed on P. 19. Specifically, the simulated scattering spectrum

xvi In this measurement, $NA_{DF} \in [1.10, 1.28]$ was used.

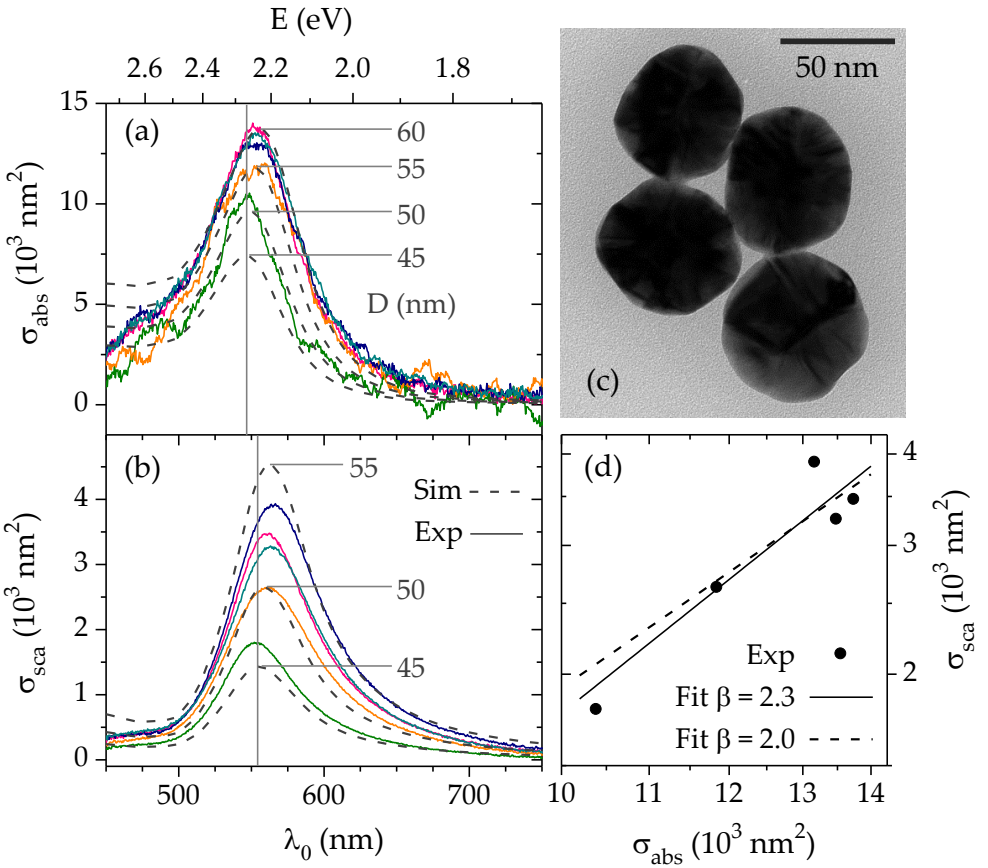

FIGURE 6.5: Absolute (a) absorption σ_{abs} and (b) scattering σ_{sca} cross-section spectra of five GNSs in a homogeneous $n = 1.52$ optical environment. Solid lines are experimental data (each colour identifying a specific GNS) and dashed lines are simulations for GNSs of different diameter D. The vertical lines indicate the LSPR of the $D = 45$ nm simulation. (c) Representative TEM micrograph of the sample acquired at the Cardiff University electron microscopy facility. (d) Log–log plot of the experimental $\sigma_{sca}(\sigma_{abs})$ peak amplitude (dots) fitted with $\sigma_{sca} = B(\sigma_{abs})^{\beta}$. The solid line ($B = (1 \pm 6) \times 10^{-6}$, $\beta = 2.3 \pm 0.6$) is the best fit obtained by varying both parameters; the dashed line ($B = (1.9 \pm 0.1) \times 10^{-5}$, $\beta = 2$) is obtained by keeping β fixed instead.

has $\lambda_{LSPR} = 562\,nm$ for $D = 55\,nm$, whereas EQ. (1.7) predicts $\lambda_{LSPR} = 540\,nm$ in the dipole limit.

As discussed on P. 15, LSPRs are broadened by both radiative and non-radiative damping, corresponding respectively to scattering and absorption of light. Non-radiative processes encompass both *intrinsic*[xvii] (collisions of electrons with other electrons and the ionic lattice) and *extrinsic* (collisions of electrons with lattice defects and material surface) relaxation mechanisms. Now, radiative damping is automatically included in numerical models by the electromagnetic solver,[xviii] whereas non-radiative damping, which stems from electron dynamics, is introduced via $\mathrm{Im}\,\varepsilon$ instead. The good agreement observed in FIG. 6.5a and b between the experimental and the simulated linewidth then indicates that the J&C dataset accounts reasonably well for the total non-radiative damping present in the GNSs.[xix] More recent ε_{Au} datasets available in literature have a smaller value of $\mathrm{Im}\,\varepsilon$ at λ_{LSPR}, see FIG. 1.2c — suggesting they refer to samples with better cristallinity — and would therefore yield narrower LSPR not compatible with our measurements. An example involving a different ε_{Au} and the quantitative linewidth comparison with J&C are reported in FIG. C.1.

It is also possible to modify by hand an analytic expression[xx] of the bulk ε to include an additional damping term Γ accounting, say, for surface scattering, and possibly dependent on size.[110] This approach is indeed common in NP

xvii The denomination indicates this would be the sole relaxation channel in a defect-free infinite crystal.

xviii However, the radiative damping in real GNSs might significantly differ from the theoretical value because of the observed deviations from a perfect spherical shape.

xix Albeit the individual contributions of the various damping mechanisms might in fact be quite different in GNSs and in the polycrystalline thin films measured by J&C.

xx At low enough energies Drude model is a good starting point, see FIG. 1.2

literature,[97,110,119,120] where Γ is essentially used as a free fitting parameter, and reported values vary by more than an order of magnitude for similar NOs, and even within the same sample, which is justified by variations of crystallinity between different NOs. Nonetheless, as J&C already provides a satisfactory fit to our data, we preferred avoiding introducing a further degree of arbitrariness in our analyses.

Comparing the absolute amplitude with quantitative simulations allows to estimate the experimental value of a geometric parameter of the model — namely D in our case. Although absolute OCS constitute precious experimental information *per se*, we regard the all-optical characterization of NO geometry one of the most promising applications of our quantitative method. Such an *optical sizing* has already been reported for GNSs by Muskens et al.[119] who used SMS to measure absolute σ_{ext} spectra of GNSs and hence infer their diameter. Quantitative measurements are particularly valuable in all those circumstances where variations of the disperse geometric parameter — such as D for small GNSs — do not give rise to distinct spectral signatures but only to changes in the OCS amplitude. Moreover, a measurement based on σ_{sca} is potentially highly accurate thanks to the sensitive size dependence.[xxi]

Looking back at the data displayed in FIG. 6.5a and b, we can estimate a size[xxii] (average ± standard deviation) of (50.6 ± 2.8) nm from σ_{sca} and of (57.0 ± 3.5) nm from σ_{abs}. The latter value is in good agreement with the manufacturer specification $\langle D \rangle = 60$ nm and the TEM characterization presented in FIG. 6.5c. Several — and possibly concurrent — reasons can lower σ_{sca} or lead to its underestimate. For example, the irregular shapes and the abundant structural defects observed

xxi For instance, assuming $\sigma_{sca} \propto D^6$, a measurement of σ_{sca} double its true value would result in an overestimate of D by only about 12 %.

xxii The estimated D for the individual GNSs are reported in FIG. C.1c and d.

in TEM micrographs could significantly quench the radiative efficiency with respect to the simulations modelling a perfect, homogeneous sphere. Alternatively, several experimental factors (systematic NA reading error, shadowing effects of the field iris, spherical aberration of the condenser,...) could contribute to damp down DF illumination, so that ξ (which σ_{sca} is proportional to) is effectively underestimated.

The experimental $\sigma_{sca}(\lambda_{LSPR})$ is plotted against $\sigma_{abs}(\lambda_{LSPR})$ for each sphere in FIG. 6.5d. The dependence has been fitted to a power law $\sigma_{sca} = B(\sigma_{sca})^{\beta}$; in the dipole limit where $\sigma_{sca} \propto D^6$ and $\sigma_{abs} \propto D^3$ (see P. 9) $\beta = 2$ is expected. The best fit of the data in FIG. 6.5d yields $\beta = 2.3 \pm 0.6$, compatible with the theoretical prediction; the fit with $\beta = 2$ is also shown for comparison. The small dynamic range of the data (due to the relatively low dispersity of the sample — nominally a single size) reflect itself on the large uncertainty of the parameter estimate.[xxiii]

The expected shot noise in these micro-spectroscopy measurements is calculated in SEC. B.3 as $\widehat{\sigma}_{abs} = 77\,nm^2$ and $\widehat{\sigma}_{sca} = 16\,nm^2$. Such a value of $\widehat{\sigma}_{sca}$ is actually comparable to the pixel-to-pixel fluctuations of the σ_{sca} spectra in FIG. 6.5b. The σ_{abs} spectra in FIG. 6.5a show instead ripples on top of the noise, which are much larger than $\widehat{\sigma}_{abs}$ and correlated over multiple channels. This indicates that the instrumental drifts (e.g. of the lamp intensity and spectrum) are not fully compensated for, and suggests that modulating the signal at low frequency rather than averaging more frames could lead to neater spectra.

GOLD RODS The second model system we investigated are colloidal GNRs (Nanopartz, A12-25-650-CTAB) drop-cast on a glass slide. These are grown in aqueous medium in presence of a surfactant, which drives the anisotropic growth by selective

xxiii A similar study with a larger dynamic range is reported by Payne et al.[121]

binding to specific crystal facets and stabilizes the colloid preventing aggregation. Cetyl-trimethyl-ammonium-bromide (CTAB) is the most commonly used surfactant for GNR growth, and has been widely reported to form a homogeneous bilayer wrapping the rod. For modelling purposes, the bilayer was described as having a refractive index of 1.435,[122] and a thickness of 3.2 nm.[123]

Electron microscopy characterization of the sample is shown in FIG. 6.6. In the aggregate in panel (a) rods are mostly aligned along the observation direction, allowing to visualize their transverse section. Although the resolution is relatively poor, the image reveals the extent of faceting, suggesting the GNRs are described well by an octagonal transverse section,

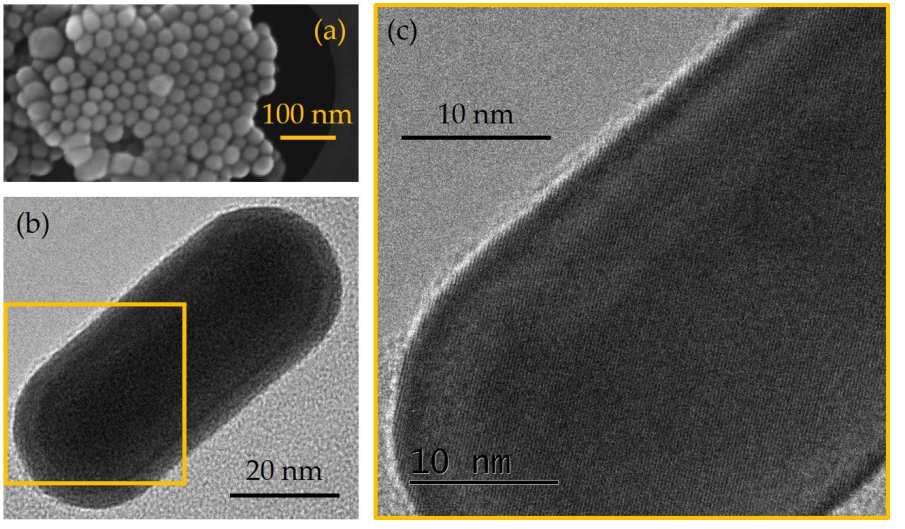

FIGURE 6.6: Electron microscopy images of colloidal GNRs. (a) was acquired using a field electron gun scanning electron microscope, whereas (b) and (c) are TEM micrographs of the same rod; correlation is highlighted by the yellow frame. Courtesy of T. Davies, electron microscopy facility, Cardiff School of Optometry & Vision Sciences.

as shown in literature by 3D reconstructions obtained with TEM tomography of a similar CTAB-coated GNR.[124] Panel (b) shows the typical shape of an individual GNR, having constant width and approximately spherical end caps. The atomic lattice visible in panel (c) extends regularly up to the edges and shows no crystal defects across the whole imaged volume; the measured interplanar spacing is $d = 2.34$ Å, identifying a {111} surface.[xxiv] The bright, thin halo encircling gold is a layer of deposited carbon, a typical degradation caused by the high energy electrons (~100 keV) used as imaging probes.

In order to assess how well our quantitative data analysis can handle the presence of an interface, we correlated spectra of the same GNR measured in different environments. In detail, we measured the rod spectra on a glass/air ($n_1 = 1.52$, $n_2 = 1.00$) interface and recorded the rod positions, then filled the air gasket with index-matching fluid ($n_2 = 1.52$), and found and measured again the same rods. In the following, we will refer to these two environments simply as "air" and "oil". The illumination polarization is adjusted for every rod to be co-polarized in the BFP with the polarizability axis ($\psi = 0$). In air, the parameters to be used in EQ. (5.6) are thus $\tau^{BF} = 0.934$ from EQ. (5.8), $\xi = 4.42$ from EQ. (5.9), $\zeta = 3.42$ from EQ. (5.25), and $\eta^{BF} = \eta^{DF} = 0.148$ from EQ. (5.26); in oil one has instead $\tau^{BF} = 1.00$, $\zeta = 5.63$, and $\eta^{BF} = \eta^{DF} = 0.148$.[xxv]

The resulting OCS spectra for a single GNR are shown in FIG. 6.7a and b, and the spectra of all the studied rods are

[xxiv] The theoretical value is $d = a/\sqrt{i^2 + j^2 + k^2} = 4.065\,\text{Å}/\sqrt{3} \simeq 2.35\,\text{Å}$, where a is the lattice parameter of gold and i, j, k the Miller indices denoting the crystal plane.

[xxv] The value of η^l is close (but not identical: They actually differ in the fourth significant digit) in the two environments owing to a fortuitous compensation between the amount of scattering in medium 2 (increasing with n_2) and the collection range θ_{obj} (decreasing with n_2).

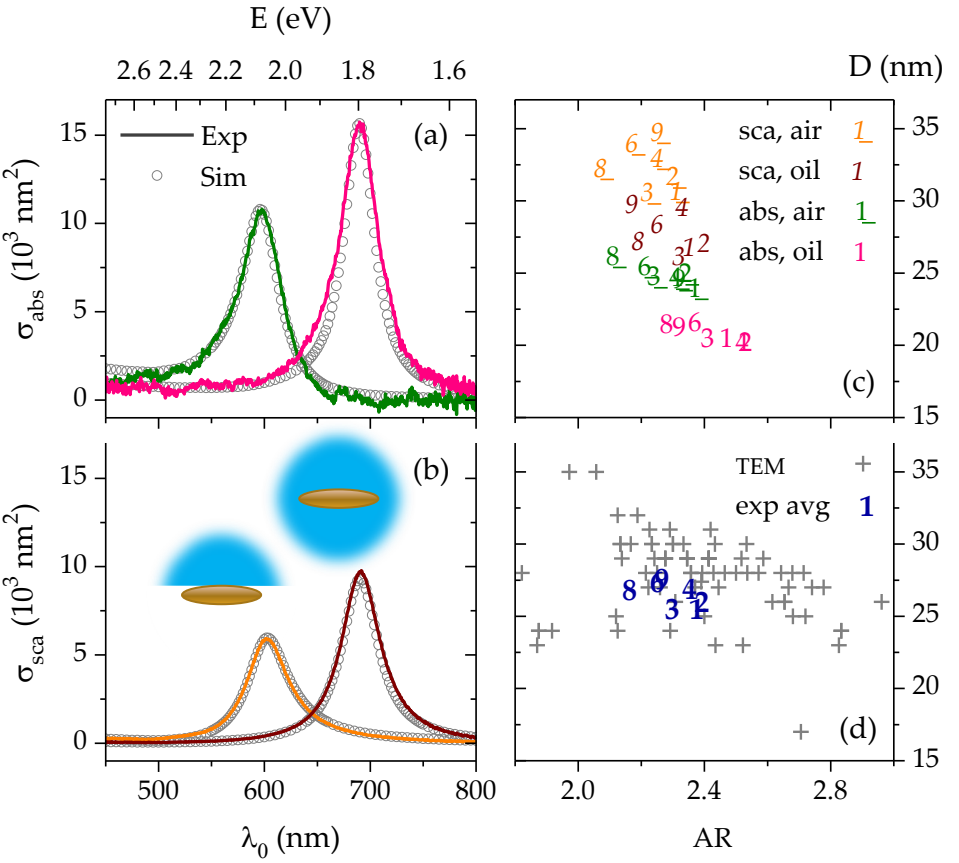

FIGURE 6.7: Absolute (a) absorption and (b) scattering cross-section spectra of an individual GNR (#6) deposited on a glass/air interface ($n_1 = 1.52$, $n_2 = 1.00$) and in a homogeneous environment ($n_1 = n_2 = 1.52$) (short and long wavelength peak respectively). Solid lines are experimental data and hollow circles are numerical simulations where the rod aspect ratio (AR) and diameter D are used as free parameters to fit the experiment. (c) AR and D estimated from the four independent fits for the measured GNRs, identified by numbers. (d) Average of the four datasets in (c), superimposed to the AR and D measured in a TEM micrograph of 80 GNRs of the same batch (each cross is a different rod, several fall outside of the plotted range).

shown in FIG. C.2. Let us comment on the main spectral features before discussing the optical sizing. The LSPR of a GNR redshifts linearly with an increasing AR as described by EQ. (1.13) for an ellipsoid, leading to a near IR λ_{LSPR} in our sample. EQ. (1.13) predicts also a redshift of the LSPR as the rod surrounding are made optically denser, which we observe as well. Small rods are known to have a narrower LSPR with respect to spheres of similar size: This has been attributed to a lower non-radiative[xxvi] damping as λ_{LSPR} is moved away from the interband absorption edge;[125] and indeed $\mathrm{Im}\,\varepsilon_{Au}$ has a minimum at about 700 nm, see FIG. 1.2c. Specifically, σ_{sca} has $\langle \mathrm{FWHM} \rangle = 44$ nm in oil, in comparison to 74 nm measured on the GNSs studied above. Overall, our results are consistent with the available literature on single-GNR spectroscopy;[97,120,125–127] nonetheless, we emphasize that this is the first time such a quantitative and correlative characterization of the optical properties of an individual NO is reported. The discussion we made on P. 171 concerning the nature of the noise in GNS spectra holds here as well for the GNRs.

The OCS of NOs on a substrate can be simulated using the model described in SEC. 4.2 along with (J&C) $\varepsilon_{Au}(\lambda_0)$ dataset.[15] The experimental illumination conditions are reproduced using the averaging method derived in SEC. 3.1.2.[xxvii] In FIG. 6.7a and b, the four OCS spectra of an individual GNR (#6) were fitted independently using the rod diameter D and its AR as free

[xxvi] In small metal NOs the radiative yield is quite small and line broadening is ruled by non-radiative plasmon decay processes.

[xxvii] In practice, for a given NO+environment geometry and illumination conditions, the factors $\sigma^{BF}_{abs}/\sigma^{(0)}_{abs}$ and $\sigma^{DF}_{sca}/\sigma^{(0)}_{sca}$ are computed once via averaging, an used thereafter to rescale $\sigma^{(0)}_{sca}$ simulations obtained with $\theta_i = 0$ illumination. These factors were found to be quite insensitive to the fine details of NO geometry, being essentially determined by α.

parameters of the simulation. Such an *inverse modelling*[xxviii] results thereby in four independent geometry estimates for each of the 7 GNRs investigated, reported in FIG. 6.7c. A good correlation between the four sets is observed (meaning, for instance, rod #2 is long and rod #8 is short in all of them) and the averages $\langle D \rangle_{exp}$ and $\langle AR \rangle_{exp}$ are both less than 10 % smaller than typical TEM values, see FIG. 6.7d. We found however systematic discrepancies between the four geometry estimates of the same GNR.

In first place, a larger D is estimated in air than in oil, both for σ_{abs} and σ_{sca}. This stems partially from the use of $\tau^{BF} = 1.00$ instead of $\tau^{BF} = 0.934$ to rescale the OCS in air,[xxix] which are thus overestimated, and so is D. Another factor selectively affecting the scattering parameters in air is the effective distance z_{NO} of the dipole from the substrate, which is disregarded in our point-like NO approximation. In fact, the analytical description of dipole radiation reported in SEC. 5.2 could be generalized for $|z_{NO}| > 0$, but the consequent variation of the measured OCS is difficult to predict on the basis of simple arguments. Alternatively, the effect of $|z_{NO}| > 0$ can be investigated via numerical modelling, see the preliminary results in TAB. 5.1, which lead indeed to a 25 % reduction of σ_{sca} in air.

In second place, a larger D is estimated from σ_{sca} than from σ_{abs}. In other terms, the ratio $\sigma_{abs}/\sigma_{sca}$ is much smaller in the measurements (average in air is 2.1) than in the simulations (6.0 for a $D = 27\,nm$, $AR = 2.4$ GNR in air). Other $\varepsilon(\lambda_0)$ datasets with lower damping bring about a smaller $\sigma_{abs}/\sigma_{sca}$ simulated ratio, but also a proportionally narrower linewidth (for a $D = 25\,nm$, $AR = 2.3$ GNR in air the FWHM is 31 nm with Babar and Weaver[17],

xxviii Retrieving structural information on an object given its optical properties is often called the *inverse problem*, as usual physical modelling aims to calculate the optical properties given complete structural information.

xxix In fact, τ^{BF} has been included in EQ. (5.6) only while writing this thesis.

36 nm with McPeak et al.[16], 41 nm with Olmon et al.[18] against 43 nm with J&C) not compatible with the experimental value $\langle \text{FWHM} \rangle = 48$ nm in air. The same systematics observed in both environments suggests that an unfaithful description of the NO was adopted in the numerical simulations rather than the quantitative method failed to account for the presence of the interface. Furthermore, for such an absorption-dominated NO, σ_{abs} is not heavily affected by the analytical description of scattering at an interface, inasmuch as ζ, η^{BF}, and η^{DF} enter just as a correction term, see EQ. (5.6a). However, σ_{abs} in oil brings about too small estimates of D with respect to the TEM averages, suggesting the explanation has to be found elsewhere.

The two main elements to adjust in the model of the system are the transverse section of the GNR and the shape of its end caps. In fact, attempts at varying within a plausible range the properties of the CTAB layer or the material composition of the rod (e. g. including a few % of silver)[128] produced only minor changes of the optical sizing. Now, the results in FIG. 6.7 refer to a circular transverse section and spherical end-caps. We adopted such end cap shape to mimic the available TEM characterization, exemplified by FIG. 6.6. An oblate (prolate) cap shape results in a sizeable shift to the blue (red) of λ_{LSPR} with constant AR,[126,129] and hence in a reduced (increased) estimate of AR; see for instance the optical sizing results in FIG. C.3 obtained with an oblate cap. On the other hand, as discussed above, a recent electron microscopy characterization (FIG. 6.6a) suggests that the studied GNRs have an octagonal transverse section rather than a circular one. Optical sizing will then be repeated with this refined geometry which, owing to the presence of sharper spatial features, is expected to increase the scattering yield and thereby improve the consistency between the four datasets. Lastly, surface roughness on the nm scale, and the as-

sociated plasmonic hot-spots, is another neglected mechanism which might justify an enhanced radiative efficiency.

In hindsight, comparing quantitative experimental spectra of GNRs (obtained with SMS) and numerical simulations has already proven a redoubtable task. The σ_{ext} spectrum of a single GNR in homogeneous environment was fitted by Muskens et al.[126] using both FEM and DDA modelling. The geometrical fitting parameters (D = 25.5 nm and AR = 1.96) were not compatible with the values observed with TEM (D = 15 nm to 20 nm and AR = 2 to 4) on the rod colloid. Two later studies[97,120] (both involving the group headed by F. Vallée and N. Del Fatti in Lyon) addressed the effect of an optical interface on the OCS and relied on optical–electron microscopy correlation on individual GNR.

Davletshin et al.[97] measured the σ_{ext} spectra of 3 "coated" GNRs embedded in a thick ($\simeq$10 nm) silica shell, providing a quasi-homogeneous dielectric environment, and 3 "bare" GNRs in air deposited on a silica TEM substrate. D and AR deduced for each GNR from TEM imaging were used for numerical simulations: A good agreement with experiment was found for the coated GNRs, whereas for the bare ones the simulated values of λ_{LSPR} are blueshifted by approximately 100 nm with respect to the experimental LSPR. Such a large spectral mismatch is not related to quantitative amplitude measurements, and points to a poor modelling of the geometry of the GNR or its local environment (for instance, the surfactant layer is not included). Although the authors appeal to the presence of a water layer around the bare rods in order to redshift the simulated spectra, they do not put forward any direct evidence of its presence — such as could be a good agreement between experiment and model for a silica/water interface. The non-standard use of boundary conditions in their COMSOL model we highlighted on P. 103 possibly contributed to the observed discrepancy.

Lombardi et al.[120], similarly to Davletshin, measured the σ_{ext} spectra of 2 "bare" GNRs deposited on a silica TEM substrate.[xxx] Differently from Davletshin, though, in this work the spectral position of the LSPR was reproduced well by adjusting the *effective refractive index* n_m of the air environment, which was argued to account for the surfactant layer and residual water close to the rod surface. However, the presence and the geometry of these two elements have not been determined independently, and the large refractive indices used ($n_m = 1.41$ and $n_m = 1.42$, corresponding to a surfactant shell occupying the whole NF region of the rod) rather seem to compensate other effects not properly accounted for, such as details of the GNR geometry. In comparison the analysis we reported, involving a quantitative and independent determination of σ_{abs} and σ_{sca} in different environments for the same GNR, allows to critically evaluate the validity of the inverse structural modelling to a higher degree. For instance, the fitted value of n_m being so close to the 1.45 refractive index of silica, essentially no redshift of the LSPR is expected if the nominally air environment is substituted by index-matching fluid. Had the authors attempted such a correlation — as we did — the measured λ_{LSPR} could have challenged their estimate of n_m.

Let us quote a few considerations drawn from a critical review by W. Barnes on the difficulties of comparing model and experiment in plasmonics,[130] as they summarize well some issues emerged in this section. The first challenge highlighted is identifying the most physically-sound ε to be used in models: Is the bulk permittivity good enough down to what size? How

[xxx] The GNRs investigated by Lombardi are very close in size to the ones studied by Davletshin, where Lombardi is the second author; therefore the two papers possibly present analogous measurements on the same colloid batch.

to account for surface roughness,[xxxi] surface contamination, or granularity? And then the author remarks: "It is all too easy for the permittivity to be used as a dumping ground for all sorts of other factors that are not fully considered or properly accounted for." Another potential pitfall mentioned is: "Are the illumination and collection conditions the same for experiment and simulation?" A large amount of effort in this thesis (CH. 3) is devoted to ensure such a condition is adequately met. On the contrary, the works discussed above[97,120,126] modelled the tightly-focused illumination of SMS experiments with a linearly-polarized plane wave — thereby disregarding the anisotropic optical response of a GNR to the wide range of polarizations contained in the illumination PSF.

6.3 WIDEFIELD IMAGE ANALYSIS

The quantitative method presented in this thesis can also be applied in conjunction with the widefield image analysis technique[63,118,121,131] developed in our group mainly by L. Payne. In this section, after a brief description of the technique, an example of quantitative image analysis is provided.

INSTRUMENTATION AND PROCEDURE Imaging has been performed using a 16-bit scientific CMOS monochrome camera (PCO, Edge 5.5) attached to the microscope body. The sensor is water cooled and contains 2560×2160 square pixels of $p = 6.5\,\mu m$ pitch and a $3 \times 10^4\,e^-$ full well capacity. The high frame rate obtained with a rolling shutter (100 frames per

[xxxi] "Roughness is a difficult aspect to deal with in models. First, the length scale associated with roughness is often comparable to the mesh size used in numerical techniques [...]. Second, [...] the detailed morphology in any given situation is often very hard to determine experimentally, and yet hot spots associated with roughness can dominate the behaviour of the system."

second with full sensor size, and up to an order of magnitude faster with reduced ROI) allows averaging a large number of frames (up to 10^5) for shot noise reduction purposes, resulting in highly sensitive extinction detection under BF illumination. Moreover, the large quantum efficiency (60 %) joint to the low readout noise (median pixel read noise 1.1 e^- RMS) enables the observation of weak scatterers under DF illumination.

In its essence, the method is a quantitative analysis of the *extinction image*

$$\mathcal{I}_{ext}(x,y) = \frac{\mathcal{I}^{BF}_{bg} - \mathcal{I}^{BF}_{NO}}{\mathcal{I}^{BF}_{bg} - \mathcal{I}dk} \tag{6.1}$$

where $\mathcal{I}^{BF}_{bg}$ is acquired by displacing the sample laterally by at least one optical resolution with respect to $\mathcal{I}^{BF}_{NO}$. FIG. 6.8 is an exemplary extinction image: The displacement referencing procedure duplicates the NO image into a bright and a dark spot. The image shows simultaneous detection of a D = 60 nm and a D = 5 nm GNS (BBI solutions), thus demonstrating the large dynamic range and sensitivity achieved. Specifically, the extinction contrast is $\Delta T = 1.5 \times 10^{-1}$ for the 60 nm GNS and $\Delta T = 2.0 \times 10^{-4}$ for the 5 nm GNS, the latter figure corresponding to $\sigma_{ext} = 10\,nm^2$, in excellent agreement with the theoretical value $\sigma_{ext} = 11\,nm^2$ reported on P. 43. Dielectric debris, on the other hand, are characterized by a contrast changing sign across the PSF due to interference between the transmitted and the scattered light, resulting in an practically null extinction, as expected from small phase objects.

Differently from the techniques discussed in SEC. 2.2.1, high sensitivity is achieved here without resorting to high frequency modulation and the complicated instrumentation related. It stems instead from the large number of frames ($\sim 10^5$) averaged to suppress shot noise, a low frequency modulation ($\sim$ 10 Hz) between the two NO positions to filter out fluctuations

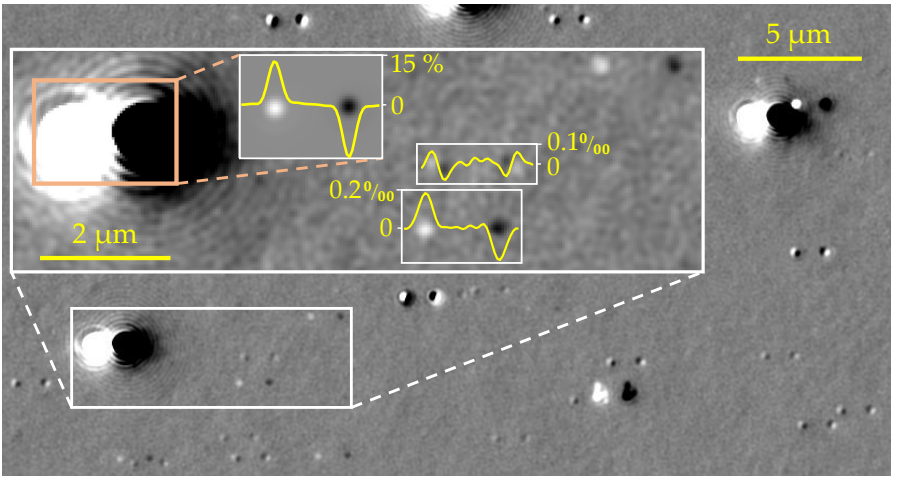

FIGURE 6.8: Extinction image (1279 × 460 pixels) of a GNS sample taken with a 1.45 NA oil-immersion objective under LED illumination of average wavelength $\langle\lambda\rangle = 530\,\text{nm}$, i. e. resonant with the LSPR of small GNSs. In the magnified inset line cuts across along the NO image separation are shown as yellow overlays: the top cut is a 60 nm GNS (adjusted contrast in the small inset), the centre cut is a dielectric debris and the bottom cut is a 5 nm GNS. Greyscale ranges (black to white) are: Main image −0.3 ‰ to 0.3 ‰, large inset −0.22 ‰ to 0.21 ‰, small inset from −18 % to 15 %. Courtesy of L. Payne.[131]

due to slow drifts (~ 10 Hz and less) of the apparatus, and a numerical deconvolution algorithm to reject read-out noise and sensor patterning effects. Using this refined version of the technique a shot-noise limited sensitivity down to $\widehat{\sigma}_{\text{ext}} = 0.4\,\text{nm}^2$ was attained,[131] where a lower bound is set in practice by the background noise originating from physical extinction inhomogeneities, such as the intrinsic roughness and cleanliness of the glass surface. On the other hand, a simplified experimental scheme (without modulation) and analysis procedure (without deconvolution) still provides a $\widehat{\sigma}_{\text{ext}} = 5\,\text{nm}^2$ sensitivity,[63] which is sufficient for many applications; the data presented in the

following have been obtained with this simplified version of the technique. In terms of sensitivity performance, widefield image analysis can be compared to another modulation-free transmission technique developed by V. Sandoghdar and co-workers,[132,133] which is capable of measuring the absorption of single molecules ($\sigma_{abs} \sim 0.1\,nm^2$) in absolute units. It is however a laser-based raster-scanning technique, and hence requires a rather complicated experimental set-up for balanced detection and heterodyning. Furthermore, a raster-scanning approach lacks the high-throughput capabilities of widefield imaging.

Image analysis is performed through a plug-in developed by L. Payne in ImageJ macro language and named *Extinction suite*.[xxxii] The software first constructs the extinction image (6.1) out of averaged BF frame stacks, and then automatically[xxxiii] individuates the NOs and integrates the extinction over a circular region A centred on both the bright and dark PSF.[xxxiv] Simultaneous analysis of all the NO found in the field of view (easily more than 100) provides a high-throughput characterization of the investigated sample. The average of the bright and dark integrals times A is σ_{ext}, corresponding to a simplified version of EQ. (5.6a) with $\tau^{BF} = 1$ and $\zeta = 0$. Therefore, in its published implementation, the technique yields accurate quantitative results in absence of an optical interface and of a sizeable scattering contribution. It has in fact been developed having in mind small metal NOs in a homogeneous optical environment.

xxxii The latest public release of Extinction Suite can be downloaded from the permanent URL `https://langsrv.astro.cf.ac.uk/Crosssection/Extinction_Suite/Extinction_Suite.html` (visited on 10/10/2017).

xxxiii This operation is outsourced to the built-in *Find Maxima* function of ImageJ; user intervention is limited to establishing a tolerance so to exclude spurious maxima due to small debris and noise spikes.

xxxiv Before integration, an offset is subtracted to the extinction, corresponding to the average local background evaluated in a ring around the PSF.

σ_{sca} can be measured by integrating in a similar fashion the *scattering image*

$$\mathcal{I}_{sca}(x, y) = \mathcal{I}^{DF}_{NO} - \mathcal{I}^{DF}_{bg} \tag{6.2}$$

constructed out of averaged DF frame stacks. $\mathcal{I}_{ext}$ and $\mathcal{I}_{sca}$ are accurately correlated via a pattern recognition routine, and the integrated scattering is referenced[xxxv] to the local illumination intensity $(S^{BF}_{NO} - S^{dk})/A$. Such calculation of σ_{sca} is thus tantamount to a simplified version of EQ. (5.6s) without τ^{BF}, ξ, and η^{DF}. There have been previous efforts towards quantitation of σ_{sca} via a scaling factor corresponding to the prefactor $\tau^{BF}\xi/\eta^{DF}$ in EQ. (5.6s). This factor was computed (for a given experimental excitation and collection conditions) by measuring both σ_{ext} and σ_{sca} for GNSs having a large range of D, and fitting the resulting $\sigma_{sca}(\sigma_{exc})$ plot with a formula derived from the known size dependence for small spheres $\sigma_{ext} \simeq \sigma_{abs} \propto D^3$ and $\sigma_{sca} \propto D^6$.[121]

In summary, the existent analysis procedure can be made accurately quantitative with respect to both σ_{abs} and σ_{sca} by incorporating EQ. (5.6). This would expand the applicability of the technique to NOs with a large scattering yield — such as dielectric ones — and placed close to an interface, as illustrated by the following measurements.

POLYSTYRENE SPHERES Polystyrene nanospheres (Polysciences, Polybeads®), also called "beads", were drop-cast on a microscope glass slide; the water solvent was let to evaporate to leave the beads in air. Polystyrene ($n = 1.59$) is transparent in the VIS and near IR range, meaning the beads have $\sigma_{abs} = 0$. Incoherent illumination with a narrow wavelength range was

[xxxv] To date, without accounting for the different illumination intensity via ξ.

provided by LEDs.[xxxvi] All other microscope components are the same used for spectroscopy and have been described in SEC. 6.1. 12 800 frames of $t_{exp} = 1\,ms$ were averaged to acquire $\mathcal{I}^{BF}_{NO}$, $\mathcal{I}^{BF}_{bg}$, and $\mathcal{I}^{dk}$; 32 frames of 1 s exposure time were averaged to acquire $\mathcal{I}^{DF}_{NO}$ and $\mathcal{I}^{BF}_{bg}$. For referencing to BF illumination, $\mathcal{I}^{BF}_{bg}$ was shifted with respect to $\mathcal{I}^{BF}_{NO}$ and $\mathcal{I}^{DF}_{NO}$ by $2\,\mu m$ — approximately the size of the extinction PSF.[xxxvii] The output of Extinction Suite was made quantitative using $\tau^{BF} = 0.934$ from EQ. (5.8), $\xi = 3.92$ from EQ. (5.9) and $\eta^{DF} = 0.125$ from EQ. (5.38).

The measured distribution of σ_{sca} is reported in FIG. 6.9. In total 51 beads were analysed within a single field of view, and three colour channels over the VIS range were acquired to achieve a coarse spectroscopy. σ_{sca} decreases with increasing λ, compatibly with the λ^{-4} dependence of Rayleigh scattering, see EQ. (1.7). Optical sizing is achieved through comparison of experiment to the simulated σ_{sca} for different values of D. As above for the GNRs, the scattering experiment was simulated using the COMSOL model described in SEC. 4.2, and microscope illumination was reproduced through the averaging formulas derived in SEC. 3.1.2. The measured distribution of D is in good agreement with the manufacturer's specification $D = (82 \pm 6)\,nm$, thereby demonstrating our quantitative method is suited for non-absorbing NOs as well. We plan to further validate and refine this preliminary investigation by enlarging the statistics and measuring σ_{abs} too, whose distribution is expected to be centred on 0.

Summarizing, for a given $\boldsymbol{\alpha}$ and dielectric environment, a straightforward application of EQ. (5.6) measures the absolute

xxxvi Alternatively, one can use broadband illumination and absorptive bandpass optical filters.

xxxvii $D_2 \simeq 3\lambda/NA_{obj} \simeq 1.8\,\mu m$ is the diameter of the second dark ring of the Airy function describing the PSF.

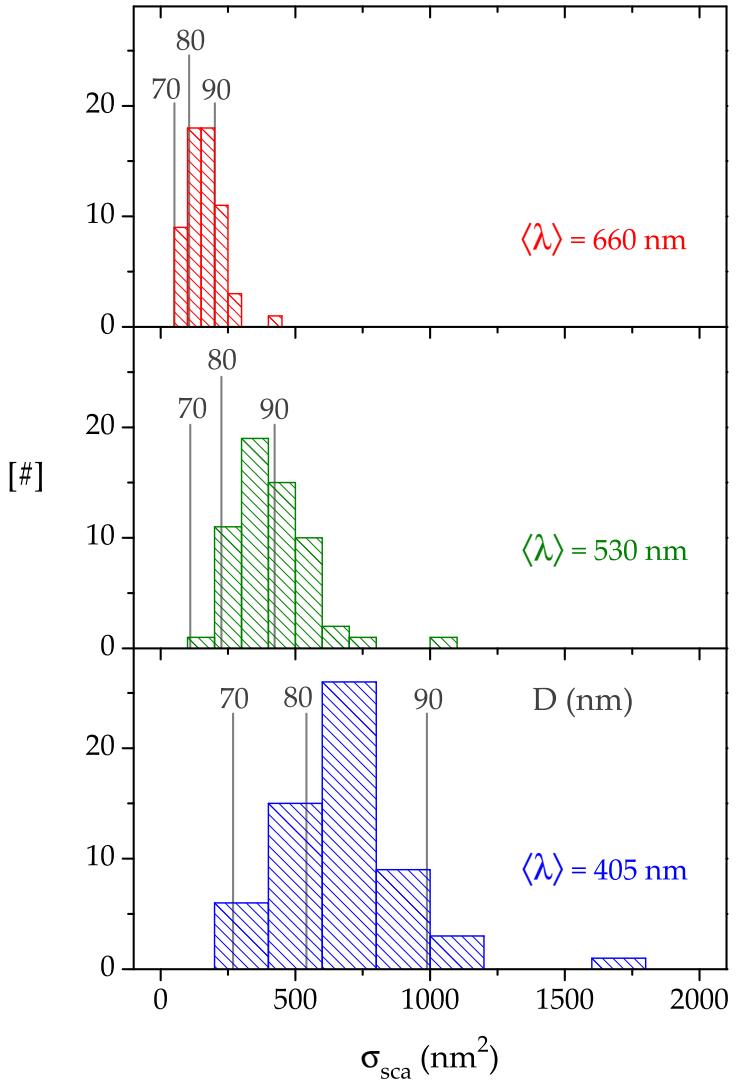

FIGURE 6.9: Distribution of the scattering cross-section σ_{sca} in three colour channels of an ensemble of 51 polystyrene beads deposited on a glass/air interface ($n_1 = 1.52$, $n_2 = 1.00$). The vertical lines indicate the simulated σ_{sca} for beads of different diameter D.

OCS at the level of a single NO. A geometrical parameter affecting the amplitude of the OCS, such as D for a sphere and its dispersity over the sample population, can be retrieved via inverse modelling. Two-parameter studies can also be conceived: For instance, diameter and asphericity of a GNS ensemble have been simultaneously characterized via polarization-resolved excitation.[121,xxxviii] In comparison to micro-spectroscopy, widefield imaging cannot provide detailed spectral information, but supplies on the other hand a high-throughput characterization via automated image analysis. Moreover, since the signal is not partitioned into multiple colour channels, imaging is intrinsically more sensitive.

Owing to its capability of an optical and structural (via optical sizing) high-throughput characterization, automated analysis of widefield images makes an ideal candidate to complement electron microscopy in NP studies. We believe it is currently the only quantitative single-particle optical technique which could be adopted outside of a research environment (e. g. in a chemical industry manufacturing NP on a large scale) because only relatively inexpensive equipment and no highly-specialized training is required. The NPs can either be drop-cast on a substrate as in the examples above, or flushed under the objective through a microfluidic system, in which case the optical anisotropy will be averaged upon the Brownian rotational motion. In view of such applications, we have recently filed a patent application describing an optical nanosizer based on quantitative image analysis.[134]

xxxviii A much more challenging scenario occurs when the two parameters are coupled — in this example, if the asphericity is large enough to affect the LSPR position and amplitude.

In contrast, colloid analysers currently on the market[xxxix] rely on dynamic light scattering (DLS) for size measurement. However, in some circumstances the hydrodynamic radius measured by DLS can significantly differ from the geometric size, and in particular misrepresents non-spherical NOs. NPs with a metal core and a transparent shell (e. g. surfactant, or other polymers) offer an example where quantitative optical measurements can complement DLS: The hydrodynamic radius corresponds to the shell size, but the OCS are ruled by the plasmonic response of the core, whose structural parameters can be determined through inverse modelling.

xxxix State-of-the-art examples are the NANO-flex® and the ZetaView® instruments produced by Particle Metrics, the ViewSizer™ 3000 by Horiba, and the Zetasizer range by Malvern.

CONCLUSIONS AND APPENDICES

CONCLUSIONS AND OUTLOOK

The optical properties of NOs are fully described by the OCS for the active optical processes. In particular, metal NOs can sustain LSPRs, typically leading to more intense absorption and scattering in comparison to dielectric NOs. According to the review presented in SEC. 1.2, LSPRs depend sensitively on the size and shape of the NO, resulting into a rich phenomenology and ample opportunities for tailoring the optical properties in view of a specific application. For these reasons most of the examples we have provided pertain to metal NOs, although the methods proposed in this thesis apply to dielectric NOs as well.

Albeit the optical properties of NOs have been the subject of experimental investigation for over a century now, researchers have preferentially focused on some observables, such as the position and linewidth of the spectral features (e. g. plasmonic modes) as functions of the NO size, shape, material composition, and surrounding environment. On the other hand, the absolute amplitude of the OCS has received comparatively little attention. In fact, we highlighted in SEC. 2.2 that only a few techniques are currently capable of quantitative measurements, and these are rather complicated to implement and not accurate when imaging strong scatterers with high NA objectives.

While the field of nanoplasmonics is nowadays mature with regard to the fundamental understanding of the plasmonic phenomenology, it still struggles to achieve the degree of control required for large-scale technological exploitation. Thus we reckon the nanoplasmonics community would benefit from adding simple quantitative methods to the experimentalist's toolbox, offering a standardized platform for comparing

different experiments and optimizing the performances of applications. This thesis strives to fill this void, by presenting new data analysis methods to measure the absolute amplitude of the OCS, and modelling recipes beyond current practise to quantitatively simulate microscopy experiments. We shall summarize below our main accomplishments.

QUANTITATIVE MEASUREMENTS In SEC. 5.1 we outlined a quite general description of quantitative measurements of the OCS, which are expressed in terms of the signals detected at the NO position and in an empty area nearby, both under BF and DF illumination. We discussed in CH. 6 how these signals can be acquired through micro-spectroscopy or widefield imaging; the latter has no intrinsic wavelength resolution, but lends itself better to high-sensitivity measurements and high-throughput characterization of colloidal solutions. These two are in fact straightforward and widespread experimental techniques, which require only a commercial microscope optically coupled to a spectrometer or an imaging array: Current users only need a few one-off calibrations of their existing set-up in order to acquire suitable data for quantitation.

The expressions of the OCS in terms of the detected signals contain a few parameters, which are determined by the geometry of the experiments. In particular, two of these account respectively for the different total scattering under BF and DF illumination, and for the finite collection of the microscope objective. These scattering parameters depend also on the polarizability of the NO, and can be computed via either analytical models or numerical simulations. The analytical model proposed in SEC. 5.3 is accurate for a NO within the electrostatic approximation and having a diagonal polarizability. The calculations are rather lengthy, but have been implemented into a MATLAB code requiring as user input only a few parameters of

the experiment. Results in closed form were given in the case of a homogeneous optical environment.

We tested the quantitative method on three model systems, including isotropic and anisotropic NOs, both in a homogeneous environment and on a substrate. To the best of our knowledge, these are the first reports of broadband quantitative scattering spectroscopy of individual NOs. As for absorption or extinction measurements, our approach outdoes all available quantitative techniques (mainly SMS) in two respects: (i) it relies on a simpler experimental set-up without lasers; and (ii) it accounts for the fraction of scattering collected by the objective. Importantly, the method refers to a NO close to a dielectric interface, and thereby covers a wide range of common experimental conditions.

QUANTITATIVE MODELLING The OCS are not intrinsic properties of the target alone, but depend on the properties of the illumination too, including its direction of incidence and polarization with respect to the target. Now, the high NA illumination adopted in modern microscopes contains a wide range of directions of incidence and exciting polarizations. Reproducing the microscope illumination in numerical models is therefore essential for a meaningful comparison to experimental results, with special regard to the absolute amplitude of the OCS. In particular, we need quantitative modelling to assess the accuracy of our quantitative measurements beyond the few simple geometries for which analytical solutions are available.

The EWFD solver we relied on for electromagnetic simulations is inherently unable to handle incoherent excitation. In SEC. 3.1 we presented two methods to mimic incoherent illumination using coherent plane waves. The first one consists in averaging the simulations results obtained with plane waves whose incidence direction sample the angular range of experimental

illumination. The second method — approximate, but less expensive computationally — is to run a single simulation with an "equivalent" exciting plane wave, whose intensity along the principal axes of the polarizability equals the intensity of microscope illumination. The accuracy of the latter method still needs to be checked systematically against the former one.

Coherent microscope illumination can be described using the known analytical expression reported in SEC. 3.2, which describes a plane wave focused by an aplanatic lens system. Importantly, this is an exact vectorial expression of the electric field, whereas the Gaussian beam formula available off-the-rack in COMSOL is derived in the paraxial regime, and therefore does not reproduce accurately the PSF created by high NA lenses. The vectorial expression was used as the exciting field in order to simulate an experiment where a third-order nonlinear process (specifically, CARS) is enhanced by a NO. Systematic comparison with the experimental results is still in a preliminary stage, but good agreement has already been found for a GNS. We believe this is the first COMSOL model of a nonlinear microscopy experiment including a realistic description of the excitation, whereas previous models of nonlinear processes we are aware of employ the full field formulation, and are thus limited to plane wave excitation. We envisage the application of the same modelling scheme to simulate other nonlinear processes, such as the 4WM experiments performed by other members of our group.

OUTLOOK While further refinements to our analytical model of scattering have been planned — such as including a finite distance between the interface and the dipoles representing the NO — computing the scattering parameters through numerical simulations would allow quantitative measurements of NOs of large size and described by an arbitrary polarizability. In fact,

this is already possible in the case of a homogeneous optical environment using the model described in SEC. 4.2, but for more complex environments the accuracy of the FF formalism adopted by COMSOL still needs to be checked systematically.

As an application of quantitative measurements, we proposed a procedure we named optical sizing: Some parameters (e. g. diameter, aspect ratio, gap size, ...) describing the shape of a NO can be estimated by comparing or fitting theoretical results (either analytical or numerical) to the experimental data. To some extent, optical sizing can be performed relying solely on spectral properties other than the OCS amplitude (e. g. the position of LSPRs); nevertheless, adding a further "dimension" to the analysis greatly boosts its scope and accuracy. Absolute OCS amplitude is particularly valuable information for optical sizing in those circumstances where it is the observable most affected by small variations of the shape parameter investigated — consider the example of spheres in the dipole limit.

Some examples of optical sizing are provided in CH. 6, where the numerical model of SEC. 4.2 was used. Good agreement with electron microscopy and nominal manufacturer's specifications was found for gold spheres and polystyrene beads, respectively. Conversely, in the case of GNRs, we observed large systematics affecting the size estimates between scattering and absorption, and between different immersion media. We expect to achieve a better consistency between datasets by simulating a rod shape which reproduces more faithfully (with particular reference to the transverse section) an electron microscopy characterization we recently obtained; further analyses are under way.

Optical sizing is particularly promising in conjunction with the high-throughput capabilities of widefield image analysis, which could provide a statistical characterization of the sample dispersity complementary to the costly and time-consuming

electron microscopy techniques. Due to the relative affordability of the experimental set-up, and the simplicity of its operation, we reckon this technique has the potential to reach out to a wider audience beyond the circle of academic groups with a well-established expertise in optical set-ups. In fact, funding by the Welsh government has been recently secured by our group with the aim to design a largely automated instrument capable of high-throughput quantitative measurements of the OCS and optical sizing. A patent application has been recently filed to protect the related intellectual property in view of future partnerships with industry.

A

PROGRAMME LISTINGS

We enclose here two programme listings where the main analytical calculations of this thesis are implemented. These are scripts written in MATLAB® language (version R2013b was used) and can be run as they are.[i] For a wider distribution, the codes can be compiled into stand-alone executables, which do not require a license (MATLAB is a proprietary software).

LISTING A.1: Computation of the parameters $\varphi_{i,p}$, $\theta_{i,p}$, and $E_{i,p}$ of the equivalent p-polarized wave introduced in SEC. 3.1.3; in particular, EQ. (3.20) and EQ. (3.21) are implemented. To compute the plots in FIG. 3.4 a `for` loop over the illumination range has been added.

```
clear all;       % Erase all variables stored in memory

%% User input
lambda0 = 550;   % Wavelength in vacuum (in nm)
n1 = 1.52;       % Refractive index of medium 1 (z>0)
n2 = 1.00;       % Refractive index of medium 2 (z<0)
psi_deg = 0;     % Linear polarisation angle (in degrees)
thetam_deg = 0;  % Minimum illumination angle (in degrees)
thetaM_deg = 38; % Maximum illumination angle (in degrees)
z1 = -20;        % Distance from the z=0 interface
%%% No user input below this point

% Angles are converted from degrees to radians
psi  =  psi_deg*pi/180;
thetam = thetam_deg*pi/180;
```

[i] When copying and pasting, care must be taken to lines broken to fit the page width: These are identified by a single line number and must in fact be executed as a single line of code.

```
16 thetaM = thetaM_deg*pi/180;
17
18 clear thetam_deg thetaM_deg psi_deg;
19
20 %% Transmitted intensity for microscope illumination
21
22 syms theta1 phi; % Declaration of symbolic variables
23
24 sin_theta2 = n1/n2*sin(theta1);         % Snell's law
25 cos_theta2 = sqrt( 1 - sin_theta2^2 );  % Trigonometric identity
26
27 % z component of wavevector in medium 2
28 k2z = - 2*pi*n2 / lambda0 * cos_theta2;
29
30 % Fresnel transmission coefficients for the field amplitudes
31 tp  = 2*n1*cos(theta1) / ( n2*cos(theta1) + n1*cos_theta2 ); % p
32 ts  = 2*n1*cos(theta1) / ( n1*cos(theta1) + n2*cos_theta2 ); % s
33
34 % Transmitted electric field
35 Ep2 = [cos_theta2*cos(phi)*cos(psi-phi),... % x component
36        cos_theta2*sin(phi)*cos(psi-phi),... % y component
37      - sin_theta2*cos(psi-phi)          ... % z component
38      ]*tp; % p field amplitude at z = 0
39
40 Es2 = [- sin(phi)*sin(psi-phi),... % x component
41          cos(phi)*sin(psi-phi),... % y component
42          0                     ... % z component
43      ]*ts; % s field amplitude at z = 0
44
45 E2_z1 = ( Ep2 + Es2 )*exp(1i*k2z*z1); % Total amplitude at z = z1
46 % The imaginary exponential accounting for propagation
47 % along x and y is omitted here as only the absolute
48 % value of the field is of relevance
49
50 % Memory is preallocated in order to populate arrays elementwise
51 I2_z1 = cell(1,3);
52 I2pol_z1 = zeros(1,3);
53
54 for j = 1:3
```

```
55      % The integrands are converted into function handles
56      % and stored inside cell arrays {...}
57      I2_z1{j} = matlabFunction( abs(E2_z1(j))^2*...
58      cos(theta1)*sin(theta1),'vars',[theta1 phi] );
59
60      % The weighed plane wave intensity is integrated
61      % over the angular range of excitation
62      I2pol_z1(j) = 2*integral2(I2_z1{j},...
63      thetam,thetaM,0,pi,'method','iterated');
64      % The iterated integration method deals better
65      % with the discontinuity at the critical angle
66
67  end
68  clear theta1 phi
69  clear sin_theta2 cos_theta2 tp ts k2z;
70  clear Ep2 Es2 E2_z1 E2_z2 I2_z1 I2_z2;
71
72  %% Parameters of the equivalent p-polarized wave
73
74  % Analytical solutions (subcritical and supercritical)
75  phiP = atan( sqrt( I2pol_z1(2)/ I2pol_z1(1) ) );
76  phiP_deg = phiP/pi*180; % Conversion to degrees
77
78  thetaP1_sub = asin( n2/n1/sqrt( 1 + (I2pol_z1(1) +
        I2pol_z1(2))/I2pol_z1(3) ) );
79  thetaP1_sup = asin( n2/n1/sqrt( 1 - (I2pol_z1(1) +
        I2pol_z1(2))/I2pol_z1(3) ) );
80  thetaP1_sub_deg = thetaP1_sub/pi*180; % Conversion to degrees
81  thetaP1_sup_deg = thetaP1_sup/pi*180; % Conversion to degrees
82
83  thetaP2_sub = asin( n1/n2*sin(thetaP1_sub) );
84  thetaP2_sup = asin( n1/n2*sin(thetaP1_sup) );
85
86  tp_sub = 2*n1*cos(thetaP1_sub) / ( n2*cos(thetaP1_sub) +
        n1*cos(thetaP2_sub) );
87  tp_sup = 2*n1*cos(thetaP1_sup) / ( n2*cos(thetaP1_sup) +
        n1*cos(thetaP2_sup) );
88
89  kP2z_sub = - 2*pi*n2 / lambda0 * cos(thetaP2_sub);
```

```
kP2z_sup = - 2*pi*n2 / lambda0 * cos(thetaP2_sup);

Ep1_sub = sqrt( sum(I2pol_z1) )/abs(tp_sub);
Ep1_sup = sqrt( sum(I2pol_z1)  / (
    2*(n1/n2*sin(thetaP1_sup))^2-1 ) )...
     *abs( exp( -1i*kP2z_sup*z1 ) / tp_sup );

%% Print output
if isreal(phiP)&& isreal(thetaP1_sub) && isreal(Ep1_sub);
    fprintf('Subcritical solution:\n');
    fprintf('phiP=%.3g%c\t thetaP1=%.3g%c\t Ep1/Em1=%.3g\n',
        phiP_deg,char(176),thetaP1_sub_deg,char(176),Ep1_sub);
else
    fprintf('No real subcritical solution found.\n')
end
if isreal(phiP)&& isreal(thetaP1_sup) && isreal(Ep1_sup);
    fprintf('Supercritical solution:\n');
    fprintf('phiP=%.3g%c\t thetaP1=%.3g%c\t Ep1/Em1=%.3g\n',
        phiP_deg,char(176),thetaP1_sup_deg,char(176),Ep1_sup);
else
    fprintf('No real supercritical solution found.\n')
end

return
```

LISTING A.2: Computation of the parameters τ, ξ, ζ, η^{BF}, and η^{DF} appearing in the absolute OCS formulas EQ. (5.6). The dipole radiation patterns reported in SEC. 5.2 and the integral equations calculated in SEC. 5.3 are implemented. Checks of the consistency of user input have been omitted. To compute the plots in FIG. 5.3 and FIG. 5.4, a `for` loop respectively over $\underline{\theta}_{DF}, \overline{\theta}_{DF}$ and n_2 has been added.

```
clear all;      % Erase all variables stored in memory

%% User input
shape = 4;     % (xx,yy,zz) elements of the polarizability tensor
               % 1=(0,0,1); 2=(1,0,0); 3=(1,1,0); 4=(1,1,1)
```

```
psi_d = 0;     % Polarization angle (in degrees) with respect to
    the mode orientation (to be specified only for shape 2)
n1 = 1.52;     % Refractive index of the illumination medium
n2 = 1.00;     % Refractive index of the detection medium
NA_obj = 0.95; % Numerical aperture of the microscope objective

% Brightfield (BF) illumination range
NAbf_min = 0;      % BF illumination starts from NA = 0
NAbf_max = NA_obj; % Condenser aperture matches the objective NA

% Darkfield (DF) illumination range
NAdf_min = 1.09;   % Numerical aperture of the darkfield ring
NAdf_max = 1.18;   % Numerical aperture of the condenser iris
%%% No user input below this point %%%

%% Parameters derived from user input

% Illumination and detection angles (in radians)
tBF_min = asin(NAbf_min/n1); % Minimum angle for BF illumination
tBF_max = asin(NAbf_max/n1); % Maximum angle for BF illumination
tDF_min = asin(NAdf_min/n1); % Minimum angle for DF illumination
tDF_max = asin(NAdf_max/n1); % Maximum angle for DF illumination
t_obj   = asin(NA_obj/n2);   % Angular acceptance of objective

psi = pi/180*psi_d;      % Polarization angle (in radians)
n = n1/n2;               % Relative refractive index
t1c = real( asin(1/n) ); % Critical angle for transmission 1 to 2
t2c = real( asin(  n) ); % Critical angle for transmission 2 to 1

%% Symbolic variables and dipole radiation patterns
% (Variables are indicated in brackets)
syms ti fi;      % Spherical angles for illumination
syms t2 fe;      % Spherical angles for emission
syms Theta Phi;  % Spherical angles for dipole orientation

sin_t1 = sin(t2)/n;            % Snell's law (t2)
cos_t1 = sqrt( 1 - sin_t1^2 ); % Trigonometric identity (t2)
sin_tt = sin(ti)*n;            % Snell's law (ti)
cos_tt = sqrt( 1 - sin_tt^2 ); % Trigonometric identity (ti)
```

```
44
45 % Fresnel transmission coefficients for the field amplitudes (ti)
46 tp  = 2*cos(ti) / ( cos(ti)/n + cos_tt   ); % p polarization
47 ts  = 2*cos(ti) / ( cos(ti)   + cos_tt/n ); % s polarization
48
49 % Transmittance (ti)
50 Tp = cos_tt/cos(ti)/n*abs(tp)^2;            % p polarization
51 Ts = cos_tt/cos(ti)/n*abs(ts)^2;            % s polarization
52
53 % Dipole radiation pattern in medium 2 (Theta,Phi,t2,fe)
54 P2p_PET = 3/2/pi*( cos(t2)*( n*cos(Theta)*sin(t2) -
       sin(Theta)*cos_t1*cos(fe-Phi) )/(  cos_t1 + n*cos(t2) ) )^2;
55 P2s_PET = 3/2/pi*( cos(t2)*                          sin(Theta)*
             sin(fe-Phi)  /(n*cos_t1 +   cos(t2) ) )^2;
56
57 P2p_TIR = 3/2/pi/(1-n^2)*cos(t2)^2*( n^4*cos(Theta)^2*sin(t2)^2
       + sin(Theta)^2*cos(fe-Phi)^2*(sin(t2)^2 - n^2) )/(
       (n^2+1)*sin(t2)^2 - n^2 );
58 P2s_TIR = 3/2/pi/(1-n^2)*cos(t2)^2*sin(Theta)^2*sin(fe-Phi)^2;
59
60 %% Total radiated power
61
62 % Taylor expansion zero-order coefficients [LukoszOC77]
63 lm_perp = 2/5*(n^5 - 1)/(n^2 - 1); %(9)
64 lm_para = 1/5*(n^5 - 1)/(n^2 - 1) - 1/2*n^2/(n + 1)*(1 -
       3*n/(n^2 + 1)) - 3/2*n^4*log( ( sqrt(n^2 + 1) - n )*(
       sqrt(n^2+1) + 1 )/n )/(n^2 + 1)^(3/2)/(n^2 - 1); %(10)
65 le_perp = 2*n^2/(n^2 + 1)*lm_para - (n^2 - 5)/(n^2 + 1)*lm_perp
       - 2; % (14)
66 le_para = (3*lm_perp - lm_para)/(n^2 + 1); % (15)
67
68 % Radiated power normalized to unbounded n2 medium (Theta)
69 if n==1
70     Ptot = 1; % Isotropic n2 environment
71 else
72     Ptot = cos(Theta)^2*le_perp + sin(Theta)^2*le_para; %
           [LukoszJOSA77a,(3.12)]
73 end
74
```

```
75 %% Excitation and detection parameters
76 switch shape
77     case 1 % Uniaxial polarizability perp to the substrate
78
79 % Calculation of the excitation parameter
80 integrand_EXC = matlabFunction(
       abs(tp*sin_tt)^2*cos(ti)*sin(ti),'vars',ti );
81 Iexc_BF = integral(integrand_EXC,tBF_min,tBF_max);
82 Iexc_DF = integral(integrand_EXC,tDF_min,tDF_max);
83 zeta = Iexc_BF / Iexc_DF; % Excitation param
84
85 % The dipole orientation is parallel to the z axis
86 P2p_PET = subs(P2p_PET,[Theta,Phi],[0,0]);
87 P2p_TIR = subs(P2p_TIR,[Theta,Phi],[0,0]);
88 Ptot = double(subs(Ptot,Theta     , 0  ));
89
90 % Calculation of the detection parameter
91 integrand_PET = matlabFunction( P2p_PET*sin(t2),'vars',t2 );
92 integrand_TIR = matlabFunction( P2p_TIR*sin(t2),'vars',t2 );
93
94 if t_obj < t2c
95     Icoll_PET = integral(integrand_PET,0  ,t_obj);
96     Icoll_TIR = 0;
97 else
98     Icoll_PET = integral(integrand_PET,0  ,t2c  );
99     Icoll_TIR = integral(integrand_TIR,t2c,t_obj);
100 end
101 etaBF = 2*pi/Ptot*(Icoll_PET + Icoll_TIR); % Detection param BF
102 etaDF = etaBF;                             % Detection param DF
103
104     case 2 % Uniaxial polarizability parallel to the substrate
105
106 % Calculation of the excitation parameter
107 integrand_EXC = matlabFunction( ( abs(tp*cos_tt)^2 + abs(ts)^2 +
       0.5*cos(2*psi)*abs(tp*cos_tt + ts)^2
       )*cos(ti)*sin(ti),'vars',ti );
108 Iexc_BF = integral(integrand_EXC, tBF_min,tBF_max);
109 Iexc_DF = integral(integrand_EXC, tDF_min,tDF_max);
110 zeta = Iexc_BF / Iexc_DF; % Excitation param
```

```
111
112 % The dipole is oriented along the x axis
113 P2p_PET = subs(P2p_PET,[Theta,Phi],[pi/2,0]);
114 P2s_PET = subs(P2s_PET,[Theta,Phi],[pi/2,0]);
115 P2p_TIR = subs(P2p_TIR,[Theta,Phi],[pi/2,0]);
116 P2s_TIR = subs(P2s_TIR,[Theta,Phi],[pi/2,0]);
117 Ptot = double(subs(Ptot,Theta     , pi/2  ));
118
119 % Calculation of the detection parameter
120 integrand_PET = matlabFunction( ( P2p_PET + P2s_PET )
        *sin(t2),'vars',[t2 fe] );
121 integrand_TIR = matlabFunction( ( P2p_TIR + P2s_TIR )
        *sin(t2),'vars',[t2 fe] );
122
123 if t_obj < t2c
124     Icoll_PET = integral2(integrand_PET, 0,  t_obj, 0,pi/2,
            'method','iterated');
125     Icoll_TIR = 0;
126 else
127     Icoll_PET = integral2(integrand_PET, 0  ,t2c,   0,pi/2,
            'method','iterated');
128     Icoll_TIR = integral2(integrand_TIR, t2c,t_obj, 0,pi/2,
            'method','iterated');
129 end
130 etaBF = 4/Ptot*(Icoll_PET + Icoll_TIR); % Detection param BF
131 etaDF = etaBF;                          % Detection param DF
132
133     case 3 % Isotropic polarizability parallel to the substrate
134
135 % Calculation of the excitation parameter
136 integrand_EXC = matlabFunction( (abs(tp*cos_tt)^2 +
        abs(ts)^2)*cos(ti)*sin(ti),'vars',ti );
137 Iexc_BF = integral(integrand_EXC,tBF_min,tBF_max);
138 Iexc_DF = integral(integrand_EXC,tDF_min,tDF_max);
139 zeta = Iexc_BF / Iexc_DF; % Excitation param
140
141 % The dipole orientation is perpendicular to the z axis
142 P2p_PET = subs(P2p_PET,[Theta,Phi],[pi/2,pi/2]);
143 P2s_PET = subs(P2s_PET,[Theta,Phi],[pi/2,pi/2]);
```

```
144 P2p_TIR = subs(P2p_TIR,[Theta,Phi],[pi/2,pi/2]);
145 P2s_TIR = subs(P2s_TIR,[Theta,Phi],[pi/2,pi/2]);
146 Ptot = double(subs(Ptot,Theta     , pi/2  ));
147
148 % Calculation of the detection parameter
149 integrand_PET = matlabFunction( ( P2p_PET + P2s_PET
        )*sin(t2),'vars',[t2 fe] );
150 integrand_TIR = matlabFunction( ( P2p_TIR + P2s_TIR
        )*sin(t2),'vars',[t2 fe] );
151
152 if t_obj < t2c
153     Icoll_PET = integral2(integrand_PET,0
            ,t_obj,0,pi/2,'method','iterated');
154     Icoll_TIR = 0;
155 else
156     Icoll_PET = integral2(integrand_PET,0  ,t2c
            ,0,pi/2,'method','iterated');
157     Icoll_TIR =
            integral2(integrand_TIR,t2c,t_obj,0,pi/2,'method','iterated');
158 end
159 etaBF = 4/Ptot*(Icoll_PET + Icoll_TIR); % Detection param BF
160 etaDF = etaBF;                          % Detection param DF
161
162     case 4 % Isotropic polarizability
163
164 % p polarisation excites a dipole with with x and z components
165 tt = asin(n*sin(ti));
166 P2p_PET_pExc = subs( P2p_PET,[Theta,Phi],[real(pi/2-tt),0] );
167 P2s_PET_pExc = subs( P2s_PET,[Theta,Phi],[real(pi/2-tt),0] );
168 P2p_TIR_pExc = subs( P2p_TIR,[Theta,Phi],[real(pi/2-tt),0] );
169 P2s_TIR_pExc = subs( P2s_TIR,[Theta,Phi],[real(pi/2-tt),0] );
170 Ptot_pExc    = subs( Ptot,    Theta     , real(pi/2-tt)    );
171 % fprintf('Theta_p = %.2f\tfor',rad2deg(real(pi/2 -
        asin(n*sin(tDF_min)))));
172 % Monitoring the dipole orientation
173
174 % s polarisation excites a dipole with with a y component only
175 P2p_PET_sExc = subs( P2p_PET,[Theta,Phi],[pi/2,pi/2] );
176 P2s_PET_sExc = subs( P2s_PET,[Theta,Phi],[pi/2,pi/2] );
```

```
177 P2p_TIR_sExc = subs( P2p_TIR,[Theta,Phi],[pi/2,pi/2] );
178 P2s_TIR_sExc = subs( P2s_TIR,[Theta,Phi],[pi/2,pi/2] );
179 Ptot_sExc    = subs( Ptot,    Theta     , pi/2       );
180
181 % Definition of integrands
182 integrand_PET = matlabFunction(...
183     ( abs(tp)^2*(P2p_PET_pExc + P2s_PET_pExc) +...
184       abs(ts)^2*(P2p_PET_sExc + P2s_PET_sExc) )...
185       *cos(ti)*sin(ti)*sin(t2),'vars',[ti t2 fe] );
186 integrand_TIR = matlabFunction(...
187     ( abs(tp)^2*(P2p_TIR_pExc + P2s_TIR_pExc) +...
188       abs(ts)^2*(P2p_TIR_sExc + P2s_TIR_sExc) )...
189       *cos(ti)*sin(ti)*sin(t2),'vars',[ti t2 fe] );
190 integrand_TOT = matlabFunction(...
191     ( abs(tp)^2*Ptot_pExc +...
192       abs(ts)^2*Ptot_sExc )...
193       *cos(ti)*sin(ti),'vars',ti);
194
195 % Collected scattered power under BF illumination
196 if t_obj < t2c
197     Pobj_PET_BF = 2*integral3(integrand_PET, tBF_min,tBF_max, 0,
          t_obj, 0,pi,'method','iterated');
198     Pobj_TIR_BF = 0;
199 else
200     Pobj_PET_BF = 2*integral3(integrand_PET, tBF_min,tBF_max, 0
          ,t2c  , 0,pi,'method','iterated');
201     Pobj_TIR_BF = 2*integral3(integrand_TIR, tBF_min,tBF_max,
          t2c,t_obj, 0,pi,'method','iterated');
202 end
203 Pobj_BF = Pobj_PET_BF + Pobj_TIR_BF;
204
205 % Collected scattered power under DF illumination
206 if t_obj < t2c
207     Pobj_PET_DF = 2*integral3(integrand_PET, tDF_min,tDF_max, 0,
          t_obj, 0,pi,'method','iterated');
208     Pobj_TIR_DF = 0;
209 else
210     Pobj_PET_DF = 2*integral3(integrand_PET, tDF_min,tDF_max, 0
          ,t2c  , 0,pi,'method','iterated');
```

```
211     Pobj_TIR_DF = 2*integral3(integrand_TIR, tDF_min,tDF_max,
            t2c,t_obj, 0,pi,'method','iterated');
212 end
213 Pobj_DF = Pobj_PET_DF + Pobj_TIR_DF;
214
215 % Total scattered power under BF or DF illumination
216 Ptot_BF = integral(integrand_TOT, tBF_min,tBF_max);
217 Ptot_DF = integral(integrand_TOT, tDF_min,tDF_max);
218
219 etaBF  = Pobj_BF / Ptot_BF; % Detection param BF
220 etaDF  = Pobj_DF / Ptot_DF; % Detection param DF
221 zeta   = Ptot_BF / Ptot_DF; % Excitation param
222
223     otherwise
224 fprintf('Error! The variable "shape" must be set to one of the
        following values.\n');
225 fprintf('\t1 = pillar; 2 = rod/dimer; 3 = disc; 4 = sphere.\n');
226     return;
227 end
228
229 %% Transmission and illumination parameters
230 integrand_tau_num = matlabFunction(
        cos(ti)*sin(ti)*(Tp+Ts),'vars',ti );
231 integrand_tau_den = matlabFunction(2*cos(ti)*sin(ti),'vars',ti );
232 tau_num = integral(integrand_tau_num,tBF_min,tBF_max);
233 tau_den = integral(integrand_tau_den,tBF_min,tBF_max);
234 tau = tau_num/tau_den; % Transmission param
235
236 xi = (NAbf_max^2 - NAbf_min^2)/(NAdf_max^2 - NAdf_min^2); %
        Illumination param
237
238 %% Print output
239 fprintf('Parameters for quantitative cross-section
        measurements:\n');
240 fprintf('\t tau = %4.3g \t xi = %4.3g \t etaBF = %4.3g \t etaDF
        = %4.3g \t zeta = %4.3g\n',tau,xi,etaBF,etaDF,zeta);
241
242 return
```

B

SET-UP PERFORMANCE

B.1 ILLUMINATION COMPONENTS

The experimental characterization of the chromatic and spherical aberrations of the condenser lens (Nikon T-C-HNAO) is reported in FIG. B.1. In both cases, the variation Δf of the focal length was determined by adjusting Köhler illumination, i. e. refocusing the image of the field diaphragm in orthoscopic mode. Focusing was achieved by moving the objective while keeping fixed the condenser height, and the position was measured according to the reading of the fine adjuster of the objective focus. A 1.45 NA oil-immersion objective was used in order to investigate the full condenser NA range.

To characterize the chromatic aberration, the illumination wavelength was defined using bandpass filters (Semrock, Brightline®). An optimum z resolution was obtained by closing the aperture diaphragm to an intermediate $\overline{\text{NA}_i}$ (0.5 to 0.8 for this condenser) so to compromise between the large depth of focus at small NA and the blurring introduced by spherical aberration at large NA. In FIG. B.1a $\Delta f/f < 0.2\,\%$ is observed over the investigated wavelength range, indicating a corrected lens systems — a ~10 times larger $\Delta f/f$ is expected for a singlet.

To characterize the spherical aberration, NA_i is varied using several DF discs and closing the aperture diaphragm to produce a narrow illumination cone of well-defined NA_i. FIG. B.1b displays a positive aberration, while the outlier at $\text{NA}_i = 1.34$ is likely produced by phenomena other than spherical aberration.

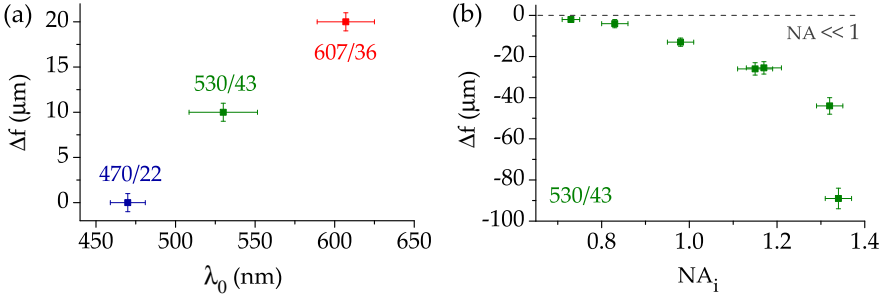

FIGURE B.1: Experimental characterization of the (a) chromatic and (b) spherical aberration of the condenser lens used in our experiments. Δf indicates the measured variation of the condenser focal length. The bandpass filters used are denoted by their centre wavelength/bandwidth, both in nm; the horizontal bars in (a) represent the bandwidth of each filter, in (b) the estimated uncertainty.

FIG. B.2 shows the manufacturer's specifications for the performance of the engineered diffuser (Thorlabs, ED1-C20) we used to produce an even illumination in the BFP of the condenser. The angular distribution of transmitted intensity $I(\theta)$ displays a top-hat pattern: Approximately flat for $|\theta| < 11°$ and dropping off abruptly outside the central range. Let us now es-

FIGURE B.2: Normalized intensity I transmitted through the ED1-C20 diffuser at several wavelengths λ_0. The angular distribution $I(\theta)$ along a plane containing the direction of incidence $\theta = 0$ is shown. Raw data were downloaded from the Thorlabs' website.

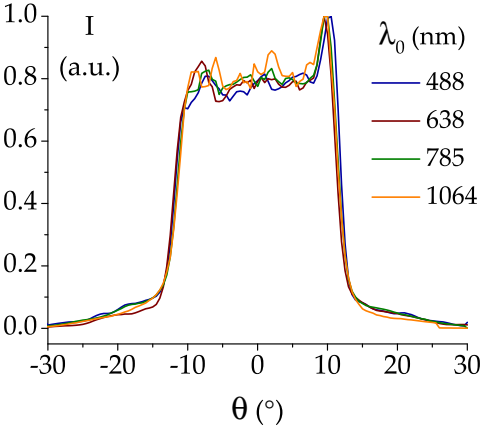

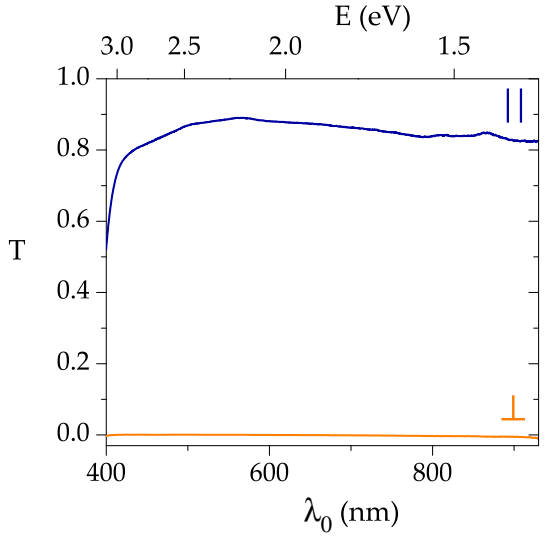

FIGURE B.3: Measured transmittance T of the MeCan WGF polarizing film as a function of wavelength λ_0 for incident light polarized along ($\parallel$) and across ($\perp$) the optical axis.

timate the diameter of the illuminated region in the condenser BFP. The image of the filament is focused onto the BFP by a *field lens* of focal length $f = 129\,\text{mm}$, see FIG. 6.1. Each point of the image is thereby diffused onto a circular region of diameter

$$2\rho = 2 \times 129\,\text{mm} \times \sin 11^\circ \simeq 49\,\text{mm} \tag{B.1}$$

where Abbe's sine condition $\rho = f \sin\theta$ has been used. Thus, the angular spread of the diffuser is deemed sufficient to diffuse homogeneously the 20 mm image of the filament over the 28 mm back aperture of the T-C-HNAO condenser.

The performance of the MeCan WGF™ polarizing film is reported in FIG. B.3. The film has been characterized in house, and offers a co-polarized transmittance $T_\parallel > 0.8$ and a polarization extinction $T_\parallel/T_\perp > 100$ (beyond the sensitivity of our instrument, Ocean Optics HR4000 spectrometer) from $\lambda = 450$ to 900 nm and beyond. In comparison, the polarizers used in Nikon components employ a polymer-based polarizing film which only operates in the range 430 nm–750 nm and has a lower $T_\parallel$ of about 0.5.

B.2 RESOLUTION OF THE SPECTROMETER

The spectrometer has been calibrated by fitting the known position of the emission lines of Kr and Hg lamps. On a day-to-day basis, the grating position is reproduced using a specific emission line of a table lamp as reference. The calibration $\lambda(x)$ is approximately linear (with a RMS error of 0.2 pixel, equivalent to 0.05 nm) so that the *spectral dispersion* is

$$\frac{d\lambda}{dx} \simeq \frac{\Delta\lambda}{N_x p} = \frac{444\,\text{nm}}{1600 \times 16\,\mu\text{m}} = 17.3\,\text{nm/mm}. \tag{B.2}$$

We remind the reader that $\Delta\lambda$ is the full-sensor bandwidth, N_x is the number of pixels along the spectral axis x, and p is the camera pixel pitch.

An ideal monochromatic line still has a finite spectral width when measured with any real instrument. Such *instrumental linewidth* $\text{FWHM}_{\text{instr}}$ is often used to characterize the spectral resolution of a spectrometer and is operatively measured using a highly monochromatic source such as a single-mode dye laser. Several factors contribute to the observed line broadening:

1. The finite spatial width of the input and output slit. For a scanning spectrometer (i. e. a monochromator) the output slit is a physical aperture, for an imaging spectrometer is the pixel size.
2. The resolving "power" of the diffraction grating.
3. The optical aberrations of mirrors and grating, and imperfections of their alignment. In a good instrument, these contribution becomes relevant only when very narrow slits and gratings with a large resolving power are used.

These effects are typically calculated assuming mutual independence, and the respective FWHM are therefore added in quadrature, analogously to the propagation of uncertainty

for independent variables. However, in our case the broadening is dominated by the input slit, which is open quite wide, and all other contributions can be neglected so that $\text{FWHM}_{\text{instr}} \simeq \text{FWHM}_{\text{slit}}$.

Specifically, the line profile is the convolution of the spatial profile of the two slits. The resulting trapezoidal lineshape has

$$\text{FWHM}_{\text{slit}} \simeq (W + p)\frac{d\lambda}{dx} = (80\,\mu\text{m} + 16\,\mu\text{m})1.7 \times 10^{-5} = 1.7\,\text{nm} \tag{B.3}$$

being W the input slit width. The theoretical resolving "power" of our diffraction grating at the $m = 1$ diffraction order is[36]

$$R = m n_g L_g = 1 \times 100\,\text{mm}^{-1} \times 76\,\text{mm} = 7.6 \times 10^3 \tag{B.4}$$

where n_g and L_g are the groove density and side length of the grating. Now, R is essentially defined as the Q factor of the diffraction-broadened peak, and thus one has

$$\text{FWHM}_{\text{diffr}} = \frac{\lambda_c}{R} = \frac{600\,\text{nm}}{7.6 \times 10^3} = 0.08\,\text{nm} \tag{B.5}$$

at the central wavelength λ_c: As expected $\text{FWHM}_{\text{diffr}} \ll \text{FWHM}_{\text{slit}}$.

B.3 SHOT NOISE IN ABSORPTION SPECTROSCOPY

The intrinsic randomness of photon production in the source, and of their conversion to photoelectrons for optical detection, brings about statistical fluctuations of the measured signal known as *shot noise*, which pose a theoretical limit to the SNR achievable in optical measurements. Specifically, subsequent events (i. e. different photons) in the production and conversion processes are uncorrelated, resulting in a Poisson distribution of detected events. Therefore, the *signal* $S = N_e$ corresponds to the average number of photoelectrons, and the variance $\widehat{S} = \sqrt{N_e}$ is the associated statistical uncertainty, or *noise*.

For shot noise evaluation purposes, EQ. (5.6) can be simplified to

$$\sigma_{abs} \simeq A\tau^{BF}\left(1 - \frac{S^{BF}_{NO}}{S^{BF}_{bg}}\frac{S^{BF}_{t_2}}{S^{BF}_{t_1}}\right) \tag{B.6a}$$

$$\sigma_{sca} \simeq A\tau^{BF}\frac{\xi}{\eta^{DF}}\frac{S^{DF}_{NO} - S^{DF}_{bg}}{S^{BF}_{bg} - S^{dk}} \tag{B.6s}$$

where we used $S^{BF}_{bg} \gg S^{dk}$, $S^{DF}_{NO} \gg S^{DF}_{bg}$, and $S^{BF}_{bg}, S^{BF}_{NO} \gg S^{DF}_{NO}$, the latter meaning the scattering contribution to σ_{abs} can be omitted altogether.[i] $S^{BF}_{t_1}$ and $S^{BF}_{t_2}$ appearing in EQ. (B.6a) are the control signal from the adjacent bins used to correct for fluctuations of the lamp intensity between the measurement of S^{BF}_{NO} at time t_1 and the measurement of S^{BF}_{bg} at time t_2, according to the procedure described on P. 166.

Assuming the signals in EQ. (B.6) are independent variables, the usual formula for uncertainty propagation (namely, a linear approximation) applies

$$\begin{aligned}\widehat{\sigma}_{abs} &= \sqrt{\left|\frac{\partial\sigma_{abs}}{\partial S^{BF}_{bg}}\right|^2\left(\widehat{S}^{BF}_{bg}\right)^2 + \left|\frac{\partial\sigma_{abs}}{\partial S^{BF}_{NO}}\right|^2\left(\widehat{S}^{BF}_{NO}\right)^2} \\ &\quad + \left|\frac{\partial\sigma_{abs}}{\partial S^{BF}_{t_1}}\right|^2\left(\widehat{S}^{BF}_{t_1}\right)^2 + \left|\frac{\partial\sigma_{abs}}{\partial S^{BF}_{t_2}}\right|^2\left(\widehat{S}^{BF}_{t_2}\right)^2 \\ &= A\tau^{BF}\sqrt{\left[\frac{S^{BF}_{NO}}{\left(S^{BF}_{bg}\right)^2}\frac{S^{BF}_{t_2}}{S^{BF}_{t_1}}\right]^2\left(\widehat{S}^{BF}_{bg}\right)^2 + \left[\frac{1}{S^{BF}_{bg}}\frac{S^{BF}_{t_2}}{S^{BF}_{t_1}}\right]^2\left(\widehat{S}^{BF}_{NO}\right)^2} \\ &\quad + \left[\frac{S^{BF}_{NO}}{S^{BF}_{bg}}\frac{S^{BF}_{t_2}}{\left(S^{BF}_{t_1}\right)^2}\right]^2\left(\widehat{S}^{BF}_{t_1}\right)^2 + \left[\frac{S^{BF}_{NO}}{S^{BF}_{bg}}\frac{1}{S^{BF}_{t_1}}\right]^2\left(\widehat{S}^{BF}_{t_2}\right)^2}\end{aligned}, \tag{B.7a}$$

i This implies $\widehat{\sigma}_{abs} \simeq \widehat{\sigma}_{ext}$ is calculated in this section.

$$\widehat{\sigma}_{sca} = \sqrt{\left|\frac{\partial\sigma_{sca}}{\partial S_{NO}^{DF}}\right|^2 \left(\widehat{S}_{NO}^{DF}\right)^2 + \left|\frac{\partial\sigma_{sca}}{\partial S_{bg}^{BF}}\right|^2 \left(\widehat{S}_{bg}^{BF}\right)^2}$$

$$= A\tau^{BF}\frac{\xi}{\eta^{DF}}\sqrt{\left[\frac{1}{S_{bg}^{BF}}\right]^2 \left(\widehat{S}_{NO}^{DF}\right)^2 + \left[\frac{S_{NO}^{DF}}{\left(S_{bg}^{BF}\right)^2}\right]^2 \left(\widehat{S}_{bg}^{BF}\right)^2}. \tag{B.7s}$$

Now, according to the discussion above $S_{NO}^{BF} = N_e^{BF}$ and $\widehat{S}_{NO}^{BF} = \sqrt{N_e^{BF}}$; analogously $S_{NO}^{DF} = N_e^{DF}$ and $\widehat{S}_{NO}^{DF} = \sqrt{N_e^{DF}}$. As for S_{bg}^{BF}, it differs from S_{NO}^{BF} only by a few % due to the NO extinction, and thus we can approximate $S_{NO}^{BF} \simeq S_{bg}^{BF}$ and consequently $\widehat{S}_{bg}^{BF} \simeq \widehat{S}_{NO}^{BF}$. Similarly, $S_{t_1}^{BF}$ and $S_{t_2}^{BF}$ differ by a few % at most between themselves (due to temporal fluctuations) and with respect to S_{bg}^{BF} (due to pixel-to-pixel variations of quantum efficiency) and are measured from both bins above and below S_{NO}^{BF} and S_{bg}^{BF}, so that counts are doubled: $S_{t_1}^{BF} \simeq S_{t_2}^{BF} \simeq 2S_{NO}^{BF}$ and consequently $\widehat{S}_{t_1} \simeq \widehat{S}_{t_2} \simeq 2\widehat{S}_{NO}^{BF}$. By substituting these expressions of the signals into EQ. (B.7) one obtains

$$\widehat{\sigma}_{abs} \simeq A\tau^{BF}\sqrt{\frac{3}{N_e^{BF}}} \tag{B.8a}$$

$$\widehat{\sigma}_{sca} \simeq A\tau^{BF}\frac{\xi}{\eta^{DF}}\sqrt{\frac{(N_e^{DF})}{(N_e^{BF})^2} + \frac{(N_e^{DF})^2}{(N_e^{BF})^3}} \tag{B.8s}$$

In order to evaluate numerically the shot noise in our measurements, we need to estimate the typical experimental values of N_e for BF and DF illumination. N_e^{BF} (N_e^{DF}) is the product of the following figures:

- 5×10^4 (4×10^4) typical counts per pixels (per bin) — saturation is $2^{16} \simeq 6.5 \times 10^4$ for the 16-bit CCD sensor used
- $b_x \times b_y = 10$ pixels binned in software corresponding to a spectral point in BF spectra

- 300 (1) frames accumulated per spectrum
- 3.3 (1.7) photoelectrons per count for 1x (2x) preamplifier and 2.5 MHz (50 kHz) readout rate used

which yield $N_e^{BF} = 5 \times 10^8$ and $N_e^{DF} = 7 \times 10^4$. Using these values and $A = 1\,\mu m^2$, $\tau^{BF} \sim 1$, and $\xi/\eta^{DF} \sim 30$ EQ. (B.8) give $\widehat{\sigma}_{abs} = 77\,nm^2$ and $\widehat{\sigma}_{sca} = 16\,nm^2$. Interestingly, $\widehat{\sigma}_{sca}$ is dominated by the signal contribution, that is, the first term in EQ. (B.7s) is much larger than the second.

C

ADDITIONAL EXPERIMENTAL DATA

C.1 GOLD NANOSPHERE SPECTROSCOPY

Optical sizing depends to a large extent on the material description adopted in the analytical calculations or numerical simulations. For example, FIG. C.1a and b contain the same experimental data as FIG. 6.5a and b, but the simulated spectra are obtained using the "single-crystal" $\varepsilon_{Au}(\lambda_0)$ dataset by Olmon et al.[18] instead of the one by Johnson and Christy (J&C).[15] The two datasets are shown in FIG. 1.2a and c. They differ little in Re ε, and thus the resulting LSPR position is the same; but Olmon displays a smaller Im ε at $\lambda_{LSPR} \simeq 560\,\text{nm}$, bringing about a sharper resonance. Consequently, a 2 to 3 nm smaller estimate of D is obtained when the permittivity by Olmon is utilized.

Comparison of the measured and simulated linewidth can help determining which dataset best describes the studied system: A good agreement ensures Im ε represents well the experimental damping. FIG. C.1c and d show that the LSPRs simulated with Olmon are significantly narrower than their experimental counterparts, whereas simulations with J&C get much closer. The latter dataset was consequently deemed more adequate to describe the GNSs and has been used for the simulations presented SEC. 6.2. Other ε_{Au} datasets available in literature display even smaller values of Im ε in this spectral region (see FIG. 1.2) and should therefore be *a fortiori* discarded.

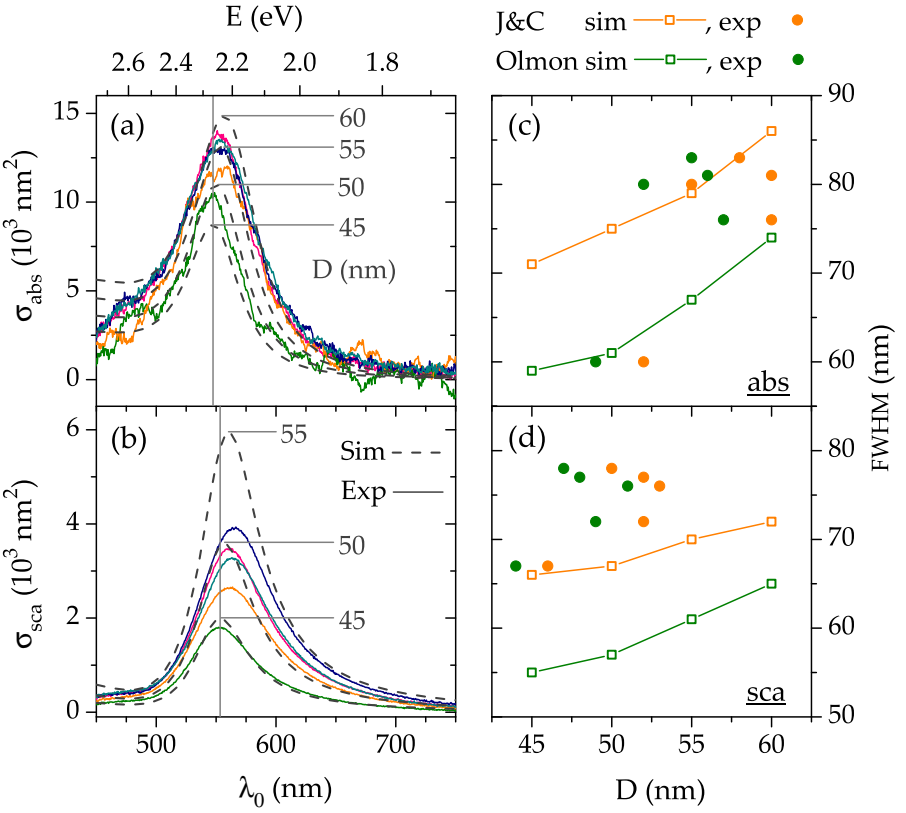

FIGURE C.1: Absolute (a) absorption σ_{abs} and (b) scattering σ_{sca} cross-section spectra of five GNSs in a homogeneous $n = 1.52$ optical environment. Solid lines are experimental data (each colour identifying a specific GNS) and dashed lines are simulations for GNSs of different diameter D using $\varepsilon_{Au}(\lambda_0)$ by Olmon et al.[18] The vertical lines indicate the LSPR of the $D = 45\,nm$ simulation. FWHM against D for the (c) σ_{abs} and (d) σ_{sca} spectra in FIG. 6.5a,b (orange) and in the panels a,b of this figure (green). In the case of experimental data (full symbols) D in abscissa is estimated comparing the OCS amplitude to simulations obtained with the corresponding ε_{Au} dataset.

C.2 GOLD NANOROD SPECTROSCOPY

Each data point in FIG. 6.7c is obtained by independently fitting an experimental OCS spectrum; all these spectra are reported in FIG. C.2. Two objects (#5 and #7) have been excluded from the analysis because they displayed spectral features inconsistent with a rod-like response — such as multiple peaks and a too weak polarization dependence.

The optical sizing presented in FIG. 6.7c largely depends on how the GNR is modelled in the simulations, particularly on the details of the shape. FIG. C.3 provides an example where the hemispherical caps (radius D/2) are replaced by oblate spheroids (semiaxis D/4). In the model with oblate caps the ε_{Au} dataset by Olmon et al. was used instead of J&C. The main effect on sizing is a reduction of the estimated AR from an average of approximately 2.3 in FIG. 6.7c to 2.0 here, further away from typical TEM values. In fact, flattening the caps results in a red shift of the LSPR,[126] and the AR must be reduced in order to compensate.

In general, high-resolution TEM imaging and TEM tomography can drive the choice of a characteristic shape for a given sample. In our case, the observed caps are only slightly oblate and closer to the hemispherical model presented in the main text, see FIG. 6.6.

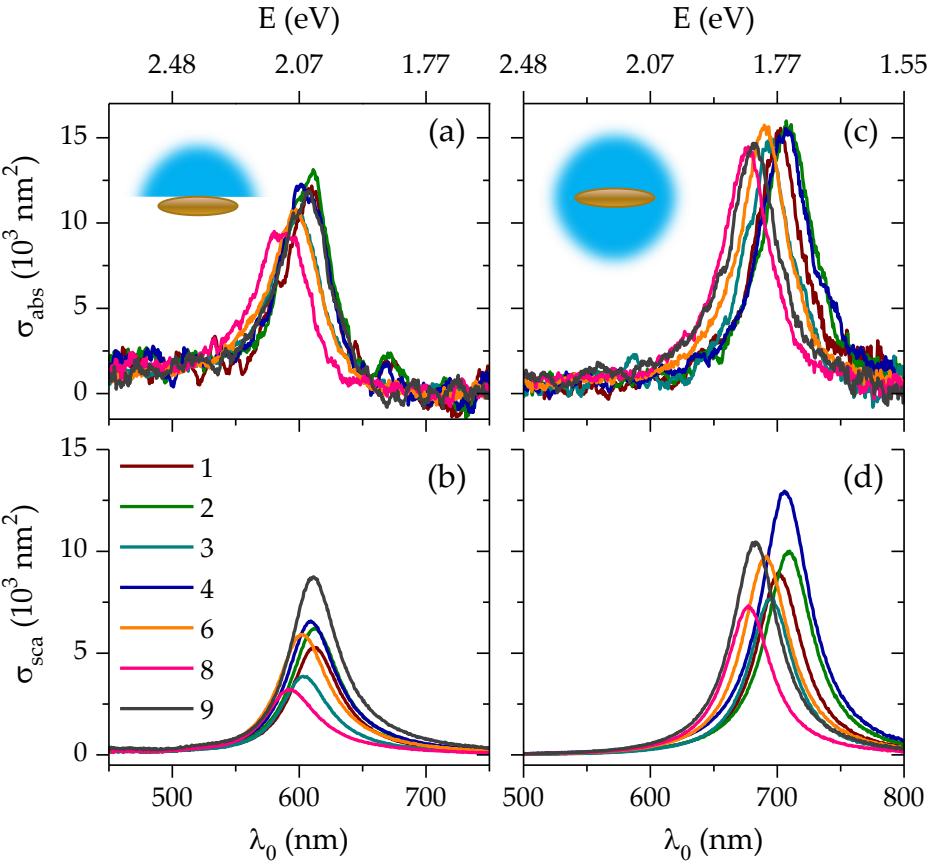

FIGURE C.2: Experimental OCS spectra of individual GNRs identified by a number. The same GNRs deposited on a glass substrate ($n_1 = 1.52$) were measured; first (a,b) immersed in air ($n_2 = 1.00$), and then (c,d) covered by index-matching fluid ($n_2 = 1.52$).

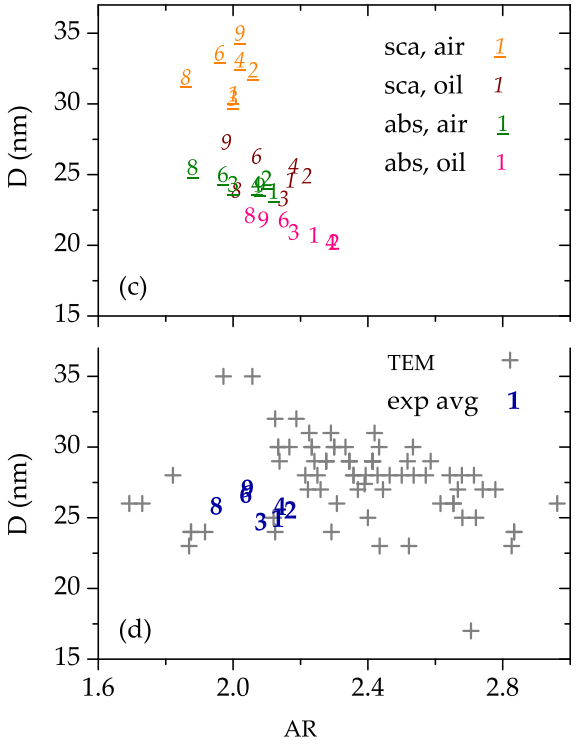

FIGURE C.3: (c) Aspect ratio (AR) and diameter D of individual GNRs determined as free parameters of a separate numerical fit of each experimental spectra in FIG. C.2. (d) Average of the four data-sets in (c), superimposed to the AR and D measured in a TEM micrograph of 80 GNRs of the same batch (each cross is a different rod, several falling outside of the plotted range).

REFERENCES

[1] R. P. Feynman, 'There's plenty of room at the bottom', Engineering and Science **23**, 22 (1960).

[2] C. F. Bohren and D. R. Huffman, 'Absorption and scattering of light by small particles' (Wiley-VCH Verlag, 1998).

[3] M. I. Mishchenko and L. D. Travis, 'Scattering, absorption, and emission of light by small particles' (NASA, 2002).

[4] X. Fan, W. Zheng and D. J. Singh, 'Light scattering and surface plasmons on small spherical particles', Light: Science & Applications **3**, e179 (2014).

[5] J. W. Strutt, 'On the light from the sky, its polarization and colour', Philos. Mag. **41**, 107 and 274 (1871).

[6] S. A. Maier, 'Plasmonics: Fundamentals and applications' (Springer, 2007).

[7] G. Mie, 'Beiträge zur optik trüber medien, speziell kolloidaler metallösungen', Ann. Phys. **330**, 377 (1908).

[8] M. Quinten, 'Optical properties of nanoparticle systems' (Wiley-VCH Verlag, 2011).

[9] M. J. Berg, C. M. Sorensen and A. Chakrabarti, 'Extinction and the optical theorem. Part I. Single particles', J. Opt. Soc. Am. A **25**, 1504 (2008).

[10] M. Faraday, 'Experimental relations of gold (and other metals) to light', Philos. Trans. Roy. Soc. London **147**, 145 (1857).

[11] M. I. Stockman, 'Nanoplasmonics: Past, present, and glimpse into future', Opt. Express **19**, 22029 (2011).

[12] M. L. Brongersma, 'Introductory lecture: Nanoplasmonics', Faraday Discuss. **178**, 9 (2015).

[13] E. Ringe, B. Sharma, A.-I. Henry, L. D. Marks and R. P. Van Duyne, 'Single nanoparticle plasmonics', Phys. Chem. Chem. Phys. **15**, 4110 (2013).

[14] E. A. Coronado, E. R. Encina and F. D. Stefani, 'Optical properties of metallic nanoparticles: Manipulating light, heat and forces at the nanoscale', Nanoscale **3**, 4042 (2011).

[15] P. B. Johnson and R. W. Christy, 'Optical constants of noble metals', Phys. Rev. B **6**, 4370 (1972).

[16] K. M. McPeak, S. V. Jayanti, S. J. P. Kress, S. Meyer, S. Iotti, A. Rossinelli and D. J. Norris, 'Plasmonic films can easily be better: Rules and recipes', ACS Photon. **2**, 326 (2015).

[17] S. Babar and J. H. Weaver, 'Optical constants of Cu, Ag, and Au revisited', Appl. Opt. **54**, 477 (2015).

[18] R. L. Olmon, B. Slovick, T. W. Johnson, D. Shelton, S.-H. Oh, G. D. Boreman and M. B. Raschke, 'Optical dielectric function of gold', Phys. Rev. B **86**, 235147 (2012).

[19] N. W. Ashcroft and N. Mermin, 'Solid state physics' (Holt, Rineheart and Winston, 1976).

[20] A. Crut, P. Maioli, N. Del Fatti and F. Vallée, 'Optical absorption and scattering spectroscopies of single nano-objects', Chem. Soc. Rev. **43**, 3921 (2014).

[21] C. Louis and O. Pluchery, eds., 'Gold nanoparticles for physics, chemistry and biology', 2nd ed. (World Scientific, 2017).

[22] S. Link, M. B. Mohamed and M. A. El-Sayed, 'Simulation of the optical absorption spectra of gold nanorods as a function of their aspect ratio and the effect of the medium dielectric constant', J. Phys. Chem. B **103**, 3073 (1999), Erratum J. Phys. Chem. B **109**, 10531 (2005).

[23] E. Ringe, M. R. Langille, K. Sohn, J. Zhang, J. Huang, C. A. Mirkin, R. P. V. Duyne and L. D. Marks, 'Plasmon length: A universal parameter to describe size effects in gold nanoparticles', J. Phys. Chem. Lett. **3**, 1479 (2012).

[24] V. Myroshnychenko, J. Rodríguez-Fernández, I. Pastoriza-Santos, A. M. Funston, C. Novo, P. Mulvaney, L. M. Liz-Marzán and F. J. G. de Abajo, 'Modelling the optical response of gold nanoparticles', Chem. Soc. Rev. **37**, 1792 (2008).

[25] P. Bobbert and J. Vlieger, 'Light scattering by a sphere on a substrate', Phys. A **137**, 209 (1986).

[26] E. Fucile, P. Denti, F. Borghese, R. Saija and O. I. Sindoni, 'Optical properties of a sphere in the vicinity of a plane surface', J. Opt. Soc. Am. AA **14**, 1505 (1997).

[27] J. Lermé, C. Bonnet, M. Broyer, E. Cottancin, D. Manchon and M. Pellarin, 'Optical properties of a particle above a dielectric interface: Cross sections, benchmark calculations, and analysis of the intrinsic substrate effects', J. Phys. Chem C **117**, 6383 (2013).

[28] A. Sommerfeld, 'Über die ausbreitung der wellen in der drahtlosen telegraphie', Ann. Phys. **333**, 665 (1909).

[29] W. Lukosz and R. Kunz, 'Fluorescence lifetime of magnetic and electric dipoles near a dielectric interface', Opt. Commun. **20**, 195 (1977).

[30] W. Lukosz and R. E. Kunz, 'Light emission by magnetic and electric dipoles close to a plane interface. I. Total radiated power', J. Opt. Soc. Am. **67**, 1607 (1977).

[31] W. Lukosz and R. E. Kunz, 'Light emission by magnetic and electric dipoles close to a plane dielectric interface. II. Radiation patterns of perpendicular oriented dipoles', J. Opt. Soc. Am. **67**, 1615 (1977).

[32] W. Lukosz, 'Light emission by magnetic and electric dipoles close to a plane dielectric interface. III. Radiation patterns of dipoles with arbitrary orientation', J. Opt. Soc. Am. **69**, 1495 (1979).

[33] L. Novotny and B. Hecht, 'Principles of nano-optics', 2nd ed. (Cambridge Univ. press, 2012).

[34] M. W. Knight, Y. Wu, J. B. Lassiter, P. Nordlander and N. J. Halas, 'Substrates matter: Influence of an adjacent dielectric on an individual plasmonic nanoparticle', Nano Lett. **9**, 2188 (2009).

[35] K. C. Vernon, A. M. Funston, C. Novo, D. E. Gómez, P. Mulvaney and T. J. Davis, 'Influence of particle–substrate interaction on localized plasmon resonances', Nano Lett. **10**, 2080 (2010).

[36] E. Hecht, 'Optics', 4th ed. (Addison-Wesley, 2002).

[37] M. José-Yacamán, L. Rendón, J. Arenas and M. C. S. Puche, 'Maya blue paint: An ancient nanostructured material', Science **273**, 223 (1996).

[38] P. Colomban, 'The use of metal nanoparticles to produce yellow, red and iridescent colour, from Bronze Age to present times in lustre pottery and glass: Solid state chemistry, spectroscopy and nanostructure', J. Nano Res. **8**, 109 (2009).

[39] I. Freestone, N. Meeks, M. Sax and C. Higgitt, 'The Lycurgus Cup — A Roman nanotechnology', Gold Bull. **40**, 270 (2007).

[40] P. Mühlschlegel, H.-J. Eisler, O. J. F. Martin, B. Hecht and D. W. Pohl, 'Resonant optical antennas', Science **308**, 1607 (2005).

[41] L. Novotny and N. van Hulst, 'Antennas for light', Nat. Photonics **5**, 83 (2011).

[42] S. Kühn, U. Håkanson, L. Rogobete and V. Sandoghdar, 'Enhancement of single-molecule fluorescence using a gold nanoparticle as an optical nanoantenna', Phys. Rev. Lett. **97**, 017402 (2006).

[43] T. H. Taminiau, F. D. Stefani, F. B. Segerink and N. F. van Hulst, 'Optical antennas direct single-molecule emission', Nat. Photonics **2**, 234 (2008).

[44] J. A. Schuller, E. S. Barnard, W. Cai, Y. C. Jun, J. S. White and M. L. Brongersma, 'Plasmonics for extreme light concentration and manipulation', Nat. Mater. **9**, 193 (2010).

[45] A. Kinkhabwala, Z. Yu, S. Fan, Y. Avlasevich, K. Müllen and W. E. Moerner, 'Large single-molecule fluorescence enhancements produced by a bowtie nanoantenna', Nat. Photonics **3**, 654 (2009).

[46] K. Li, M. I. Stockman and D. J. Bergman, 'Self-similar chain of metal nanospheres as an efficient nanolens', Phys. Rev. Lett. **91**, 227402 (2003).

[47] M. A. Garcia, 'Surface plasmons in metallic nanoparticles: Fundamentals and applications', J. Phys. D: Appl. Phys. **44**, 283001 (2011), Erratum J. Phys. D: Appl. Phys. **45**, 389501 (2012).

[48] E. C. Dreaden, A. M. Alkilany, X. Huang, C. J. Murphy and M. A. El-Sayed, 'The golden age: Gold nanoparticles for biomedicine', Chem. Soc. Rev. **41**, 2740 (2012).

[49] N. S. Abadeer and C. J. Murphy, 'Recent progress in cancer thermal therapy using gold nanoparticles', J. Phys. Chem. C **120**, 4691 (2016).

[50] X. Huang, I. H. El-Sayed, W. Qian and M. A. El-Sayed, 'Cancer cell imaging and photothermal therapy in the near-infrared region by using gold nanorods', J. Am. Chem. Soc. **128**, 2115 (2006).

[51] D. O'Neal, L. R. Hirsch, N. J. Halas, J. D. Payne and J. L. West, 'Photo-thermal tumor ablation in mice using near infrared-absorbing nanoparticles', Cancer Lett. **209**, 171 (2004).

[52] Nanospectra Biosciences, Inc., *Pilot study of AuroLase™ therapy in refractory and/or recurrent tumors of the head and neck*, `https://clinicaltrials.gov/ct2/show/study/NCT00848042` (visited on 31/07/2017).

[53] C. Clavero, 'Plasmon-induced hot-electron generation at nanoparticle/metal-oxide interfaces for photovoltaic and photocatalytic devices', Nat. Photonics **8**, 95 (2014).

[54] H. A. Atwater and A. Polman, 'Plasmonics for improved photovoltaic devices', Nat. Mater. **9**, 205 (2010).

[55] H. R. Stuart and D. G. Hall, 'Absorption enhancement in silicon-on-insulator waveguides using metal island films', Appl. Phys. Lett. **69**, 2327 (1996).

[56] K. Saha, S. S. Agasti, C. Kim, X. Li and V. M. Rotello, 'Gold nanoparticles in chemical and biological sensing', Chem. Rev. **112**, 2739 (2012).

[57] K. M. Mayer and J. H. Hafner, 'Localized surface plasmon resonance sensors', Chem. Rev. **111**, 3828 (2011).

[58] G. L. Liu, Y.-T. Long, Y. Choi, T. Kang and L. P. Lee, 'Quantized plasmon quenching dips nanospectroscopy via plasmon resonance energy transfer', Nat. Methods **4**, 1015 (2007).

[59] B. Luk'yanchuk, N. I. Zheludev, S. A. Maier, N. J. Halas, P. Nordlander, H. Giessen and C. T. Chong, 'The Fano resonance in plasmonic nanostructures and metamaterials', Nat. Mater. **9**, 707 (2010).

[60] T. Xie, C. Jing and Y.-T. Long, 'Single plasmonic nanoparticles as ultrasensitive sensors', Analyst **142**, 409 (2017).

[61] P. Nordlander, C. Oubre, E. Prodan, K. Li and M. I. Stockman, 'Plasmon hybridization in nanoparticle dimers', Nano Lett. **4**, 899 (2004).

[62] C. Sönnichsen, B. M. Reinhard, J. Liphardt and A. P. Alivisatos, 'A molecular ruler based on plasmon coupling of single gold and silver nanoparticles', Nat. Biotechnol. **23**, 741 (2005).

[63] L. Payne, G. Zoriniants, F. Masia, K. P. Arkill, P. Verkade, D. Rowles, W. Langbein and P. Borri, 'Optical microspectroscopy of single metallic nanoparticles: Quantitative extinction and transient resonant four-wave mixing', Faraday Discuss. **184**, 305 (2015).

[64] R. Boyd, 'Nonlinear optics', 3rd ed. (Elsevier, 2008).

[65] Y. Wang, C.-Y. Lin, A. Nikolaenko, V. Raghunathan and E. O. Potma, 'Four-wave mixing microscopy of nanostructures', Adv. Opt. Photon. **3**, 1 (2011).

[66] H. Wang, T. B. Huff, D. A. Zweifel, W. He, P. S. Low, A. Wei and J.-X. Cheng, '*In vitro* and *in vivo* two-photon luminescence imaging of single gold nanorods', Proc. Natl. Acad. Sci. USA **102**, 15752 (2005).

[67] M. Lippitz, M. A. van Dijk and M. Orrit, 'Third-harmonic generation from single gold nanoparticles', Nano Lett. **5**, 799 (2005).

[68] F. Masia, W. Langbein, P. Watson and P. Borri, 'Resonant four-wave mixing of gold nanoparticles for three-dimensional cell microscopy', Opt. Lett. **34**, 1816 (2009).

[69] G. Zoriniants, F. Masia, N. Giannakopoulou, W. Langbein and P. Borri, 'Background-free 3D nanometric localization and sub-nm asymmetry detection of single plasmonic nanoparticles by four-wave mixing interferometry with optical vortices', Phys. Rev. X **7**, 041022 (2017).

[70] J. Olson, S. Dominguez-Medina, A. Hoggard, L.-Y. Wang, W.-S. Chang and S. Link, 'Optical characterization of single plasmonic nanoparticles', Chem. Soc. Rev. **44**, 40 (2015).

[71] A. Arbouet, D. Christofilos, N. Del Fatti, F. Vallée, J. R. Huntzinger, L. Arnaud, P. Billaud and M. Broyer, 'Direct measurement of the single-metal-cluster optical absorption', Phys. Rev. Lett. **93**, 127401 (2004).

[72] D. Christofilos, J.-C. Blancon, J. Arvanitidis, A. S. Miguel, A. Ayari, N. Del Fatti and F. Vallée, 'Optical imaging and absolute absorption cross section measurement of individual nano-objects on opaque substrates: Single-wall carbon nanotubes on silicon', J. Phys. Chem. Lett. **3**, 1176 (2012).

[73] P. Billaud, S. Marhaba, N. Grillet, E. Cottancin, C. Bonnet, J. Lermé, J.-L. Vialle, M. Broyer and M. Pellarin, 'Absolute optical extinction measurements of single nano-objects by spatial modulation spectroscopy using a white lamp', Rev. Sci. Instrum. **81**, 043101 (2010).

[74] M. Husnik, S. Linden, R. Diehl, J. Niegemann, K. Busch and M. Wegener, 'Quantitative experimental determination of scattering and absorption cross-section spectra of individual optical metallic nanoantennas', Phys. Rev. Lett. **109**, 233902 (2012).

[75] D. Boyer, P. Tamarat, A. Maali, B. Lounis and M. Orrit, 'Photothermal imaging of nanometer-sized metal particles among scatterers', Science **297**, 1160 (2002).

[76] S. Berciaud, L. Cognet, G. A. Blab and B. Lounis, 'Photothermal heterodyne imaging of individual nonfluorescent nanoclusters and nanocrystals', Phys. Rev. Lett. **93**, 257402 (2004).

[77] P. Berto, E. B. Ureña, P. Bon, R. Quidant, H. Rigneault and G. Baffou, 'Quantitative absorption spectroscopy of nano-objects', Phys. Rev. B **86**, 165417 (2012).

[78] C. R. Carey, T. LeBel, D. Crisostomo, J. Giblin, M. Kuno and G. V. Hartland, 'Imaging and absolute extinction cross-section measurements of nanorods and nanowires through polarization modulation microscopy', J. Phys. Chem. C **114**, 16029 (2010).

[79] H. Siedentopf and R. Zsigmondy, 'Uber sichtbarmachung und größenbestimmung ultramikoskopischer teilchen, mit besonderer anwendung auf goldrubingläser', Ann. Phys. **315**, 1 (1902).

[80] L. J. E. Anderson, K. M. Mayer, R. D. Fraleigh, Y. Yang, S. Lee and J. H. Hafner, 'Quantitative measurements of individual gold nanoparticle scattering cross sections', J. Phys. Chem. C **114**, 11127 (2010).

[81] J. Ortega-Arroyo and P. Kukura, 'Interferometric scattering microscopy (iSCAT): New frontiers in ultrafast and ultrasensitive optical microscopy', Phys. Chem. Chem. Phys. **14**, 15625 (2012).

[82] K. Lindfors, T. Kalkbrenner, P. Stoller and V. Sandoghdar, 'Detection and spectroscopy of gold nanoparticles using supercontinuum white light confocal microscopy', Phys. Rev. Lett. **93**, 037401 (2004).

[83] C. McPhee, G. Zoriniants, W. Langbein and P. Borri, 'Measuring the lamellarity of giant lipid vesicles with differential interference contrast microscopy', Biophys. J. **105**, 1414 (2013).

[84] G. Wang, W. Sun, Y. Luo and N. Fang, 'Resolving rotational motions of nano-objects in engineered environments and live cells with gold nanorods and differential interference contrast microscopy', J. Am. Chem. Soc. **132**, 16417 (2010).

[85] I. Pope, L. Payne, G. Zoriniants, E. Thomas, O. Williams, P. Watson, W. Langbein and P. Borri, 'Coherent anti-Stokes Raman scattering microscopy of single nanodiamonds', Nat. Nanotechnol. **9**, 940 (2014).

[86] B. E. A. Saleh and M. C. Teich, 'Fundamentals of photonics', 2nd ed. (Wiley, 2007).

[87] B. Richards and E. Wolf, 'Electromagnetic diffraction in optical systems. II. Structure of the image field in an aplanatic system', Proc. R. Soc. A **253**, 358 (1959).

[88] J. Parsons, C. Burrows, J. Sambles and W. Barnes, 'A comparison of techniques used to simulate the scattering of electromagnetic radiation by metallic nanostructures', J. Mod. Opt. **57**, 356 (2010).

[89] J. Zhao, A. O. Pinchuk, J. M. McMahon, S. Li, L. K. Ausman, A. L. Atkinson and G. C. Schatz, 'Methods for describing the electromagnetic properties of silver and gold nanoparticles', Acc. Chem. Res. **41**, 1710 (2008).

[90] J.-M. Jin, 'The finite element method in electromagnetics', 3rd ed. (IEEE Comp. Soc. press, 2014).

[91] P. Monk, 'Finite element methods for Maxwell's equations' (Oxford Univ. press, 2003).

[92] J. A. Stratton and L. J. Chu, 'Diffraction theory of electromagnetic waves', Phys. Rev. **56**, 99 (1939).

[93] P. S. Carney, J. C. Schotland and E. Wolf, 'Generalized optical theorem for reflection, transmission, and extinction of power for scalar fields', Phys. Rev. E **70**, 036611 (2004).

[94] A. Small, J. Fung and V. N. Manoharan, 'Generalization of the optical theorem for light scattering from a particle at a planar interface', J. Opt. Soc. Am. A **30**, 2519 (2013).

[95] J. Yang, J.-P. Hugonin and P. Lalanne, 'Near-to-far field transformations for radiative and guided waves', ACS Photon. **3**, 395 (2016).

[96] S. Zhang, K. Bao, N. J. Halas, H. Xu and P. Nordlander, 'Substrate-induced Fano resonances of a plasmonic nanocube: A route to increased-sensitivity localized surface plasmon resonance sensors revealed', Nano Lett. **11**, 1657 (2011).

[97] Y. R. Davletshin, A. Lombardi, M. F. Cardinal, V. Juvé, A. Crut, P. Maioli, L. M. Liz-Marzán, F. Vallée, N. Del Fatti and J. C. Kumaradas, 'A quantitative study of the environmental effects on the optical response of gold nanorods', ACS Nano **6**, 8183 (2012).

[98] J.-X. Cheng and X. S. Xie, eds., 'Coherent Raman scattering microscopy' (CRC Press, 2013).

[99] A. Zumbusch, G. R. Holtom and X. S. Xie, 'Three-dimensional vibrational imaging by coherent anti-Stokes Raman scattering', Phys. Rev. Lett. **82**, 4142 (1999).

[100] E. Liang, A. Weippert, J.-M. Funk, A. Materny and W. Kiefer, 'Experimental observation of surface-enhanced coherent anti-Stokes Raman scattering', Chem. Phys. Lett. **227**, 115 (1994).

[101] C. Steuwe, C. F. Kaminski, J. J. Baumberg and S. Mahajan, 'Surface-enhanced coherent anti-Stokes Raman scattering on nanostructured gold surfaces', Nano Lett. **11**, 5339 (2011).

[102] T.-W. Koo, S. Chan and A. A. Berlin, 'Single-molecule detection of biomolecules by surface-enhanced coherent anti-Stokes Raman scattering', Opt. Lett. **30**, 1024 (2005).

[103] T. Ichimura, N. Hayazawa, M. Hashimoto, Y. Inouye and S. Kawata, 'Local enhancement of coherent anti-Stokes Raman scattering by isolated gold nanoparticles', J. Raman Spectrosc. **34**, 651 (2003).

[104] T. Ichimura, N. Hayazawa, M. Hashimoto, Y. Inouye and S. Kawata, 'Tip-enhanced coherent anti-Stokes Raman scattering for vibrational nanoimaging', Phys. Rev. Lett. **92**, 220801 (2004).

[105] S. Yampolsky, D. A. Fishman, S. Dey, E. Hulkko, M. Banik, E. O. Potma and V. A. Apkarian, 'Seeing a single molecule vibrate through time-resolved coherent anti-Stokes Raman scattering', Nat. Photonics **8**, 650 (2014).

[106] Y. Zhang, Y.-R. Zhen, O. Neumann, J. K. Day, P. Nordlander and N. J. Halas, 'Coherent anti-Stokes Raman scattering with single-molecule sensitivity using a plasmonic Fano resonance', Nat. Commun. **5**, 4424 (2014).

[107] G. Eesley, M. Levenson and W. Tolles, 'Optically heterodyned coherent Raman spectroscopy', IEEE J. Quantum Electron. **14**, 45 (1978).

[108] E. O. Potma, C. L. Evans and X. S. Xie, 'Heterodyne coherent anti-Stokes Raman scattering (CARS) imaging', Opt. Lett. **31**, 241 (2006).

[109] I. Pope, W. Langbein, P. Watson and P. Borri, 'Simultaneous hyperspectral differential-CARS, TPF and SHG microscopy with a single 5 fs Ti:Sa laser', Opt. Express **21**, 7096 (2013).

[110] F. Masia, W. Langbein and P. Borri, 'Measurement of the dynamics of plasmons inside individual gold nanoparticles using a femtosecond phase-resolved microscope', Phys. Rev. B **85**, 235403 (2012).

[111] U. Gubler and C. Bosshard, 'Optical third-harmonic generation of fused silica in gas atmosphere: Absolute value of the third-order nonlinear optical susceptibility $\chi^{(3)}$', Phys. Rev. B **61**, 10702 (2000).

[112] A. Karuna, F. Masia, P. Borri and W. Langbein, 'Hyperspectral volumetric coherent anti-Stokes Raman scattering microscopy: Quantitative volume determination and NaCl as nonresonant standard', J. Raman Spectrosc. **47**, 1167 (2016).

[113] R. W. Boyd, Z. Shi and I. D. Leon, 'The third-order nonlinear optical susceptibility of gold', Opt. Commun. **326**, 74 (2014).

[114] J. Renger, R. Quidant, N. van Hulst and L. Novotny, 'Surface-enhanced nonlinear four-wave mixing', Phys. Rev. Lett. **104**, 046803 (2010).

[115] E. Poutrina, C. Ciracì, D. J. Gauthier and D. R. Smith, 'Enhancing four-wave-mixing processes by nanowire arrays coupled to a gold film', Opt. Express **20**, 11005 (2012).

[116] B. Jin and C. Argyropoulos, 'Enhanced four-wave mixing with nonlinear plasmonic metasurfaces', Sci. Rep. **6**, 28746 (2016).

[117] P. D. Maker and R. W. Terhune, 'Study of optical effects due to an induced polarization third order in the electric field strength', Phys. Rev. **137**, A801 (1965).

[118] L. Payne, 'Optical extinction and coherent multiphoton microspectroscopy of single nanoparticles', PhD thesis (Cardiff University, 2015).

[119] O. L. Muskens, P. Billaud, M. Broyer, N. Del Fatti and F. Vallée, 'Optical extinction spectrum of a single metal nanoparticle: Quantitative characterization of a particle and of its local environment', Phys. Rev. B **78**, 205410 (2008).

[120] A. Lombardi, M. Loumaigne, A. Crut, P. Maioli, N. Del Fatti, F. Vallée, M. Spuch-Calvar, J. Burgin, J. Majimel and M. Tréguer-Delapierre, 'Surface plasmon resonance properties of single elongated nano-objects: Gold nanobipyramids and nanorods', Langmuir **28**, 9027 (2012).

[121] L. Payne, W. Langbein and P. Borri, 'Polarization-resolved extinction and scattering cross-section of individual gold nanoparticles measured by wide-field microscopy on a large ensemble', Appl. Phys. Lett. **102**, 131107 (2013).

[122] P. Kekicheff and O. Spalla, 'Refractive index of thin aqueous films confined between two hydrophobic surfaces', Langmuir **10**, 1584 (1994).

[123] S. Gómez-Graña, F. Hubert, F. Testard, A. Guerrero-Martínez, I. Grillo, L. M. Liz-Marzán and O. Spalla, 'Surfactant (bi)layers on gold nanorods', Langmuir **28**, 1453 (2011).

[124] B. Goris, S. Bals, W. V. den Broek, E. Carbó-Argibay, S. Gómez-Graña, L. M. Liz-Marzán and G. V. Tendeloo, 'Atomic-scale determination of surface facets in gold nanorods', Nat. Mater. **11**, 930 (2012).

[125] C. Sönnichsen, T. Franzl, T. Wilk, G. von Plessen, J. Feldmann, O. Wilson and P. Mulvaney, 'Drastic reduction of plasmon damping in gold nanorods', Phys. Rev. Lett. **88**, 077402 (2002).

[126] O. L. Muskens, G. Bachelier, N. Del Fatti, F. Vallée, A. Brioude, X. Jiang and M.-P. Pileni, 'Quantitative absorption spectroscopy of a single gold nanorod', J. Phys. Chem. C **112**, 8917 (2008).

[127] L. S. Slaughter, W.-S. Chang, P. Swanglap, A. Tcherniak, B. P. Khanal, E. R. Zubarev and S. Link, 'Single-particle spectroscopy of gold nanorods beyond the quasi-static limit: Varying the width at constant aspect ratio', J. Phys. Chem. C **114**, 4934 (2010).

[128] C. J. Orendorff and C. J. Murphy, 'Quantitation of metal content in the silver-assisted growth of gold nanorods', J. Phys. Chem. B **110**, 3990 (2006).

[129] K.-S. Lee and M. A. El-Sayed, 'Dependence of the enhanced optical scattering efficiency relative to that of absorption for gold metal nanorods on aspect ratio, size, end-cap shape, and medium refractive index', J. Phys. Chem. B **109**, 20331 (2005).

[130] W. L. Barnes, 'Comparing experiment and theory in plasmonics', J. Opt. A: Pure Appl. Opt. **11**, 114002 (2009).

[131] L. M. Payne, W. Langbein and P. Borri, 'Wide-field imaging of single-nanoparticle extinction with sensitivity better than 1 nm^2', Phys. Rev. Appl., accepted (Dec 2017).

[132] P. Kukura, M. Celebrano, A. Renn and V. Sandoghdar, 'Single-molecule sensitivity in optical absorption at room temperature', J. Phys. Chem. Lett. **1**, 3323 (2010).

[133] M. Celebrano, P. Kukura, A. Renn and V. Sandoghdar, 'Single-molecule imaging by optical absorption', Nat. Photonics **5**, 95 (2011).

[134] W. Langbein, P. Borri, L. Payne and A. Zilli, 'Analysing nano-objects', British pat. req. GB1,711,886.0 (24th July 2017).

DECLARATION AND STATEMENTS

DECLARATION This thesis has not been submitted in substance for any other degree or award at this or any other university or place of learning, nor is being submitted concurrently in candidature for any other degree or award.

Signed _____ Date _____

STATEMENT This thesis is being submitted in partial fulfilment of the requirements for the degree of PhD.

Signed _____ Date _____

STATEMENT This thesis is the result of my own independent work/investigation, except where otherwise stated, and the thesis has not been edited by a third party beyond what is permitted by Cardiff University's Policy on the Use of Third Party Editors by Research Degree Students. Other sources are acknowledged by explicit references. The views expressed are my own.

Signed _____ Date _____

STATEMENT I hereby give consent for my thesis, if accepted, to be available online in the University's Open Access repository and for inter-library loans after expiry of a bar on access previously approved by the Academic Standards & Quality Committee.

Signed _____ Date _____